Experimental and Numerical Investigation of Multi-phase Multicomponent Drug Delivery through a Patient-specific Respiratory Airway using Pressurized Metered-dose Inhalers (pMDIs)

by

Mahsa Jahed

M.Sc., Tabriz University of Technology, Tabriz, Iran, 2017

B.Sc., University of Isfahan, Isfahan, Iran, 2014

A Thesis Submitted to
The Faculty of Graduate Studies of
Lakehead University
in partial fulfillment of the requirements of the degree of
Doctor of Philosophy, Biotechnology

Thunder Bay, Ontario, Canada, 2025

*To my loving husband, **Amir**, the light of my life, whose love, patience, and encouragement carried me through moments of doubt and inspired me to keep moving forward.*

*To my dear **mother** and **father**, whose sacrifices and unconditional love have made everything possible and whose faith in me has always lifted me higher.*

*To my beloved brother, **Sajjad**, whose kindness and unwavering belief in me have been a constant reminder that I never walk alone on this journey.*

Author's Declaration

I, **Mahsa Jahed**, do hereby declare that I am the sole composer of this document and that this document has not been submitted, in whole or in part, in any previous application for a degree or professional qualification. This document has been authored solely by myself and is comprised of my own work, except where otherwise stated by reference or acknowledgement.

I authorize Lakehead University to lend this document to other institutions and/or other individuals for the purpose of academic and/or scholarly research. I further authorize Lakehead University to reproduce this document, in whole or in part, via photocopying and/or digital scanning at the request of other institutions and/or individuals for the purpose of academic and/or scholarly research.

I authorize Lakehead University to make this document available electronically to the public.

Mahsa Jahed

Abstract

Experimental and Numerical Investigation of Multi-phase Multicomponent Drug Delivery through a Patient-specific Respiratory Airway using Pressurized Metered-dose Inhalers

Mahsa Jahed

Respiratory diseases such as asthma and chronic obstructive pulmonary disease (COPD) are among the leading causes of morbidity and mortality worldwide, and their treatment often relies on efficient delivery of aerosolized drugs to the lungs. Pressurized metered-dose inhalers (pMDIs) remain the most widely used devices for this purpose due to their portability, affordability, and rapid therapeutic action; however, their efficiency is limited by a complex interplay of actuator design, airway geometry, breathing pattern, and inhalation technique. To address these challenges, this thesis presents a comprehensive, multi-scale investigation that integrates computational fluid dynamics (CFD) with in vitro validation and patient-specific airway modelling. Large-eddy simulation (LES) resolved the transient airflow structures, while a Lagrangian discrete-phase model (DPM) and a four-way coupled dense-discrete-phase model (DDPM) captured aerosol transport and deposition behaviour. In-vitro experiments using 3D-printed airway replicas, a next-generation impactor (NGI), and high-performance liquid chromatography (HPLC) provided quantitative validation of the numerical results. The integrated approach systematically examined the coupled effects of actuator geometry, thermal conditions, mucus presence, airway dynamics, and real-life inhalation irregularities on pMDI performance. Twin-nozzle actuators produced higher jet velocities and plume collapse, leading to increased mouth–throat deposition. Thermal analysis revealed that cooling the plume from 10 °C to –54 °C reduced overall deposition by ~15% and enlarged the mean deposited particle size by ~34.5%. Mucus enhanced deposition efficiency by up to 11%, particularly under colder plume conditions. Patient-specific analyses revealed that female COPD airways experienced stronger turbulence and higher mouth–throat deposition, while transient breathing reduced upper-airway losses by up to 67% compared to steady inhalation. Dynamic wall motion slightly decreased overall deposition but had a limited influence due to the brief injection duration of pMDIs. Simulations of irregular breathing behaviors such as coughing and premature exhalation, indicated strong vortex formation and redirection of fine particles, leading to significant drug loss. Finally, a comparison between one-way and four-way coupled frameworks demonstrated that although the LES and k–ω–DPM models predicted similar overall

deposition fractions, the k–ω–DDPM model revealed distinct flow attenuation and particle redistribution toward downstream regions, driven by interphase momentum exchange and particle–particle interactions. Despite slightly underestimating total deposition relative to in vitro data, the DDPM framework provided critical insight into the dense-phase behaviour of pMDI aerosols and their influence on jet dynamics. Altogether, this work establishes a unified understanding of aerosol transport mechanisms in realistic airways, emphasizing that optimal pMDI performance requires both improved device design and patient-tailored inhalation strategies for effective and consistent pulmonary drug delivery.

Acknowledgements

I am profoundly grateful to my supervisor, Dr. Leila Pakzad, for her steadfast support and exceptional mentorship throughout my research. I also thank my co-supervisor, Dr. Janusz Kozinski, for his valuable insights and technical guidance.

My sincere thanks go to Dr. Francisco Ramos Pallares, Dr. Muhammad Khalid, and Dr. Zahra Keshavarz-Motamed for their constructive feedback and thoughtful evaluation of this work. I also extend my appreciation to Dr. Brenda Magajna and Dr. Ahmed Elshaer for their valuable roles in organizing and facilitating the defense session.

A warm thank you to my labmates, Farnia Dastoorian, Taha Sadeghi, and Mona Mohammadkhani, at the Multi-Phase Flow Research (MFR) lab, for their unwavering support and companionship throughout this journey.

I would like to acknowledge Lakehead University for providing access to LUHPCC, as well as the Digital Research Alliance of Canada for their high-performance virtual computing platforms, which greatly accelerated the progress of this study. This research would not have been possible without the financial support from the Natural Sciences and Engineering Research Council of Canada, for which I am sincerely thankful. My thanks also go to the Ingenuity Centre at Lakehead University and the Engineering Student Society Maker Space for supplying a 3D printer, and to the Department of Chemistry at Lakehead University for providing access to the HPLC instrument.

Contents

Table of Figures

Table of Tables

Chapter 1 - Introduction

1.1 Introduction

Respiratory diseases are among the major public health problems, which cause thousands of deaths each year in industrialized countries. Pulmonary drug delivery, which involves the inhalation of drug particles through the oral or nasal cavity into the respiratory tract, plays a crucial role in the treatment or control of these diseases (Ahookhosh et al., 2021; Lim et al., 2021). For effective treatment, the amount of drug that reaches or deposits in the lungs, and the amount lost due to deposition in the mouth-throat (MT) region, are essential measurements. The drug deposited in the MT region is important to measure because the drug in this area is often associated with local and systemic side effects, as well as reduced drug availability at the site of action (i.e., the lungs) (Kaviratna et al., 2019). The deposition pattern in the lungs depends on both biological and physical factors. The biological factors include the lung's geometrical structure, different breathing patterns, and the viscous mucus layer and periciliary layer. On the other hand, physical factors include fluid–particle dynamics, fluid dynamics, particle physical properties (Islam et al., 2019).

The four main delivery systems for inhaled therapies are nebulizers, pressurized metered-dose inhalers (pMDIs), dry powder inhalers (DPIs), and soft mist inhalers (SMIs). Each system generates fine particles suitable for inhalation through distinct mechanisms and possesses unique features. An analysis of lung deposition data showed that most inhaler systems deliver only a small percentage of the dose to the lungs (Newman, 2017). Therefore, there remains a significant need to further optimize drug delivery. Current inhalers still result in a substantial portion of the drug being lost due to oropharyngeal deposition or exhalation before reaching the lungs. Therefore, increasing the fraction of the drug that successfully deposits in the lungs while minimizing wastage is essential (Newman, 2017; Oliveira et al., 2012; Sou and Bergström, 2021).

The pMDI is the most commonly used device; however, treatment efficiency is often low, with only 5–30% of the drug reaching the intended target (F. Huang et al., 2021; Kunda et al., 2017; McKiernan, 2019; Sheth et al., 2017). Over the past few decades, numerous studies have provided valuable insights into how key parameters affect pMDI performance. However, a comprehensive understanding of the complex mechanisms governing effective drug delivery through these devices

is still lacking. Despite advancements, significant gaps remain, particularly in the availability of reliable *in-silico* data, which now plays a central role in device design and optimization.

Based on these considerations, the main objective of this thesis is to investigate the impact of key factors on pMDI performance and contribute to the optimization of inhaler-based drug delivery systems. This research study combines experimental and *in-silico* approaches to comprehensively examine multiphase, multicomponent drug delivery in a patient-specific respiratory airway model.

1.2 Thesis Structure

This thesis is categorized into ten chapters.

1. This chapter introduces the fundamentals of inhalation therapy and outlines the critical factors influencing drug delivery efficiency across various inhaler types. It provides an overview of various delivery mechanisms and highlights the challenges and opportunities in optimizing aerosolized drug administration, thereby laying the foundation for the study.

2. A comprehensive literature review is presented with a focus on pMDIs. The chapter examines how key parameters, including airway geometry, airflow rate, mucus presence, airflow and aerosol temperature conditions, and particle size, affect pMDI performance. The review identifies current knowledge gaps and sets the stage for the subsequent experimental and numerical investigations.

3. This chapter outlines the experimental methodology employed in the study, including the theoretical background and the instrumentation used. It discusses the use of the Next Generation Impactor (NGI) for aerodynamic particle sizing and High-Performance Liquid Chromatography (HPLC) for drug quantification. The integration of 3D printing for fabricating anatomically accurate airway models is also described.

4. This chapter introduces the application of computational fluid dynamics (CFD) to simulate airflow and particle transport in human airways. It outlines the governing equations and emphasizes the role of advanced turbulence modeling strategies, particularly the Reynolds-Averaged Navier-Stokes (RANS) equations with the k-ω model and Large Eddy Simulation (LES), in capturing complex flow behavior. The chapter also presents the Discrete Phase Model (DPM) as a key framework for modeling particle dynamics and their interactions with the continuous airflow.

5. This chapter examines the impact of actuator nozzle design and environmental conditions on the efficiency of drug delivery using pressurized metered-dose inhalers (pMDIs). Two nozzle types, single conventional and twin nozzle, are compared using CFD to evaluate deposition patterns in the MT region. The study reveals that the behaviour of aerosol plumes significantly differs between open-air and anatomically realistic airway environments. Moreover, the twin-nozzle design, despite producing higher aerosol velocities, results in increased drug deposition in the MT region, suggesting potential inefficiencies from premature deposition. This study was published in *Biomechanics and Modeling in Mechanobiology*.

6. In this chapter, both experimental and numerical analyses are conducted to assess the effects of plume temperature, airway temperature, and the mucus layer on drug deposition in a realistic MT geometry. Using a 3D-printed replica, *in-vitro* measurements are validated with CFD simulations incorporating LES and DPM models. The results show that colder plume temperatures reduce overall deposition but increase the size of deposited particles, with changes in airflow pattern being the dominant influencing factor. Mucus is found to affect localized deposition patterns and efficiency under varying thermal and flow conditions. This study was published in the *Journal of Aerosol Science*.

7. This chapter presents a comparative investigation of aerosol deposition in two patient-specific airway geometries, male and female models. Using validated CFD models with LES and DPM model, the study examines the effects of airway wall motion, breathing patterns, and mucus presence. The findings demonstrate significant gender-based differences in airflow and deposition. While dynamic wall motion slightly reduces total deposition, its effect is constrained by the brief duration of pMDI injection. Mucus plays a substantial role in altering local airflow and the distribution of shear stress. This study was published in the *Journal of Drug Delivery Science and Technology*.

8. This chapter presents the effects of inhalation irregularities on particle transport and deposition. Using a realistic male airway geometry extending from the mouth to the fourth bronchial generation, we focus on understanding the behaviour of particles emitted from a pMDI when the patient experiences a sudden interruption during inhalation, such as an unexpected pause, unintentional exhalation, or an urge to cough. Even brief disturbances markedly alter airflow and turbulence, increasing upper-airway impaction and reducing distal deposition. These

findings emphasize the importance of proper inhalation techniques for consistent pMDI drug delivery. This study was published in *Pharmaceutical Research*.

9. This chapter enhances the realism of inhaled drug simulation by implementing a dense discrete phase model (DDPM) with full four-way coupling. The model accounts for interactions among particles, airflow, walls, and inter-particle collisions. The simulation includes both the active pharmaceutical ingredient (API) and the hydrofluoroalkane (HFA) propellant, representing the complete aerosol formulation. Although the DDPM framework slightly underestimates overall deposition relative to experimental data, it captures regional deposition trends more accurately. This study offers a deeper understanding of aerosol–airflow coupling in pMDI delivery and underscores the importance of dense-phase modelling for realistic inhalation simulations. This study is currently under review in *Powder Technology*.
10. The final chapter summarizes the significant findings across all experimental and computational studies. Recommendations for future work and potential improvements in pMDI-based drug delivery systems are also discussed.

1.3 Nomenclature

Abbreviations

3D	three dimensional
API	active pharmaceutical ingredient
CFD	computational fluid dynamics
DDPM	dense discrete phase model
DPIs	dry powder inhalers
DPM	discrete phase model
HFA	hydrofluoroalkane
HPLC	high-performance liquid chromatography
LES	large eddy simulation
MT	mouth-throat
NGI	next generation impactor
pMDIs	pressurized metered-dose inhalers
RANS	Reynolds-averaged Navier-Stokes

SMIs	soft mist inhalers

1.4 References

Ahookhosh, K., Saidi, M., Mohammadpourfard, M., Aminfar, H., Hamishehkar, H., Farnoud, A., Schmid, O., 2021. Flow structure and particle deposition analyses for optimization of a pressurized metered dose inhaler (pMDI) in a model of tracheobronchial airway. Eur. J. Pharm. Sci. 164, 105911. https://doi.org/10.1016/j.ejps.2021.105911

Huang, F., Zhang, Y., Tong, Z.B., Chen, X.L., Yang, R.Y., Yu, A.B., 2021. Numerical investigation of deposition mechanism in three mouth–throat models. Powder Technol. 378, 724–735. https://doi.org/10.1016/j.powtec.2018.11.095

Islam, M.S., Saha, S.C., Sauret, E., Ong, H., Young, P., Gu, Y., 2019. Euler–Lagrange approach to investigate respiratory anatomical shape effects on aerosol particle transport and deposition. Toxicol. Res. Appl. 3, 239784731989467. https://doi.org/10.1177/2397847319894675

Kaviratna, A., Tian, G., Liu, X., Delvadia, R., Lee, S., Guo, C., 2019. Evaluation of bio-relevant mouth-throat models for characterization of metered dose inhalers. AAPS PharmSciTech 20, 130. https://doi.org/10.1208/s12249-019-1339-6

Kunda, N.K., Hautmann, J., Godoy, S.E., Marshik, P., Chand, R., Krishna, S., Muttil, P., 2017. A novel approach to study the pMDI plume using an infrared camera and to evaluate the aerodynamic properties after varying the time between actuations. Int. J. Pharm. 526, 41–49. https://doi.org/10.1016/j.ijpharm.2017.04.051

Lim, S.H., Park, S., Lee, C.C., Ho, P.C.L., Kwok, P.C.L., Kang, L., 2021. A 3D printed human upper respiratory tract model for particulate deposition profiling. Int. J. Pharm. 597. https://doi.org/10.1016/j.ijpharm.2021.120307

McKiernan, A.P., 2019. Inhaler spray investigation using high-speed phase-contrast X-Ray and schlieren imaging. Pharm. Res. 36. https://doi.org/10.1007/s11095-019-2657-9

Newman, S.P., 2017. Drug delivery to the lungs: challenges and opportunities. Ther. Deliv. 8, 647–661. https://doi.org/10.4155/tde-2017-0037

Oliveira, R.F., Teixeira, S., Teixeira, J.C., Silva, L.F., Antunes, H., 2012. pMDI sprays: theory, experiment and numerical simulation, in: Liu, C. (Ed.), Advances in Modeling of Fluid Dynamics. IntechOpen, Rijeka. https://doi.org/10.5772/46099

Sheth, P., Grimes, M.R., Stein, S.W., Myrdal, P.B., 2017. Impact of droplet evaporation rate on resulting in vitro performance parameters of pressurized metered dose inhalers. Int. J. Pharm. 528, 360–371. https://doi.org/10.1016/j.ijpharm.2017.06.014

Sou, T., Bergström, C.A.S., 2021. Contemporary formulation development for inhaled pharmaceuticals. J. Pharm. Sci. 110, 66–86. https://doi.org/10.1016/j.xphs.2020.09.006

Chapter 2 - Literature Review

2.1 Anatomy of the Human Respiratory Airway

The human respiratory tract is a very complex structure. It consists of the extrathoracic (ET) region, the tracheobronchial (TB) region (including the bronchial region, the bronchiolar region) and the alveolar region, as schematically shown in **Fig. 2-1**. The ET region, also known as the upper respiratory tract, is comprised of the oral cavity, nasal cavities, pharynx, and larynx. The pharynx is further subdivided into three parts based on its anatomical position, including oropharynx (posterior to the mouth), nasopharynx (posterior to the nasal chambers) and laryngopharynx (posterior to the pharynx). The TB region is the area from the trachea to the terminal bronchi (i.e., Generations 0-16). The primary function of the TB region is to conduct air to the gas-exchange regions (i.e., the alveolar region). The two airways branching from the trachea are called the main bronchus. These branches enter the large lobe bronchi (two in the left lung and three in the right lung) and then branch into segmental bronchi. The alveolar region refers to the G17–G23 region where gas exchange occurs (Fen Huang et al., 2021; Lim et al., 2021).

The inner surface of the airways is lined by airway surface liquid (ASL), a thin layer of fluid. For approximately the first 16 generations, ASL is a bilayer, with a serous sublayer (similar to serum) and a mucus layer on top. Although the serum predominantly exhibits Newtonian behaviour, airway mucus is often reported as highly non-Newtonian (Cone, 2009; Erken et al., 2023). Approximately 90–95% of airway mucus consists of water, followed by high-molecular-weight mucin glycoproteins at 2–5%. It additionally includes fractional amounts of lipids, salts, and cell debris (Erken et al., 2023; Haut et al., 2021). An essential function of the airway ASL is to condition inhaled air. Heat is supplied by the tissues surrounding the respiratory tract to the ASL–lumen interface, allowing the air in the lumen to warm up and the water in the ASL to evaporate (Haut et al., 2021).

Asthma and chronic obstructive pulmonary disease (COPD) both lead to airway wall inflammation. In asthma, the thickness of the internal airway wall tissue, including the smooth muscle layer, increases, leading to a reversible rise in airway resistance (Kuwano et al., 1993). This increase typically ranges from 34% to 51% compared to the normal level of 24% (Yanai et al., 1992). This thickening, combined with the normal shortening of smooth muscles, contributes

to the abnormalities in airway function. In COPD, the walls of the airways become thicker both inside and outside the smooth muscle layer. This thickening contributes to increased airway responsiveness and sensitivity in COPD (Kuwano et al., 1993). Given these structural and functional alterations in the airways, effective drug delivery becomes critical to managing both asthma and COPD. One of the most widely used devices for this purpose is the pressurized metered-dose inhaler (pMDI).

2.2 Pressurized Metered-Dose Inhalers (pMDIs)

The first pMDI was introduced in 1956 (Ahookhosh et al., 2019; McKiernan, 2019). It is the most commonly prescribed and favored device among both physicians and patients. Its popularity stems from its compact size, portability, affordability, and ability to deliver consistent doses (Ahookhosh et al., 2021). The pMDI design consists of three parts, as shown in **Fig. 2-2**: a disposable canister where drug, liquid propellant and/or excipients are stored, a metering valve which ensures a correct dose of the formulation is delivered, and a plastic actuator for atomization (Chen et al., 2017; Ogrodnik et al., 2016). The pMDI formulation contains the drug in solution or suspension form and includes a highly volatile propellant (e.g., hydrofluoroalkane (HFA)-134a or HFA-227) that enables atomization. It also incorporates other components, such as volatile excipients (e.g., cosolvents, such as ethanol) or non-volatile excipients (e.g., surfactants, such as oleic acid), which facilitate interaction between the drug and the propellant (Sheth et al., 2017).

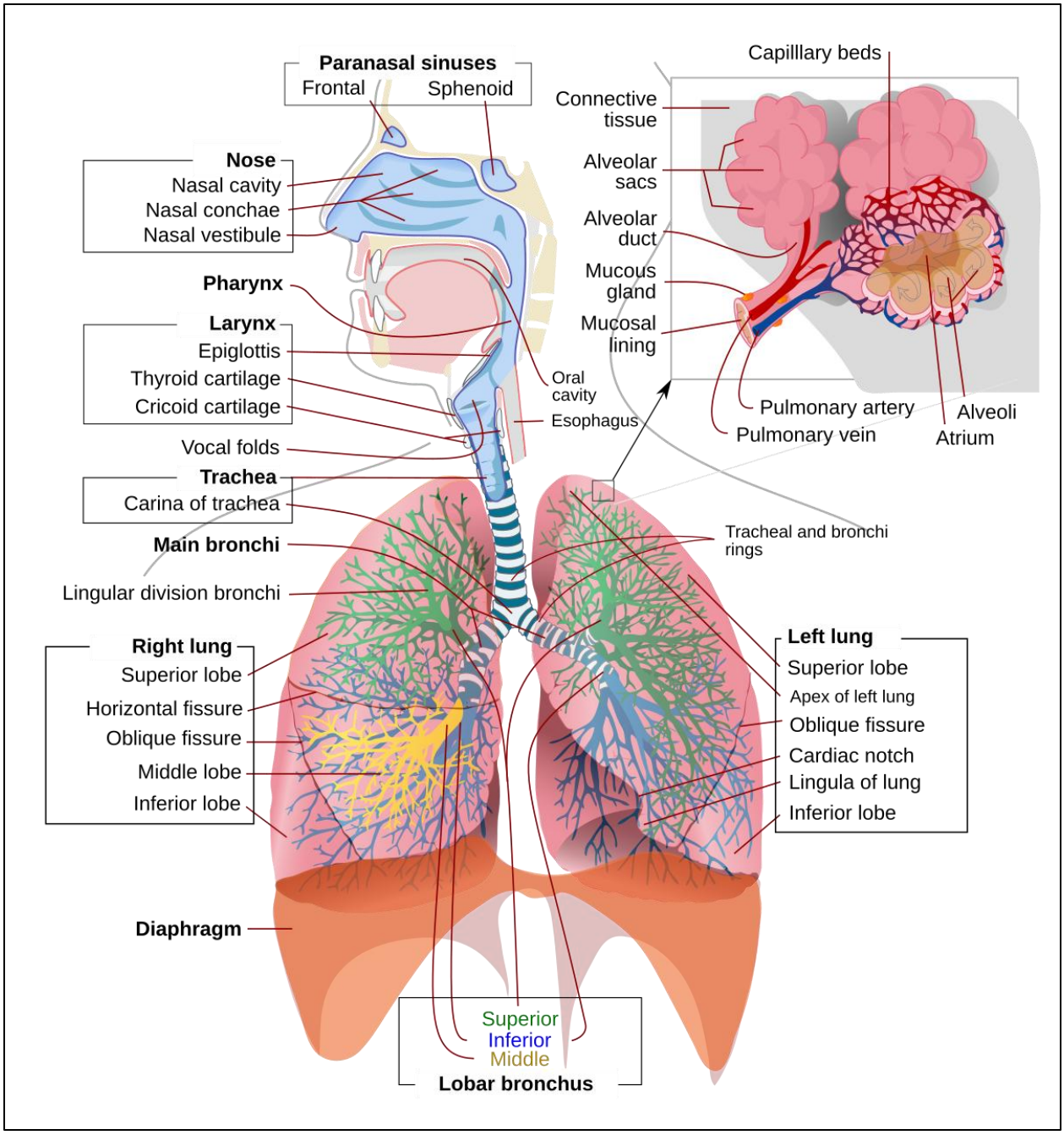

Fig. 2-1: A schematic of the structures of the human respiratory system, including the oral and nasal cavity, pharynx, trachea, bronchi, and lungs (Adapted from CFCF, Anatomy of the upper and lower airways, Wikimedia Commons, CC BY-SA 3.0).

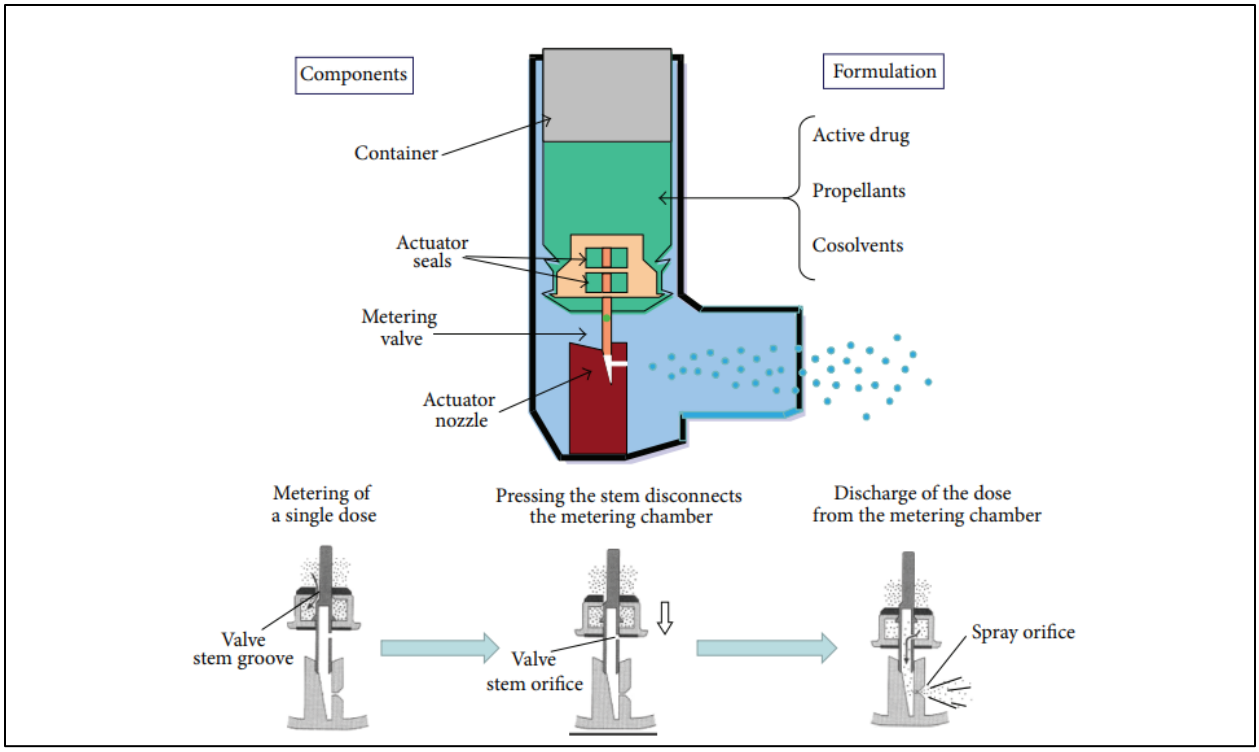

Fig. 2-2: Components of a pressurized metered-dose inhaler and the process of aerosol generation (Lavorini, 2013).

Actuation of pMDI occurs within a very short period (0.1–0.2 s), and the spray droplets exit the nozzle at high speeds (100-150 m/s) (Talaat et al., 2022b). During actuation, the pressure generated by the propellant transforms the dissolved or suspended drug into a liquid-gas spray. As the propellant and any co-solvents evaporate, this spray forms aerosol particles. The characteristics of the spray plume and the resulting particle size are primarily influenced by the propellant's vapor pressure, formulation components, metering valve, ambient conditions, and the design of the actuator nozzle (Chen et al., 2017; Smyth et al., 2006). To quantify these characteristics, Alatrash and Matida (2016) used Phase Doppler Anemometry (PDA) to measure particle size distributions (PSDs) across various pMDI types. **Fig. 2-3** illustrates the PSD measured for the Ventolin HFA pMDI and three fitted probability density functions: Rosin-Rammler, Log-normal, and Nakagami. The histogram shows a right-skewed distribution with a peak around 2 µm. Among the fitted models, the Rosin-Rammler distribution closely matches the measured data across the entire range, particularly in capturing the gradual decay in the tail region. In contrast, the Log-normal distribution overestimates the peak probability at smaller diameters, while the Nakagami distribution underestimates the likelihood in the mid-to-large diameter range.

As these particles travel through the respiratory tract, several complex mechanisms govern their deposition, the main ones including inertial impaction, gravitational sedimentation, and Brownian diffusion. Additional factors, such as turbulence-induced mixing, electrostatic precipitation, and interception — particularly for elongated particles like fibres — also contribute to aerosol deposition (Darquenne, 2020).

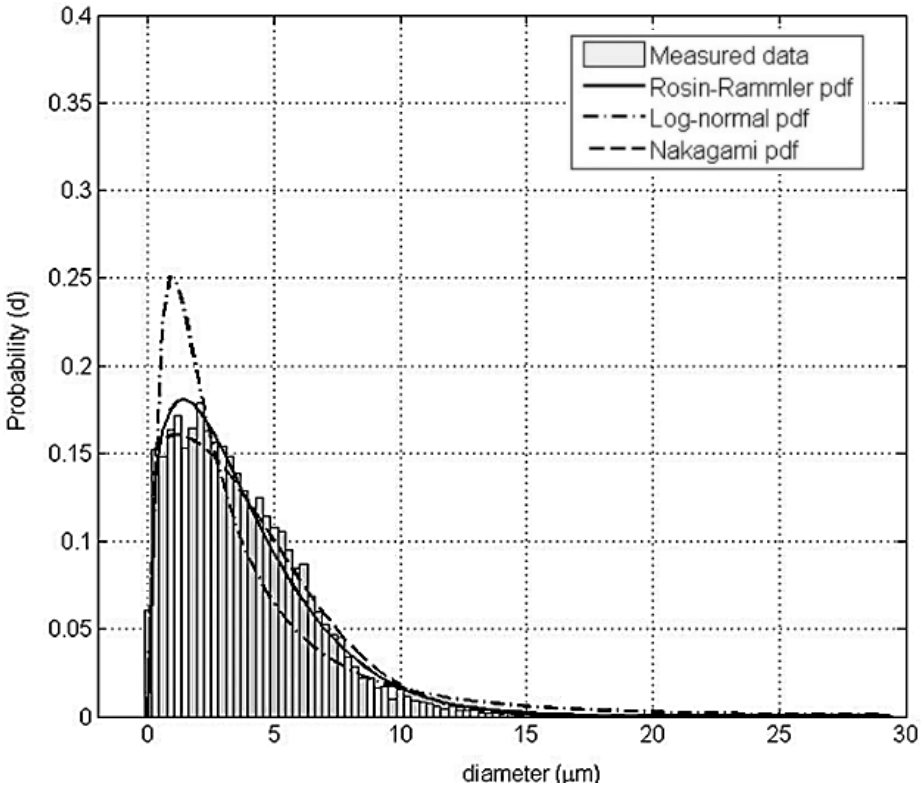

Fig. 2-3: Histogram of the experimental data of particle diameter for Ventolin HFA with curve fitting of probability distribution functions (at 0 mm) (Alatrash and Matida, 2016).

Inertial impaction is the dominant deposition mechanism for particles larger than 5 μm and can also affect particles as small as 2 μm, depending on the airflow rate. It occurs when airflow changes direction abruptly, causing particles, due to their inertia, to continue along their original paths and collide with airway walls, leading to their deposition. The tendency of a particle to deviate from airflow streamlines is characterized by the Stokes number (Stk), which quantifies this behavior based on the particle's properties and flow conditions. It is defined as:

$$\mathrm{Stk} = \rho_p d_p^2 u / 18 \mu d \tag{2.1}$$

where ρ_p and d_p are the density and diameter of the particle, respectively. u and μ are the velocity and dynamic viscosity of air, and d is the airway diameter (Finlay, 2019).

Deposition by gravitational sedimentation is most effective for particles in the 1–8 μm size range. Gravitational sedimentation refers to the process by which particles settle to the bottom under the influence of gravity. When the gravitational force equals the opposing viscous resistive forces of the air, particles reach their terminal settling velocity. The third main mechanism of deposition in the lung is Brownian diffusion, which results from particles' random motion due to collisions with gas molecules. Unlike impaction and sedimentation, deposition by Brownian diffusion increases with decreasing particle size and becomes the dominant mechanism of deposition for particles <0.5 μm in diameter. Deposition by Brownian diffusion primarily occurs in the acinar region of the lungs. However, it should be noted that for very small particles (smaller than 0.01 μm), deposition by diffusion is also significant in the nose, mouth, and pharyngeal airways (Darquenne, 2020; Finlay, 2001).

Studies reported that aerodynamic diameters in the range from 0.5 to 3 μm will result in alveolar deposition, in the range from 2 μm to 6 μm will result in tracheobronchial deposition, and greater than 5 μm will result in deposition in the upper airways (Borojeni et al., 2023; Gurumurthy and Kleinstreuer, 2021; Kadota et al., 2022; Mirzaaghaian et al., 2024; Zhang et al., 2017). Although a significant portion of aerosol particles emitted by pMDIs, around 40%, fall within the respirable range (mass median aerodynamic diameter < 5 μm), and dosing is generally consistent from puff to puff, pMDIs remain relatively inefficient. For HFA-based pMDIs that generate extra-fine particles, only about 40%–50% of the emitted dose actually reaches the lungs. A substantial amount of the drug is instead deposited in the mouth and oropharynx, potentially leading to both local and systemic side effects due to rapid absorption (Lavorini, 2013). This highlights the need for optimized device design and improved user education, both of which depend on a detailed understanding of device performance and the parameters that influence drug delivery efficiency.

Another important consideration is the plume temperature from the pMDI. Brambilla et al. (2011) measured the aerosol plumes emitted from various pMDIs formulated with different drug types, propellants, and co-solvent contents to assess the impact of these formulation variables on plume characteristics. **Fig. 2-4** illustrates the variation in Mean Minimum Plume Temperature (MMPT) with distance from the actuator mouthpiece for different HFA-based pMDIs. Qvar with 50- and 100-μl metering valves maintains a relatively stable, warmer plume temperature across all distances. At the same time, Flixotide and Ventolin Evohalers exhibit significantly colder plumes

near the mouthpiece, with MMPTs dropping below –50 °C at 20 mm. As the distance increases, temperatures gradually rise and converge for all devices, reaching a range of 0–5 °C. This temperature is too low, and it may reduce delivery efficiency and cause adverse sensory experiences for the patient.

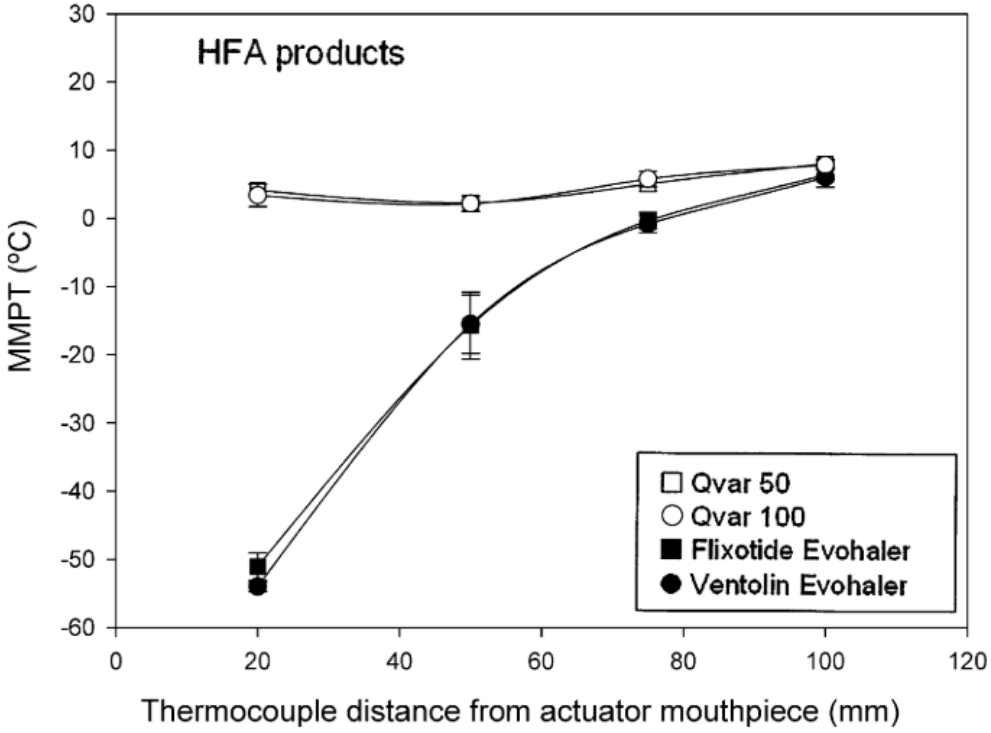

Fig. 2-4: MMPT for marketed products as a function of thermocouple distance from the actuator mouthpiece (n=5, mean ± standard deviation) (Brambilla et al., 2011).

2.3 Factors Influencing pMDI Drug Delivery Efficiency

The effectiveness of pMDIs in delivering medication to the lower respiratory tract depends on a complex interplay of factors. The inefficiency is influenced by multiple parameters, including patient-related factors such as inhalation technique, breath coordination, and actuation timing, as well as device-specific elements like aerosol particle size distribution, spray plume characteristics, and formulation properties. Moreover, anatomical variability of the airways and physiological breathing patterns can further affect the transport and deposition of aerosolized drugs.

It has been established that the mouth-throat (MT) geometry is highly variable within and among subjects. Furthermore, the extrathoracic deposition of inhaled pharmaceutical aerosols is significantly influenced by MT geometry. As a result, high variability in the MT deposition of

these aerosols is expected and has been widely observed (Longest and Hindle, 2009). Kaviratna et al. (2019) investigated various bio-relevant MT models, including USP induction port (USP IP), Alberta Idealized Throat (AIT), and 3D printed large/medium/small-sized VCU (Virginia Commonwealth University) models, as shown in **Fig. 2-5** were evaluated using two MDI drug products: a solution MDI containing beclomethasone dipropionate (BDP-MDI) and a suspension MDI containing fluticasone propionate (FP-MDI). These *in-vitro* testing results demonstrated significant differences among MT models in deposition and fine particle fraction (FPF). The suspension MDI was more sensitive to geometric differences in the MT models than the solution. The lowest deposition observed for the USP IP was approximately 40%, whereas the small-volume VCU profile reached 80%.

In terms of the influence of geometry in a research study, Xi et al. (2018) developed a mouth–lung geometry model with controllable glottal apertures to numerically investigate the influence of glottis motion on airflow features. The glottis was specified to move in phase with the inhalation profile, which widens and contracts periodically at an amplitude typical of a human adult. They found that a wider glottal aperture decreased the mean flow speed and reduced the vortex intensity. There were two aspects regarding the widening glottis effects: a weaker laryngeal jet and a yielding boundary. When the velocity decreased, less kinetic energy was converted into vortex growth, which, in turn, diminished the transport of the vortex filament and the formation of ring vortices. Moreover, the expanding glottal aperture delayed the boundary layer separation by yielding to the laryngeal jet, thereby deferring the vortex growth.

Moreover, Sul et al. (2019) investigated the impact of tracheal size on airflow by comparing steady-state airflow in a rigid airway with that in airways exhibiting tracheal contraction. The study considered three levels of tracheal cross-sectional area reduction: 33% (mild), 50% (moderate), and 75% (severe). As shown in **Fig. 2-6**, during inhalation, tracheal contraction significantly alters airflow patterns in the trachea and lower-generation airways. Large deviations in airflow patterns under moderate and severe conditions suggest that, if tracheal contraction during inhalation results in a change in cross-sectional area of more than 50%, tracheal dynamics should be considered when investigating flow. In particular, the significant deviation in airflow patterns during moderate to severe contractions suggests that, unlike most computational models that assume rigid airways to predict drug delivery, airway contraction should be considered in the design of drug inhalers.

(a)

(b)

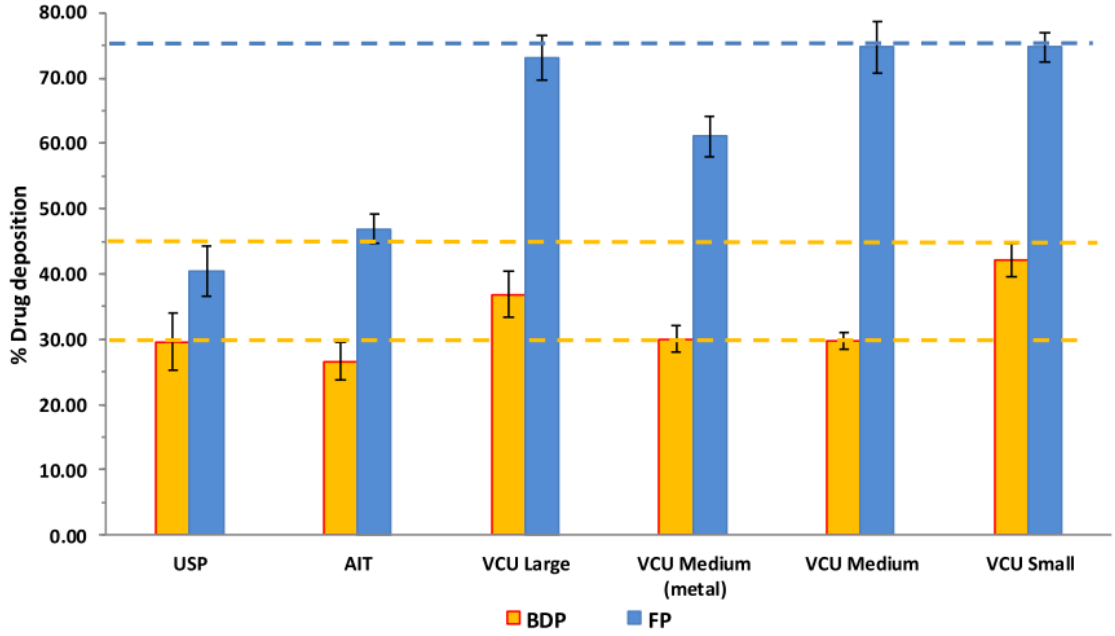

Fig. 2-5: (a) The USP induction port; Alberta Idealized Throat (AIT); large-, medium-, and small-sized VCU models in transparent resin; and VCU medium model in polished gold-plated steel; **(b)** the mouth-throat deposition (% emitted dose) of fluticasone propionate and beclomethasone dipropionate measured across various models (Kaviratna et al., 2019).

The influence of static deformation in the airway and dynamic wall motion on airflow dynamics was investigated by Gunatilaka et al. (2020). They compared five static computational fluid dynamics (CFD) simulations: four static models using airway surfaces obtained at four different phases of breathing, and one static model using the ungated airway, an average image over many breaths during the scan, with time-dependent wall motion.

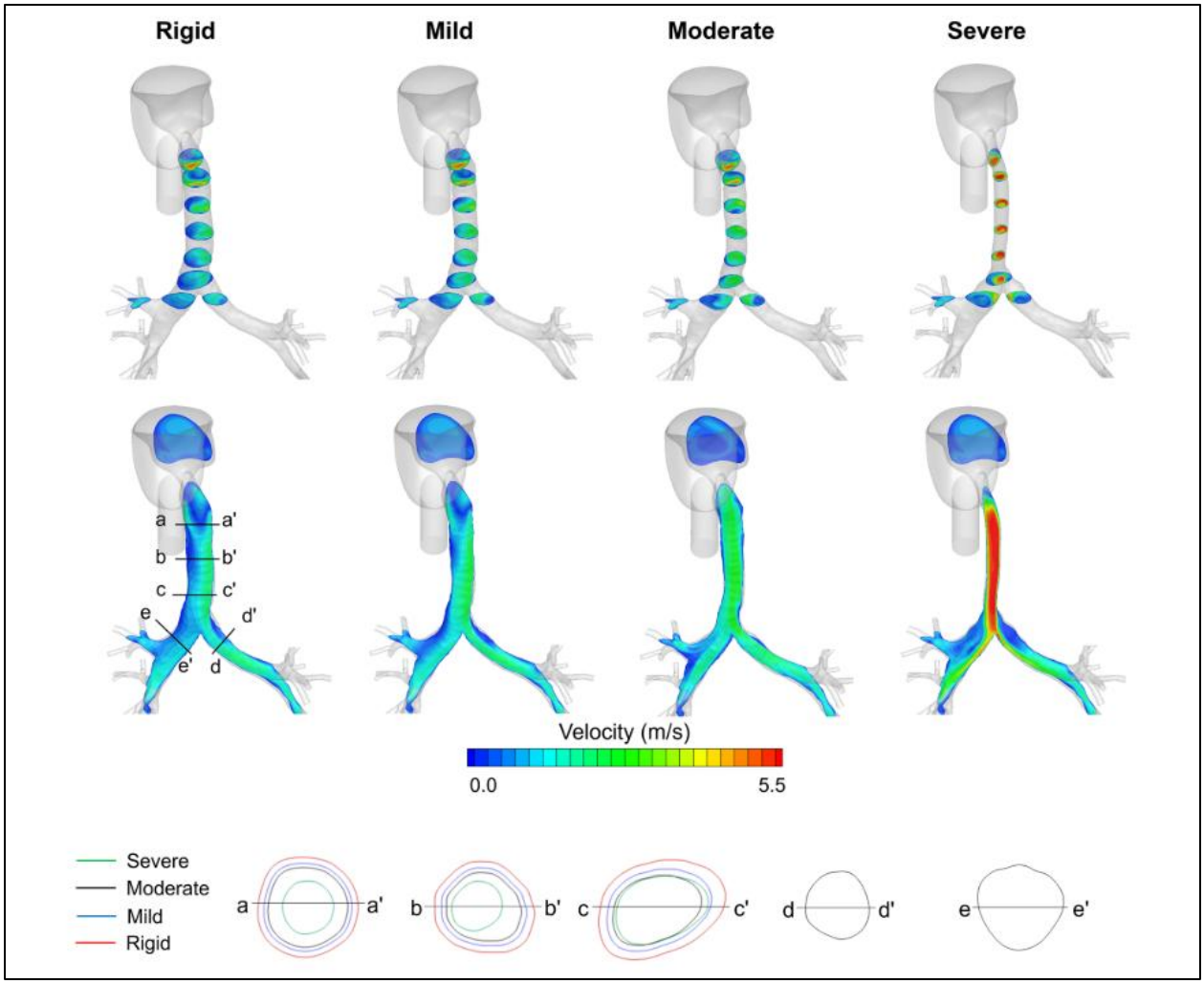

Fig. 2-6: Comparison of airflow velocity, for steady inhalation at a flow rate of 200 ml/s, between airways showing deformations of 0% (rigid), 33% (mild), 50% (moderate), and 75% (severe) of the maximal change in tracheal cross-sectional area (Sul et al., 2019).

This study demonstrated the importance of incorporating unsteady boundary conditions, including tracheal motion and airflow rates throughout the breathing cycle, when performing CFD simulations of respiratory airflow. The tracheal area varies considerably during the breathing cycle, particularly in its lower region, which directly affects the resulting respiratory airflow metrics. Indeed, this study found that airway resistance and pressure drop across the trachea differ significantly between dynamic and static airway simulations in both healthy and diseased conditions.

In addition to geometric influences, the breathing pattern itself plays a critical role in determining particle deposition efficiency throughout the respiratory tract. Liu et al. (2023) compare particle

deposition patterns under constant and circulatory respiration using a computed tomography (CT)-based human airway model that extends from the mouth to the fifth-generation bronchi. Simulations were conducted at flow rates of 30, 60, and 90 L/min with particle sizes of 5 and 10 µm. Results showed that most particles deposit in the oropharyngeal region, while the bronchial region sees increased deposition with smaller particles and lower inhalation velocities. For 5 µm particles, deposition patterns were similar between both breathing types. However, for 10 µm particles, circulatory respiration resulted in slightly higher deposition in the bronchial region at higher flow rates. In both respiration modes, particle deposition was greater in the right lung than in the left (**Fig. 2-7**).

(a) Constant Respiration **(b)** Circulatory Respiration

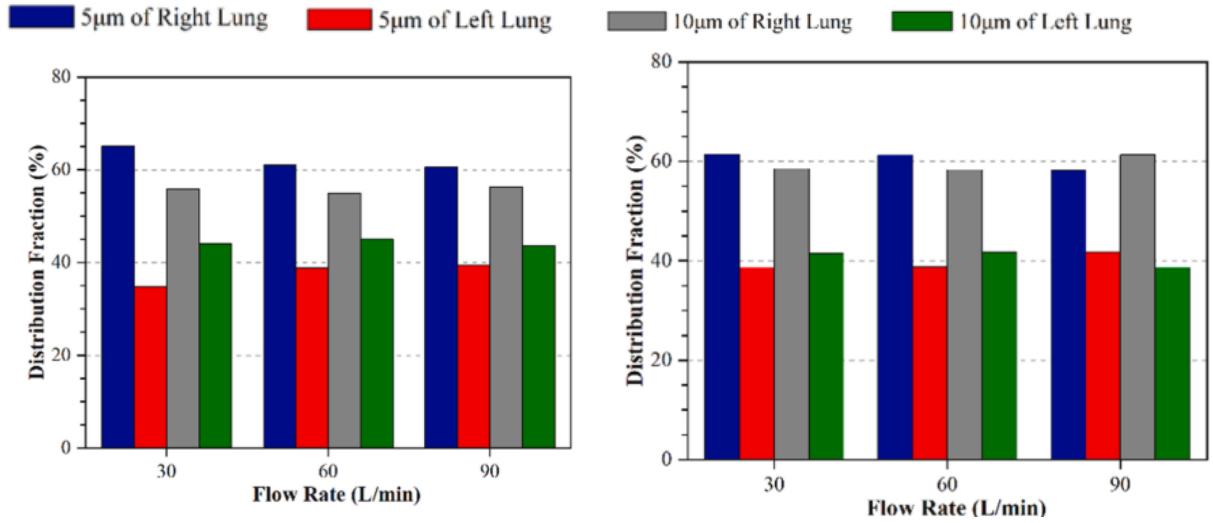

Fig. 2-7: The distribution fraction of particles within the bronchial region for: **(a)** Constant respiration; and **(b)** Circulatory respiration (Liu et al., 2023).

Also, a study by Ahookhosh et al. (2021) conducted a numerical investigation on aerosol deposition from a pMDI in a patient-derived human airway model across a wide range of inspiratory flow rates. Their results showed that increasing the inhalation flow rate from 30 to 120 L/min leads to higher particle inertia and turbulence levels, which results in higher particle deposition in the airways especially in the MT (from 15.6% to 36.4%), the trachea (from 1.2% to 6%) and the 3rd and 4th generations of the bronchial region (from 1.41% to 3.5%).

The role of ambient conditions, including humidity and temperature, is another key aspect in understanding the behavior of hygroscopic aerosols. Variations in water vapor concentration

within the airways can significantly influence particle trajectories, as changes in humidity can alter droplet size through evaporation or condensation processes. These size changes, in turn, affect particle momentum and ultimately determine the site of deposition within the respiratory tract (Rajaraman et al., 2020; Yang et al., 2023).

Aghaei et al. (2023) investigated the behavior of water droplets with an initial size of 1–30 μm in the nasal airways of a healthy male individual under cyclic inspiratory flow. They considered the effect of inhaled air humidity. **Fig. 2-8** illustrates the dispersion and size distribution of 5 μm water droplets from a lateral view of the left nasal cavity at the end of the inhalation phase (2 s). The results indicate that inhaled air humidity significantly influences droplet behaviour. At low humidity levels, a majority of the droplets evaporate, leaving only a few remaining in the nasal cavity. In contrast, higher humidity reduces droplet evaporation, resulting in a greater number of droplets at the end of inhalation.

Furthermore, accurately predicting the transport and deposition of hygroscopic aerosols requires accounting for heat transfer at the airway wall, including both convective heat transfer and latent heat of evaporation. Narayanan et al. (2022) incorporated mucus-layer and airway-tissue models to provide detailed predictions of flow and temperature fields using Large Eddy Simulation (LES). They investigated the effects of three particle sizes (3 μm, 5 μm, and 6 μm) at inlet flow rates of 15 L/min and 30 L/min, both in the presence and absence of a mucus layer. They modeled only the thermal effect of the mucus layer. The results (**Fig. 2-9**) indicate that for smaller particle sizes (3 μm), deposition primarily occurs in the throat region. As particle size increases, a greater number of particles begin to deposit in the mouth region. Although the presence of a mucus layer has a minimal effect on deposition locations, the total number of deposited particles increases significantly. For 6 μm particles, the presence of a mucus layer increased the deposition in MT from 0.68% to 4.13%. The mucus layer lowers the temperature near the MT wall compared to cases without mucus, exposing particles near the wall to a cooler flow. This reduction in temperature increases particle residence time in those regions, potentially leading to higher deposition rates. The effect of the mucus layer evaporation feature, in addition to convection heat transfer, was investigated by Chen et al. (2018). They considered a similar simplified MT model. Results demonstrated that the latent heat of evaporation can generate a temperature gradient in the mucus-tissue region, reducing the mucus layer's average temperature by up to 1.11 °C, whereas

convection alone results in only a 0.2 °C reduction. However, the combined heat transfer effect can locally lower the temperature to 32.81 °C. Considering latent heat loss from evaporation, the deposition efficiency can decrease by up to 9.93%.

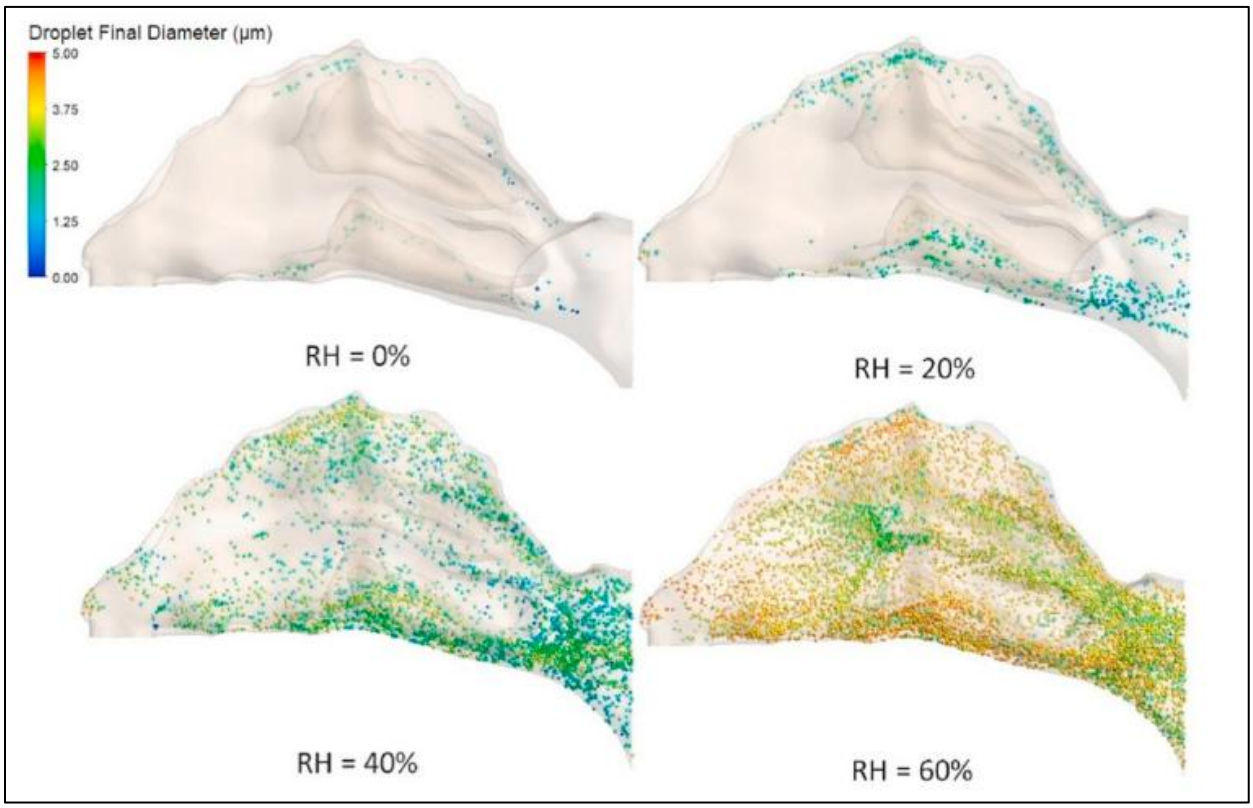

Fig. 2-8: The effect of inhaled air humidity on dispersion and size distribution of initial 5 µm droplets at the end of the inhalation phase (2 s) (Aghaei et al., 2023).

Considering the vital role of CFD modelling in this area and the rapid development and applications of CFD techniques, it is essential that the simulated behavior of particles closely matches *in-vivo* outcomes, allowing CFD to serve as a reliable alternative to *in-vivo* testing when sufficient accuracy is achieved. The studies outlined above have explored different modelling approaches, employing various turbulence and particle tracking models depending on their objectives. Turbulence models such as Reynolds-Averaged Navier–Stokes (RANS), LES, and Direct Numerical Simulation (DNS) have been used to capture the complex airflow characteristics within the respiratory tract. Similarly, particle-tracking methods, including Lagrangian and Eulerian approaches, have been used to simulate particle transport, deposition, and interactions with airflow under diverse conditions (Feng et al., 2021a; Fen Huang et al., 2021).

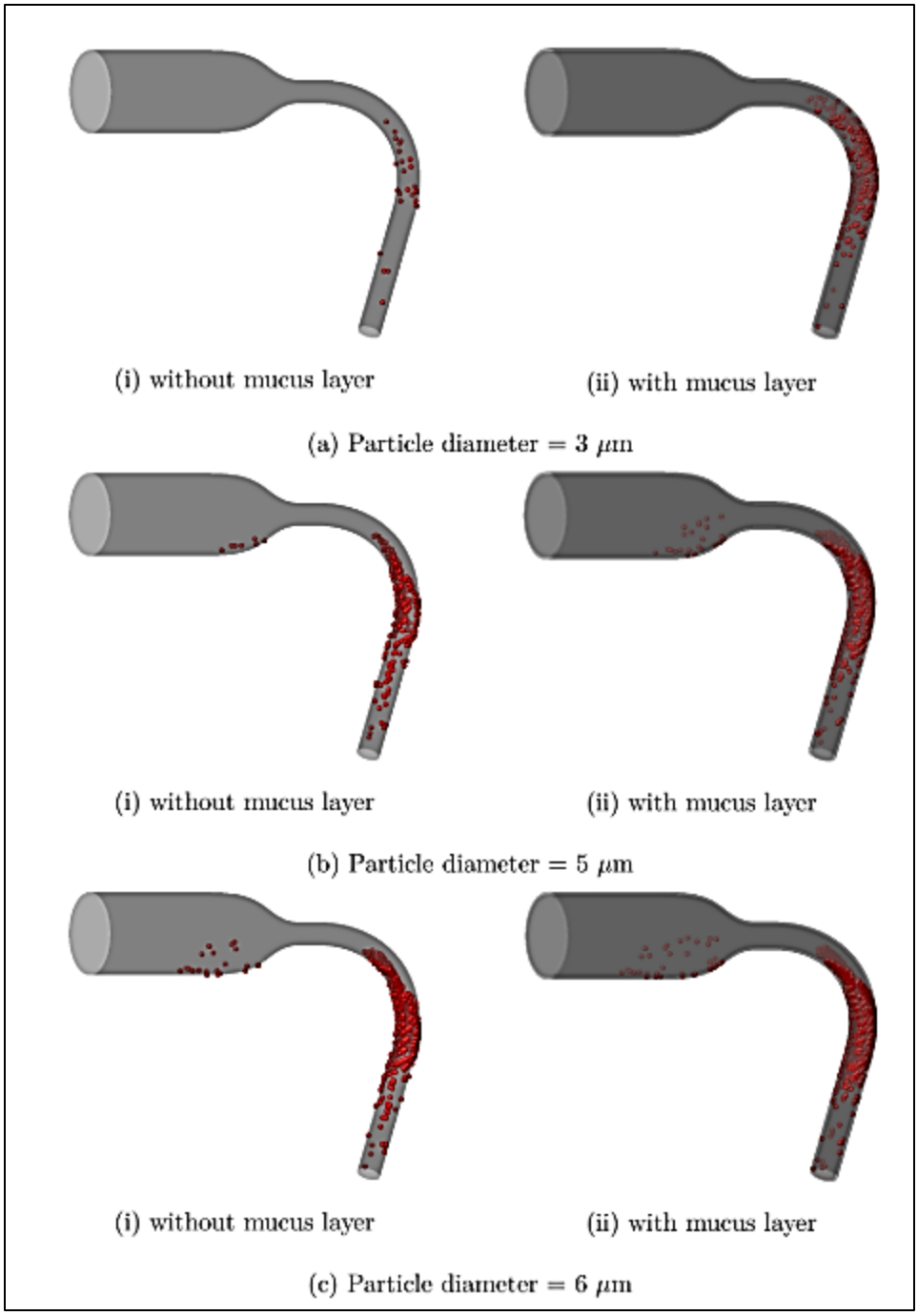

Fig. 2-9: Particle deposition patterns for a flow rate of 30 L/min and an inlet air temperature of 15 °C with varying particle diameters with and without a mucus layer (Narayanan et al., 2022).

Among RANS models, the standard k-ε and standard k-ω models are widely used due to their relatively low computational demands. The standard k-ε model performs well in high-Reynolds-number flows with small pressure gradients (Huang et al., 2021). In contrast, the standard k-ω model provides better accuracy in the ET region and more reliable particle-deposition predictions

than the k-ε model. Low-Reynolds-number (LRN) variants of the k-ε and k-ω models offer improved resolution of near-wall flow characteristics, which is crucial for simulating deposition on airway surfaces. These models have shown good agreement with experimental data when predicting deposition of particles larger than 5 μm in the ET region, although they tend to overpredict deposition for particles smaller than 5 μm (Bass and Worth Longest, 2018; Longest and Xi, 2007; Srivastav et al., 2019; Zhang et al., 2009; Zhang and Kleinstreuer, 2011). The Shear Stress Transport (SST) model combines the advantages of both the k-ε and k-ω models by applying the k-ω formulation in the near-wall region and the k-ε formulation in the core flow. This hybrid approach eliminates the need for additional damping functions and provides deposition predictions comparable to LRN models, often outperforming standard two-equation RANS models in both airflow and particle transport simulations (Ball et al., 2008; F. Huang et al., 2021; Kolanjiyil and Kleinstreuer, 2016; P. Koullapis et al., 2018).

LES offers a balance between accuracy and computational efficiency by resolving large-scale turbulent structures while modeling only the smaller sub-grid eddies. LES accounts for instantaneous turbulent fluctuations, making it particularly suitable for capturing transitional flow from laminar to turbulent regimes, especially in the ET and TB regions. It has also been shown to yield more accurate predictions of aerosol deposition compared to Reynolds-Averaged Navier–Stokes (RANS) models (Breuer et al., 2006; Koullapis et al., 2018; Zhang and Kleinstreuer, 2011).

DNS is the most accurate approach, as it solves the full Navier–Stokes equations without any turbulence modeling. However, its extremely high computational cost makes it impractical for large or complex geometries, and it's also difficult to couple with particle tracking models, such as the Discrete Phase Model (DPM) (Nicolaou and Zaki, 2013; Stylianou et al., 2016).

For modeling aerosols such as droplets or particles, both Eulerian and Lagrangian frameworks are commonly used, each offering distinct advantages and limitations. The Eulerian approach treats aerosols as a secondary continuous phase and predicts their behavior through mass and momentum conservation equations. While this method is computationally efficient, it struggles with accurately capturing interphase exchange and boundary conditions where aerosol removal occurs. In contrast, the Lagrangian approach models aerosol particles individually within a continuous gas phase, solving their motion via Newton's second law. Although it is more computationally demanding due to the need to track numerous particles, it provides a more realistic and physically intuitive

representation of particle behavior (Adamczyk et al., 2014; Cristea and Conti, 2018; Dehbi, 2008). Lagrangian models are further divided into those that consider particle-particle interactions and those that do not. The DPM neglects these interactions, while the Discrete Element Method (DEM) explicitly resolves them using contact mechanics. As a result, DEM offers higher accuracy in dense flows or scenarios involving complex interactions, such as powder dispersion in inhalers, albeit at a significantly higher computational cost (Ariyaratne et al., 2018; Fen Huang et al., 2021).

While CFD modeling has become a valuable tool for exploring aerosol behavior and inhalation processes, it remains a cutting-edge method with notable challenges. Current models often struggle to fully capture the intricacies of human respiratory anatomy, dynamic airflow patterns, and the interaction between particles and airway surfaces. To move beyond these limitations, future studies should aim to refine patient-specific modelling approaches, incorporate more detailed representations of physiological conditions, and strengthen the connection between simulation outcomes and experimental or clinical data. These efforts will help improve accuracy and broaden the application of CFD in respiratory research. The present work addresses several of these aspects by incorporating realistic geometry, transient breathing patterns, physiological conditions, and polydisperse aerosol behaviour, as well as their interactions.

2.4 Research Gaps

A comprehensive review of the literature has revealed several key research gaps in studies involving pMDIs, including the following:

- Realistic Airway Geometry

Many studies still rely on idealized or simplified geometries, while patient-specific or population-representative geometries are underused, despite their importance in accurately predicting aerosol behavior and deposition.

- Influence of Age and Sex on Drug Delivery

The anatomical and physiological differences across age groups (e.g., pediatric vs. adult) and between sexes are often overlooked in pMDI studies. Variations in airway geometry, lung volume, and breathing patterns can all affect aerosol transport and deposition.

- Breathing Pattern Variability

Most simulations assume idealized inhalation profiles (e.g., steady or sinusoidal), which do not reflect the variability found in patients with respiratory diseases or during incorrect inhaler usage (e.g., breath-holding, coughing, early exhalation).

- Dynamic Airway Motion

The effect of airway deformation during breathing, particularly in the upper and central airways, is often neglected, yet it can significantly influence airflow and particle transport.

- Mucus Layer and Wall Interaction

Limited studies incorporate realistic mucus properties, thickness, and dynamics, which affect particle-wall interactions, drug dissolution, and eventual absorption.

- Experimental Limitations in Capturing Breathing Patterns and Airway Wall Motion

Validation of CFD models is often constrained by the lack of high-fidelity experimental data that captures realistic, time-resolved breathing patterns and dynamic airway wall motion. Most available *in-vitro* setups use static geometries and simplified inhalation profiles, making it challenging to validate simulations under physiologically relevant conditions.

- Polydispersity and Particle Cohesion

Many models simplify aerosols as monodisperse and non-interacting, whereas real pMDI sprays are polydisperse and can involve agglomeration or breakup, especially under humid, warm conditions in the airways.

- Effects of Disease Conditions

There is a need for more simulations involving diseased airway geometries (e.g., bronchoconstriction, inflammation) to better understand drug delivery in individuals with non-healthy airways.

- Effect of Environmental Conditions (Temperature and Humidity)

Most pMDI studies assume constant ambient or airway conditions. Yet, the real inhalation process involves rapid transitions in temperature and relative humidity (RH) from the external environment

to the warm, humid airway. These changes can significantly influence particle size through hygroscopic growth or evaporation, thereby impacting deposition patterns.

2.5 Research Objectives

The primary objective of this study is to obtain accurate, physiologically relevant data on the behavior of pMDIs under conditions that closely replicate *in-vivo* scenarios. This was achieved through a combined experimental and numerical approach, incorporating anatomically realistic models, precise measurement techniques, and validated CFD simulations. Ultimately, the insights from this realistic, validated dataset can guide the optimization of pMDI device design and inhalation strategies to improve drug delivery efficiency and therapeutic outcomes.

Five principal objectives form the foundation of this study, each targeting a specific aspect of how critical factors influence particle dynamics and deposition patterns.

2.5.1 Objective one: Evaluation of nozzle design and surrounding flow conditions effects on pMDI spray performance

The first objective is to investigate the influence of nozzle design and surrounding flow conditions on the behaviour of sprays generated by pMDIs. A comprehensive CFD study was conducted using the LES-DPM approach to resolve detailed flow structures and droplet dynamics. Two spray models were implemented and injected through both conventional and twin nozzles into two environments: open air and an anatomically realistic MT geometry. The simulations were designed to capture the impact of varying nozzle parameters, including shape, orifice diameter, and length, on the spatial dispersion, transport, and deposition patterns of the aerosolized drug particles. To ensure the reliability of the numerical predictions, the CFD results were validated against experimentally obtained data, enabling a more accurate and insightful evaluation of how device and environmental factors influence pMDI spray performance. This work aims to provide a foundation for optimizing inhaler design to enhance drug delivery efficiency in realistic inhalation scenarios.

2.5.2 Objective two: Thermal effects on pMDI aerosol transport and deposition in realistic upper airway geometry

This objective aims to explore the influence of thermal conditions on particle transport and deposition within the human upper airway during pMDI administration. Using LES-DPM

simulations, we investigated the combined effects of plume temperature, inhaled airflow temperature, and the thermal structure of the airway wall on aerosol behavior. Four different plume temperatures (−54 °C, −20 °C, 0 °C, and 10 °C) and three inlet airflow temperatures (−15 °C, 22 °C, and 45 °C) were analyzed using realistic MT geometry. The model incorporated a physiologically accurate airway wall with a total thickness of 0.51 mm, comprising a 0.5 mm airway tissue layer and a 10 μm mucus layer, with water-like thermal properties. This setup enabled the simulation of heat transfer between the inhaled aerosol and the airway surfaces. The study provided detailed insights into how thermal gradients affect droplet evaporation, particle trajectories, and regional deposition patterns, thereby contributing to the development of more effective inhalation drug-delivery strategies under realistic *in-vivo* thermal conditions.

2.5.3 Objective three: Influence of anatomical, breathing, and wall dynamics on pMDI aerosol deposition in patient-specific airways

This objective focuses on understanding how gender-specific anatomical differences, breathing patterns, airway wall motion, and the presence of a mucus layer influence the transport and deposition of drug aerosols delivered by a pMDI. To achieve this, we developed two patient-specific airway models, one for males and one for females, based on CT scans of individuals with COPD. These anatomically accurate geometries, incorporating the mouth-throat region, trachea, and bronchial tree up to the fourth generation (G0–G4), were combined with a medium-sized MT model from VCU. Experimental validation was performed using rapid prototyping to fabricate the airway models and to conduct *in-vitro* deposition tests at a constant inhalation rate of 30 L/min under static wall conditions.

Complementary computational simulations were conducted using a validated CFD framework that employed the LES model for airflow and the DPM model for aerosol tracking. To account for physiologically realistic features, we implemented a user-defined function (UDF) to simulate sinusoidal wall deformation representing dynamic breathing. The mucus layer was incorporated using the Eulerian Wall Film (EWF) model, enabling simulation of drug interactions with the airway surface, including thermal and evaporation effects.

2.5.4 Objective four: Impact of inhalation irregularities on pMDI aerosol transport and deposition in realistic airways

This objective addresses a critical gap in current research by investigating the effects of disrupted or irregular inhalation patterns, such as coughing, breath-holding, and premature termination of inhalation, on aerosol transport and deposition from pMDIs. Although previous studies have provided essential insights under idealized or controlled breathing conditions, real-world pMDI usage often deviates from these scenarios. To capture these irregular behaviors, we employed a patient-specific male airway geometry extending from the oral cavity to the fourth-generation bronchi. The study simulated several physiologically relevant disruptions, including sudden pauses in inhalation, unintentional exhalation, and coughing, using a time-dependent boundary condition framework to model varying flow rates and directions. By analyzing the resulting airflow and particle trajectories with LES-DPM, this work aims to quantify how these irregular events influence aerosol dispersion and regional deposition. The findings are expected to improve understanding of pMDI performance under non-ideal conditions.

2.5.5 Objective five: Modeling Dense pMDI Aerosol Plumes: Integrating DDPM and Experimental Validation for Improved Drug Deposition Prediction

This objective aims to enhance the accuracy of numerical simulations of aerosol behavior from pMDIs by addressing common oversimplifications in existing models, particularly the assumption that aerosols are highly diluted systems containing only the API. In most CFD studies, the volumetric and dynamic effects of the HFA propellant are neglected, despite their significant role in influencing plume dynamics and deposition efficiency. Given the high injection velocity of pMDIs (approximately 100 m/s), particle-particle interactions and turbulent dispersion become substantial, potentially altering the droplet size distribution and aerodynamic behavior. To account for these complexities, this study employs a more realistic modeling framework by integrating the Dense Discrete Phase Model (DDPM) with four-way coupling in ANSYS Fluent, thereby capturing interactions among particles, the carrier gas, and the airway walls. The aerosol solution modeled includes both the API (100 µg per actuation) and the HFA propellant (0.05 mL per actuation). Simulations were performed using the medium-sized VCU MT geometry. The study further compares three modeling approaches—LES-DPM (dilute phase), k-ω-DPM (dilute phase), and k-ω-DDPM (dense phase)—in terms of computational efficiency and predictive accuracy.

2.6 Nomenclature

Abbreviations

3D	three dimensional
AIT	Alberta idealized throat
API	active pharmaceutical ingredient
ASL	airway surface liquid
BDP	beclomethasone dipropionate
CFD	computational fluid dynamics
COPD	chronic obstructive pulmonary disease
CT	computed tomography
DDPM	dense discrete phase model
DEM	discrete element method
DNS	direct numerical simulation
DPM	discrete phase model
ET	extrathoracic
EWF	Eulerian wall film
FP	fluticasone propionate
FPF	fine particle fraction
G	generation
HFA	hydrofluoroalkane
HPLC	high-performance liquid chromatography
LES	large eddy simulation
LRN	low-Reynolds number
MT	mouth-throat
NGI	next generation impactor
PDA	phase doppler anemometry
pMDIs	pressurized metered-dose inhalers
PSD	particle size distribution
RANS	Reynolds-averaged Navier-Stokes
RH	relative humidity

SST	shear stress transport
TB	tracheobronchial
UDF	user-defined function
VCU	Virginia Commonwealth University

Notation

Stk	Stokes number
d_p	particle diameter (m)
ρ_p	particle density (kg/m^3)
d	airway diameter (m)
u	velocity of airflow (m/s)
μ	dynamic viscosity of airflow (Pa.s)

2.7 References

Adamczyk, W.P., Klimanek, A., Białecki, R.A., Węcel, G., Kozołub, P., Czakiert, T., 2014. Comparison of the standard Euler-Euler and hybrid Euler-Lagrange approaches for modeling particle transport in a pilot-scale circulating fluidized bed. Particuology 15, 129–137. https://doi.org/10.1016/j.partic.2013.06.008

Aghaei, Y., Sajadi, B., Ahmadi, G., 2023. The effect of the mucus layer and the inhaled air conditions on the droplets fate in the human nasal cavity: A numerical study. J. Aerosol Sci. 171, 106163. https://doi.org/10.1016/j.jaerosci.2023.106163

Ahookhosh, K., Saidi, M., Mohammadpourfard, M., Aminfar, H., Hamishehkar, H., Farnoud, A., Schmid, O., 2021. Flow structure and particle deposition analyses for optimization of a pressurized metered dose inhaler (pMDI) in a model of tracheobronchial airway. Eur. J. Pharm. Sci. 164, 105911. https://doi.org/10.1016/j.ejps.2021.105911

Ahookhosh, K., Yaqoubi, S., Mohammadpourfard, M., Hamishehkar, H., Aminfar, H., 2019. Experimental investigation of aerosol deposition through a realistic respiratory airway replica: An evaluation for MDI and DPI performance. Int. J. Pharm. 566, 157–172. https://doi.org/10.1016/j.ijpharm.2019.05.058

Alatrash, A., Matida, E., 2016. Characterization of medication velocity and size distribution from pressurized metered-dose inhalers by phase doppler anemometry. J. Aerosol Med. Pulm. Drug Deliv. 29, 501–513. https://doi.org/10.1089/jamp.2015.1264

Ariyaratne, W.K.H., Manjula, E.V.P.J., Ratnayake, C., Melaaen, M.C., 2018. CFD Approaches for Modeling Gas-Solids Multiphase Flows - A Review. Proc. 9th EUROSIM Congr. Model. Simulation, EUROSIM 2016, 57th SIMS Conf. Simul. Model. SIMS 2016 142, 680–686. https://doi.org/10.3384/ecp17142680

Ball, C.G., Uddin, M., Pollard, A., 2008. High resolution turbulence modelling of airflow in an idealised human extra-thoracic airway. Comput. Fluids 37, 943–964. https://doi.org/10.1016/j.compfluid.2007.07.021

Bass, K., Worth Longest, P., 2018. Recommendations for simulating microparticle deposition at conditions similar to the upper airways with two-equation turbulence models. J. Aerosol Sci. 119, 31–50. https://doi.org/10.1016/j.jaerosci.2018.02.007

Borojeni, A.A.T., Gu, W., Asgharian, B., Price, O., Kuprat, A.P., Singh, R.K., Colby, S., Corley, R.A., Darquenne, C., 2023. In silico quantification of intersubject variability on aerosol deposition in the oral airway. Pharmaceutics 15, 160. https://doi.org/10.3390/pharmaceutics15010160

Brambilla, G., Church, T., Lewis, D., Meakin, B., 2011. Plume temperature emitted from metered dose inhalers. Int. J. Pharm. 405, 9–15. https://doi.org/10.1016/j.ijpharm.2010.11.037

Breuer, M., Baytekin, H.T., Matida, E.A., 2006. Prediction of aerosol deposition in 90{ring operator} bends using LES and an efficient Lagrangian tracking method. J. Aerosol Sci. 37, 1407–1428. https://doi.org/10.1016/j.jaerosci.2006.01.013

Chen, X., Feng, Y., Zhong, W., Kleinstreuer, C., 2017. Numerical investigation of the interaction, transport and deposition of multicomponent droplets in a simple mouth-throat model. J. Aerosol Sci. 105, 108–127. https://doi.org/10.1016/j.jaerosci.2016.12.001

Chen, X., Kleinstreuer, C., Zhong, W., Feng, Y., Zhou, X., 2018. Effects of thermal airflow and mucus-layer interaction on hygroscopic droplet deposition in a simple mouth–throat model.

Aerosol Sci. Technol. 52, 900–912. https://doi.org/10.1080/02786826.2018.1476751

Chen, Y., Young, P.M., Murphy, S., Fletcher, D.F., Long, E., Lewis, D., Church, T., Traini, D., 2017. High-Speed Laser Image Analysis of Plume Angles for Pressurised Metered Dose Inhalers: The Effect of Nozzle Geometry. AAPS PharmSciTech 18, 782–789. https://doi.org/10.1208/s12249-016-0564-5

Cristea, E.D., Conti, P., 2018. Hybrid eulerian multiphase-dense discrete phase model approach for numerical simulation of dense particle-laden turbulent flows within vertical multi-stage cyclone heat exchanger. Am. Soc. Mech. Eng. Fluids Eng. Div. FEDSM 2, 1–15. https://doi.org/10.1115/FEDSM2018-83058

Darquenne, C., 2020. Deposition mechanisms. J. Aerosol Med. Pulm. Drug Deliv. 33, 181–185. https://doi.org/10.1089/jamp.2020.29029.cd

Dehbi, A., 2008. A CFD model for particle dispersion in turbulent boundary layer flows. Nucl. Eng. Des. 238, 707–715. https://doi.org/10.1016/j.nucengdes.2007.02.055

Erken, O., Fazla, B., Muradoglu, M., Izbassarov, D., Romanò, F., Grotberg, J.B., 2023. Effects of elastoviscoplastic properties of mucus on airway closure in healthy and pathological conditions. Phys. Rev. Fluids 8, 1–26. https://doi.org/10.1103/PhysRevFluids.8.053102

Feng, Y., Zhao, J., Hayati, H., Sperry, T., Yi, H., 2021. Tutorial : Understanding the transport , deposition , and translocation of particles in human respiratory systems using Computational Fluid-Particle Dynamics and Physiologically Based Toxicokinetic models. J. Aerosol Sci. 151, 105672. https://doi.org/10.1016/j.jaerosci.2020.105672

Finlay, W.H., 2019. The Mechanics of Inhaled Pharmaceutical Aerosols: An Introduction. Elsevier Science.

Finlay, W.H., 2001. The Mechanics of Inhaled Pharmaceutical Aerosols: An Introduction.

Gunatilaka, C.C., Schuh, A., Higano, N.S., Woods, J.C., Bates, A.J., 2020. The effect of airway motion and breathing phase during imaging on CFD simulations of respiratory airflow. Comput. Biol. Med. 127, 104099. https://doi.org/10.1016/j.compbiomed.2020.104099

Gurumurthy, A., Kleinstreuer, C., 2021. Helical fluid-particle flow dynamics for controlling

micron-particle deposition in a representative human upper lung-airway model. J. Aerosol Sci. 151. https://doi.org/10.1016/j.jaerosci.2020.105656

Haut, B., Nonclercq, A., Buess, A., Rabineau, J., Rigaut, C., Sobac, B., 2021. Comprehensive analysis of heat and water exchanges in the human lungs. Front. Physiol. 12. https://doi.org/10.3389/fphys.2021.649497

Huang, F., Zhang, Y., Tong, Z.B., Chen, X.L., Yang, R.Y., Yu, A.B., 2021. Numerical investigation of deposition mechanism in three mouth–throat models. Powder Technol. 378, 724–735. https://doi.org/10.1016/j.powtec.2018.11.095

Huang, Fen, Zhu, Q., Zhou, X., Gou, D., Yu, J., Li, R., Tong, Z., Yang, R., 2021. Role of CFD based in silico modelling in establishing an in vitro-in vivo correlation of aerosol deposition in the respiratory tract. Adv. Drug Deliv. Rev. https://doi.org/10.1016/j.addr.2020.09.007

Kadota, K., Matsumoto, K., Uchiyama, H., Tobita, S., Maeda, M., Maki, D., Kinehara, Y., Tachibana, I., Sosnowski, T.R., Tozuka, Y., 2022. In silico evaluation of particle transport and deposition in the airways of individual patients with chronic obstructive pulmonary disease. Eur. J. Pharm. Biopharm. 174, 10–19. https://doi.org/10.1016/j.ejpb.2022.03.010

Kaviratna, A., Tian, G., Liu, X., Delvadia, R., Lee, S., Guo, C., 2019. Evaluation of bio-relevant mouth-throat models for characterization of metered dose inhalers. AAPS PharmSciTech 20, 130. https://doi.org/10.1208/s12249-019-1339-6

Kolanjiyil, A. V., Kleinstreuer, C., 2016. Computationally efficient analysis of particle transport and deposition in a human whole-lung-airway model. Part I: Theory and model validation. Comput. Biol. Med. 79, 193–204. https://doi.org/10.1016/j.compbiomed.2016.10.020

Koullapis, P., Kassinos, S.C., Muela, J., Perez-Segarra, C., Rigola, J., Lehmkuhl, O., Cui, Y., Sommerfeld, M., Elcner, J., Jicha, M., Saveljic, I., Filipovic, N., Lizal, F., Nicolaou, L., 2018. Regional aerosol deposition in the human airways: The SimInhale benchmark case and a critical assessment of in silico methods. Eur. J. Pharm. Sci. 113, 77–94. https://doi.org/10.1016/j.ejps.2017.09.003

Kuwano, K., Bosken, C.H., Pare, P.D., Bai, T.R., Wiggs, B.R., Hogg, J.C., 1993. Small airways dimensions in asthma and in chronic obstructive pulmonary disease. Am. Rev. Respir. Dis.

148, 1220–1225. https://doi.org/10.1164/ajrccm/148.5.1220

Lavorini, F., 2013. The Challenge of Delivering Therapeutic Aerosols to Asthma Patients. ISRN Allergy 2013, 1–17. https://doi.org/10.1155/2013/102418

Lim, S.H., Park, S., Lee, C.C., Ho, P.C.L., Kwok, P.C.L., Kang, L., 2021. A 3D printed human upper respiratory tract model for particulate deposition profiling. Int. J. Pharm. 597. https://doi.org/10.1016/j.ijpharm.2021.120307

Liu, H., Ma, S., Hu, T., Ma, D., 2023. Computational investigation of flow characteristics and particle deposition patterns in a realistic human airway model under different breathing conditions. Respir. Physiol. Neurobiol. 314, 104085. https://doi.org/10.1016/j.resp.2023.104085

Longest, P.W., Xi, J., 2007. Effectiveness of direct Lagrangian tracking models for simulating nanoparticle deposition in the upper airways. Aerosol Sci. Technol. 41, 380–397. https://doi.org/10.1080/02786820701203223

McKiernan, A.P., 2019. Inhaler spray investigation using high-speed phase-contrast X-Ray and schlieren imaging. Pharm. Res. 36. https://doi.org/10.1007/s11095-019-2657-9

Mirzaaghaian, A., Zhao, M., Rahman, M.M., Dong, K., 2024. Numerical simulation of targeted drug delivery to different regions of realistic human lung model under realistic aerosol breathing condition. Powder Technol. 444, 120039. https://doi.org/10.1016/j.powtec.2024.120039

Narayanan, J.K., Lin, J., Feng, Y., Cui, X., 2022. Numerical study on the impact of mucus layer and inlet air-temperatures on the particle deposition in a highly idealized mouth-throat model using LES. Powder Technol. 395, 455–475. https://doi.org/10.1016/j.powtec.2021.09.073

Nicolaou, L., Zaki, T.A., 2013. Direct numerical simulations of flow in realistic mouth-throat geometries. J. Aerosol Sci. 57, 71–87. https://doi.org/10.1016/j.jaerosci.2012.10.003

Ogrodnik, N., Azzi, V., Sprigge, E., Fiset, S., Matida, E., 2016. Nonuniform deposition of pressurized metered-dose aerosol in spacer devices. J. Aerosol Med. Pulm. Drug Deliv. 29, 490–500. https://doi.org/10.1089/jamp.2015.1257

Rajaraman, P.K., Choi, J., Hoffman, E.A., O'Shaughnessy, P.T., Choi, S., Delvadia, R., Babiskin, A., Walenga, R., Lin, C.L., 2020. Transport and deposition of hygroscopic particles in asthmatic subjects with and without airway narrowing. J. Aerosol Sci. 146, 105581. https://doi.org/10.1016/j.jaerosci.2020.105581

Sheth, P., Grimes, M.R., Stein, S.W., Myrdal, P.B., 2017. Impact of droplet evaporation rate on the resulting in vitro performance parameters of pressurized metered dose inhalers. Int. J. Pharm. 528, 360–371. https://doi.org/10.1016/j.ijpharm.2017.06.014

Smyth, H., Brace, G., Barbour, T., Gallion, J., Grove, J., Hickey, A.J., 2006. Spray pattern analysis for metered dose inhalers: Effect of actuator design. Pharm. Res. 23, 1591–1596. https://doi.org/10.1007/S11095-006-0280-Z

Srivastav, V.K., Paul, A.R., Jain, A., 2019. Capturing the wall turbulence in the CFD simulation of human respiratory tract. Math. Comput. Simul. 160, 23–38. https://doi.org/10.1016/j.matcom.2018.11.019

Stylianou, F.S., Sznitman, J., Kassinos, S.C., 2016. Direct numerical simulation of particle-laden flow in a human airway bifurcation model. Int. J. Heat Fluid Flow 61, 677–710. https://doi.org/10.1016/j.ijheatfluidflow.2016.07.013

Sul, B., Altes, T., Ruppert, K., Qing, K., Hariprasad, D.S., Morris, M., Reifman, J., 2019. Dynamics of the tracheal airway and its influences on respiratory airflows: An exemplar study. J. Biomech. Eng. 141, 1–12. https://doi.org/10.1115/1.4043723

Talaat, M., Si, X., Xi, J., 2022. Effect of MDI actuation timing on inhalation dosimetry in a human respiratory tract model. Pharmaceuticals 15, 61. https://doi.org/10.3390/ph15010061

Worth Longest, P., Hindle, M., 2009. Evaluation of the Respimat soft mist inhaler using a concurrent cfd and in vitro approach. J. Aerosol Med. Pulm. Drug Deliv. 22, 99–112. https://doi.org/10.1089/jamp.2008.0708

Xi, J., April Si, X., Dong, H., Zhong, H., 2018. Effects of glottis motion on airflow and energy expenditure in a human upper airway model. Eur. J. Mech. B/Fluids 72, 23–37. https://doi.org/10.1016/j.euromechflu.2018.04.011

Yanai, M., Sekizawa, K., Ohrui, T., Sasaki, H., Takishima, T., 1992. Site of airway obstruction

in pulmonary disease: direct measurement of intrabronchial pressure. J. Appl. Physiol. 72, 1016–1023. https://doi.org/10.1152/jappl.1992.72.3.1016

Yang, H., Wang, Y., Chen, X., Sun, B., Tao, F., Xie, X., Zhang, Y., 2023. The effects of temperature and humidity on the deposition of nebulized droplet in an idealized mouth-throat model. Flow Meas. Instrum. 91, 102359. https://doi.org/10.1016/j.flowmeasinst.2023.102359

Zhang, R., Song, X., Zhan, S., Hu, J., Tan, W., 2017. Investigation of influence factors on particle size measurement with pMDI. Biomed. Res. 28, 9582–9588.

Zhang, Z., Kleinstreuer, C., 2011. Laminar-to-turbulent fluid–nanoparticle dynamics simulations: Model comparisons and nanoparticle-deposition applications. Int. J. Number. Method. Biomed. Eng. 27, 1930–1950. https://doi.org/10.1002/cnm.1447

Zhang, Z., Kleinstreuer, C., Kim, C.S., 2009. Comparison of analytical and CFD models with regard to micron particle deposition in a human 16-generation tracheobronchial airway model. J. Aerosol Sci. 40, 16–28. https://doi.org/10.1016/j.jaerosci.2008.08.003

Chapter 3 - Experimental Methodology

3.1 Experimental Setup

In this study, various airway geometries were used to investigate particle transport and deposition in pressurized metered-dose inhalers (pMDIs). The first model represents the mouth-throat (MT) region, a commonly used in vitro model for simulating upper airway behavior. The second model extends from the oral cavity to the fourth-generation bronchi (G4), capturing more complex anatomical features and enabling a detailed assessment of airflow and particle dynamics deeper in the respiratory tract. The construction and characteristics of each model are described in the following sections.

3.1.1 Pressurized Metered-Dose Inhaler (pMDI)

In this study, the SANIS HFA pMDI was used as the aerosol delivery device (**Fig. 3-1**). This inhaler contains salbutamol sulphate as the active pharmaceutical ingredient (API), delivering 100 μg of salbutamol per actuation. The formulation is suspended in hydrofluoroalkane (HFA-134a), a propellant that replaces chlorofluorocarbons (CFCs) and is widely used due to its reduced environmental impact. No ethanol or co-solvents are included in this formulation. Each inhaler provides up to 200 actuations and is designed to deliver a fine aerosol suitable for deep lung deposition (Sanis Health Inc., 2021). The SANIS HFA is considered a generic equivalent to the Ventolin® HFA inhaler.

Studies examining the characteristics of the Ventolin® HFA inhaler have reported a mean minimum plume temperature of $-35.9 \pm 12.7\,^{\circ}C$ and a mean maximum temperature of $19.02 \pm 0.58\,^{\circ}C$. The low minimum plume temperature results from rapid flash evaporation of the HFA propellant, which absorbs large amounts of heat during phase change, leading to intense evaporative cooling that lowers the plume temperature. The average plume duration was 156 ± 58 ms. The emitted aerosol demonstrated a mass median aerodynamic diameter (MMAD) ranging from 2.3 to 2.4 μm, with a fine particle fraction (FPF; particles < 5 μm) of $31 \pm 2\%$ (Biswas et al., 2017; McCabe et al., 2012).

3.1.2 Airway Geometries

3.1.2.1 Mouth-Throat (MT)

The MT model was developed by the Respiratory and Aerosol Dynamics Research Group of Virginia Commonwealth University (VCU) by combining the oral cavity structure based on measurements of a dental impression with an approximate half-mouth opening (Cheng et al., 1997), with computed tomography (CT) scan data covering the pharyngeal to laryngeal regions. The CT images were obtained from a healthy adult using a multi-slice helical scanner with 1 mm slice thickness.

Fig. 3-1: Salbutamol HFA pressurized metered-dose inhaler, suspension (SANIS®, Sanis Health Inc.®, Canada).

As a primary simplification, the cross-sections of this realistic model were replaced with elliptical segments that maintain the same hydraulic diameter and flow area. The simplified elliptical model retains many similarities with the original one, including identical axial curvature. The elliptical cross-sections were carefully positioned to replicate the local flow areas observed in realistic geometry. Additionally, this model features a simplified oral cavity that omits the small tooth-cheek cavities present in actual anatomy. It also replaces the triangular glottic opening of the realistic model with an elongated oval with a high length-to-width ratio (Xi and Longest, 2007). Key geometric features of the MT model include an expanded oral cavity, a tongue curvature that partially impedes flow entering the mouth, an elliptic larynx, and a sloped trachea.

For the experimental study, the model was segmented into three distinct regions, the mouth, pharynx, and trachea, to enable measurement of regional particle deposition. The model was fabricated using a fused deposition modeling (FDM) 3D printer (UltiMaker S3, Netherlands). As shown in **Fig. 3-2**, a hollow airway structure with an outer wall thickness of 3 mm was printed using polylactic acid (PLA) filament. PLA was chosen due to its ease of printing, dimensional stability, and sufficient mechanical strength, making it suitable for replicating complex anatomical geometries in airflow experiments.

To preserve internal volume while improving surface finish, the inner walls of the 3D-printed MT model were smoothed with acetonitrile to reduce layer lines that were created during printing. The model was then rinsed with distilled water to remove any residual solvent, as PLA remains stable in water.

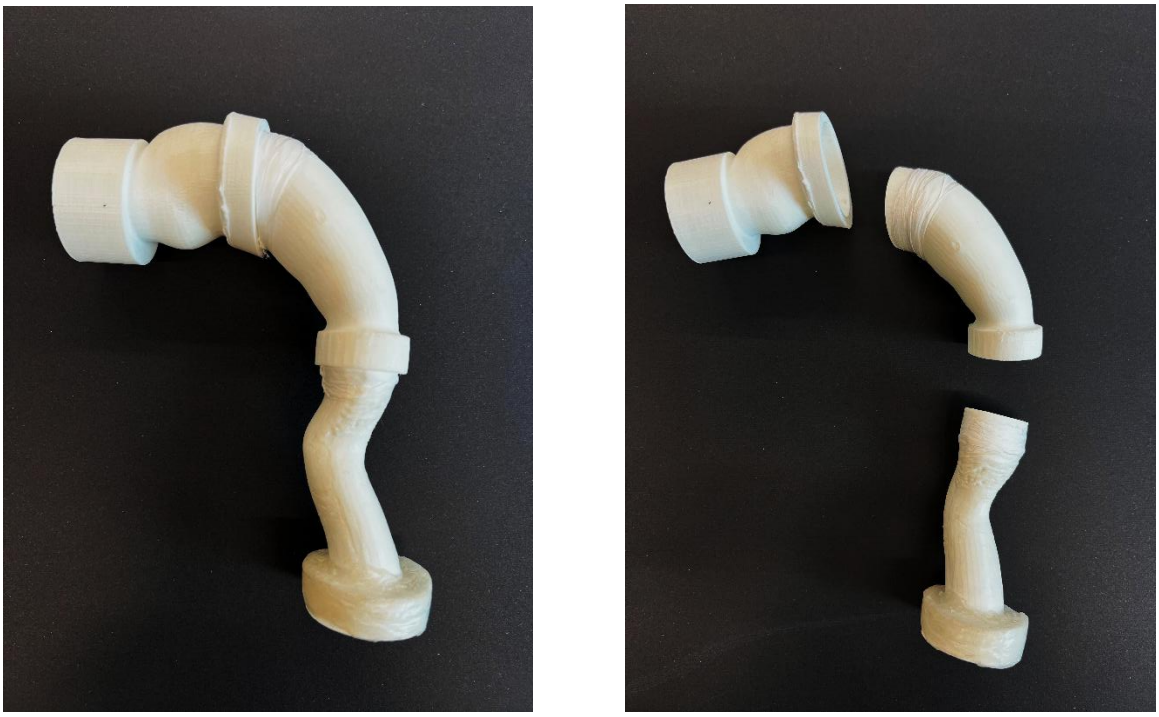

Fig. 3-2: Fabricated mouth-throat (MT) model using polylactic acid (PLA) filament by a 3D printer (UltiMaker S3, Netherlands).

3.1.2.2 Realistic bronchial tree model up to generation 4 (G4)

Two tracheobronchial geometries were reconstructed from CT scans of two COPD patients: a 60-year-old male and a 67-year-old female (**Fig. 3-3**). These scans were provided by the Iran Imaging Center in Tabriz, Iran. The chest CT scans were acquired using a multi-slice scanner, which

produced 249 axial slices with a thickness of 0.5 mm, saved in digital imaging and communications in medicine (DICOM) format. These images were processed using 3D Slicer medical imaging software, where slice-by-slice visual inspection and segmentation were performed to reconstruct the airway structures. The resulting models were exported as stereolithography (STL) files and imported into SOLIDWORKS® CAD Software 2022 (Dassault Systèmes) for further refinement. In this step, the models were smoothed, and the bronchi were extended to minimize reverse flow at the outlets.

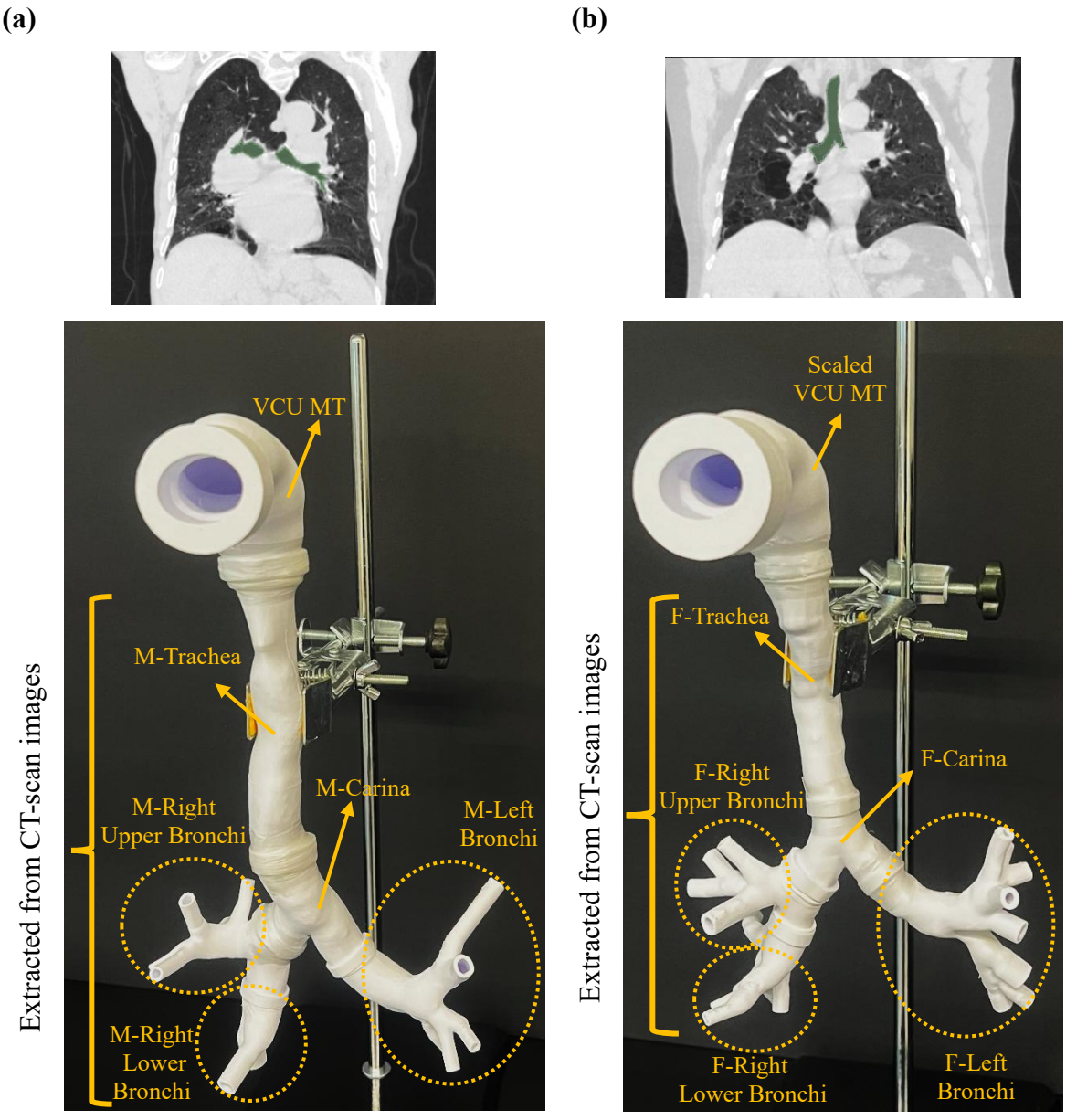

Fig. 3-3: Tracheobronchial tree geometries for **(a)** male (M); and **(b)** female (F) extracted from CT-scan images.

For experimental use, hollow airway models with an outer wall thickness of 2 mm were fabricated. Each model was divided into six distinct sections: main trachea, carina, left bronchus, upper right bronchus, and lower right bronchus. The final 3D-printed models were produced using a Prusa Mk4 printer (Prusa Research, Czech Republic) with FDM technology and PLA filament, as illustrated in **Fig. 3-3**.

Table 3-1 summarizes the average cross-sectional areas and lengths of the first- and second-generation (G1 and G2) airways. Results show that both the trachea and bronchi were longer in the male model than in the female model, with male airway cross-sectional areas nearly double those in the female model. The medium-sized MT model obtained from VCU was combined with the male tracheobronchial geometry and then proportionally scaled to fit the female airway configuration.

Table 3-1: Dimensions of different regions of tracheobronchial airways.

Segments		**Male**		**Female**	
		Length (mm)	**Mean cross-section area (mm^2) ± SD**	**Length (mm)**	**Mean cross-section area (mm^2) ± SD**
Trachea		119.06	255.58 ± 27.33	83.40	126.25 ± 16.32
Left Bronchi	**G1**	44.16	172.73 ± 19.19	40.38	85.18 ± 6.98
	G2	12.93	139.08 ± 2.03	12.35	71.00 ± 4.43
	G3	10.58	73.57 ± 2.39	9.14	41.21 ± 7.58
Right Bronchi	**G1**	24.84	226.30 ± 10.82	19.14	106.00 ± 3.85
	G2	5.78	97.63 ± 13.90	8.30	63.85 ± 3.36
	G3	25.60	165.00 ± 9.05	21.24	80.43 ± 7.20

3.1.3 Next Generation Impactor (NGI)

Accurate assessment of aerosol particle size distribution and regional deposition is essential in evaluating the performance of inhalation drug delivery devices, such as pMDIs. Among the various techniques developed for this purpose, the Next Generation Impactor (NGI) has become a widely accepted standard for *in-vitro* characterization of aerodynamic particle behavior. Designed to mimic the sequential deposition of particles in the human respiratory tract, the NGI enables quantification of fine particle fraction (FPF) and MMAD, which are critical metrics for

determining drug delivery efficiency and therapeutic effectiveness (Shekunov et al., 2007; Sou and Bergström, 2021).

The NGI is a high-performance, precision cascade impactor widely used for characterizing the aerodynamic particle size distribution (APSD) of orally inhaled and nasal drug products. As shown in **Fig. 3-4,** it consists of seven stages plus a Micro Orifice Collector (MOC), with aerodynamic cut-off diameters ranging from 0.54 µm to 6.12 µm, allowing operation at flow rates between 30 and 100 L/min. This flexibility enables the NGI to accommodate various inhalation products under different testing conditions (Copley Scientific Limited, 2020). The NGI operates on the principle of inertial impaction, which separates aerosol particles based on their aerodynamic diameter. During testing, an aerosolized formulation is introduced into the NGI at a controlled volumetric flow rate. The flow is directed sequentially through a series of precision-engineered nozzles and impaction stages, each designed to capture particles above a specific aerodynamic cut-off diameter.

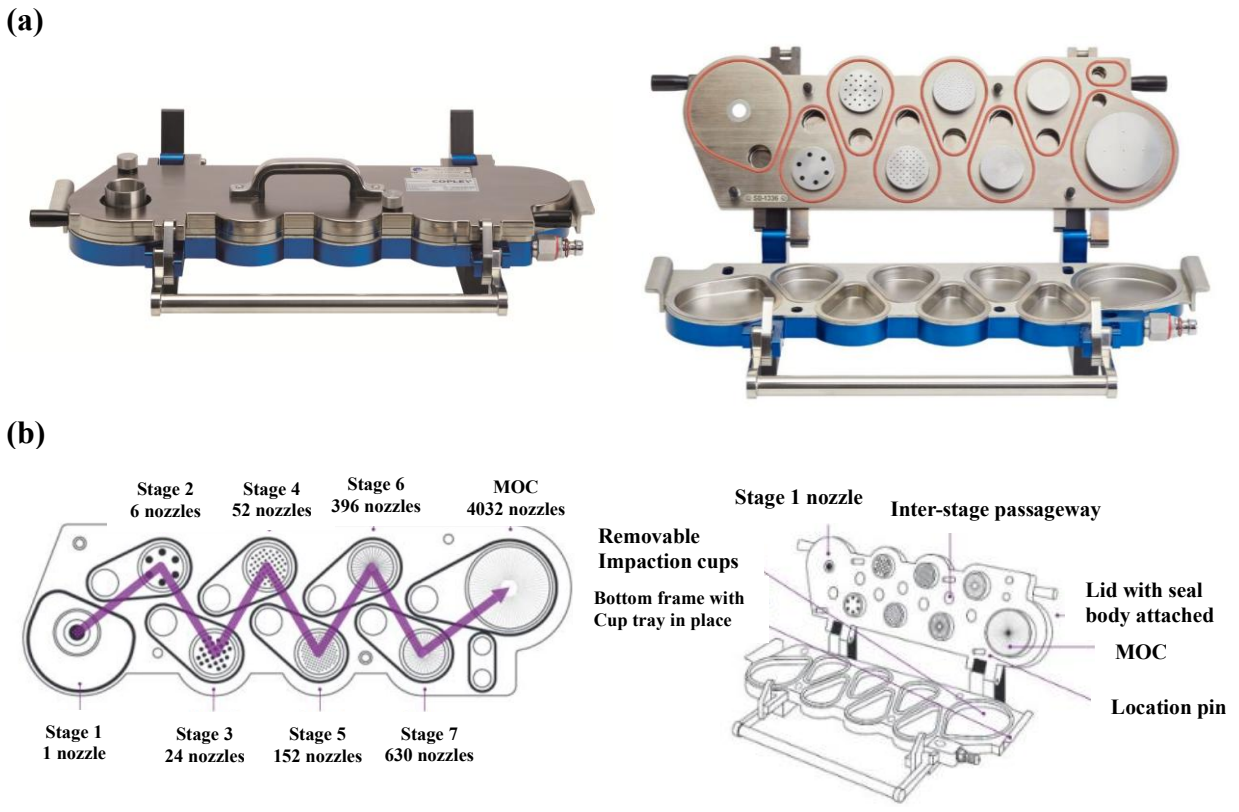

Fig. 3-4: Structure and flow path of the Next Generation Impactor (NGI): **(a)** External and internal views of the NGI showing the seven stages and collection cups; and **(b)** Schematic of particle separation based on aerodynamic diameter through sequential impaction from Stage 1 to the Micro-Orifice Collector (MOC).

As the aerosol-laden air passes through each nozzle, it accelerates and is directed toward an impaction plate or cup. Particles with sufficient inertia (i.e., larger aerodynamic diameter) are unable to follow the curved airflow streamlines and instead impact the collection surface. Smaller particles with lower inertia remain entrained in the airstream and proceed to the next stage. This size-selective deposition process is repeated across all seven stages, culminating in the final MOC, which captures the smallest particles remaining suspended in the flow. Each impaction stage corresponds to a defined aerodynamic diameter range, as reported in **Table 3-2**. The cut-off diameters are designed to mimic deposition behavior in the human respiratory tract, allowing the NGI to simulate how particles distribute across different regions of the airways. The collected drug mass at each stage is later quantified, typically via high-performance liquid chromatography (HPLC), to construct the APSD profile of the formulation (Copley Scientific Limited, 2020; Shekunov et al., 2007).

Table 3-2: NGI cut-off sizes at different flow rates (Copley Scientific Limited, 2020).

Stage	15 L/min	30 L/min	60 L/min	100 L/min
Stage 1	14.10	11.72	8.06	6.12
Stage 2	8.61	6.40	4.46	3.42
Stage 3	5.39	3.99	2.82	2.18
Stage 4	3.30	2.30	1.66	1.31
Stage 5	2.08	1.36	0.94	0.72
Stage 6	1.36	0.83	0.55	0.40
Stage 7	0.98	0.54	0.34	0.24
Stage 8	0.70	0.36	0.14	0.05

In the experimental configuration shown in **Fig. 3-5**, the NGI is housed in a temperature-controlled chamber equipped with an NGI Cooler™ to minimize evaporative losses during aerosol collection. Upstream of the NGI, the DFM 2000 flow meter (Copley Scientific, UK) and MT replica are connected to a mouthpiece adaptor (MP), which securely holds the inhaler device in place. The inhaled aerosol passes through the MT into the NGI, where it is fractionated by aerodynamic diameter. Downstream of the NGI, the system is connected to a critical flow controller (TPK 2000, Copley Scientific, UK), which regulates the volumetric airflow rate to ensure consistent sampling rates of 15-100 L/min, depending on the inhaler type. Finally, a vacuum pump (HCP5, Copley

Scientific, UK) is connected to the flow controller outlet, providing the required negative pressure to draw the aerosol through the entire system.

In the second experimental setup (**Fig. 3-6**), the NGI and cooling chamber were omitted to directly evaluate regional drug deposition within patient-specific airway replicas, as shown in **Fig. 3-3**. Instead of aerodynamic size separation, this configuration focused on capturing the total deposited mass at different airway regions. The test aerosol was introduced through the mouthpiece, and all distal branch outlets of the airway models were individually connected to 0.3 µm pore size filters (303 Respirgard II™, Vital Signs) using flexible silicone tubing. These filters served as collection points for particles that passed through the airway geometry, enabling the quantification of the drug mass delivered to each anatomical region.

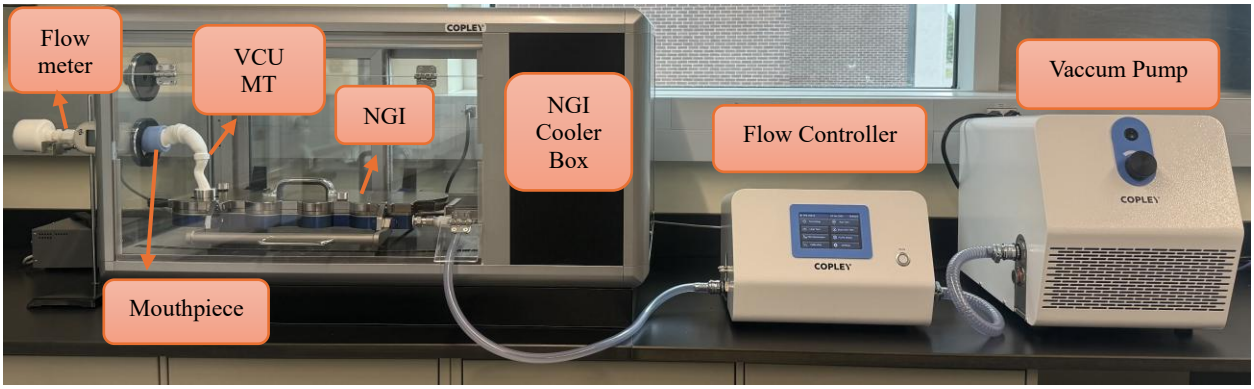

Fig. 3-5: Experimental setup includes Salbutamol HFA pMDI, VCU MT replica, NGI setup within cooler box, flow controller, and vacuum pump.

3.1.1 High Performance Liquid Chromatography (HPLC)

HPLC is a highly sensitive and widely used analytical technique for the separation, identification, and quantification of components in liquid samples. HPLC systems are composed of several key components: a solvent reservoir, pump, injector, analytical column, detector, and data processing unit (**Fig. 3-7(a)**). The mobile phase composition and flow rate can be precisely controlled to optimize separation. Various types of HPLC exist, depending on the stationary and mobile phases used, including reversed-phase HPLC, normal-phase HPLC, ion-exchange chromatography, and size-exclusion chromatography.

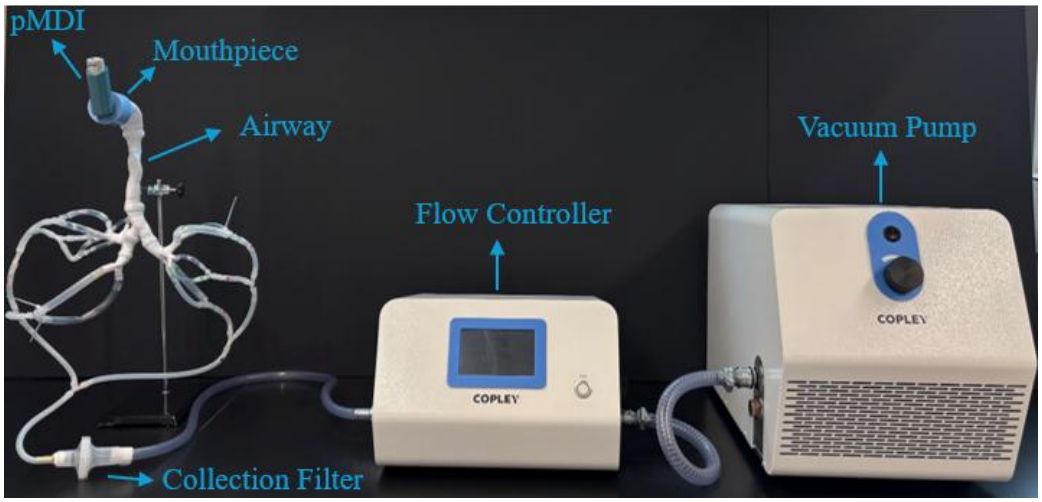

Fig. 3-6: Experimental setup includes Salbutamol HFA pMDI, male airway replica extracted from CT-scan images, flow controller, and vacuum pump.

As described by Snyder, Kirkland, and Dolan (2010), the HPLC mechanism is based on the differential interactions of solute molecules with a stationary phase (typically a packed column) and a mobile phase (solvent) under high-pressure flow conditions. As the sample travels through the column, each compound partitions differently between the mobile and stationary phases depending on its chemical properties, such as polarity, size, and solubility, resulting in temporal separation. **Fig. 3-7(b)** shows a schematic of this separation, where a polar mobile phase carries analytes through a non-polar stationary phase (e.g., a C18 column). Polar analytes (A) interact less with the non-polar stationary phase and elute faster, while less polar analytes (C) exhibit stronger retention due to greater affinity for the stationary phase.

HPLC is widely used in pharmaceutical analysis for drug purity testing, content uniformity, stability studies, and *in-vitro* assays, such as quantifying the mass of drugs collected on filters or stages in inhalation drug delivery experiments. In this study, reversed-phase one (RP-HPLC) was employed to quantify the drug mass collected on replicas and NGI stages. The system was equipped with a ZORBAX Eclipse XDB-C18 column (5 µm, 4.6 × 150 mm; Agilent Technologies), which contains a non-polar C18 stationary phase, making it well-suited for the analysis of moderately polar pharmaceutical compounds. The column was maintained at 40 °C to ensure consistent retention and peak shape. A 1525 Binary HPLC pump delivered a mobile phase of water and acetonitrile containing 0.1% formic acid, and detection was performed with a 2489

UV/Visible detector (Waters, USA), enabling selective and sensitive quantification of the active pharmaceutical ingredient.

(a)

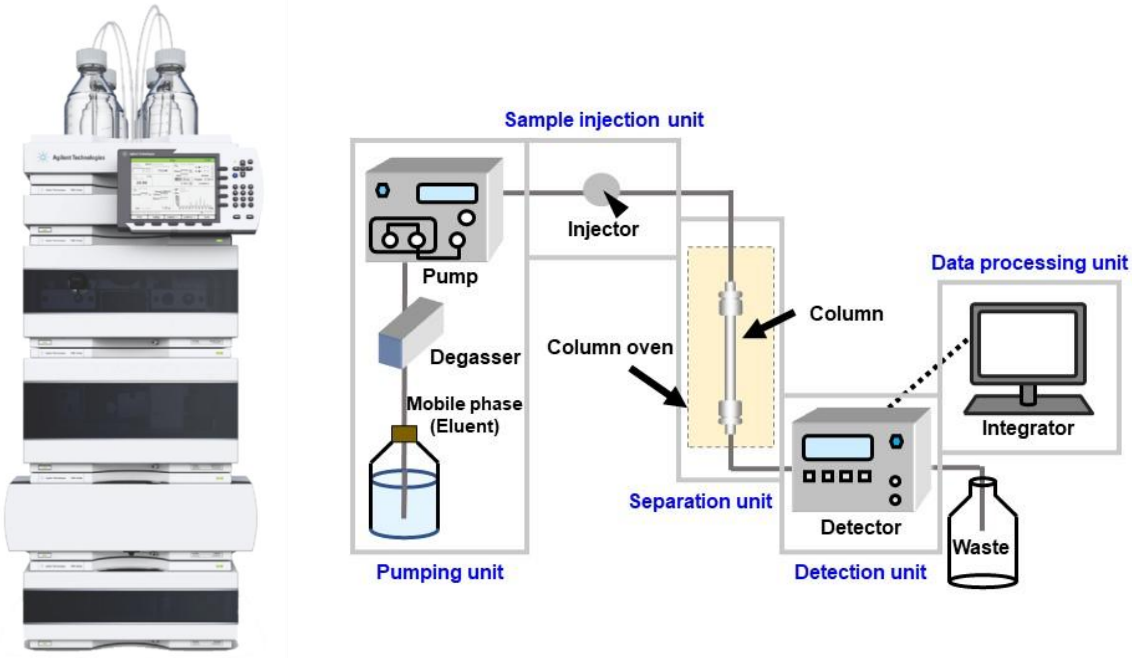

(b)

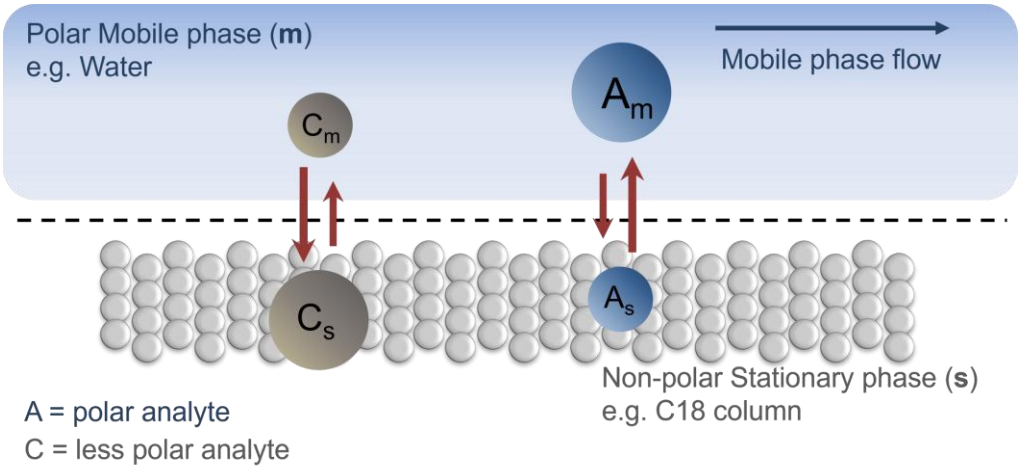

Fig. 3-7: (a) Schematic of a reversed-phase HPLC system showing key components: pumping, injection, separation, detection, and data processing units; and **(b)** Separation principle: polar analytes elute faster in the polar mobile phase, while less polar analytes interact more with the non-polar stationary phase (e.g., C18) and elute later.

3.2 Nomenclature

Abbreviations

3D	three dimensional
APSD	aerodynamic particle size diameter
CFC	chlorofluorocarbons
COPD	chronic obstructive pulmonary disease
CT	computed tomography
DICOM	digital imaging and communications in medicine
FDM	fused deposition modeling
FPF	fine particle fraction
FPF	fine particle fraction
G	generation
HFA	hydrofluoroalkane
HPLC	high-performance liquid chromatography
MMAD	mass median aerodynamic diameter
MOC	micro orifice collector
MT	mouth-throat
NGI	next generation impactor
PLA	polylactic acid
pMDIs	pressurized metered-dose inhalers
STL	stereolithography
VCU	Virginia Commonwealth University

3.3 References

Biswas, R., Hanania, N.A., Sabharwal, A., 2017. Factors determining in vitro lung deposition of albuterol aerosol delivered by a ventolin metered-dose inhaler. J. Aerosol Med. Pulm. Drug Deliv. 30, 256–266. https://doi.org/10.1089/jamp.2015.1278

Cheng, K.H., Cheng, Y.S., Yeh, H.C., Swift, D.L., 1997. Measurements of airway dimensions and calculation of mass transfer characteristics of the human oral passage. J. Biomech. Eng. 119, 476–482. https://doi.org/10.1115/1.2798296

Copley Sientific Limited, 2020. Driving Results in Inhaler Testing. Driv. Results Inhaler Test.

McCabe, J.C., Koppenhagen, F., Blair, J., Zeng, X.-M., 2012. ProAir ® HFA Delivers Warmer, Lower-Impact, Longer-Duration Plumes Containing Higher Fine Particle Dose Than Ventolin ® HFA. J. Aerosol Med. Pulm. Drug Deliv. 25, 104–109. https://doi.org/10.1089/jamp.2011.0891

Sanis Health Inc., 2021. Product Monograph: SANIS HFA (Salbutamol Sulfate Inhalation Aerosol, 100 mcg/actuation). [WWW Document]. URL https://health-products.canada.ca/dpd-bdpp/index-eng.jsp

Shekunov, B.Y., Chattopadhyay, P., Tong, H.H.Y., Chow, A.H.L., 2007. Particle size analysis in pharmaceutics: Principles, methods and applications. Pharm. Res. 24, 203–227. https://doi.org/10.1007/s11095-006-9146-7

Sou, T., Bergström, C.A.S., 2021. Contemporary formulation development for inhaled pharmaceuticals. J. Pharm. Sci. 110, 66–86. https://doi.org/10.1016/j.xphs.2020.09.006

Xi, J., Longest, P.W., 2007. Transport and Deposition of Micro-Aerosols in Realistic and Simplified Models of the Oral Airway. Ann. Biomed. Eng. 35, 560–581. https://doi.org/10.1007/s10439-006-9245-y

Chapter 4 - CFD Model Development

While *in-vivo* studies provide the most accurate and physiologically relevant data, serving as a reference standard for validating other methods, they are associated with several limitations. These include the high cost of imaging equipment, the time-consuming nature of experimental protocols, technical challenges in labelling and tracking aerosols, and ethical concerns regarding radiation exposure (Huang et al., 2021; Williams et al., 2022). As a result, researchers are increasingly relying on *in-vitro* models to evaluate aerosol delivery performance. However, *in-vitro* studies also face significant limitations that affect their translational accuracy.

Most *in-vitro* models lack anatomical and functional realism. Although 3D-printed or cast airway replicas capture the general geometry, they often overlook critical physiological features, such as mucociliary clearance, wall motion, humidity, and thermal gradients. These factors play a vital role in determining aerosol transport and deposition but are typically absent from rigid, static in *in-vitro* setups. Additionally, breathing patterns in such systems are often oversimplified using steady or sinusoidal flow profiles, which fail to reflect inter-patient variability or disease-specific dynamics. Regional deposition measurements also involve complex segmentation and rinsing techniques that may introduce variability and limit reproducibility. Together, these limitations hinder the development of robust *in-vitro–in-vivo* correlations and challenge the predictive reliability of *in-vitro* data alone (Huang et al., 2021; Talaat et al., 2022a).

With the rapid advancement of computational power, *in-silico* modeling has emerged as a powerful complementary approach to bridge the gap between *in-vitro* and *in-vivo* research. In particular, computational fluid dynamics (CFD) models have been widely adopted to simulate aerosol transport within the respiratory tract and optimize inhaler design. By solving the Navier–Stokes equations for air–aerosol multiphase flows, CFD enables detailed, non-invasive prediction of airflow, particle trajectories, and both total and regional deposition patterns under a wide range of physiologically realistic conditions. These simulations offer an efficient, customizable, and cost-effective means of understanding drug delivery mechanisms, providing valuable insights that are often difficult to obtain through experimental methods alone (Bhardwaj et al., 2022; Kadota et al., 2022; Wu et al., 2022). Despite its advantages, CFD-based aerosol simulation has limitations, including reliance on idealized assumptions, uncertainties across different modeling frameworks,

high computational cost, and the need for experimental validation to ensure physiological relevance.

4.1 CFD Modeling of Airflow

CFD models simulate airflow by numerically solving the Navier–Stokes (NS) equations, which treat air as a continuous fluid governed by the conservation of mass and momentum. For laminar flows, especially in smaller airways where turbulence is minimal, the NS equations can be solved directly without additional modeling assumptions. However, in upper airway regions such as the mouth-throat (MT) and extrathoracic (ET) zones, flow is often transitional or fully turbulent, conditions that significantly influence aerosol behavior and deposition (Feng et al., 2021a; Longest and Vinchurkar, 2009; Longest and Vinchurkar, 2007). To address these complexities, turbulence effects are incorporated into CFD via the eddy viscosity concept, which is calculated using turbulence models. More computationally feasible approaches, such as unsteady Reynolds-Averaged Navier–Stokes (URANS) models and Large Eddy Simulation (LES), are widely used to approximate these effects while maintaining manageable computational costs (Huang et al., 2021). In this study, these models were selected based on the flow conditions and modeling requirements.

The conservation of mass and momentum:

$$\nabla.(\overline{\boldsymbol{u}}) = S_{DPM} \tag{4.1}$$

$$\rho(\partial/\partial t\,(\overline{\boldsymbol{u}}) + \nabla.(\overline{\boldsymbol{u}}\overline{\boldsymbol{u}})) = -\nabla\bar{P} + \nabla.(\bar{\sigma}) - \nabla.(\bar{\tau}) + \boldsymbol{F}_i \tag{4.2}$$

$$\bar{\sigma} = \mu(\nabla\overline{\boldsymbol{u}} + (\nabla\overline{\boldsymbol{u}})^T) - 2/3\,\nabla.\overline{\boldsymbol{u}}I \tag{4.3}$$

$$\bar{\tau} = -2\mu_t\bar{S} \tag{4.4}$$

$$\bar{S} = 1/2(\nabla\overline{\boldsymbol{u}} + (\nabla\overline{\boldsymbol{u}})^T) \tag{4.5}$$

where ρ is the mixture (air, water vapor, and droplet vapor) density, $\overline{\boldsymbol{u}}$ is the time-averaged velocity in the URANS model or filtered in the LES model, S_{DPM} is the mass transfer from the discrete phase to the continuous phase, $\bar{P}$ is time-averaged pressure in URANS or filtered pressure in LES, $\bar{\bar{\sigma}}$ is the stress tensor due to molecular viscosity, $\bar{\tau}$ is Reynolds stress tensor in URANS or sub-grid scale (SGS) stress tensor in LES, $\boldsymbol{F_i}$ is the body force, μ is the dynamic viscosity of the mixture μ_t is eddy viscosity, and $\bar{S}$ is the time-averaged rate-of-strain tensor in URANS or the filtered rate-

of-strain tensor in LES. The eddy viscosity in Eq. (4.4) is calculated using turbulence models, which are discussed in the following section.

4.1.1 Turbulent Models

4.1.1.1 The Unsteady Reynolds Averaged Navier-Stokes (URANS)

In URANS, the instantaneous flow variables are decomposed into mean and fluctuating components, and the time-averaged equations are solved. This allows for modeling the effect of turbulence directly without resolving all turbulent scales. Various turbulence models, such as the standard k-ε and k-ω models, are used within the URANS framework to approximate the turbulent stresses (Wilcox, 1993). This model (RANS) is particularly suitable for steady-state simulations and has been widely applied to study airflow in the respiratory tract, especially in regions where a fully resolved turbulence structure is not critical. The k-ε model is computationally efficient and performs well in simulating flows with small pressure gradients, such as in free-stream regions. However, studies indicate that the standard k-ε model struggles to accurately capture flow behaviour in the ET region, particularly in regions with recirculation zones, free-shear layers, and curved streamlines. Additionally, it is not well-suited for modeling low-Reynolds-number turbulent flows near the wall.

While the k-ω model improves near-wall resolution and performs better in boundary-layer predictions, it can be overly sensitive to free-stream boundary conditions, limiting its reliability in regions away from walls. To overcome the combined limitations of both the k-ε and standard k-ω models, the Shear Stress Transport (SST) k-ω model was employed in this study. This model blends the strengths of both approaches by using the k-ω formulation near walls and transitioning to the *k-ε* formulation in the far field (Huang et al., 2021; Menter, 1994). It also incorporates shear stress transport modifications to better predict flow separation and adverse pressure gradients.

4.1.1.2 Shear Stress Transport (SST) k-ω Turbulence Model

The SST k-ω model is a two-equation eddy-viscosity model that solves separate transport equations for the turbulent kinetic energy (k) and the specific dissipation rate (ω), as follows:

$$\mu_t = \rho k/\omega \tag{4.6}$$

$$\rho(\partial/\partial t\,(k) + \nabla.(\overline{\boldsymbol{u}})) = P_k - \beta^*\rho\omega k + \nabla.[(\mu + \sigma_k\mu_t)\nabla k] \tag{4.7}$$

$$\rho(\partial/\partial t\,(\omega) + \nabla.\left(\bar{\boldsymbol{u}}_p\omega\right)) = P_k\omega/k - \beta\rho\omega^2 + +\nabla.[(\mu + \sigma_\omega\mu_t)\nabla\omega] + 2(1 - F_l)\rho\sigma_{\omega 2}1/\omega\nabla k.\nabla\omega \quad (4.8)$$

$$F_l = \tanh\left(\min\left(\max\left(\sqrt{k}/\beta^*\omega y, 500\mu/y^2\rho\omega\right), 4\rho\sigma_{\omega 2}k/CD_{k\omega}y^2\right)\right) \quad (4.9)$$

where k is turbulent kinetic energy, ω is specific dissipation rate, P_k is the production of turbulent kinetic energy, $\beta^*$is an empirical constant, σ_k is the turbulent Prandtl number for k, β is an empirical constant, $\sigma_\omega$is the turbulent Prandtl number for ω, F_l is a Blending function used to switch between k−ω (near-wall) and k−ϵ (far-field) formulations. y is the distance to the nearest wall, and $CD_{k\omega}$is the cross-diffusion term (Wilcox, 1993).

4.1.1.3 Large Eddy Simulation (LES)

LES is a turbulence modeling approach in CFD that balances accuracy and computational cost by directly resolving the large, energy-containing turbulent eddies while modeling only the smaller, more isotropic sub-grid scales. Unlike RANS models, which model the entire spectrum of turbulence, LES uses a filtering operation to separate large eddies from small ones. The large eddies are numerically resolved, and the small-scale motions are captured through SGS models.

In this research, SGS turbulence was modeled using two approaches, depending on the model's complexity. The kinetic energy transport model (Eqs. (4.10-11)) was employed to estimate sub-grid-scale turbulence energy, providing a more dynamic and physically accurate representation of unresolved motions.

$$\mu_t = C_k {k_{sgs}}^{1/2}\Delta_f \quad (4.10)$$

$$\partial/\partial t\,(\bar{k}_{sgs}) + \nabla.\left(\bar{\boldsymbol{u}}\bar{k}_{sgs}\right) = \bar{\tau}(\nabla.\bar{\boldsymbol{u}}) - C_\varepsilon\rho\, k_{sgs}^{3/2}/\Delta_f + \nabla.\left(\mu_t/\sigma_k\,\nabla.k_{sgs}\right) \quad (4.11)$$

where k_{sgs} is dynamic kinetic energy. Δ_f is the filter size computed from $\Delta_f = V^{1/3}$ (where V is the volume of the computational cell), and C_k and C_ε are constants determined dynamically (Kim and Menon, 1997).

Additionally, the Wall-adapting Local Eddy-Viscosity (WALE) model was used as the subgrid-scale model. WALE is particularly well-suited for capturing near-wall turbulent structures, as it accounts for both strain and rotation rates, ensuring the eddy viscosity smoothly vanishes near walls without the need for wall functions.

$$\mu_t = \rho L_s^2 \left(S_{ij}^d S_{ij}^d\right)^{3/2} / \left(\left(\bar{S}_{ij}\bar{S}_{ij}\right)^{5/2} + \left(S_{ij}^d S_{ij}^d\right)^{5/4}\right) \tag{4.12}$$

$$L_s = min\left(k_K d, C_w V^{1/3}\right) \tag{4.13}$$

$$S_{ij}^d = \partial \bar{u}_i / \partial x_j \tag{4.14}$$

where L_s is the mixing length for sub-grid scales, k_K is the von Kármán constant, d is the distance to the closest wall, and C_w is the WALE constant, which is 0.325 (Nicoud and Ducros, 1999).

4.1.2 Energy Equation

To predict the temperature distribution in the airway, the following energy (E) equation for airflow is solved:

$$\rho(\partial/\partial t\,(E) + \nabla.\left((\overline{\boldsymbol{u}})(E)\right)) = \nabla.\left(k_{eff}\nabla T - \sum_s h_s \vec{J}_s + \left(\bar{\tau}_{eff}.\overline{\boldsymbol{u}}\right)\right) \tag{4.15}$$

where $k_{eff} = k + k_t$ is effective conductivity in which k_t is turbulent thermal conductivity, T is temperature, h_s is the species enthalpy, $\vec{J}_s$ is the diffusion flux of species, and $\bar{\tau}_{eff}$ is the effective shear stress.

4.2 Modeling Aerosol Dynamics

Modeling aerosol dynamics treats aerosols as individual particles in a continuous gas phase and solves their motion using Newton's second law. Depending on interaction modeling, it is divided into a discrete phase model (DPM) (ignoring particle-particle interactions) and the discrete element method (DEM) (explicitly resolving them). DEM provides more detailed predictions in dense flows but at significantly higher computational cost, making DPM more practical for dilute aerosol simulations.

4.2.1 Discrete Phase Model (DPM)

In the Lagrangian framework, particle motion is calculated by integrating the force balance equation. This equation relates the particle's inertia to the external forces acting on it, as presented in equation (4.15):

$$m_p \, \mathrm{d}u_p/d\mathrm{t} = 18\mu/\rho_p d_p^2 \frac{m_d C_{Dd} Re_p}{24}\left(\overline{\boldsymbol{u}} - u_p\right) + g\left(\rho_p - \rho\right)/\rho_d + F_d \tag{4.15}$$

where u_p ρ_p, d_p, and m_p are the velocity, density, diameter, and mass of the particles, respectively. (Ahookhosh et al., 2021; Narayanan et al., 2022). F_d is the sum of additional forces acting on a particle, such as Saffman's lift force, buoyancy, pressure force, Basset force, and virtual mass effects. These forces are typically considered in high-shear flow conditions, especially when the particle size is small, and the density difference between the particle and the fluid is not large. In inhalation drug delivery, particle motion is primarily governed by drag and gravitational forces, which typically dominate over other secondary forces (Aghaei et al., 2023; Feng et al., 2021a; Talaat et al., 2022a).

$$C_{Dd} = C_D/C_c \tag{4.16}$$

$$C_D = \begin{cases} 24/Re_d & Re_d \le 0.1 \\ 24/Re_d(1 + 0.15Re_d^{0.687}) & 0.1 \le Re_d \le 1000 \\ 0.44 & Re_d > 1000 \end{cases} \tag{4.17}$$

$$C_c = 1 + 2\lambda/d_d\left(1.257 + 0.4e^{-(11d_d/2\lambda)}\right) \tag{4.18}$$

$$Re_d = \rho_d d_d |\overline{\boldsymbol{u}} - \overline{\boldsymbol{u}}_{\boldsymbol{d}}|/\mu \tag{4.19}$$

where C_D represents the drag coefficient, C_c denotes the Cunningham correction factor (Morsi and Alexander, 1972), λ indicates the molecular mean free path, and Re_d is the Reynolds number of particles.

Aerosol generated by a pressurized metered-dose inhaler (pMDI) is inherently polydisperse. This particle size distribution (PSD) plays a critical role in determining aerosol behavior and deposition within the respiratory tract. PSD is influenced by several factors, including the internal geometry of the pMDI device (e.g., nozzle shape and orifice diameter), the physicochemical properties of the formulation (e.g., propellant type, viscosity, and surface tension), and the ambient conditions

during actuation (e.g., temperature and humidity). To mathematically characterize this distribution, several analytical models have been fitted to the data (Alatrash, 2018; Alderliesten, 2013; de Charras et al., 2022). Rosin–Rammler distribution, log-normal, and Nakagami distributions as shown in **Fig. 4-1**. These distributions use two primary adjustable parameters, the scale parameter (representing characteristic diameter) and the shape parameter (controlling the spread or uniformity), to fit the experimental data. Among these, the Rosin–Rammler distribution (red line) is widely used in aerosol modeling due to its simplicity and ability to capture the right-skewed nature of atomized sprays. The Rosin–Rammler distribution, expressed as:

$$M = 1 - \exp\left(-[x/\acute{x}]^n\right) \tag{4.20}$$

M is the mass or volume fraction of particles with sizes smaller than or equal to x, assuming constant mass density of all particles, and x is the particle size. $\acute{x}$ is the characteristic particle size of the distribution, defined as the size at which 63.2% of the particles are smaller (by volume or mass), and 36.8% are larger, and n is the spread parameter of the distribution.

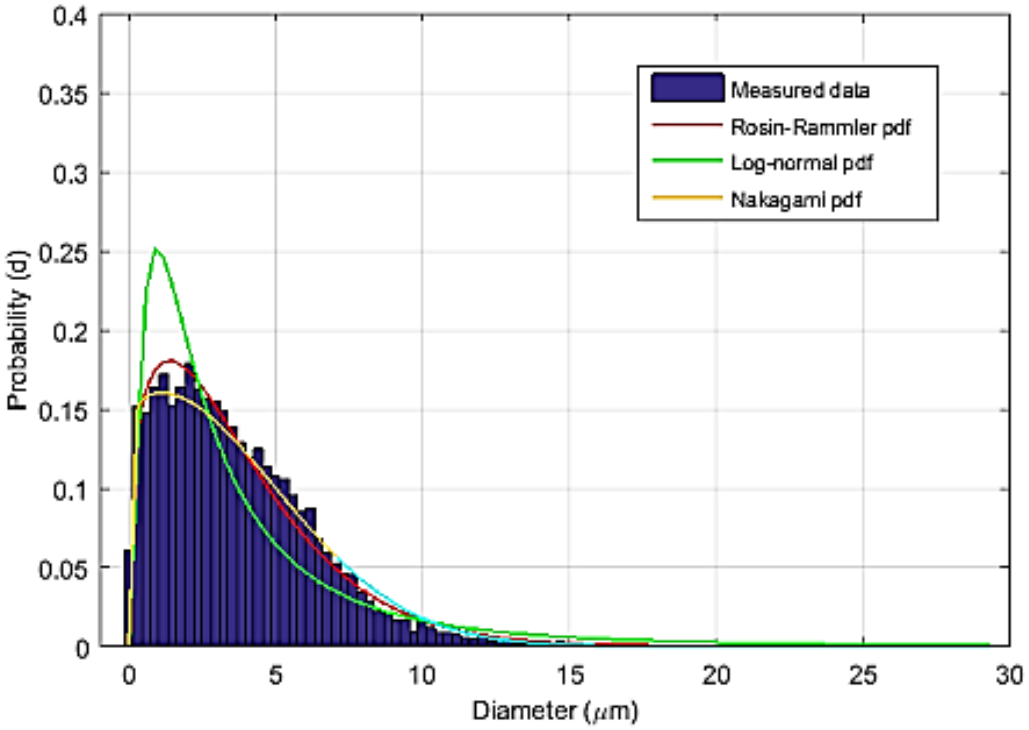

Fig. 4-1: Histogram of the experimental data of particle diameter with curve fitting of probability distribution functions for Ventolin® inhaler (Alatrash, 2018).

In addition to airflow temperature, particle heat and mass transfer are also modeled to capture the thermal and evaporative behavior of inhaled aerosol particles. As particles travel through the warm and humid environment of the respiratory tract, they exchange heat with the surrounding air and lose mass through evaporation. These interactions affect their temperature and size, which are critical factors influencing deposition patterns, drug delivery efficiency, and therapeutic outcomes.

The temperature of the particles is estimated based on the convective and latent heat transfer between them and the airflow:

$$m_p c_p dT_p/dt = h_c A_p\left(T - T_p\right) + dm_p/dt(h_{fg}) \tag{4.21}$$

where c_p and A_p are the particles' heat capacity and surface area. h_c is the convective heat transfer coefficient, and h_{fg} is the latent heat (Aghaei et al., 2023).

The convective heat transfer coefficient h_c is calculated (Aghaei et al., 2023):

$$Nu = h_c\, d_p/k = (\ln(1 + B_T)/B_T)\left(2 + 0.6Re_p^{1/2}Pr^{1/3}\right) \tag{4.22}$$

Nu is the Nusselt number and B_T is the Spalding heat transfer number defined as follows (ANSYS, 2020):

$$B_T = \left(c_p\left(T - T_p\right)\right)/h_{fg} - \left(\dot{q}_p/\dot{m}_p\right) \tag{4.23}$$

where $\dot{q}_p$ is the heat transfer rate to the particle and $\dot{m}_p$ is the particle evaporation rate.

4.3 Modeling the Mucus Layer

The respiratory tract plays a vital role in preparing inhaled air before it reaches the alveoli, ensuring that it is both warmed to body temperature and fully humidified. This air conditioning process is primarily facilitated by the mucus layer lining the airway surfaces. Since inhaled air is often cooler and drier than the airway mucosa, heat and moisture are transferred from the epithelial tissues to the airflow. Specifically, thermal energy flows from the tissue to the airway lumen, while water evaporates from the mucus layer, enriching the inspired air with moisture. This mechanism results in a net transfer of heat and water vapour from the body with each breath. A schematic of this process is shown in **Fig. 4-2**.

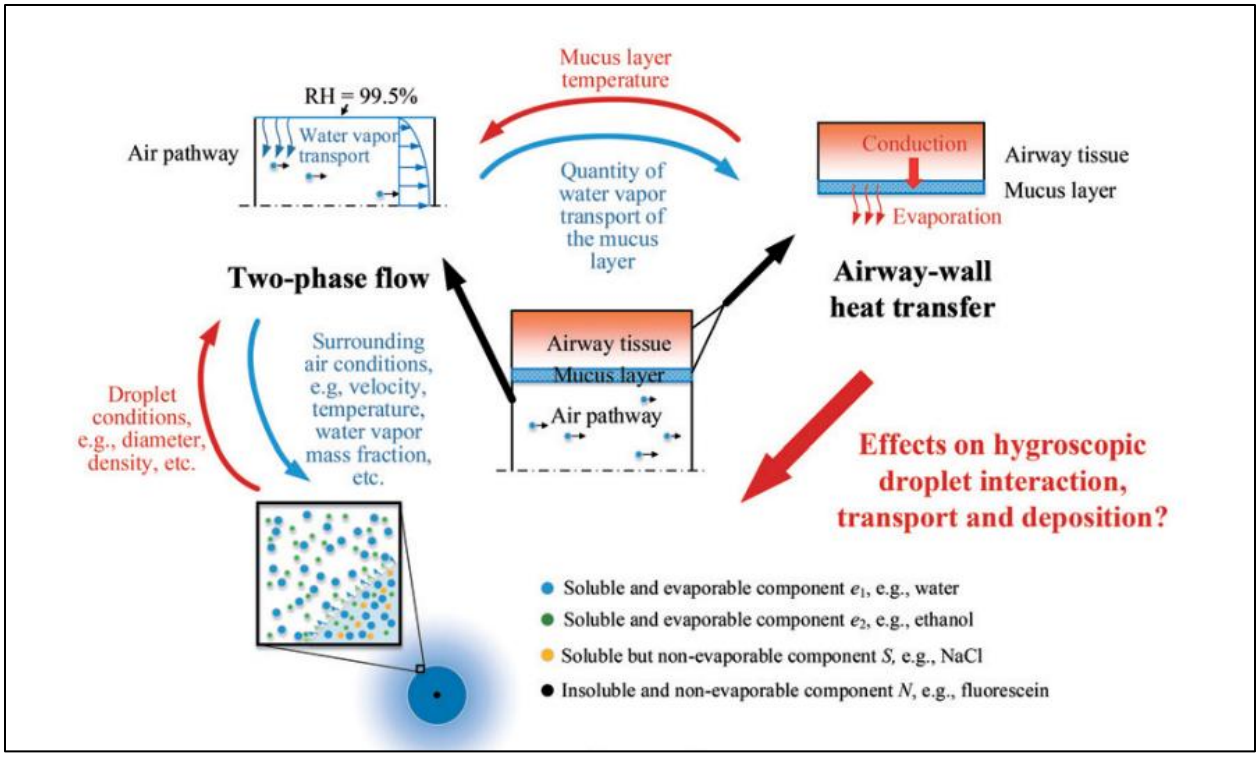

Fig. 4-2: Schematic illustration of hygroscopic droplet transport and interaction with the mucus layer and airway wall (Chen et al., 2018).

In this study, two different approaches were employed to model the mucus layer. The first approach focused on its thickness and thermal effects, considering only heat transfer between the airway wall and the inhaled airflow, as represented in Eq. (4.21). In this model, the airway tissue and mucus layer, assumed to have thicknesses of 0.5 mm and 10 μm, respectively, were treated as uniform solid materials with thermophysical properties approximated to those of water, given that airway mucus is composed of approximately 95% water.

$$\partial(\rho_m h_m)/\partial t = \partial(k_m \partial T_m/\partial x_j)/\partial x_j \tag{4.24}$$

where ρ_m, h_m, k_m, and T_m are density, enthalpy, thermal conductivity, and temperature of the mucus layer, respectively.

The second approach implemented the Eulerian wall film (EWF) model, which enables simulation of a thin liquid film on the airway surface and accounts for both heat and mass transfer, providing a more comprehensive representation of mucus layer dynamics. The conservation of mass for a two-dimensional film is expressed as follows (Kakimpa et al., 2016; Ren et al., 2020):

$$\partial \rho_f H/\partial t = \dot{m}_s \tag{4.25}$$

where ρ_f and H are the film density and height, respectively. $\dot{m}_s$ is a mass source per unit wall area due to particle absorption and phase change. Conservation of film energy is also expressed as follows (O'Rourke and Amsden, 1996):

$$\partial \rho_f H T_f/\partial t = 1/C_p\left[2k_f/H\left(T_s + T_w + 2T_{half}\right) + \dot{q}_{imp} + \dot{m}_{vap}L\right] \tag{4.26}$$

where T_f, T_s, T_w, and T_{half} are the average film temperature, film surface temperature, wall temperature, and film half-depth temperature, respectively. $\dot{q}_{imp}$ is the heat flux source resulting from airflow and particle impingement on the wall. $\dot{m}_{vap}$ is the mass vaporization or condensation rate, and L is the latent heat associated with the phase change.

4.4 Boundary Conditions

In this research, the inlet boundary condition was set to a mass-flow inlet corresponding to the breathing flow rate. The outlet boundary condition was set to zero pressure, and the airway walls were assigned a no-slip boundary condition. In the DPM framework, a trap boundary condition was applied to the airway walls, while an escape boundary condition was set for particles at the airway outlets. Mathematically, when a particle trajectory intersected the wall at time t_c, its motion was stopped:

$$X_p(t > t_c) = X_p(t_c) \quad , \quad u_p(t > t_c) = 0 \tag{4.27}$$

where X_p is the position of the tracked particle. Its mass was added to the deposited mass on that boundary. When a particle reached the outlet, its trajectory was terminated, and its mass was added to the escaped mass, i.e., it was removed from the domain without rebound or further interaction.

4.5 Simulation Solver Setting

In this study, airflow and aerosol transport within airway geometries were simulated using ANSYS Fluent 2020R2 and 2024R1 (ANSYS Inc., Canonsburg, PA), with a focus on capturing transient phenomena. The governing Navier–Stokes equations for incompressible flow were solved in integral form over control volumes, consistent with the finite-volume method used by Fluent. The computational domain was discretized into an unstructured mesh. Governing equations for mass, momentum, energy, and scalar transport were iteratively solved using a pressure-based segregated solver.

For transient LES simulations, the kinetic energy transport and WALE subgrid-scale models were employed to better resolve near-wall turbulence. A bounded central differencing scheme was employed for the spatial discretization of the momentum equations to maintain numerical accuracy in resolving large-scale eddies. Temporal discretization was handled via the bounded second-order implicit scheme. Second-order upwind schemes were used for subgrid kinetic energy, energy, and scalar transport variables. Pressure–velocity coupling was achieved using the SIMPLEC algorithm, ensuring robust transient resolution under dynamically deforming boundaries.

For the SST k-ω model, pressure–velocity coupling was handled using the Phase-Coupled SIMPLE algorithm, which is well-suited to multiphase flows. Spatial discretization schemes were selected to enhance solution stability and accuracy. The PRESTO scheme was used for pressure interpolation, which is particularly suited for swirling flows and stratified multiphase flows. The Least Squares Cell-Based method was applied for gradient calculations. For the momentum, turbulent kinetic energy, specific dissipation rate, and energy equations, second-order upwind schemes were employed to enhance accuracy and minimize numerical diffusion.

4.6 Nomenclature

CFD	computational fluid dynamics
DEM	discrete element method
DPM	discrete phase model
ET	extrathoracic
EWF	Eulerian wall film
LES	large eddy simulation
MT	mouth-throat
NS	Navier-Stokes
pMDI	pressurized metered-dose inhaler
PSD	particle size diameter
RANS	Reynolds-averaged Navier-Stokes
SGS	sub-grid scale
SST	shear stress transport
WALE	wall-adapting local eddy viscosity

Notations

$\vec{J}_s$	diffusion flux of species ($kg/m^2.s$)
$\dot{m}_p$	particle evaporation rate (kg/s)
$\dot{m}_s$	mass source ($kg/m^2.s$)
$\dot{m}_{vap}$	mass vaporization or condensation rate ($kg/m^2.s$)
$\dot{q}_{imp}$	source term due to airflow and particle impingement on the wall (W/m^2)
$\dot{q}_p$	heat transfer rate to particle (J/s)
$\bar{\tau}_{eff}$	effective shear stress (Pa)
Δ_f	filter size (m)
h_c	convective heat transfer coefficient ($W/m^2.K$)
h_{fg}	latent heat (J/kg)
h_s	species enthalpy (J/kg)
A_p	particle surface area (m^2)
B_T	spalding heat transfer number (-)
C_{Dd}	drag force coefficient (-)
$CD_{k\omega}$	cross-diffusion term ($kg/m^3.s^2$)
C_k	constant (-)
C_w	WALE constant (-)
C_ε	constant (-)
F_L	blending function to switch between $k-\omega$ (-)
F_d	additional forces acting on a particle ($kg/m.s^2$)
L_s	mixing length for sub-grid scales (m)
P_k	production of turbulent kinetic energy (m^2/s^2)
Re_p	particle Reynolds number (-)
$\bar{S}$	time-averaged or filtered rate-of-strain tensor ($1/s$)
S_{DPM}	mass transfer from the discrete phase to the continuous phase ($kg/m^2.s$)
S_{ij}^d	modified rate-of-strain tensor ($1/s$)
T_{half}	film half-depth temperature (K)
T_f	film temperature (K)

T_m	mucus layer temperature (K)
T_s	film surface temperature (K)
T_w	wall temperature (K)
T_p	particle temperature (K)
c_p	particle heat capacity ($J/kg\,.K$)
$\vec{g}$	gravitational acceleration (m/s^2)
k_K	Von Kármán constant (-)
k_{eff}	effective conductivity ($W/m\,.K$)
k_m	mucus layer thermal conductivity ($W/m\,.K$)
k_{sgs}	subgrid scale dynamic kinetic energy (m^2/s^2)
k_t	turbulent thermal conductivity ($W/m\,.K$)
u_p	particle velocity (m/s)
$\acute{x}$	location parameter of the distribution (m)
$\overline{\boldsymbol{P}}$	time-averaged or filtered pressure (Pa)
$\overline{\boldsymbol{u}}$	time-averaged or filtered velocity (m/s)
β^*	empirical constant (-)
μ_t	turbulent dynamic viscosity ($Pa.s$)
ρ_f	film density (kg/m^3)
ρ_m	mucus layer density (kg/m^3)
$\bar{\sigma}$	stress tensor (Pa)
σ_k	turbulent Prandtl number for k (-)
σ_ω	turbulent Prandtl number for ω (-)
$\bar{\tau}$	subgrid-scale stress (Pa)
C_c	Cunningham correction (-)
C_D	drag coefficient (-)
d_p	particle diameter (m)
E	thermal energy (J)
$\boldsymbol{F_i}$	body force (N)
H	film height (m)

m_p	particle mass (kg)
T	temperature (K)
λ	molecular mean free path (m)
μ	mixture dynamic viscosity $(Pa.s)$
ρ_p	particle density (kg/m^3)
L	latent heat (J/kg)
M	mass or volume fraction of particles (-)
Nu	Nusselt number (-)
V	computational cell volume (m^3)
d	distance (m)
k	turbulent kinetic energy (m^2/s^2)
n	spread parameter of the distribution (-)
x	particle size in Rosin–Rammler distribution (m)
y	distance to the nearest wall in the k−ω model (m)
β	empirical constant (-)
ρ	mixture density (kg/m^3)
ω	specific dissipation rate $(1/s)$

4.7 References

Aghaei, Y., Sajadi, B., Ahmadi, G., 2023. The effect of the mucus layer and the inhaled air conditions on the droplets fate in the human nasal cavity: A numerical study. J. Aerosol Sci. 171, 106163. https://doi.org/10.1016/j.jaerosci.2023.106163

Ahookhosh, K., Saidi, M., Mohammadpourfard, M., Aminfar, H., Hamishehkar, H., Farnoud, A., Schmid, O., 2021. Flow structure and particle deposition analyses for optimization of a pressurized metered dose inhaler (pMDI) in a model of tracheobronchial airway. Eur. J. Pharm. Sci. 164, 105911. https://doi.org/10.1016/j.ejps.2021.105911

Alatrash, A., 2018. Experimental and Numerical Study of Inhaler Spray Characterization (Size Distributions and Velocity). PhD Thesis, Carlt. Univ. Ottawa. Carleton University, Ottawa, Ontario. https://doi.org/10.22215/etd/2018-12966

Alderliesten, M., 2013. Mean Particle Diameters. Part VII. The Rosin-Rammler Size Distribution: Physical and Mathematical Properties and Relationships to Moment-Ratio Defined Mean Particle Diameters. Part. Part. Syst. Charact. 30, 244–257. https://doi.org/10.1002/ppsc.201200021

ANSYS, 2020. ANSYS FLUENT Theory Guide, 2020 R2. ed. ANSYS, Inc. and Ansys Europe, Ltd. are UL registered ISO 9001: 2015 companies.

Bhardwaj, S., Koullapis, P., Kassinos, S.C., Sznitman, J., 2022. Fate of inhaled aerosols under the influence of glottal motion in a realistic in silico human tracheobronchial tree model. Eur. J. Pharm. Sci. 173. https://doi.org/10.1016/j.ejps.2022.106172

Chen, X., Kleinstreuer, C., Zhong, W., Feng, Y., Zhou, X., 2018. Effects of thermal airflow and mucus-layer interaction on hygroscopic droplet deposition in a simple mouth–throat model. Aerosol Sci. Technol. 52, 900–912. https://doi.org/10.1080/02786826.2018.1476751

de Charras, Y.L., Ramírez-Rigo, M.V., Bertin, D.E., 2022. Prediction of the particle size distribution of the aerosol generated by a pressurized metered-dose inhaler. Powder Technol. 399, 117151. https://doi.org/10.1016/J.POWTEC.2022.117151

Feng, Y., Zhao, J., Hayati, H., Sperry, T., Yi, H., 2021. Tutorial : Understanding the transport, deposition, and translocation of particles in human respiratory systems using Computational Fluid-Particle Dynamics and Physiologically Based Toxicokinetic models. J. Aerosol Sci. 151, 105672. https://doi.org/10.1016/j.jaerosci.2020.105672

Huang, F., Zhu, Q., Zhou, X., Gou, D., Yu, J., Li, R., Tong, Z., Yang, R., 2021. Role of CFD based in silico modelling in establishing an in vitro-in vivo correlation of aerosol deposition in the respiratory tract. Adv. Drug Deliv. Rev. https://doi.org/10.1016/j.addr.2020.09.007

Kadota, K., Matsumoto, K., Uchiyama, H., Tobita, S., Maeda, M., Maki, D., Kinehara, Y., Tachibana, I., Sosnowski, T.R., Tozuka, Y., 2022. In silico evaluation of particle transport and deposition in the airways of individual patients with chronic obstructive pulmonary disease. Eur. J. Pharm. Biopharm. 174, 10–19. https://doi.org/10.1016/j.ejpb.2022.03.010

Kakimpa, B., Morvan, H., Hibberd, S., 2016. The depth-averaged numerical simulation of laminar thin-film flows with capillary waves. J. Eng. Gas Turbines Power 138.

https://doi.org/10.1115/1.4033471

Kim, W.W., Menon, S., 1997. Application of the localized dynamic subgrid-scale model to turbulent wall-bounded flows. 35th Aerosp. Sci. Meet. Exhib. 1–12. https://doi.org/10.2514/6.1997-210

Longest, P.W., Vinchurkar, S., 2009. Inertial deposition of aerosols in bifurcating models during steady expiratory flow. J. Aerosol Sci. 40, 370–378. https://doi.org/10.1016/j.jaerosci.2008.11.007

Morsi, S.A., Alexander, A.J., 1972. An investigation of particle trajectories in two-phase flow systems. J. Fluid Mech. 55, 193–208. https://doi.org/10.1017/S0022112072001806

Narayanan, J.K., Lin, J., Feng, Y., Cui, X., 2022. Numerical study on the impact of mucus layer and inlet air-temperatures on the particle deposition in a highly idealized mouth-throat model using LES. Powder Technol. 395, 455–475. https://doi.org/10.1016/j.powtec.2021.09.073

Nicoud, F., Ducros, F., 1999. Subgrid-scale stress modelling based on the square of the velocity. Flow Meas. Instrum. 62, 183–200. https://doi.org/https://doi.org/10.1023/A:1009995426001

O'Rourke, P.J., Amsden, A.A., 1996. A particle numerical model for wall film dynamics in port-injected engines, in: SAE Technical Papers. https://doi.org/10.4271/961961

Ren, S., Li, W., Wang, L., Shi, Y., Cai, M., Hao, L., Luo, Zihao, Niu, J., Xu, W., Luo, Zujin, 2020. Numerical analysis of airway mucus clearance effectiveness using assisted coughing techniques. Sci. Rep. 10, 1–10. https://doi.org/10.1038/s41598-020-58922-7

Talaat, M., Si, X., Liu, X., Xi, J., 2022. Count- and mass-based dosimetry of MDI spray droplets with polydisperse and monodisperse size distributions. Int. J. Pharm. 623, 121920. https://doi.org/10.1016/j.ijpharm.2022.121920

Wilcox, D.C., 1993. Turbulence Modelling for CFD 3rd Edition, Turbulence Modeling for CFD.

Williams, J., Kolehmainen, J., Cunningham, S., Ozel, A., Wolfram, U., 2022. Effect of patient inhalation profile and airway structure on drug deposition in image-based models with particle-particle interactions. Int. J. Pharm. 612, 121321.

https://doi.org/10.1016/j.ijpharm.2021.121321

Worth Longest, P., Vinchurkar, S., 2007. Validating CFD predictions of respiratory aerosol deposition: Effects of upstream transition and turbulence. J. Biomech. 40, 305–316. https://doi.org/10.1016/j.jbiomech.2006.01.006

Wu, C., Yan, W., Chen, R., Liu, Y., Li, G., 2022. Numerical study on targeted delivery of magnetic drug particles in realistic human lung. Powder Technol. 397, 116984. https://doi.org/10.1016/j.powtec.2021.11.028

Chapter 5 - The Impact of Actuator Nozzle and Surroundings Condition on Drug Delivery using Pressurized-metered Dose Inhalers

5.1 Introduction

Respiratory diseases such as asthma and chronic obstructive pulmonary disease (COPD) are among the leading causes of severe illness and death worldwide (Ahookhosh et al., 2021; Kunda et al., 2017; Williams et al., 2022). Direct delivery of inhaled drugs to the lungs provides rapid therapeutic responses for these conditions (Kaviratna et al., 2019; Narayanan et al., 2022). With aerosolized drugs, ensuring sufficient deposition in the target region is crucial to maximize efficacy and minimize systemic side effects (Ahookhosh et al., 2019; Kaviratna et al., 2019).

pMDIs remain the most widely used devices for delivering aerosolized drugs to the respiratory tract (Biswas et al., 2017; Kunda et al., 2017; Ogrodnik et al., 2016; Sheth et al., 2017). They are popular due to their compactness, portability, and affordability (Ahookhosh et al., 2021; Duke et al., 2021). However, despite these advantages, only 5–30% of the emitted drug typically reaches the lungs, with most depositing in the MT region (McKiernan, 2019). Improving efficiency requires a deeper understanding of the initial plume formation and expansion. Yet, characterizing pMDI sprays is challenging due to their inherently transient, turbulent, three-dimensional, and multiphase nature (Duke et al., 2019; Ogrodnik et al., 2016).

A key component of a pMDI is the actuator nozzle, which governs atomization by shaping plume dynamics and droplet size distribution (Kleinstreuer et al., 2007). Lung deposition largely depends on the fine particle fraction (FPF), which in turn is influenced by both formulation design and actuator geometry (Biswas et al., 2017). Numerous studies have sought to optimize these parameters. For example, Kleinstreuer et al. (2007) demonstrated that a smaller 0.25 mm nozzle produced finer droplets and improved tracheal penetration compared to a 0.5 mm nozzle. However, the use of a spacer complicated the interpretation. More recently, Sadeghi et al. (2023) demonstrated that nozzle positioning within the mouth significantly alters deposition, with deeper placement increasing drug delivery to the throat. Ahookhosh et al. (2020) and Kadota et al. (2022) used CFD to highlight how patient-specific airflow patterns strongly influence deposition rates, while Spasov et al. (2022) showed that particle–particle interactions and flow dynamics (steady vs. swirling) produce notable differences in deposition outcomes.

Other actuator design features also play a critical role. Smyth et al. (2006) linked orifice length and sump depth to spray patterns and particle size. Chen et al. (2017) found that nozzle design and materials influence plume configuration, though not necessarily deposition. Dastoorian et al. (2022) reported that plume angle affects deposition patterns, with narrower cone angles producing larger particles and wider angles increasing mouth deposition. Duke et al. (2021) showed that twin-hole actuators with smaller orifices (0.22 mm) generated up to 75% more FPF than conventional single-hole designs, and that larger length-to-diameter ratios improved nozzle performance. Importantly, most of these findings were obtained from open-environment tests, even though plume behavior changes substantially under confined conditions or during inhalation (Moraga-Espinoza et al., 2018). Talaat et al. (2022b) emphasized the need to study plume dynamics under realistic inhalation conditions, though such experiments remain technically challenging.

CFD has therefore become an essential tool for investigating plume dynamics, transport, and deposition within realistic airway geometries, offering insights that are difficult to obtain from in vivo or in vitro studies (Bhardwaj et al., 2022; Kadota et al., 2022; Wu et al., 2022). In this work, we used CFD to examine how actuator nozzle geometry influences plume behavior under near-physiological conditions. Specifically, we compared a conventional single-orifice nozzle with a twin-orifice design featuring a longer channel length, and we evaluated hydrodynamic parameters in realistic MT geometry rather than the simplified USP induction port model used in Duke et al. (2021). Our findings highlight the importance of incorporating anatomical realism when evaluating inhaler performance and optimizing respiratory drug delivery.

5.2 CFD Model Development

The 3D model geometry drawing and mesh generation for the MT airway and actuator shapes of the pMDI were carried out in ANSYS Workbench (ANSYS, Inc.).

5.2.1 Geometry and Mesh Generation

Fig. 5-1 (a-c) shows the geometry of a cylindrical space with a diameter of 60 mm and a length of 100 mm, representing an open-air environment, a real MT airway, and two different nozzles of pMDI (model A: MT connected to a conventional nozzle and model B: MT connected to a twin nozzle). The real geometry of the MT model was developed by the Respiratory and Aerosol Dynamics Research Group of Virginia Commonwealth University (School of Engineering, led by Dr. Worth Longest) (Byron et al., 2010; Delvadia et al., 2016, 2012; Longest and Xi, 2007; Xi

and Longest, 2008) and provided by the Respiratory Drug Deliver website (RDD) (Newman, 2015). The geometry of the inhaler nozzles was generated according to Duke et al. (2021) & (2019); the spray was modelled as an injection of droplets composed of the drug (i.e., ipratropium bromide), the propellant (hydrofluoroalkane (HFA) 134a), and the co-solvent (ethanol). The properties of these components are provided in **Table 5-1**.

Our geometries, including a cylinder representing the open-air environment, two nozzle geometries, and the real MT model, were discretized using tetrahedral elements in ANSYS® Workbench (ANSYS, Inc.). Prism elements with eight layers of thickness and a transition ratio of 0.272 were generated in the region near the airway wall to capture the high gradients at the wall (Feng et al., 2021; Talaat et al., 2022). The geometries and mesh were imported into ANSYS Fluent 2020R2 (ANSYS, Inc.). The tetrahedral and prism elements were then converted to polyhedral and poly-prism meshes, respectively, as shown in **Fig. 5-1**. Published studies (Feng et al., 2021) have demonstrated better convergence, greater accuracy due to increased cell connectivity, and lower computational cost; therefore, we employed the polyhedron-based mesh in our current work.

Mesh independence tests were performed for both open-air and MT models, and each setup was simulated until the end of spray injection. **Table 5-2** shows the number of meshes for each model. The open-air model's geometry was divided into six coaxial cylinders of varying lengths to generate multiple mesh sizes (**Fig. 5-1(a)**). This allowed the mesh size to increase from the inner cylinder outward, avoiding the unnecessary computational cost associated with high mesh counts.

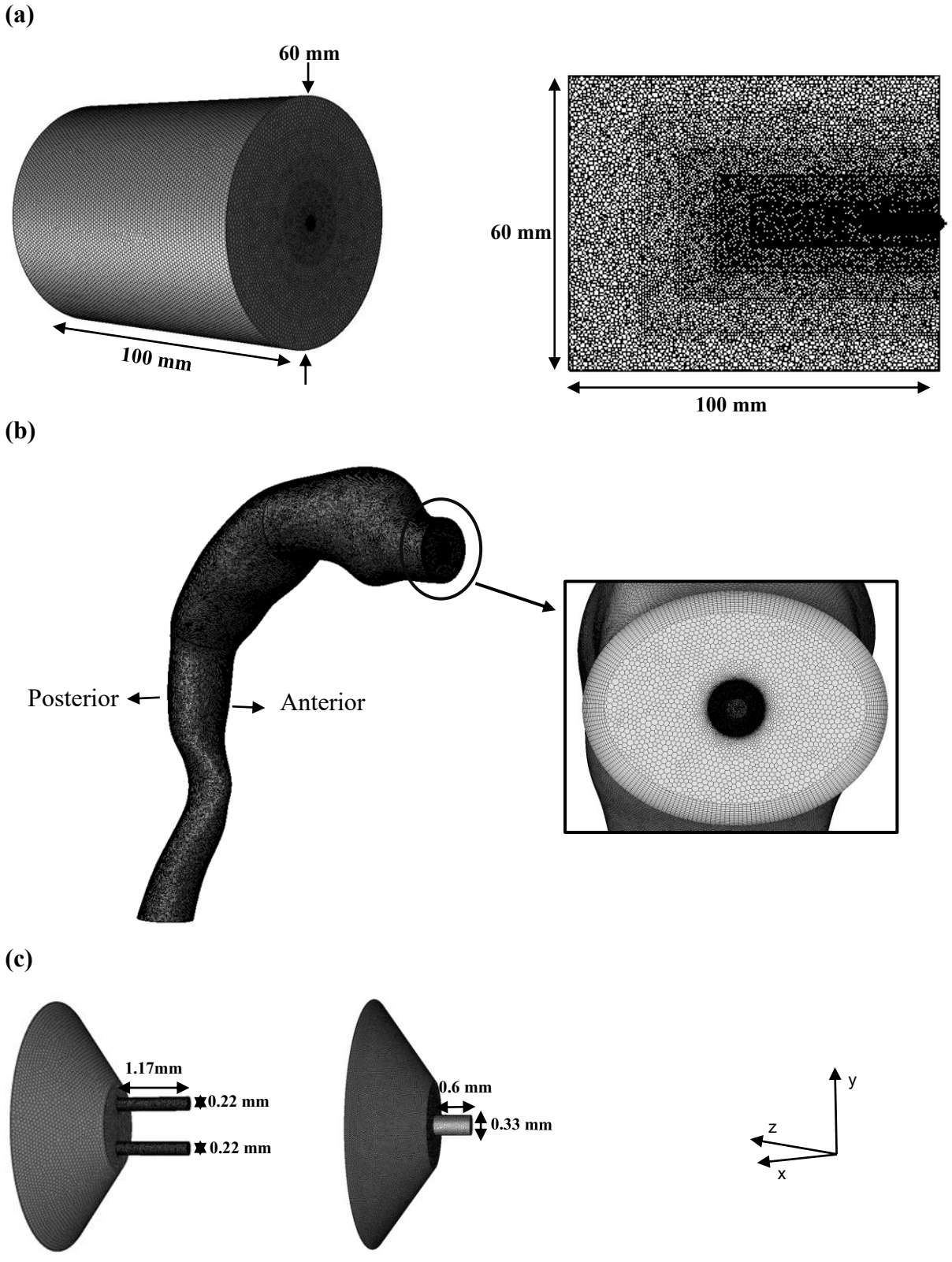

Fig. 5-1: Geometry and mesh structure of **(a)** open-air model; **(b)** MT model; and **(c)** conventional nozzle and twin nozzle of pMDI.

Table 5-1: Properties of propellant (HFA-134a), ethanol (co-solvent), and drug (ipratropium bromide).

Properties	HFA-134a	Ethanol	Drug
Density (kg/m^3)	1,311	790	1,311
Viscosity (kg/m.s)	0.000211	0.0012	-
Specific heat (J/kg.K)	982	2,470	-

Table 5-2: Number of meshes in open-air and MT models.

Case	Open-air Model	Case	MT Model
	Number of Mesh		Number of Mesh
Case 1	687,018	Case A	1,408,125
Case 2	1,157,272	Case B	2,629,917
Case 3	1,868,138	Case C	5,612,303
Case 4	3,183,662	-	-

Fig. 5-2 shows the mean velocity profile at the end of the injection time point, t = 0.1 s, for different mesh sizes. **Fig. 5-2(a)** presents the mean axial velocity of the plume along the centerline, from the nozzle exit to 100 mm away for the open-air model. This figure shows that the axial velocity is independent of mesh size near the nozzle exit. However, at a distance of almost 50 mm, we observe a difference between Case 2 and Case 3 due to the changing mesh size in this area. Percent root mean squared error (RMSE%) was utilized to quantify the differences among the profiles: $\text{RMSE\%} = \frac{\sqrt{\sum_{i,j=1}^{n}(u_i - u_j)^2/n}}{(\sum_{i=1}^{n} u_i)/n} \times 100$ (Khan et al., 2020), where u_i and u_j are aerosol velocities of Cases with different mesh numbers. RMSE% of Case 1 and Case 2, Case 2 and Case 3, and Case 3 and Case 4 were 10.48%, 7.59%, and 4.73%, respectively. Since the difference between Case 3 and Case 4 was below 5%, we proceeded with our simulations using Case 3, which had 1,868,138 meshes.

The MT model was segmented into three regions: the mouth, pharynx, and trachea, as shown in **Fig. 5-2(b)**. The mean axial velocities through the radial direction of three cross-sections, one in each of the mouth (MM′), pharynx (PP′), and trachea (TT′) regions, were compared in **Fig. 5-2**

(b)(i-iii). In the mouth region, the RMSE% of Case A and Case B was 48.28%, and Case B and Case C was 7.45%. In the pharynx area, the percentages were 70.02% and 9.43%, respectively. In the trachea region, they were 8.1% and 5.88%, respectively. Because the difference between Case B and Case C across all regions was less than 10%, Case B (2,629,917 meshes) was chosen.

5.2.2 Continuous Phase

Drug delivery in the airway is a multi-phase flow phenomenon. The complexity of the MT airway geometry creates a transition from laminar to turbulent flow (Ahookhosh et al., 2021; Chen et al., 2017). We used the large-eddy simulation (LES) model for our simulations. LES modelling of airflow in the MT geometry is comparable to *in-vitro* studies and can accurately predict the transition from laminar to turbulent flow (Cui and Gutheil, 2011; Huang et al., 2021).

Considering air as a continuous phase, we used ANSYS Fluent (ANSYS® release 2020 R2 v20.2) to solve the unsteady, three-dimensional, and incompressible Navier-Stokes equations (Equations (4.1)-(4.5) and (4.10)-(4.11).

We adopted the inhalation flow rate of 30 L/min (the normal maximum inspiratory flow rate for an adult at rest) to simulate breathing conditions (Biswas et al., 2017; Gurumurthy and Kleinstreuer, 2021; Worth Longest and Hindle, 2009; Wu et al., 2022; Zhang et al., 2006). The inlet and outlet were set to inlet velocity and outlet-pressure conditions, respectively, and the nozzle and MT wall were set to the no-slip boundary condition. The time step size for this simulation was set at 0.2 ms.

5.1.1 Discrete Phase Model (DPM)

The spray emitted from a pMDI is a high-speed, transient, turbulent, multi-component flow comprising propellant, ethanol, and the active pharmaceutical ingredient (API). The Lagrangian discrete phase model (DPM) was employed to inject a multi-component solution into the pMDI flow field. The mass fractions of propellant, ethanol, and drug were 85%, 14.79%, and 0.21%, respectively (Duke et al., 2019). Due to the dilute particle flow, a one-way coupling between the fluid and particles, which neglects particle-particle interactions, was considered (Ahookhosh et al., 2021; Rahman et al., 2021). The Rosin-Rammler method (in size ranges from 1 μm to 20 μm) was employed to describe the particle distribution. The set injection properties of a solid-cone injection for both nozzles are provided in **Table 5-3**.

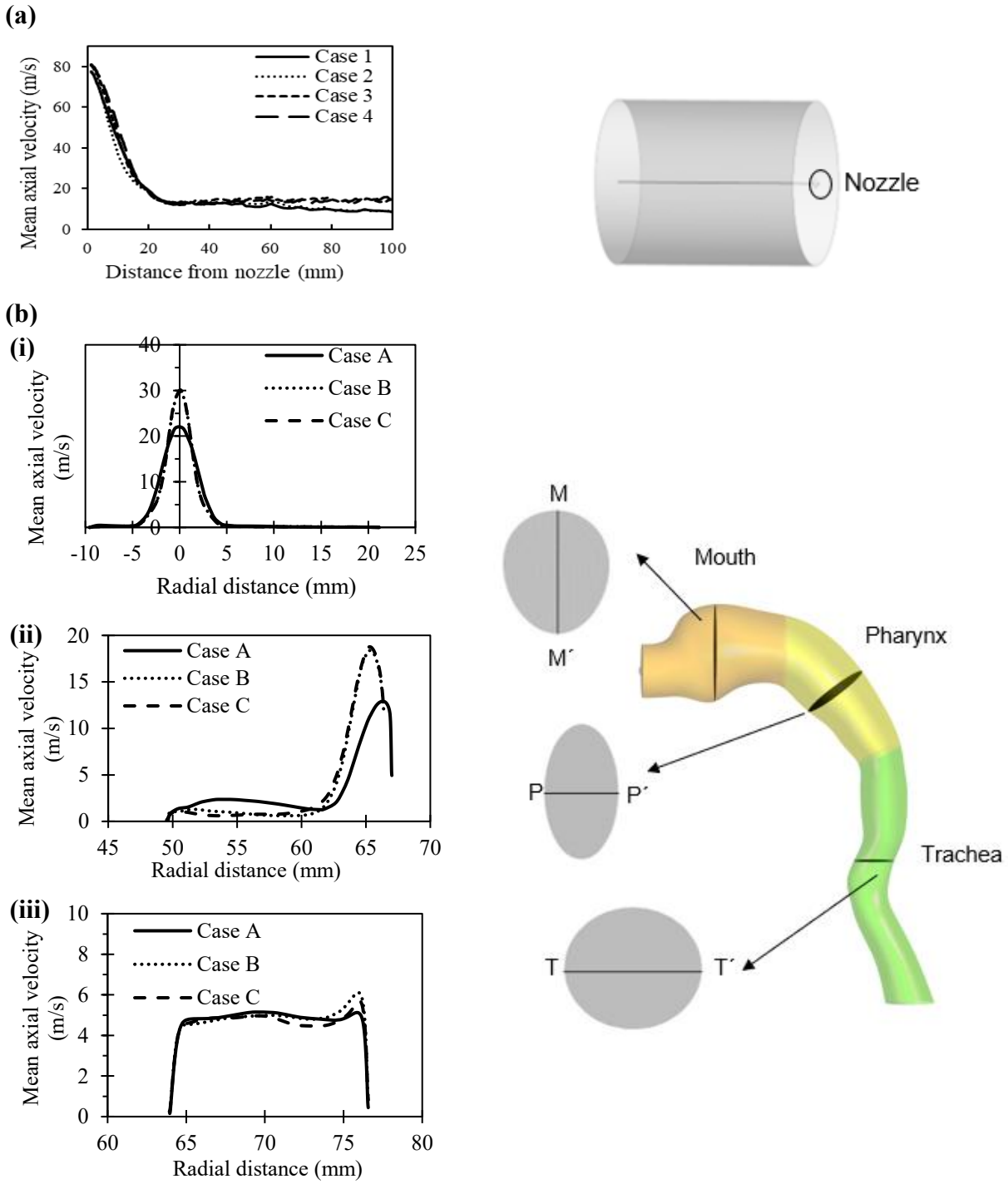

Fig. 5-2: Mean axial velocity (m/s) of the plume **(a)** along the centerline from the nozzle in the open-air model, without airflow for four mesh cases according to **Table 5-2**; and **(b)** through the radial distance (mm) of each cross-section of the **(i)** mouth (MM´), **(ii)** pharynx (PP´), and **(iii)** trachea (TT´).

Table 5-3: Properties of the injection model for two nozzles.

Properties	**Conventional nozzle**	**Twin nozzle**
Spray duration (s)	0.1*	0.1*
Cone angle (°)	9.9 *	8*
Velocity magnitude (m/s)	75	95
Total flow rate (kg/s) **		
HFA-134a	85×10^{-8}	85×10^{-8}
Ethanol	14.79×10^{-8}	14.79×10^{-8}
Drug	21×10^{-10}	21×10^{-10}
Diameter of particle (µm)		
Min. diameter	1	1
Max. diameter	20	20

*(Duke et al., 2021)
** (Duke et al., 2019)

The trajectory of inhaled particles is derived from the Lagrangian approach, based on Newton's second law as described in **Section 4.2.1**.

In the present work, a "trap" boundary condition was applied at the airway wall, and an "escape" boundary condition was applied at the outlet. The SIMPLEC (semi-implicit method for -linked equations-consistent) pressure-velocity coupling algorithm was used to solve the models, and the least-squares cell-based, second-order, and second-order upwind schemes were applied to calculate the cell gradients, pressure, and momentum, respectively. In addition, bounded central differencing was employed for the discretization of momentum. The average simulation times for the open-air and MT models were approximately 24 hours and 50 hours, respectively. For these simulations, we utilized the Niagara cluster, which comprises 40 Intel Cascade Lake cores operating at 2.5 GHz, an 80-core processor, and 20 GB/202 GB of RAM per node.

5.3 Results and Discussion

5.3.1 CFD Model Validation

Fig. 5-3 shows the velocity of the generated plume at different distances from the nozzles. Our CFD results agreed reasonably well with the data reported by Versteeg et al. (2017), who used a

high-speed imaging technique (RMSE% < 10%). A comparison with Buchmann et al. (2014) yielded a higher RMSE% of about 40% due to the known underestimation of velocities in their imaging method (laser-sheet high-speed imaging). Also, in the latter study, they were unable to measure velocity near the exit nozzle due to limitations in their experimental setup. Therefore, their results are available at a distance of 25 mm from the nozzle, as shown in **Fig. 5-3(a).**

There is a difference between our results and those of Duke et al. (2021), although the trend is the same. Duke et al. (2021) estimated spray velocity near the nozzle using an image cross-correlation technique for the initial velocity of the plume (U_0) and by assuming axisymmetric spray, utilized a simple mathematical model to calculate the velocity at different distances from the nozzle:

$$U(x) \approx U_0 \frac{{w_o}^2}{w(x)^2} \tag{5.11}$$

where w_0 is the plume width at the location where its velocity is U_0 and $w(x)$ is plume width where velocity is $U(x)$. The differences between Duke et al. (2021)'s results and others confirm that their proposed correlation is unable to sufficiently predict plume velocity.

The twin nozzle was a novel idea proposed by Duke et al. (2021). **Fig. 5-3(b)** compares our results and those of the plume velocity for the twin nozzle. The experimental data were limited to a distance of 40 mm from the nozzle; hence, the reported results were constrained within this range. Although the CFD data exhibits a similar trend, there are quantitative discrepancies between the datasets. It is worth mentioning that the proposed correlation by Duke et al. (2021), as demonstrated in **Fig. 5-3(a)** for a single nozzle, lacks accuracy in predicting the velocity profile because their model is not a measurement, but a simplified mathematical correlation based on several strong assumptions that do not hold for real pMDI plumes. Based on this, it can be concluded that our spray model is sufficiently valid.

(a)

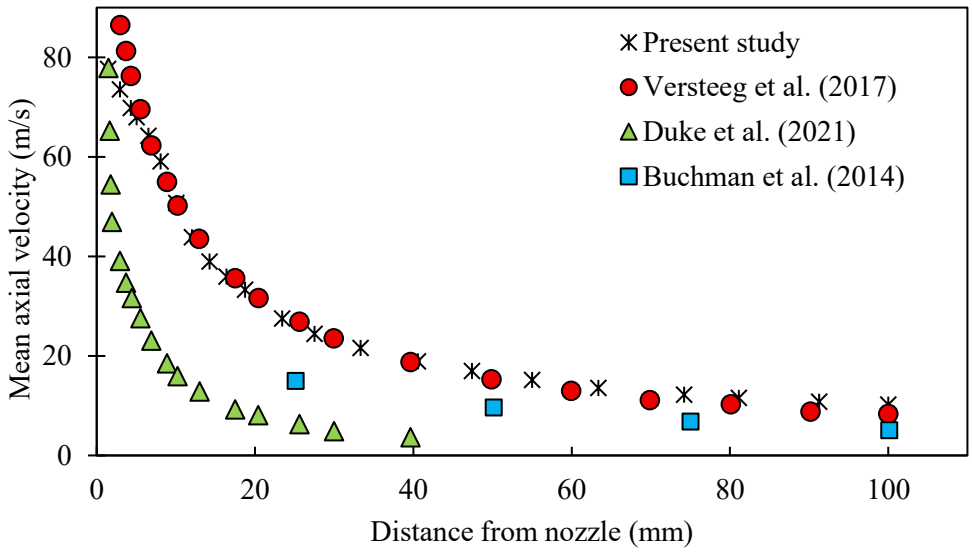

(b)

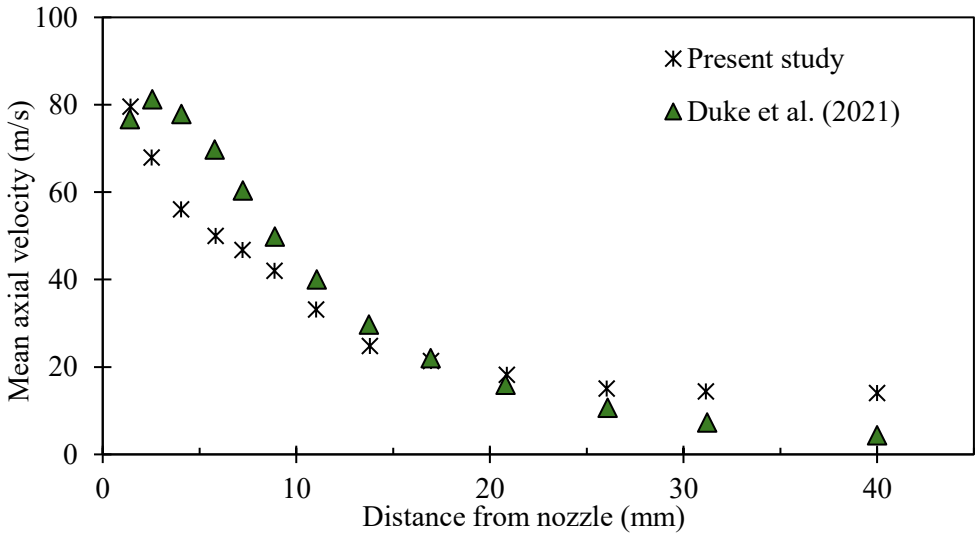

Fig. 5-3: Comparison of plume mean axial velocity (m/s) in the open-air model, without airflow, at different distances (mm) from the nozzle exit of pMDI of the present study and in-vitro results for **(a)** conventional nozzle; and **(b)** twin nozzle.

After validating our spray model in an open-air environment, the next step was to validate our CFD model for aerosol deposition in MT geometry. **Fig. 5-4** shows the MT deposition efficiency as a function of the impaction parameter (the product of the square of the aerodynamic diameter and the volumetric flow rate). This figure demonstrates that our CFD results align with those from other literature sources, including *in-vivo* testing (Stahlhofen et al., 1989) and *in-vitro* experiments

(Cheng et al., 2015; Zhou et al., 2011). Stahlhofen et al. (1989) proposed a semi-empirical model of aerosol deposition in the airways, based on available *in-vivo* data as a function of the impaction parameter. The solid line and dashed lines (corresponding to the standard deviation of the *in-vivo* data) in **Fig. 5-4** are relevant to their model. According to our data, particles with a size of less than 5 microns are more likely to pass through the MT, while larger particles tend to have a higher deposition rate. Given the variety of MT geometries and breathing patterns used in in-vivo studies, our CFD model underestimated the average in-vivo deposition efficiency for small particles. The lower deposition predicted for small particles is expected, as small-particle deposition in the MT region is highly sensitive to mucus adhesion, hygroscopic growth, and geometric variability, effects that are not fully represented in CFD. However, the trend of our results is similar to that reported in the *in-vitro* model of Zhou et al. (2011) and the model (b) of Cheng et al. (2015)'s study, which are more morphologically similar.

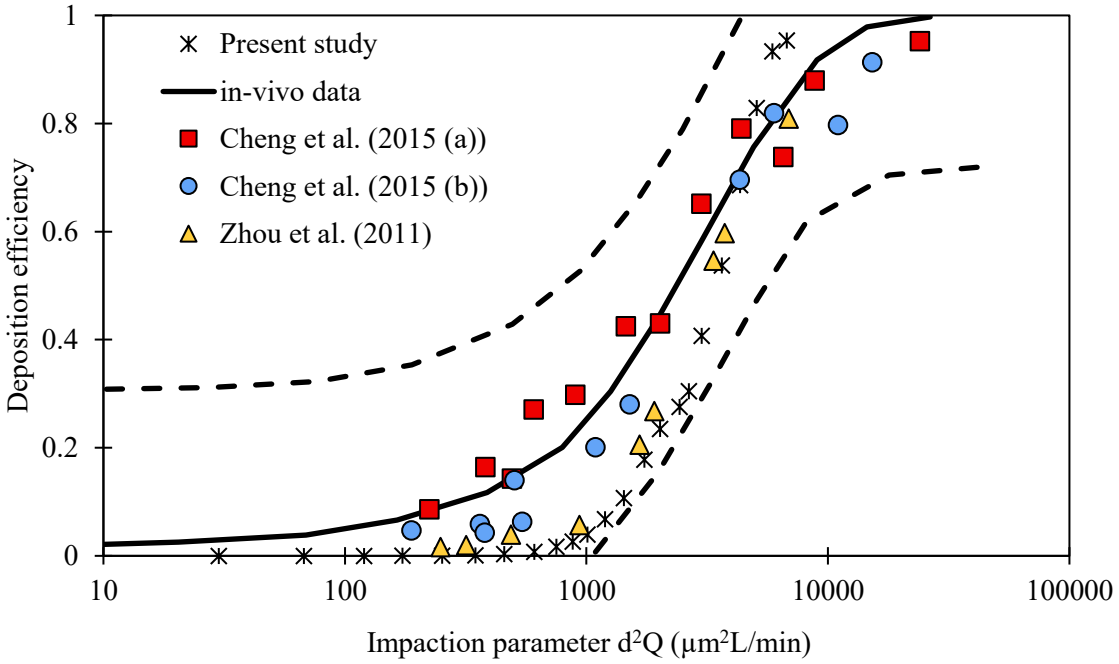

Fig. 5-4: Comparison of deposition efficiencies (-) in the MT model, with 30 L/min of airflow between the present study and in-vitro and in-vivo results as a function of impaction parameters ($\mu m^2 L/min$) for the conventional nozzle.

5.3.2 Plume Behaviour

The plume injected by pMDIs and the size of the generated particles depend on the formulation of the canister, the actuator structure, and the surrounding environment (Chen et al., 2017;

McKiernan, 2019). The effects of the latter two parameters on the plume are shown in **Fig. 5-5** and **Fig. 5-7**. Effects of the surrounding conditions are discussed in **Section 5.4.3**.

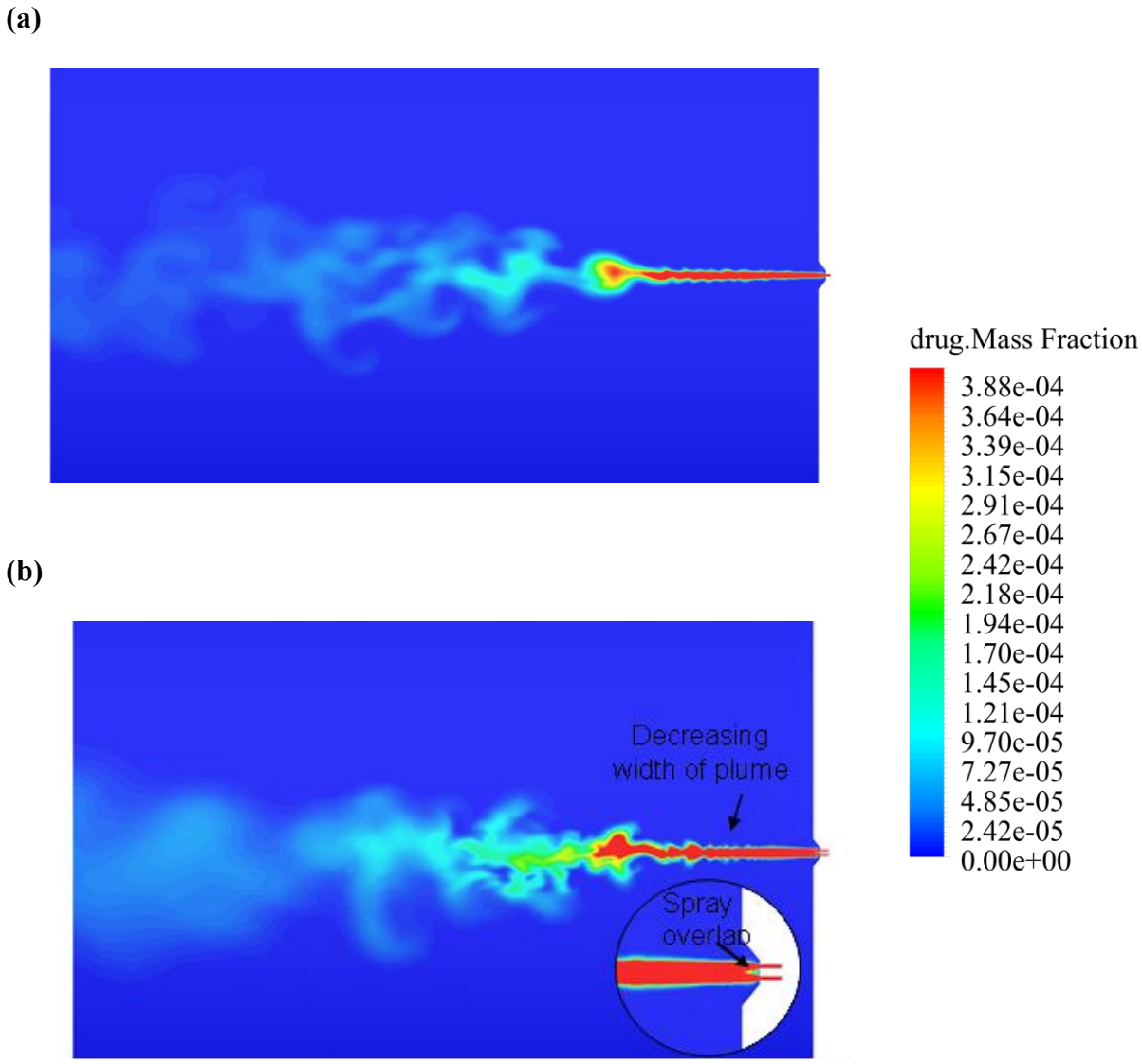

Fig. 5-5: Comparison of plume generated in terms of drug mass fraction (kg/kg) from **(a)** conventional nozzle; and **(b)** twin nozzle in the open-air model without airflow rate at 0.05 s of injection.

Fig. 5-5 shows the plume generated from conventional (**Fig. 5-5(a)**) and twin nozzles (**Fig. 5-5(b)**) in the open-air region. **Fig. 5-5(b)** shows how the two separated plumes of the twin nozzle expand after they exit the nozzles within the bowl. Then, the two plumes collapse before entirely leaving

the actuator structure, and a single continuous plume appears, similar to the conventional one. Our result is aligned with that of Duke et al. (2021).

The spray collapse phenomenon results in a decrease in plume width and an increase in tip penetration (Chang et al., 2023; Nishida et al., 2009). Given that the twin nozzle has a smaller diameter than the conventional one, the smaller diameter and plume collapse can affect plume penetration compared to the conventional one. As can be seen in **Fig. 5-5(b)**, the width of the twin nozzle plume (after collapse) starts declining, in contrast to the conventional one, which increases steadily (**Fig. 5-5(a)**) and thus, it has a narrower plume than the conventional one. Indeed, each jet exits at a higher velocity, producing stronger central momentum and reduced lateral spreading, suppressing shear-layer entrainment. With less surrounding air drawn into the jet, the plume contracts rather than widening, resulting in a narrower profile than the conventional nozzle.

Fig. 5-6(a) presents the mean particle diameter in different cross-sections of the plume, calculated for both nozzles. The twin nozzle injected finer particles than the conventional one, in agreement with Duke et al. (2021). Since the difference between the penetration rates of these two nozzles (**Fig. 5-6(b)**) was not remarkable (13%), fine particles were likely produced by the two jets mixing at high speed at a short distance from the plume's exit in the twin model. Producing finer particles may reduce deposition in the upper airway and, consequently, increase the efficiency of pMDI.

Fig. 5-7 illustrates the plume velocities obtained at the midpoint of the injection time (0.05 s), spanning from the nozzle exit to a distance of 40 mm from the centerline. The velocities were calculated for both the open-air (unconfined) and MT (confined) models, using both the conventional and twin-nozzle configurations. We observed a notable difference in the results between the open-air and MT scenarios, with a 22% difference for the conventional nozzle and a more substantial 58% difference for the twin nozzle. The confined, intricate geometry of the MT model, coupled with a flow rate of 30 L/min into the mouth, results in a steeper decrease in plume velocity compared to the open-air model and the no-flow condition.

The twin nozzle configuration exhibits a significantly greater reduction in velocity intensity than the conventional nozzle. This remarkable decrease can be attributed to the collision of the two jet streams at an early stage. The collision introduces additional turbulence, which amplifies the decline in velocity intensity. The findings, as represented in **Fig. 5-7**, emphasize the importance of studying drug delivery from inhalers under realistic breathing flow conditions, accounting for the

complex airway geometry. It highlights the need to incorporate airway geometry simulations to accurately evaluate inhaler device performance.

From a clinical perspective, these findings are highly relevant because plume velocity directly influences aerosol penetration, MT deposition, and the fraction of drug reaching the lower airways. A rapid reduction in plume velocity within the MT region increases the likelihood of oropharyngeal deposition, which is clinically associated with reduced lung-delivered dose, increased drug wastage, and potential local side effects. The markedly greater velocity decay observed for the twin-nozzle configuration under inhalation conditions suggests that device designs that perform favorably in open-air testing may not necessarily yield improved drug delivery in actual patient use.

5.3.3 Flow Pattern in MT Model

Fig. 5-8 illustrates the velocity contours at mid-plane in the extrathoracic (ET) region (in the MT model) for the conventional nozzle (model A) and twin nozzle (model B) at 0.05 s after injection. We can observe vortices near the palate due to geometric expansion and flow separation. This expansion within the mouth alters the airflow dynamics, causing disturbances and changes in its direction and intensity (Inthavong et al., 2011; Shang et al., 2019). The velocity contour illustrates that the flow behaves differently in the MT models. The vortices in models A and B vary in location and intensity, which could be attributed to differences in injection velocities.

In contrast to model A, the pharynx region of model B exhibits a greater flow velocity and a more distinct mixing zone, resulting in the emergence of vorticity in this area. One plausible explanation for this phenomenon is the high-velocity plume's forceful impact with the wall at the end of the throat, which influences the flow dynamics. The observed vorticity zones play a crucial role in determining the particle deposition pattern (Gunatilaka et al., 2020; Sarkar et al., 2017). In addition, we noticed that the dominance of the main flow in the trachea area for model B, under the influence of the pharynx region’s flow, displaced the vorticity adjacent to the posterior wall, which can increase the probability of deposition in these areas.

(a)

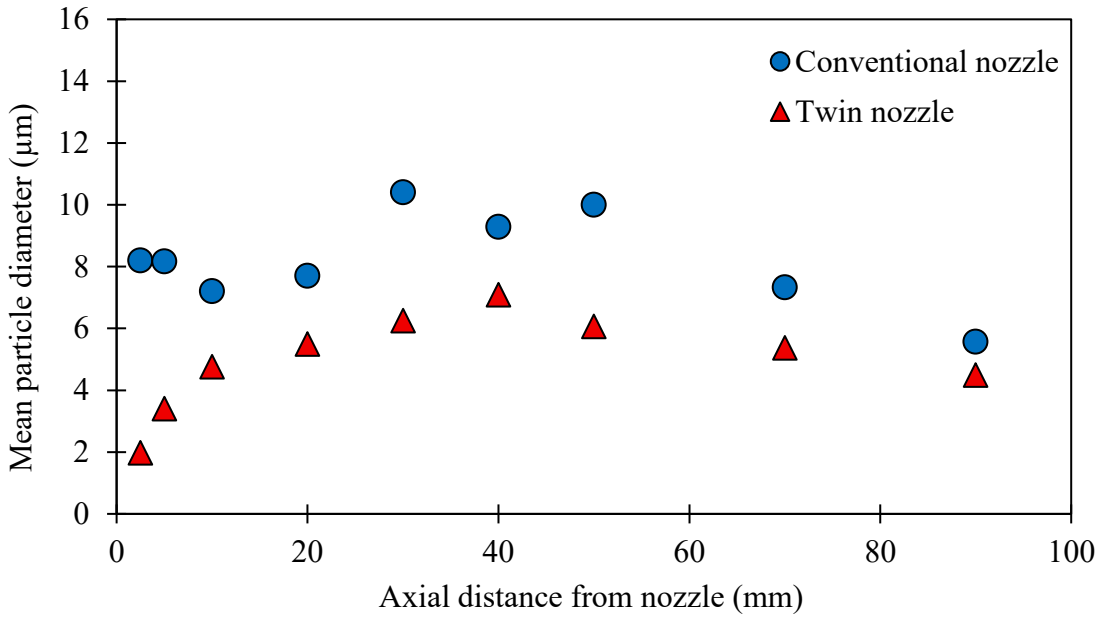

(b)

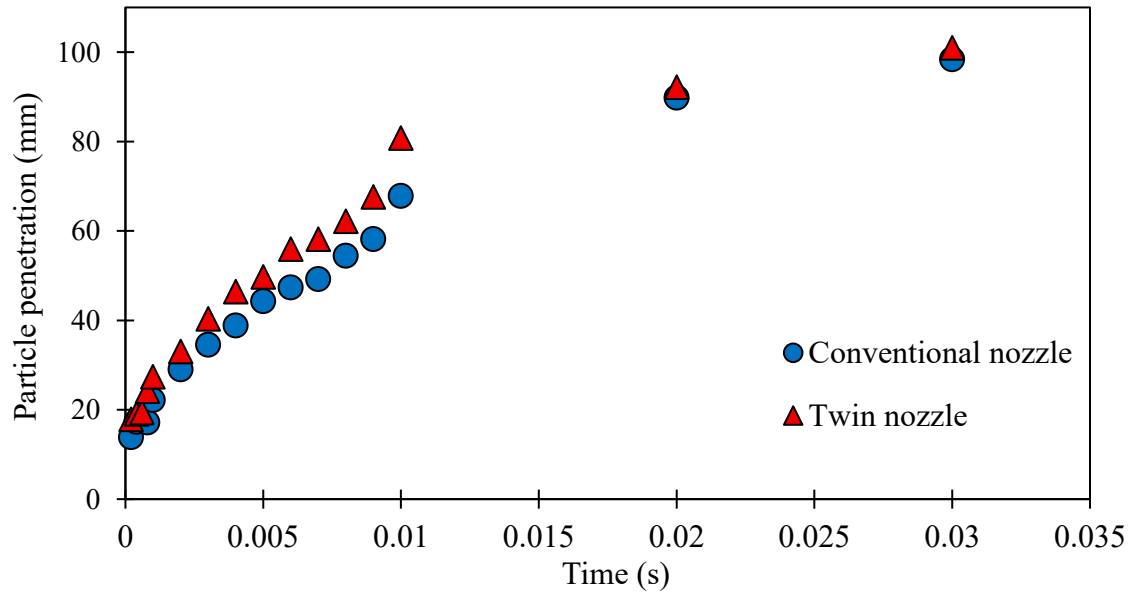

Fig. 5-6: Comparison of **(a)** mean particle diameter (µm); and **(b)** particle penetration rate (mm) of particles injected from nozzles at the different cross-sections of the plume in the open-air model without airflow.

(a)

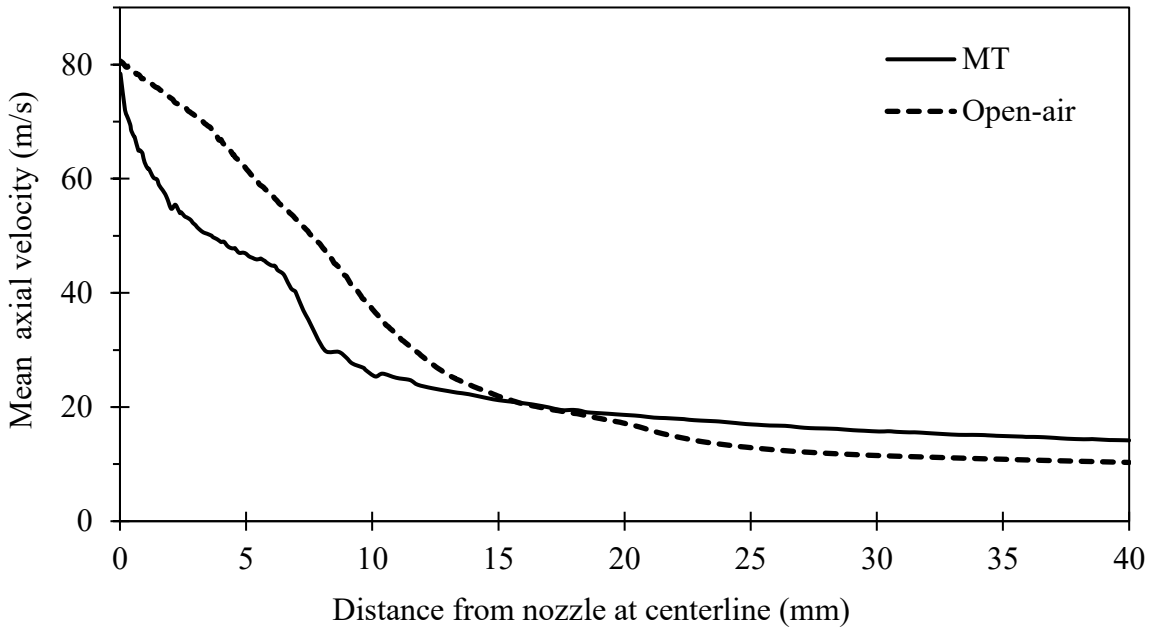

(b)

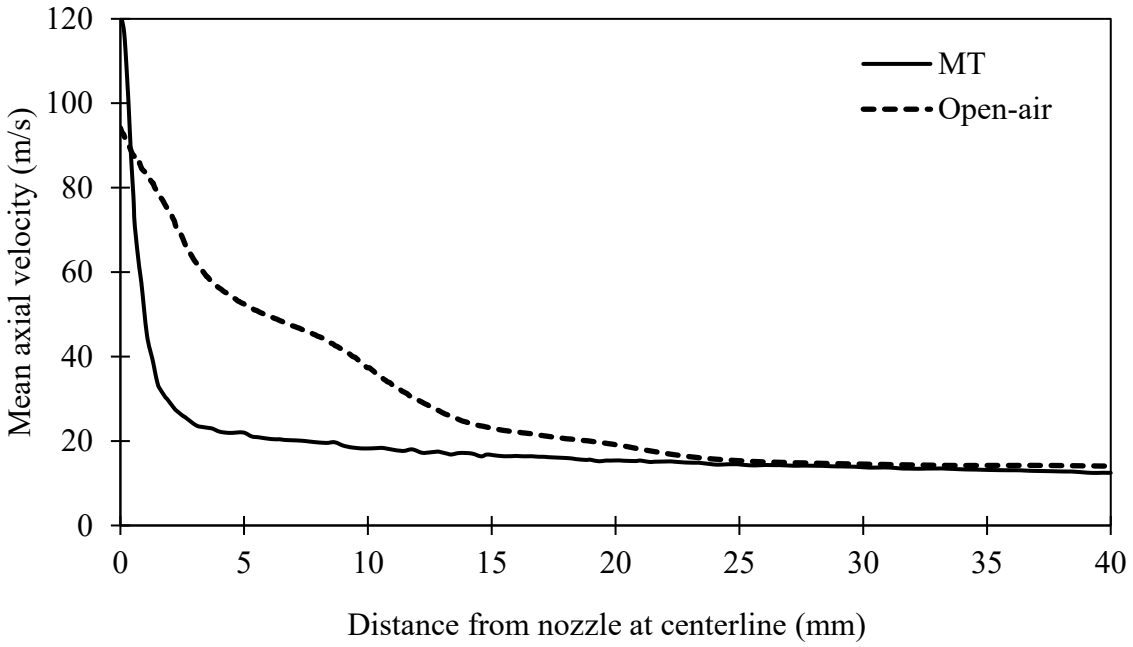

Fig. 5-7: Comparison of axial velocity (m/s) of the plume at the centerline of the nozzles in the open-air model, without airflow, and within the MT model, with 30 L/min of airflow: for **(a)** conventional nozzle; and **(b)** twin nozzle.

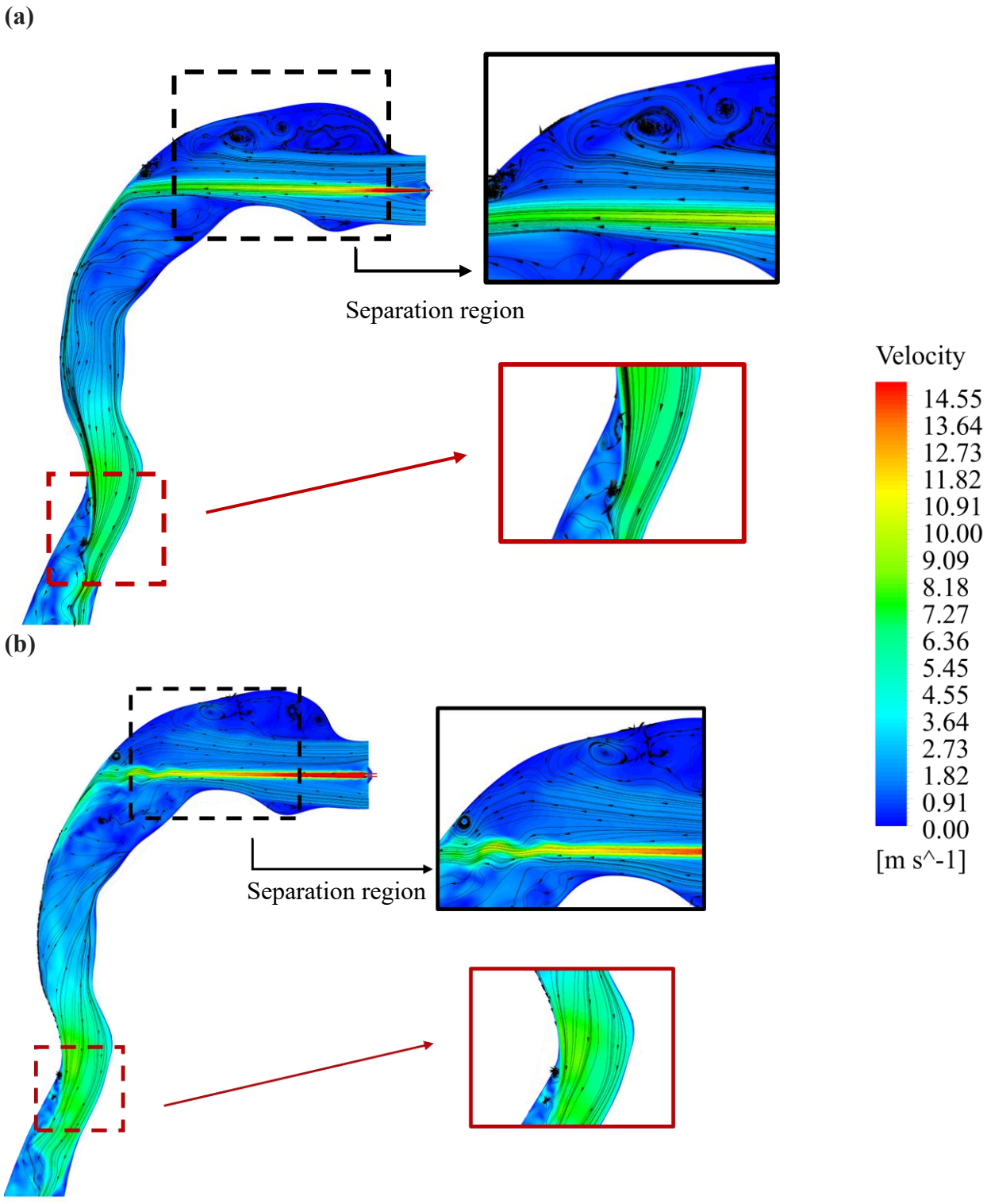

Fig. 5-8: Comparison of velocity magnitude (m/s) contour at mid-plane at 0.05 s between **(a)** model A; and **(b)** model B.

Particle trajectories shown in **Fig. 5-9** indicate that the aerosol severely impinges on the throat wall because of the high inertia of aerosols. Model B, with its higher velocity (**Fig. 5-9(b)**), caused the aerosol flow to spread widely, rotate, and nearly reach the anterior wall of the throat. On the contrary, the injected plume of model A, as shown in **Fig. 5-8(a)**, remained in the posterior part of the throat wall after collision. The flow dispersion obtained in model B affected the amount and location of drug deposition. Due to the bends and geometric complexity of the MT, a secondary flow was generated along with the primary flow. The secondary flow pattern through throat cross sections is shown in **Fig. 5-10** in different positions: pharynx (P1 and P2), larynx (P3), and trachea (P4 and P5), and compared with the flow field injected by two nozzles (models A and B). In the pharynx area (P1 and P2), the aerosol flow, injected at high velocity, impinged on the throat wall at the posterior position; the high velocity is evident in the contour velocity plot in this MT region. On the other hand, when the flow enters the end of the pharynx region (P2), the main flow field is pushed into the center of the throat; this effect is particularly noticeable in model B, as the force of gravity overcomes the centrifugal force at the end of the bend; this effect is particularly noticeable in model B; higher inertia of its flow resulted in a more significant flow displacement towards the throat's central region.

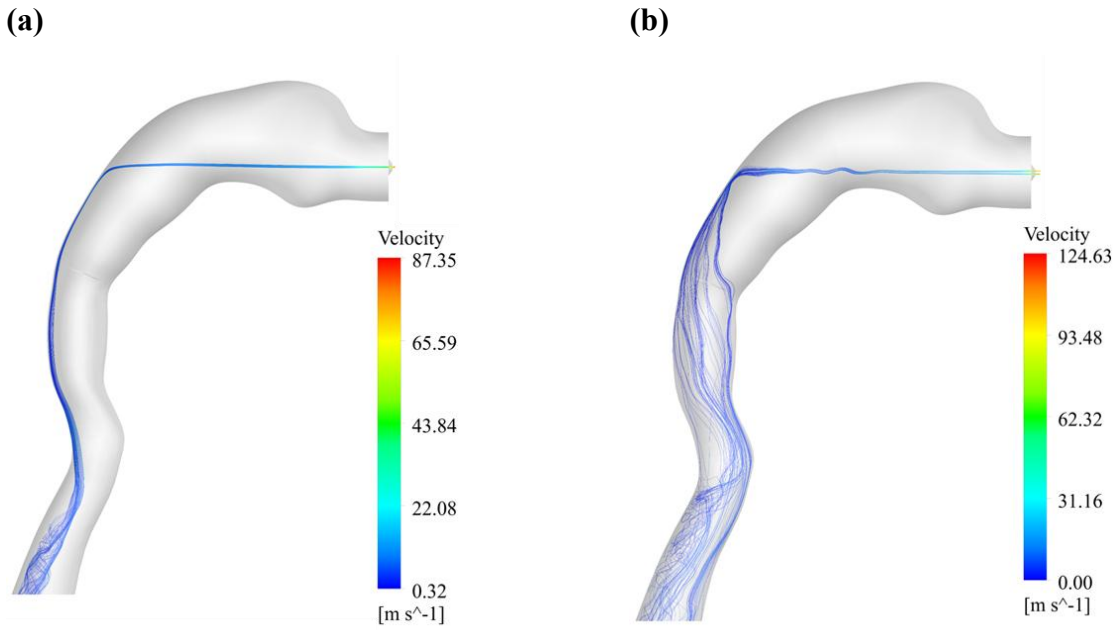

Fig. 5-9: Comparison of flow velocity (m/s) streamlines at mid-plane at 0.05 s between **(a)** model A; and **(b)** model B.

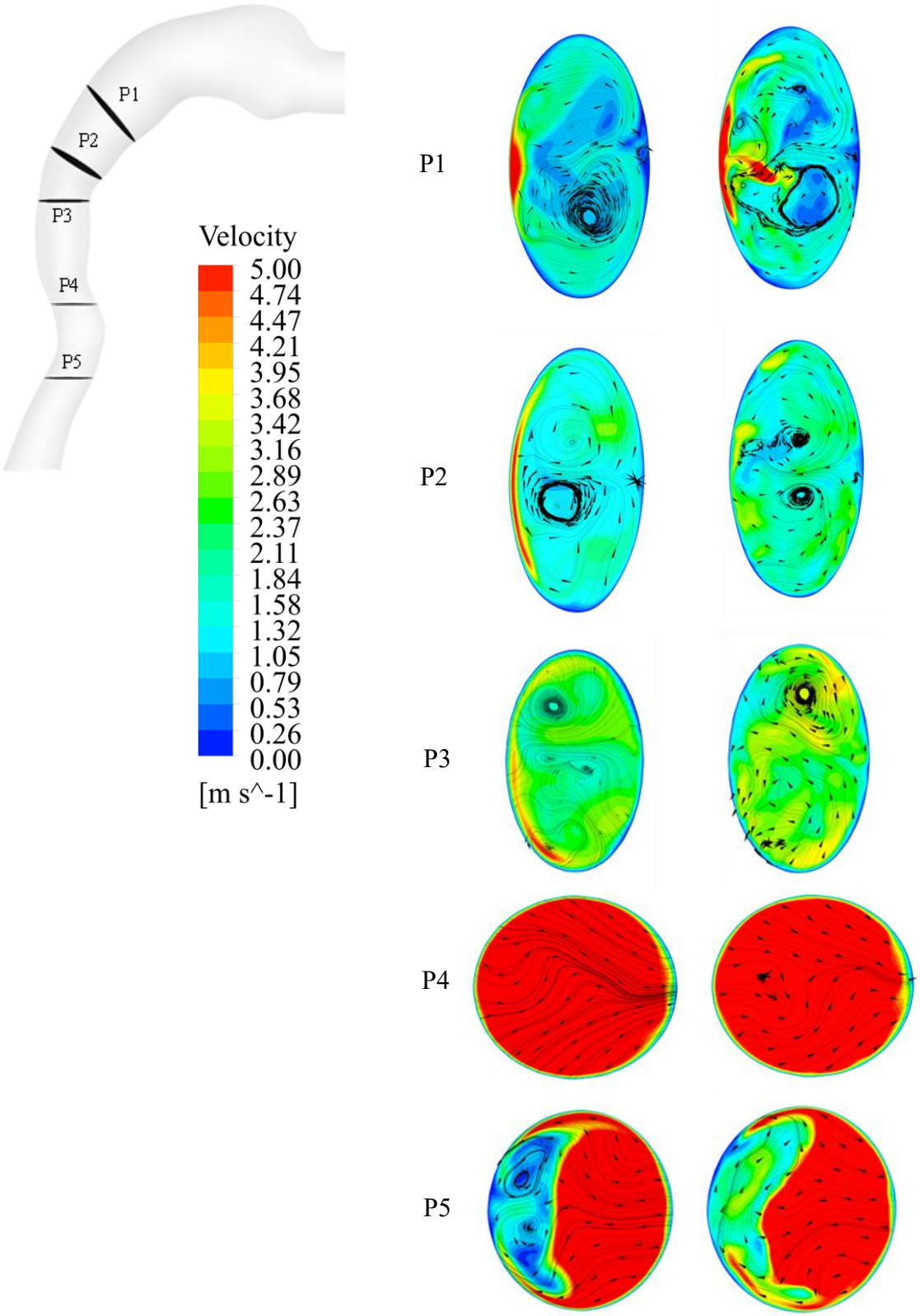

Fig. 5-10: Velocity magnitude (m/s) contour and streamlines at cross-sections of MT model, model A (left side), and model B (right side) at 0.1 s.

The secondary streamlines in the larynx region (P3) indicate two vorticities on the left side for both models. However, we observe more dominant recirculation flows in model B, which likely contribute to a higher spray rate of around 10 m/s in the pharynx region, compared to the 6 m/s spray rate in model A. The heightened turbulence intensity in model B contributed to the substantial mixing effect observed.

After the flow entered the tracheal region (P4 and P5), the laryngeal jet dominated, and the velocity magnitude increased significantly, leading to the disappearance of most recirculation flows in both models. However, due to the expansion of the trachea after plane P4 and centrifugal force (Cui and Gutheil, 2011; Zhang et al., 2002), the recirculation region re-developed, and the central flow occurred in the anterior portion of the trachea. In model B, the development of the recirculation zone was more irregular, and there were no vorticities. In contrast, two weak symmetrical vortices in the circulation region at the posterior side of P5 were noticed in model A. These results indicate that spray momentum has a significant influence on the flow field through the MT airway. This flow pattern can alter the transport and deposition patterns of medication particles in the respiratory system (Longest et al., 2009).

5.3.4 Regional Deposition

Fig. 5-11 displays particle dispersion based on the particle size in the ET region for both models. Inhaled particles can be deposited in the respiratory system through various mechanisms, including inertial impaction, gravitational sedimentation, and Brownian motion. Brownian motion primarily affects smaller submicron particles, while inertial impaction is more influential for larger micron particles in the upper airway (Chen et al., 2018; Kadota et al., 2017; Sosnowski, 2021, 2018). As the injected particles had the same density and shape, and airflow was constant, only particle size and inertia could affect the deposition mechanism in the ET region (Sosnowski, 2018). The figure shows that particles larger than 4μm are predominantly found in this area, indicating that inertial impaction primarily influences their deposition. For model A, using a conventional nozzle, more particles were deposited on the posterior wall of the throat, pharynx region, and upper side of the trachea, as reported by Xi et al. (2016), while in model B, deposition was observed on the anterior side as well as in the exact locations as in model A. These results are supported in **Fig. 5-9(b)**, which verifies the dispersion of particles in the specified region for model B. This figure shows that particles move after colliding with the posterior wall, ultimately covering a significant portion

of the anterior area. Consequently, the scattering of particles in the anterior area contributes to their deposition in that region.

(a)

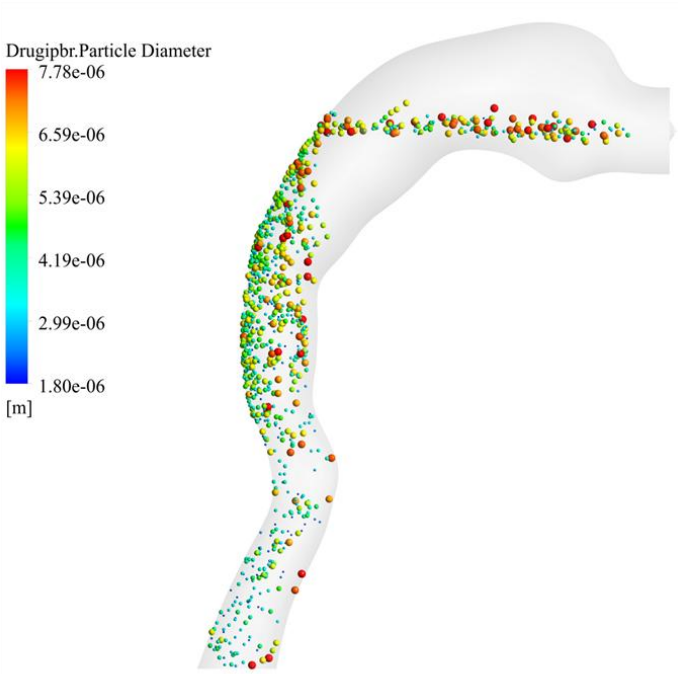

(b)

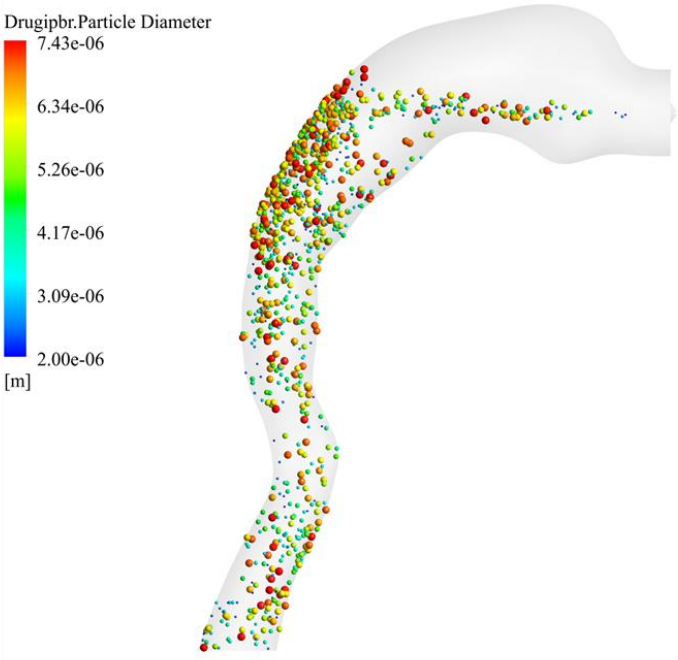

Fig. 5-11: Particle dispersion diameter (μm) in the entire MT region in **(a)** model A; and **(b)** model B.

Fig. 5-12 shows the particle deposition fractions in all MT airway regions (mouth, pharynx, trachea, and lung). It compares the effect of aerosol bursts and momentum on drug deposition. About 55% of the particles injected from the conventional pMDI nozzle deposited in the MT, and the remaining particles passed through the trachea, in agreement with *in-vitro* results (Biswas et al., 2017; Kaviratna et al., 2019; Lim et al., 2021) and CFD modelling studies (Kleinstreuer et al., 2007; Walenga and Longest, 2016) with similar MT geometries: less than 2% and 3% deposited in the mouth and trachea region, respectively. Switching to a twin nozzle with a smaller diameter and a higher plume speed increased MT airway deposition by around 97%; less than 3% of the particles reached the deeper lung region. About 74% and 22% of drugs were deposited in the pharynx and trachea regions, respectively. Our results contrast with those of Duke et al. (2021), who found that a twin nozzle improved pMDI performance. They used the USP-IP, a simplified model of the MT airway geometry compared to that used in the present simulations. Previous studies have illustrated that airway geometry significantly influences the transport and deposition of aerosol particles in the MT area (Islam et al., 2021; Kadota et al., 2022; Kaviratna et al., 2019; Longest et al., 2012b; Longest and Hindle, 2009). From the particle trajectory shown in **Fig. 5-9(b)**, higher drug deposition in the pharynx and trachea regions was expected for model B. However, we found that, despite generating finer particle sizes, the higher turbulence intensity of aerosol injected by the twin nozzles, combined with jet-to-jet collisions, resulted in less aerosolized drug reaching the lung (our treatment target) than with the conventional nozzle.

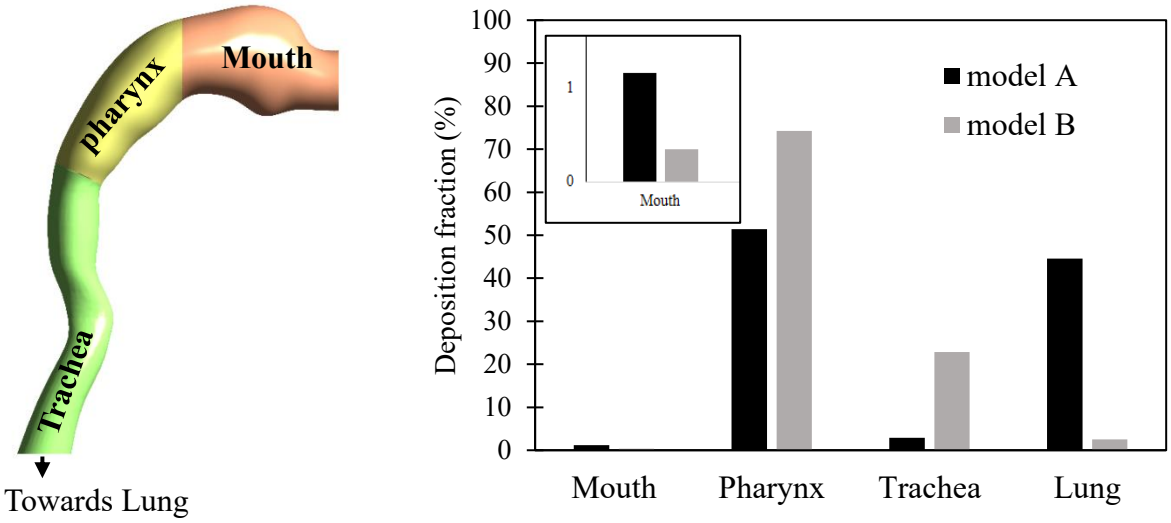

Fig. 5-12: Regional particle deposition (%) in models A and B.

From a patient outcome perspective, these results indicate that inhaler designs optimized under simplified conditions may not necessarily improve lung delivery in real clinical use, underscoring the importance of evaluating device performance under physiologically realistic airflow and anatomical conditions.

5.4 Conclusions

We conducted a CFD study, injecting two spray models through two nozzles (conventional and twin) into open-air and MT geometries. The LES-DPM model was used to predict accurate flow fields and to investigate the effects of surrounding conditions on the behaviour of a pMDI-generated plume. Additionally, the effects of the nozzle's shape, diameter, and length on drug transport and deposition were investigated. Finally, we validated our CFD models with experimental results.

We noticed that the two separated aerosol sprays from the twin nozzle collapsed at a short distance after exiting the orifices. One continuous plume entered the space with a higher speed, shorter width, and finer diameter of particles compared to the plume generated by the conventional one. However, we found that the aerosol spray developed in an open-air environment (representing an unconfined region) and with no breathing flow parameter, behaved considerably differently from the case in which the spray was injected into the MT geometry in the presence of airflow. Thus, it is essential to investigate the plume behaviour in the MT geometry. We note that it is currently not technically possible to conduct such experiments, which is why we rely on CFD.

As a vital part of the pMDI, the actuator structure can remarkably change the inhaler's efficiency. Our data showed that, in the real MT airway, which influences the flow field distribution, the twin nozzle enhanced drug deposition in the MT region. According to the present study, not only does the higher velocity of aerosol generated by a twin nozzle not improve pMDI drug delivery, but it also worsens its efficiency.

5.5 Limitations and Future Directions

- Only the nozzle structure of the pMDI was modeled. Future simulations incorporating the full canister, metering chamber, and nozzle assembly would provide a more accurate characterization of plume formation and early jet breakup.

- The model captured the mouth–throat (MT) and tracheal regions but did not include deeper bronchial branches. Extending the geometry to multiple airway generations would enable evaluation of drug transport into distal regions, which are often the primary therapeutic targets.
- Droplet–droplet collisions and agglomeration were not considered. These phenomena can alter particle trajectories, evaporation rates, and deposition hotspots, particularly in high-momentum pMDI sprays.
- Although the DPM was coupled to the airflow, the local mass loading remained low. Future work could investigate conditions in which droplets significantly affect the gas-phase turbulence, potentially influencing deposition patterns.

5.6 Nomenclature

Abbreviation	
3D	three dimensional
ANSYS	analysis of systems
CFD	computational fluid dynamics
COPD	chronic obstructive pulmonary disease
DPM	discrete phase model
ET	extrathoracic
FPF	fine particle fraction
GB	gigabyte
GHz	gigahertz
GiB	gibibyte
HFA	hydrofluoroalkane
LES	large eddy simulation
MT	mouth-throat
NSERC	natural sciences and engineering council of Canada
pMDI	pressurized-metered dose inhaler
RAM	random access memory
RDD	respiratory drug delivery

RMSE	root mean squared error
SIMPLEC	semi-implicit method for pressure-linked equations-consistent
SMI	soft mist inhaler
USP-IP	United States Pharmacopeia induction port
Notations	
$\boldsymbol{a_i}$	constant (-)
$\boldsymbol{C_D}$	drag coefficient (-)
C_k , C_ε	constants (-)
$\boldsymbol{d_p}$	particle diameter (m)
$\boldsymbol{F_i}$	body force (N)
k_{sgs}	dynamic kinetic energy (J/kg)
$\boldsymbol{m_p}$	particle mass (kg)
$\boldsymbol{\bar{P}}$	time-averaged pressure (Pa)
$\boldsymbol{Re_p}$	particle Reynolds number (-)
$\boldsymbol{u_f}$	fluid velocity (m/s)
$\boldsymbol{\bar{u}_i}$	time-averaged velocity (m/s)
$\boldsymbol{u_p}$	particle velocity (m/s)
$U(x)$	plume velocity (m/s)
U_0	initial velocity of plume (m/s)
V	volume of computational cell (m^3)
$w(x)$	plume width (m)
w_0	plume width at the location where velocity is U_0 (m)
ρ	mixture density (kg/m^3)
$\boldsymbol{\rho_p}$	particle density (kg/m^3)
μ	mixture viscosity (m^2/s)
μ_s	dynamic viscosity at sub-grid (m^2/s)

5.7 References

Ahookhosh, K., Pourmehran, O., Aminfar, H., Mohammadpourfard, M., Sarafraz, M.M., Hamishehkar, H., 2020. Development of human respiratory airway models: A review. Eur. J. Pharm. Sci. 145, 105233. https://doi.org/10.1016/j.ejps.2020.105233

Ahookhosh, K., Saidi, M., Mohammadpourfard, M., Aminfar, H., Hamishehkar, H., Farnoud, A., Schmid, O., 2021. Flow structure and particle deposition analyses for optimization of a pressurized metered dose inhaler (pMDI) in a model of tracheobronchial airway. Eur. J. Pharm. Sci. 164, 105911. https://doi.org/10.1016/j.ejps.2021.105911

Ahookhosh, K., Yaqoubi, S., Mohammadpourfard, M., Hamishehkar, H., Aminfar, H., 2019. Experimental investigation of aerosol deposition through a realistic respiratory airway replica: An evaluation for MDI and DPI performance. Int. J. Pharm. 566, 157–172. https://doi.org/10.1016/j.ijpharm.2019.05.058

ANSYS, 2020. ANSYS FLUENT Theory Guide, 2020 R2. ed. ANSYS, Inc. and Ansys Europe, Ltd. are UL registered ISO 9001: 2015 companies.

Bhardwaj, S., Koullapis, P., Kassinos, S.C., Sznitman, J., 2022. Fate of inhaled aerosols under the influence of glottal motion in a realistic in silico human tracheobronchial tree model. Eur. J. Pharm. Sci. 173. https://doi.org/10.1016/j.ejps.2022.106172

Biswas, R., Hanania, N.A., Sabharwal, A., 2017. Factors determining in vitro lung deposition of albuterol aerosol delivered by ventolin metered-dose inhaler. J. Aerosol Med. Pulm. Drug Deliv. 30, 256–266. https://doi.org/10.1089/jamp.2015.1278

Buchmann, N.A., Duke, D.J., Shakiba, S.A., Mitchell, D.M., Stewart, P.J., Traini, D., Young, P.M., Lewis, D.A., Soria, J., Honnery, D., 2014. A Novel High-Speed Imaging Technique to Predict the Macroscopic Spray Characteristics of Solution Based Pressurised Metered Dose Inhalers, in: Pharmaceutical Research. pp. 2963–2974. https://doi.org/10.1007/s11095-014-1391-6

Chang, M., Kim, H., Zhou, B., Park, S., 2023. Spray collapse resistance of GDI injectors with different hole structures under flash boiling conditions. Energy 268, 126689. https://doi.org/10.1016/j.energy.2023.126689

Chen, X., Feng, Y., Zhong, W., Kleinstreuer, C., 2017. Numerical investigation of the interaction, transport and deposition of multicomponent droplets in a simple mouth-throat model. J. Aerosol Sci. 105, 108–127. https://doi.org/10.1016/j.jaerosci.2016.12.001

Chen, X., Kleinstreuer, C., Zhong, W., Feng, Y., Zhou, X., 2018. Effects of thermal airflow and

mucus-layer interaction on hygroscopic droplet deposition in a simple mouth–throat model. Aerosol Sci. Technol. 52, 900–912. https://doi.org/10.1080/02786826.2018.1476751

Chen, Y., Young, P.M., Murphy, S., Fletcher, D.F., Long, E., Lewis, D., Church, T., Traini, D., 2017. High-Speed Laser Image Analysis of Plume Angles for Pressurised Metered Dose Inhalers: The Effect of Nozzle Geometry. AAPS PharmSciTech 18, 782–789. https://doi.org/10.1208/s12249-016-0564-5

Cheng, Y.S., Zhou, Y., Su, W.C., 2015. Deposition of particles in human mouth-throat replicas and a USP induction port. J. Aerosol Med. Pulm. Drug Deliv. 28, 147–155. https://doi.org/10.1089/jamp.2013.1105

Cui, X.G., Gutheil, E., 2011. Large eddy simulation of the unsteady flow-field in an idealized human mouth-throat configuration. J. Biomech. 44, 2768–2774. https://doi.org/10.1016/j.jbiomech.2011.08.019

Dastoorian, F., Pakzad, L., Kozinski, J., Behzadfar, E., 2022. A CFD Investigation on the Aerosol Drug Delivery in the Mouth–Throat Airway Using a Pressurized Metered-Dose Inhaler Device. Processes 10, 1230. https://doi.org/10.3390/pr10071230

Delvadia, R.R., Longest, P.W., Byron, P.R., 2012. In Vitro Tests for Aerosol Deposition. I: Scaling a Physical Model of the Upper Airways to Predict Drug Deposition Variation in Normal Humans. J. Aerosol Med. Pulm. Drug Deliv. 25, 32–40. https://doi.org/10.1089/jamp.2011.0905

Delvadia, R.R., Wei, X., Longest, P.W., Venitz, J., Byron, P.R., 2016. In Vitro Tests for Aerosol Deposition. IV: Simulating Variations in Human Breath Profiles for Realistic DPI Testing. J. Aerosol Med. Pulm. Drug Deliv. 29, 196–206. https://doi.org/10.1089/jamp.2015.1215

Duke, D.J., Nguyen, D.T., Dos Reis, L.G., Silva, D.M., Neild, A., Edgington-Mitchell, D., Young, P.M., Honnery, D.R., 2021. Increasing the fine particle fraction of pressurised metered dose inhaler solutions with novel actuator shapes. Int. J. Pharm. 597, 120341. https://doi.org/10.1016/j.ijpharm.2021.120341

Duke, D.J., Scott, H.N., Kusangaya, A.J., Kastengren, A.L., Matusik, K., Young, P., Lewis, D., Honnery, D., 2019. Drug distribution transients in solution and suspension-based

pressurised metered dose inhaler sprays. Int. J. Pharm. 566, 463–475. https://doi.org/10.1016/j.ijpharm.2019.05.067

Feng, Y., Zhao, J., Hayati, H., Sperry, T., Yi, H., 2021. Tutorial : Understanding the transport, deposition, and translocation of particles in human respiratory systems using Computational Fluid-Particle Dynamics and Physiologically Based Toxicokinetic models. J. Aerosol Sci. 151, 105672. https://doi.org/10.1016/j.jaerosci.2020.105672

Gunatilaka, C.C., Schuh, A., Higano, N.S., Woods, J.C., Bates, A.J., 2020. The effect of airway motion and breathing phase during imaging on CFD simulations of respiratory airflow. Comput. Biol. Med. 127, 104099. https://doi.org/10.1016/j.compbiomed.2020.104099

Gurumurthy, A., Kleinstreuer, C., 2021. Helical fluid-particle flow dynamics for controlling micron-particle deposition in a representative human upper lung-airway model. J. Aerosol Sci. 151. https://doi.org/10.1016/j.jaerosci.2020.105656

Huang, F., Zhu, Q., Zhou, X., Gou, D., Yu, J., Li, R., Tong, Z., Yang, R., 2021. Role of CFD based in silico modelling in establishing an in vitro-in vivo correlation of aerosol deposition in the respiratory tract. Adv. Drug Deliv. Rev. https://doi.org/10.1016/j.addr.2020.09.007

Inthavong, K., Ge, Q., Se, C.M.K., Yang, W., Tu, J.Y., 2011. Simulation of sprayed particle deposition in a human nasal cavity including a nasal spray device. J. Aerosol Sci. 42, 100–113. https://doi.org/10.1016/j.jaerosci.2010.11.008

Islam, M.S., Larpruenrudee, P., Hossain, S.I., Rahimi-Gorji, M., Gu, Y., Saha, S.C., Paul, G., 2021. Polydisperse aerosol transport and deposition in upper airways of age-specific lung. Int. J. Environ. Res. Public Health 18. https://doi.org/10.3390/ijerph18126239

Kadota, K., Matsumoto, K., Uchiyama, H., Tobita, S., Maeda, M., Maki, D., Kinehara, Y., Tachibana, I., Sosnowski, T.R., Tozuka, Y., 2022. In silico evaluation of particle transport and deposition in the airways of individual patients with chronic obstructive pulmonary disease. Eur. J. Pharm. Biopharm. 174, 10–19. https://doi.org/10.1016/j.ejpb.2022.03.010

Kadota, K., Nishimura, T., Nakatsuka, Y., Kubo, K., Tozuka, Y., 2017. Assistance for Predicting Deposition of Tranilast Dry Powder in Pulmonary Airways by Computational Fluid Dynamics. J. Pharm. Innov. 12, 249–259. https://doi.org/10.1007/s12247-017-9285-x

Kaviratna, A., Tian, G., Liu, X., Delvadia, R., Lee, S., Guo, C., 2019. Evaluation of bio-relevant mouth-throat models for characterization of metered dose inhalers. AAPS PharmSciTech 20, 130. https://doi.org/10.1208/s12249-019-1339-6

Khan, M.A., Pierre, J.W., Wold, J.I., Trudnowski, D.J., Donnelly, M.K., 2020. Impacts of swinging door lossy compression of synchrophasor data. Int. J. Electr. Power Energy Syst. 123, 1–10. https://doi.org/10.1016/j.ijepes.2020.106182

Kim, W.W., Menon, S., 1997. Application of the localized dynamic subgrid-scale model to turbulent wall-bounded flows. 35th Aerosp. Sci. Meet. Exhib. 1–12. https://doi.org/10.2514/6.1997-210

Kleinstreuer, C., Shi, H., Zhang, Z., 2007. Computational Analyses of a Pressurized Metered Dose Inhaler and a New Drug–Aerosol Targeting Methodology. J. Aerosol Med. 20, 294–309. https://doi.org/10.1089/jam.2006.0617

Kunda, N.K., Hautmann, J., Godoy, S.E., Marshik, P., Chand, R., Krishna, S., Muttil, P., 2017. A novel approach to study the pMDI plume using an infrared camera and to evaluate the aerodynamic properties after varying the time between actuations. Int. J. Pharm. 526, 41–49. https://doi.org/10.1016/j.ijpharm.2017.04.051

Lim, S.H., Park, S., Lee, C.C., Ho, P.C.L., Kwok, P.C.L., Kang, L., 2021. A 3D printed human upper respiratory tract model for particulate deposition profiling. Int. J. Pharm. 597. https://doi.org/10.1016/j.ijpharm.2021.120307

Longest, P.W., Hindle, M., 2009. Evaluation of the Respimat soft mist inhaler using a concurrent cfd and in vitro approach. J. Aerosol Med. Pulm. Drug Deliv. 22, 99–112. https://doi.org/10.1089/jamp.2008.0708

Longest, P.W., Hindle, M., Das Choudhuri, S., 2009. Effects of Generation Time on Spray Aerosol Transport and Deposition in Models of the Mouth-Throat Geometry. J. Aerosol Med. Pulm. Drug Deliv. 22, 67–83. https://doi.org/10.1089/jamp.2008.0692

Longest, P.W., Tian, G., Walenga, R.L., Hindle, M., 2012. Comparing MDI and DPI aerosol deposition using in vitro experiments and a new stochastic individual path (SIP) model of the conducting airways. Pharm. Res. 29, 1670–1688. https://doi.org/10.1007/s11095-012-0691-y

Longest, P.W., Xi, J., 2007. Effectiveness of direct Lagrangian tracking models for simulating nanoparticle deposition in the upper airways. Aerosol Sci. Technol. 41, 380–397. https://doi.org/10.1080/02786820701203223

McKiernan, A.P., 2019. Inhaler spray investigation using high-speed phase-contrast X-Ray and schlieren imaging. Pharm. Res. 36. https://doi.org/10.1007/s11095-019-2657-9

Moraga-Espinoza, D.F., Eshaghian, E., Shaver, A., Smyth, H.D.C., 2018. Effect of Inhalation Flow Rate on Mass-Based Plume Geometry of Commercially Available Suspension pMDIs. AAPS J. 20. https://doi.org/10.1208/s12248-018-0241-6

Morsi, S.A., Alexander, A.J., 1972. An investigation of particle trajectories in two-phase flow systems. J. Fluid Mech. 55, 193–208. https://doi.org/10.1017/S0022112072001806

Narayanan, J.K., Lin, J., Feng, Y., Cui, X., 2022. Numerical study on the impact of mucus layer and inlet air-temperatures on the particle deposition in a highly idealized mouth-throat model using LES. Powder Technol. 395, 455–475. https://doi.org/10.1016/j.powtec.2021.09.073

Newman, S., 2015. RDD Online Respiratory Drug Delivery, Metered Dose Inhalers [WWW Document]. 2015-08-18. URL http://www.rddonline.com/education/online_training/MDIs/player.html

Nishida, K., Tian, J., Sumoto, Y., Long, W., Sato, K., Yamakawa, M., 2009. An experimental and numerical study on sprays injected from two-hole nozzles for DISI engines. Fuel 88, 1634–1642. https://doi.org/10.1016/j.fuel.2009.01.003

Ogrodnik, N., Azzi, V., Sprigge, E., Fiset, S., Matida, E., 2016. Nonuniform deposition of pressurized metered-dose aerosol in spacer devices. J. Aerosol Med. Pulm. Drug Deliv. 29, 490–500. https://doi.org/10.1089/jamp.2015.1257

Rahman, M.M., Zhao, M., Islam, M.S., Dong, K., Saha, S.C., 2021. Aging effects on airflow distribution and micron-particle transport and deposition in a human lung using CFD-DPM approach. Adv. Powder Technol. 32, 3506–3516. https://doi.org/10.1016/j.apt.2021.08.003

Sadeghi, T., Pakzad, L., Fatehi, P., 2023. Evaluation of soft mist inhaler aerosol velocity, size, and deposition inside the mouth - A computational fluid dynamics study. J. Biomech. Eng.

145. https://doi.org/10.1115/1.4056967

Sarkar, S., Peri, S.P., Chaudhuri, B., 2017. Investigation of multiphase multicomponent aerosol flow dictating pMDI-spacer interactions. Int. J. Pharm. 529, 264–274. https://doi.org/10.1016/j.ijpharm.2017.07.005

Shang, Y., Dong, J., Tian, L., Inthavong, K., Tu, J., 2019. Detailed computational analysis of flow dynamics in an extended respiratory airway model. Clin. Biomech. 61, 105–111. https://doi.org/10.1016/j.clinbiomech.2018.12.006

Sheth, P., Grimes, M.R., Stein, S.W., Myrdal, P.B., 2017. Impact of droplet evaporation rate on resulting in vitro performance parameters of pressurized metered dose inhalers. Int. J. Pharm. 528, 360–371. https://doi.org/10.1016/j.ijpharm.2017.06.014

Smyth, H., Brace, G., Barbour, T., Gallion, J., Grove, J., Hickey, A.J., 2006. Spray pattern analysis for metered dose inhalers: Effect of actuator design. Pharm. Res. 23, 1591–1596. https://doi.org/10.1007/S11095-006-0280-Z

Sosnowski, T.R., 2021. Inhaled aerosols: Their role in COVID-19 transmission, including biophysical interactions in the lungs. Curr. Opin. Colloid Interface Sci. 54, 101451. https://doi.org/10.1016/j.cocis.2021.101451

Sosnowski, T.R., 2018. Particles on the lung surface - physicochemical and hydrodynamic effects. Curr. Opin. Colloid Interface Sci. 36, 1–9. https://doi.org/10.1016/j.cocis.2017.12.003

Spasov, G.H., Rossi, R., Vanossi, A., Cottini, C., Benassi, A., 2022. A critical analysis of the CFD-DEM simulation of pharmaceutical aerosols deposition in extra-thoracic airways. Int. J. Pharm. 629, 122331. https://doi.org/10.1016/j.ijpharm.2022.122331

Stahlhofen, W., Rudolf, G., James, A.C., 1989. Intercomparison of Experimental Regional Aerosol Deposition Data. J. Aerosol Med. Depos. Clear. Eff. Lung 2, 285–308. https://doi.org/10.1089/jam.1989.2.285

Talaat, M., Si, X., Xi, J., 2022. Effect of MDI actuation timing on inhalation dosimetry in a human respiratory tract model. Pharmaceuticals 15, 61. https://doi.org/10.3390/ph15010061

Versteeg, H.K., Hargrave, G.K., Myatt, B.J., Lewis, D.A., Church, T., Brambilla, G., 2017. Using Phase Doppler Anemometry and High Speed Imaging to Analyze MDI Spray Plume Dynamics. Respir. Drug Deliv. Eur.

Walenga, R.L., Longest, P.W., 2016. Current inhalers deliver very small doses to the lower tracheobronchial airways: Assessment of healthy and constricted lungs. J. Pharm. Sci. 105, 147–159. https://doi.org/10.1016/j.xphs.2015.11.027

Williams, J., Kolehmainen, J., Cunningham, S., Ozel, A., Wolfram, U., 2022. Effect of patient inhalation profile and airway structure on drug deposition in image-based models with particle-particle interactions. Int. J. Pharm. 612, 121321. https://doi.org/10.1016/j.ijpharm.2021.121321

Wu, C., Yan, W., Chen, R., Liu, Y., Li, G., 2022. Numerical study on targeted delivery of magnetic drug particles in realistic human lung. Powder Technol. 397, 116984. https://doi.org/10.1016/j.powtec.2021.11.028

Xi, J., Longest, P.W., 2008. Effects of oral airway geometry characteristics on the diffusional deposition of inhaled nanoparticles. J. Biomech. Eng. 130, 13–17. https://doi.org/10.1115/1.2838039

Xi, J., Yuan, J.E., Yang, M., Si, X., Zhou, Y., Cheng, Y.S., 2016. Parametric study on mouth–throat geometrical factors on deposition of orally inhaled aerosols. J. Aerosol Sci. 99, 94–106. https://doi.org/10.1016/j.jaerosci.2016.01.014

Zhang, Y., Chia, T.L., Finlay, W.H., 2006. Experimental measurement and numerical study of particle deposition in highly idealized mouth-throat models. Aerosol Sci. Technol. 40, 361–372. https://doi.org/10.1080/02786820600615055

Zhang, Z., Kleinstreuer, C., Kim, C.S., 2002. Micro-particle transport and deposition in a human oral airway model. J. Aerosol Sci. 33, 1635–1652. https://doi.org/10.1016/S0021-8502(02)00122-2

Zhou, Y., Sun, J., Cheng, Y.S., 2011. Comparison of deposition in the USP and physical mouth-throat models with solid and liquid particles. J. Aerosol Med. Pulm. Drug Deliv. 24, 277–284. https://doi.org/10.1089/jamp.2011.0882

Chapter 6 - Mucus, Airway and Plume Temperature Effects on pMDI-Drug Delivery in a Mouth-Throat Airway: Experimental and Numerical Studies

6.1 Introduction

Previous studies have emphasized the importance of comprehensively understanding airflow dynamics in the human airway to accurately determine the movement and deposition of aerosolized drugs in the respiratory system. Factors such as airway shape, particle size, and inhalation flow rate significantly influence particle transport and deposition in the upper airway, as thoroughly discussed by Finlay (2001). Additionally, device features, including the structure of the actuator and the formulation in the canister, also have an impact on this process (Jahed et al., 2023; Sadeghi et al., 2023; Dastoorian et al., 2022; McKiernan, 2019; Chen et al., 2017; Kleinstreuer et al., 2007; Smyth et al., 2006). However, there is limited discussion of biologically essential parameters, such as airway wall temperature and the presence of a mucus layer, as well as the temperature of the inhaler's spray, which can alter respiratory tract flow patterns through heat transfer. The temperature of the drug cloud released by pressurized metered-dose inhalers (pMDIs) depends on the formulation of the canister (i.e., drug, propellant, and co-solvent content) and the inhaler structure, including the metering volume, actuator orifice diameter, and add-on devices (Brambilla et al., 2011).

Moreover, the deposition and trajectory of aerosol particles are influenced by hygroscopic properties, including evaporation and condensation. In the human upper respiratory tract, the relative humidity (RH) of inhaled air reaches approximately 99.8% at the tracheal bifurcation during inhalation, creating a conducive environment for hygroscopic particle growth. However, the hygroscopic growth of particles under these conditions may be limited by factors such as particle concentration, composition, and initial size (Haddrell et al., 2014; Morrow, 1986). Previous studies have modelled the impact of particles' hygroscopic characteristics within the human airways, analyzing their influence on particle size and deposition distribution throughout the respiratory system (Finlay and Stapleton, 1995; Eisner et al., 1990; Ferron et al., 1989, 1988; Martonen, 1982). Finlay and Stapleton (1995) demonstrated that evaporation/condensation of particles has a significantly greater influence in the extrathoracic region than in the bronchiolar and alveolar regions. Martonen (1982) proposed an analytical model to predict the deposition

patterns of hygroscopic aerosols. Their research, using NaCl aerosols as a case study, indicates that the hygroscopic growth of submicron NaCl particles significantly accelerates their diameter increase, thereby increasing deposition efficiency.

Additionally, Ferron et al. (1989) found that particles with an initial diameter of 0.5-2 μm significantly change in size when exposed to a constant RH, accounting for airway temperature and RH distributions. In addition to the initial particle size, the theoretical model proposed by Eisner et al. (1990) suggests that growth rates, deposition probabilities of hygroscopic aerosols, and deposition locations depend on the initial particle concentration. The study emphasizes the importance of considering heat and mass transfer within the mucus layer on the wall, along with their interactions with hygroscopic aerosol growth rates. This causes particles to grow exclusively in close proximity to the wall. Neglecting this interplay results in substantial aerosol growth across all areas.

Regarding the influence of airway geometry, several mouth-throat (MT) models have been studied for predicting *in-vitro* particle deposition. The USP induction port, which features a metallic tube with a 90° bend, is a standard model for oral cavity deposition. However, this design overlooks the crucial geometrical features of the MT region, which are essential for accurately predicting *in-vivo* deposition (Kaviratna et al., 2019). Although the Alberta Idealized Throat (AIT) model offers a more realistic portrayal of the upper airway (Stapleton et al., 2000), its simplified design presents some limitations (Lim et al., 2021; Kaviratna et al., 2019; Ruzycki et al., 2019). Replacing a simple airway geometry with a realistic respiratory replica enhances the reliability and approximation of *in-vivo* data. However, it shows limited utility for studying particle deposition in the human respiratory system.

Furthermore, there are significant variations in the transport and deposition of inhaled particles among different individuals and even within the same individual during respiration (Xi and Yang, 2019; Golshahi et al., 2013a, 2013b). In a study conducted by Yang et al. (2017), the predictive capability of existing modeled equations proposed by Cheng et al. (2015), Golshahi et al. (2013a), Cheng (2003), ICRP (1994), and Stahlhofen et al. (1989), for extrathoracic deposition, was compared with *in-vivo* data. They found that the extrathoracic deposition fraction predicted by Golshahi et al. (2013a) was the most accurate, followed by the ICRP (1994) model. Also, Yang et al. (2017) demonstrated that larger particles, faster inhalation flow rates, and smaller characteristic

diameters are expected to result in higher deposition in this region. However, this trend was not consistently observed across all individuals in their *in-vivo* study. Geometric variation, as well as the dynamic nature of the airways, which change in size and shape during respiration, play a crucial role in deposition distribution. According to a numerical study by Xi et al. (2016), among various geometric factors, the glottis area was identified as a predominant factor affecting the deposition of medium-sized particles (6-12 μm). Furthermore, Bhardwaj et al. (2022) found that using a generalized kinematic glottis motion function in their *in-silico* simulations for lower glottal deformation led to more pronounced regional differences in particle deposition than a static glottis.

Lim et al. (2021) and Ahookhosh et al. (2019) conducted experimental studies on the deposition of aerosol particles in a complex replica of the human airway, including the MT region and tracheobronchial tree. Also, Szabová et al. (2023) conducted a numerical investigation of the deposition of nebulized liposomal aerosols throughout the entire airway replica, including the bronchial tree. These studies provided valuable data on realistic regional deposition patterns in the respiratory tract, highlighting the dominance of inertial impaction in both the upper airway and the tracheobronchial tree. However, they did not consider the effect of the body temperature and wall tissue properties.

The use of computational methods to analyze particle transport and deposition is crucial for simulating respiratory drug delivery, particularly when incorporating detailed biological airway wall features to complement laboratory experiments. In a study by Narayanan et al. (2022), it was found that the highly idealized MT geometry, which contains a mucus layer and various inlet air temperatures, has a limited impact on the deposition locations of drug particles. However, it was found that the amount of deposition could increase by up to 15% depending on particle size and temperature. It is essential to note that the study did not account for the effects of aerosol temperature, polydisperse diameter, and a realistic upper airway, nor did it model the interaction between droplets and vapour. In a similar simplified upper airway model, Chen et al. (2021) incorporated the mucus layer into their computational fluid dynamics (CFD) models and investigated the impact of varying inlet flow rates on drug aerosol deposition. Their numerical results showed that droplet-vapour interactions, as well as heat and mass transfer in the mucus-tissue layer, significantly affected the accurate prediction of aerosol transport and deposition. Neglecting realistic thermal boundary conditions resulted in more than 10% differences in

deposition efficiency at an inlet flow rate of 15 L/min and approximately 6% differences at 30 L/min.

Shemirani et al. (2013) conducted a study on the drug particle deposition within the AIT model and the delivery of various solution and suspension pMDI formulations to the lungs. The study examined different RH conditions, environmental temperatures, and airflow rates. Their results revealed that airflow rate had minimal impact on both formulations. However, RH had a more significant influence on the drug delivery of the suspensions compared to the solutions, leading to increased (MT) airway deposition. On the other hand, increased air temperature enhanced the lung delivery of the solutions, whereas it had little to no effect on the suspension types. Also, Xu et al. (2021) found that ambient temperature and humidity can affect particle hygroscopic growth, which, in turn, influences the total deposition fraction in the respiratory system. The hygroscopic growth of inhaled aerosols significantly influenced the particles' pathways and deposition locations in the respiratory system. Chen et al. (2018) emphasized that the interaction between thermal airflow and the mucus layer substantially impacted hygroscopic growth, potentially reducing the deposition efficiency of multicomponent droplets by up to 10%. However, Aghaei et al. (2023) showed that, although the mucus layer significantly decreased droplet evaporation, the level of humidity in the inhaled air and the mucus layer itself had minimal impact on the deposition fraction in the nasal cavity.

Previous studies did not consider the characteristics of plumes emitted by high-velocity, low-temperature inhalers. It has been noted that the nozzle exit velocities of pMDIs are close to sonic velocity (Longest et al., 2012; Kleinstreuer et al., 2007), and Brambilla et al. (2011) indicated that the plume temperatures of pMDIs could range from -54 to 19°C. Both factors are significant and should be incorporated into the modeling. Additionally, most research efforts investigating particle transport and deposition from inhalers into the airway fail to simultaneously consider the realistic geometry of the airway, the high velocity and low temperature of the aerosol injected, as mentioned earlier, and the tissue features of the airway wall. By neglecting to consider the collective effects of these parameters, the accurate behavior of particles in the airway has not been fully understood. Thus, our computational model aimed to evaluate the amount of particle deposition by simultaneously accounting for all these parameters. However, it required validation through experiments. For this purpose, we fabricated a realistic upper airway geometry (VCU medium-

sized MT airway) using 3D printing. We then examined the deposition efficiency of the pMDI using a next-generation impactor (NGI).

Coating a fabricated model with a mucus layer in an experimental study poses several challenges. These include achieving uniformity across the entire surface with constant thickness, ensuring adhesion to specific fabricated materials, maintaining durability under varying conditions such as flow rate (Longest et al., 2012; Sandberg et al., 2009), and rinsing deposited particles. These challenges highlight the need for CFD to aid in modeling and simulating airflow in the upper airway, accounting for realistic MT geometry, tissue layers, thermal boundary conditions, and humidity features. In the MT model, the complexity of the realistic airway geometry creates a transition flow regime from laminar to turbulent (Ahookhosh et al., 2021; X. Chen et al., 2017). The Reynolds number in the MT geometry (developed by Longest et al. (2009) and also utilized in our study) with a constant flow rate of 30 L/min ranges from 1,854 to 3,945 (Longest et al., 2009).

We employed large-eddy simulation (LES) modelling to accurately predict transient behaviour in the airway (Huang et al., 2021; Cui and Gutheil, 2011). Subsequently, our model was utilized to analyze the temperature distribution of aerosol injection and the inlet airflow. We investigated the injection of polydisperse particles ranging from 1 to 20 μm at a high velocity of 80 m/s using the pMDI injection structure. Additionally, we explored various plume temperatures, including -54°C, -20°C, 0°C, and 10°C.

6.2 Experimental Method

6.2.1 Fabrication of the MT Model

To construct our MT model for experimental and CFD studies, we used the realistic adult airway geometry developed by the Respiratory and Aerosol Dynamics Research Group of Virginia Commonwealth University (Delvadia et al., 2016, 2012; Longest et al., 2008; Xi and Longest, 2008), and downloaded from The Respiratory Drug Delivery Online (Newman, 2015). We initially imported the stereolithography file of the airway geometry, which was divided into three parts (mouth, pharynx, and trachea), into SOLIDWORKS® CAD Software. Then, we used a 3D printer (UltiMaker S3, Netherlands) with fused deposition modelling to create a hollow airway geometry with a 3 mm thickness on the outward side, using polylactic acid (PLA) filament (**Fig. 6-1(a)**). The

inner walls of the airway were smoothed using cotton soaked in acetonitrile to refine the raised areas formed by the 3D printer, while maintaining the shape's internal volume unchanged. Since PLA is poorly soluble in acetonitrile, applying mechanical pressure helped eliminate surface roughness without altering the shape. Finally, the model was rinsed with distilled water to prepare for testing, as PLA is not water-soluble. The joints of the three parts were then tightened and sealed with Teflon tape to prevent leakage. Ahookhosh et al. (2019) also used PLA to replicate the realistic geometry of the MT, trachea, and tracheobronchial tree up to the fourth generation, and they validated their regional deposition with literature (Borojeni et al., 2014; Golshahi et al., 2012; Golshahi and Finlay, 2012; Cheng et al., 1999; Hofmann et al., 1989; Stahlhofen et al., 1989; Chan and Lippmann, 1980; Schlesinger et al., 1977).

6.2.2 Experimental Setup and Sample Preparation

We used a 200-metered-dose (100 μg of drug per actuation, as labelled) Salbutamol Sulphate bioequivalent Ventolin® pMDI (SANIS Health, Canada) connected to the 3D-printed realistic MT airway. The exterior of the mouth section of the replica was designed to match the dimensions of NGI's mouthpiece (length: 40 mm, diameter: 38.1 mm), ensuring precise alignment with the centerline of the inhaler's mouthpiece (length: 25.4 mm from the orifice to the tip). Additionally, the wall at the end of the trachea was expanded to securely connect to the inlet of the NGI system (Copley Scientific, UK), without the use of an NGI pre-separator. The NGI setup comprises an eight-stage impactor, a critical flow controller (TPK 2000, Copley Scientific, UK), and a vacuum pump (HCP5, Copley Scientific, UK), as shown in **Fig. 6-1**. The replica and the impactor were placed within a cooler box to maintain a controlled temperature (22 ± 2°C) and RH (50 ± 5%) for testing. The vacuum pump was adjusted to deliver a constant flow rate of 30 L/min, corresponding to the typical adult tidal breathing flow rate at rest (Wu et al., 2022; Biswas et al., 2017; Longest & Hindle, 2009).

To assess the concentration of deposited Salbutamol Sulphate within the airway replica and NGI's cups, a high-performance liquid chromatography (HPLC) assay (XSelect CSH Prep C18 5 μm OBD 19x150 mm column, 40˚C, 1525 Binary HPLC pump, 2489 UV/Visible detector) (Waters, US) was conducted. The calibration curve spanned a concentration range of 0.2–20 ppm and showed a strong linear relationship ($R^2 = 0.998$). The limit of quantification (LOQ) was determined at 1.7 ppm. We conducted the analysis at room temperature using a mobile phase composed of a

65%:35 % mixture of HPLC-grade water and acetonitrile. The mobile-phase flow rate was 1 mL/min, and the injected sample volume was 100 µL. Salbutamol Sulphate was detected at 254 nm with a retention time of 4.5 min.

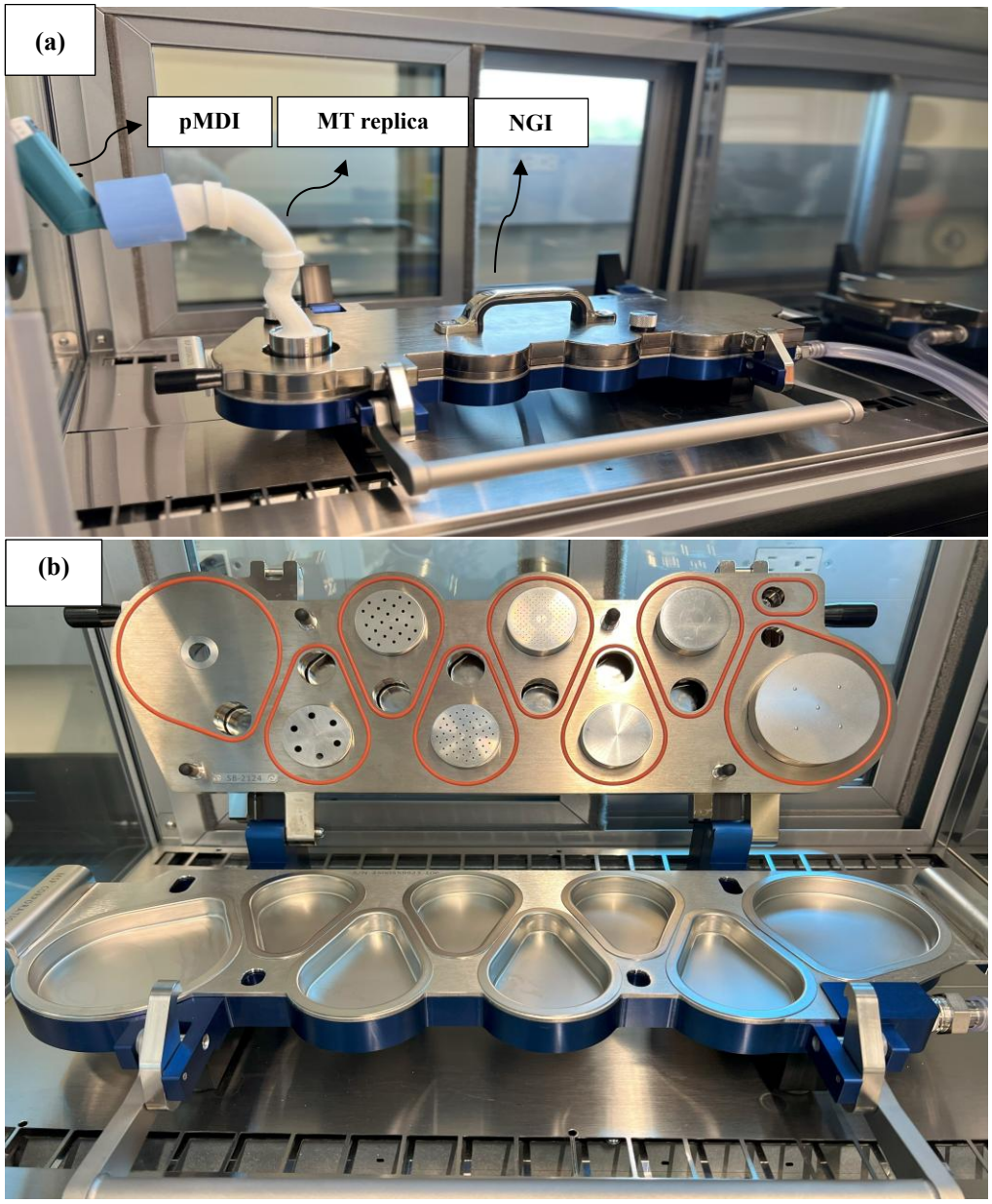

Fig. 6-1: Experimental setup: **(a)** Salbutamol pMDI, MT replica, and NGI; and **(b)** NGI's inside view included the different sizes of nozzles and impaction cups.

For each test, the inhaler was shaken and then connected to the MT airway. It was actuated 5 times at 10-second intervals to ensure that the drug (Salbutamol Sulphate) was deposited on the MT and cups in amounts exceeding the HPLC detection limit. Each experiment was repeated three times.

Following each test, the MT airway geometry segments, the inhaler mouthpiece, and the NGI cups were rinsed with 15 mL, 10 mL, and 10 mL HPLC water plus 0.1% formic acid (Fisher Scientific, US), respectively. Each sample was then filtered once through a Whatman® nitrocellulose membrane filter with a pore size of 0.45 μm for analysis by the HPLC assay.

6.3 CFD Model Development

6.3.1 Geometry and Mesh Generation

Fig. 6-2 depicts the geometry of the pMDI inhaler, the MT airway model (VCU-medium size), and the airway wall structure. The thickness of the airway wall was 0.51 mm, consisting of an airway tissue layer and a mucus layer with thicknesses of 0.5 mm, and 10 μm, respectively (Xu et al., 2021; Chen et al., 2018; Kamm, 1999). The ANSYS Workbench 2020R2 from ANSYS, Inc. was used to create tetrahedral meshes in the fluid zone and prism meshes in the wall region. The wall-region meshes consisted of 13 layers, with a thickness transition ratio of 0.272, to capture the high gradients near the walls (Talaat et al., 2022b; Feng et al., 2021b). An LES turbulent model requires a finer mesh resolution (Fen Huang et al., 2021) to accurately predict the flow properties and particle transport within the airway. Thus, our mesh independence study was conducted using four mesh resolutions: 1,040,882 (Case A), 2,168,661 (Case B), 4,170,143 (Case C), and 7,916,485 (Case D), with a constant airflow of 30 L/min.

Fig. 6-3(a-d) shows the axial velocity for four regions: inhaler (II"), mouth (MM"), pharynx (PP"), and trachea (TT"). Given that the percentage root mean square error (RMSE%) (presented in Jahed et al., 2023) between Mesh C and Mesh D in all regions was less than 10% (**Fig. 6-3**), Mesh C with a mesh number of 4,170,143 was selected for our CFD model. Also, the particle size distribution deposited on MT for different mesh sizes was obtained and is shown in Fig. 6-- **3(e)**. This was done to assess the mesh independence concerning particle behavior within the model. The RMSE% between Mesh C and Mesh D, as presented in the table in **Fig. 6-3**, was found to be 6.35%. This further validates the selection of the chosen mesh size (Mesh C). Moreover, the Taylor microscale (Charalambidou et al., 2023; Calmet et al., 2019; Escudié and Liné, 2003) was measured across the entire model. The measurements revealed a range of 1 to 1.5 mm in regions of high turbulence, exceeding the selected mesh size of 0.5 mm for Mesh C. After running the time-step independence test, the time step was set to 0.1 ms.

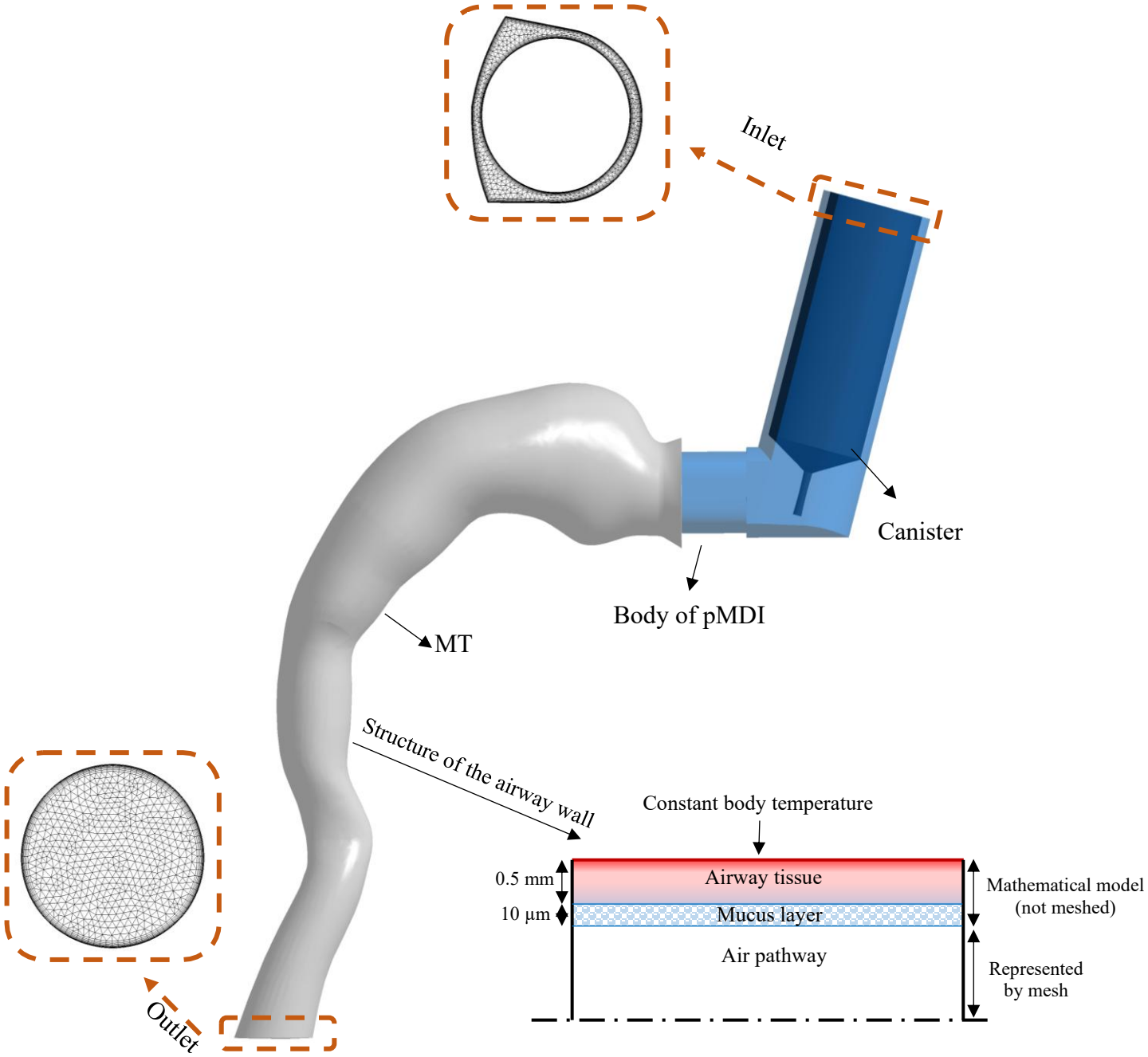

Fig. 6-2: Geometry of the MT model attached to the pMDI device, its wall structure and generated mesh.

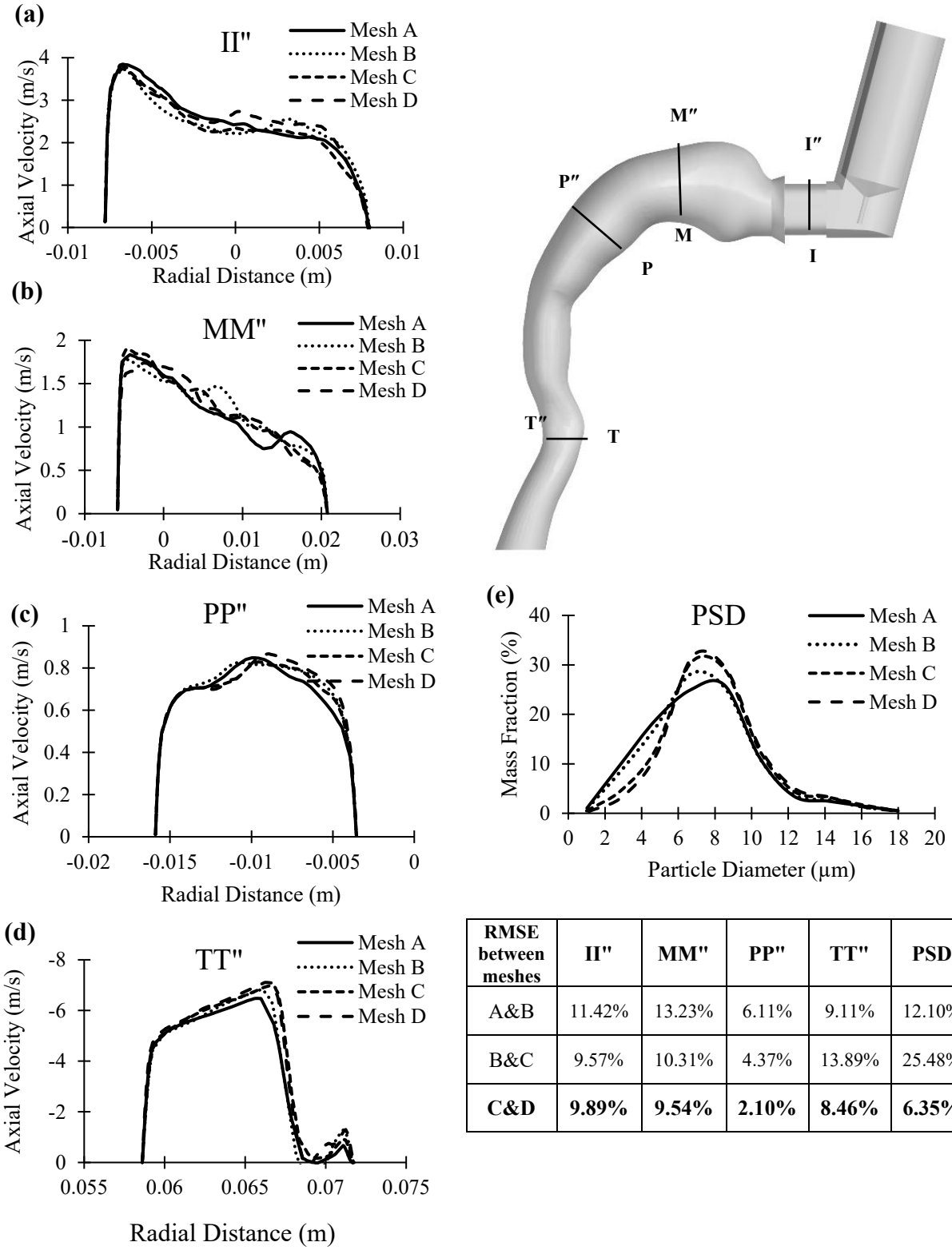

RMSE between meshes	II"	MM"	PP"	TT"	PSD
A&B	11.42%	13.23%	6.11%	9.11%	12.10%
B&C	9.57%	10.31%	4.37%	13.89%	25.48%
C&D	**9.89%**	**9.54%**	**2.10%**	**8.46%**	**6.35%**

Fig. 6-3: Comparison of mean axial velocity through the radial direction of each cross-section of **(a)** inhaler (II"); **(b)** mouth (MM"); **(c)** pharynx (PP"); and **(d)** trachea (TT") for different mesh sizes; and **(e)** deposited particle size distribution (PSD) on MT wall for different meshes.

6.3.2 Governing Equation

6.3.2.1 Airflow as a Continuous Phase

To simulate the airflow field in the MT plus inhaler setup, the unsteady, three-dimensional, and incompressible Navier–Stokes equations were solved using ANSYS Fluent (ANSYS Release 2020 R2, v20.2). We utilized the LES model (Equations (4.1-4.5)) with dynamic kinetic energy (k_{sgs}) (Equations (4.10-6.11)) to model the sub-grid scale stresses for our simulations:

The thermal energy (E) equation for air is shown below (Equations (6.8-6.12)) to predict the temperature distribution in the airway:

$$\rho(\partial/\partial t\,(E) + \nabla.\left(\overline{\boldsymbol{u}}(E)\right)) = \nabla.\left(k_{eff}\nabla T - \sum_{s} h_s\vec{J}_s + \left(\bar{\tau}_{eff}.\overline{\boldsymbol{u}}\right)\right) \tag{6.8}$$

$$E = h - \bar{P}/\rho + u^2/2 \tag{6.9}$$

$$h = \sum_{s} Y_s h_s + \bar{P}/\rho \tag{6.10}$$

$$h_s = \int c_{P,s}dT \tag{6.11}$$

$$\vec{J}_s = -(\rho D_{s,m} + \mu_t/Sc_t)\nabla Y_s - D_{T,s}\,\nabla T/T \tag{6.12}$$

where $k_{eff} = k + k_t$ is the effective thermal conductivity, which k_t is turbulent thermal conductivity, T is temperature, h_s is the species enthalpy, $\bar{\tau}_{eff}$ is the effective shear stress, $\vec{J}_s$ is the diffusion flux of species s, h is sensible enthalpy, Y_s is the species mass fraction, $C_{P,s}$ is the species-specific heat, and $D_{s,m}$ and $D_{T,s}$ are the mass and thermal diffusion coefficients (Xu et al., 2021; ANSYS, 2020). The Schmidt number (*Sc*) of 0.9 was calculated using the correlation proposed by Zhang et al. (2006) for the oral airway: $Sh = 0.421(ReSc)^{0.446}$ where *Sh* is the Sherwood number, and *Re* is the Reynolds number. They conducted a numerical study on the evaporation, hygroscopicity, transport, deposition, and mass transfer coefficient of isotonic saline droplets in the upper airways of the human body.

The transport equation for both components of humidified air, dry air, and water vapor, is given by (Feng et al., 2021b):

$$\rho(\partial/\partial t\,(Y_s) + \nabla.(\bar{\boldsymbol{u}}Y_s)) = -\nabla.\vec{J}_s + S_s \quad (6.13)$$

S_s is the source term arising from the discrete phase due to the evaporation/condensation of water droplets.

Boundary conditions for the inlet and outlet, as shown in **Fig. 6-2**, were set to a mass-flow-inlet of 6.45×10^{-4} kg/s, equivalent to a breathing flow rate of 30 L/min (typical for adult tidal breathing) and a zero-pressure-outlet to approximate atmospheric conditions, respectively. We set the CFD model's inlet and outlet boundary conditions to match the experiment. In the experiment, air with a mass flow rate of 30 L/min was sucked out by a vacuum pump at the outlet. The no-slip boundary condition was applied for MT and the inhaler's wall.

Table 6-1 provides the temperature conditions used in the CFD modeling. Three different inhaler inlet humidified air temperatures were considered: -15°C, 22°C, and 45°C. The inlet air temperatures were selected based on the research undertaken by Narayanan et al. (2022) and the average cold-season weather temperatures worldwide. We also considered four different plume temperatures (-54°C, -20°C, 0°C, and 10°C), based on the study by Brambilla et al. (2011). They measured the plume temperature of various pMDIs, including Ventolin®, using a thermocouple. The outer wall temperature of the MT airway was set to 37°C, representing human body temperature. The temperature of the inhaler's wall was set to 22°C.

Table 6-1: Different conditions of temperature considered in the CFD model.

Parameters	**Values**					
	C1	**C2**	**C3**	**C4**	**C5**	**C6**
Air temperature of the environment (°C)	22	22	22	22	-15	45
Temperature of MT wall (°C)	kept constant at 37°C					
Temperature of pMDI's plume (°C)	-54	-20	0	10	-20	-20

6.3.2.2 Mucus Layer Modelling

Airway mucus is composed of mucins, water (95%), and other gel-like constituents. Particles can penetrate this layer (Ding et al., 2021). In the oral cavity, saliva is mainly composed of 99% water, with the remaining 1% consisting of proteins and salts (Iorgulescu, 2009). In our model, airway tissue and mucus layer, each with thicknesses of 0.5 mm and 10 μm, respectively, were assumed

to be composed of a uniformly solid material with properties similar to water (refer to **Table 6-2**) (Aghaei et al., 2023; Narayanan et al., 2022; Xu et al., 2021; Chen et al., 2018). The movement of mucus over the tissue layer was neglected due to its significantly slower transport velocity compared to that of air and particles (Narayanan et al., 2022; Chen et al., 2018; Cheng et al., 2015). Furthermore, this thin layer of water on the wall creates thermal resistance by reducing the airflow's conductivity between the wall and the airflow. The airflow would interact with a lower-temperature surface (the mucus layer) compared to a dry wall, affecting the heat flux from the flow to the wall and the heat transfer from the wall. The heat transfer between the airflow and the mucus layer was calculated using Eq. (6.8).

6.3.2.3 Discrete Phase Model (DPM) for Particle Transport

The transport of individual particles injected from a pMDI nozzle into the airway model was simulated using a two-way Lagrangian discrete-phase model (DPM). This model did not account for particle-particle interactions because the particle flow was highly diluted, with a particle mass fraction as low as 0.16%, a finding also reported by Rahman et al. (2021).

Table 6-2: Material properties and variables used in CFD models.

Properties	**Materials**				
	Air	**Water vapour**	**HFA-134a (droplet)**	**HFA-134a (vapour)**	**Mucus layer**
$\rho\ (kg/m^3)$	1.225	0.5542	Table 6-3	Table 6-3	998.2
$\mu\ (kg/m.s)$	1.789×10^{-5}	1.34×10^{-5}	Table 6-3	Table 6-3	-
$C_p\ (J/kg.K)$	1006.43	*	1418.37	853.53	4182
$k\ (W/m.K)$	0.0242	0.0261	-	0.014	0.6
$h_{fg}\ (kJ/kg)$	-	-	217.2	-	-
Variables	**Values**				
S_c	0.9				
σ_k	1.0				

$* C_p = 1563.077 + 1.603755T - 0.002932784T^2 + 3.216101e^{-6}T^3 - 1.156827e^{-9}T^4$

Since the propellant (hydrofluoroalkane, HFA-134a or HFA-227a) constitutes the majority of the mass fraction in the canister of pMDIs (about 99%) (Duke et al., 2019; Sheth et al., 2017; Sou and Bergström, 2021), the HFA-134a was considered a property of the particles. The properties of this

material are provided in **Table 6-3**. The density and viscosity properties of this propellant were defined as a polynomial function of temperature (Zephex®, 2019).

The Rosin-Rammler method was used to determine the polydisperse particle diameter in the 1-20 μm size range. We used this size range to encompass the data from our experimental results, as we did not have data on the initial injected particle size of pMDI. The Rosin-Rammler distribution is defined as (Alatrash, 2018):

$$Q = exp\left(-d_p/\bar{d}\right)^q \tag{6.14}$$

where Q represents the fraction of the total mass contained in particles with diameters greater than d_p, and $\bar{d}$ denotes the mean particle diameter. The spread parameter, q, indicates the polydispersity of the spray. We tested various combinations of spread parameters and mean diameters and fitted them into the results (Ranade and Gupta, 2014; Alderliesten, 2013).

Table 6-3: Material properties (Zephex®, 2019).

HFA-134a	**Droplet**	**Vapor**
Density (kg/m^3)	$\rho = a + b\mathrm{x} + cx^2 + dx^3 + ex^4$ $x = (1 - (T/T_c))^{1/3}, T_c = 374.15\ K$	
	a=508, *b*=967.57693, *c*=298.02172, *d*=79.877831, and *e*=89.838713	For -50°C < T < 0°C *a*= -113.51, *b*=3335.18, *c*= -11368.8, *d*=13688.75, and *e*=-5583.8 For 0°C < T < 80°C *a*= 388.752, *b*= 84.07428, *c*= -3500.71, *d*= 5252.284, and *e*= -2202.55
Viscosity (cP)	$\ln \mu = a + b/T + cT + dT^2$	0.0122
	a= -9.707292, *b*= 1140.7291, *c*= 0.0282451, and *d*= -4.6720 × 10^{-5}	

*ρ and μ are the density and viscosity of HFA-134a, and *a*, *b*, *c*, *d*, and *e* are constants. T and T_c are the temperature and critical temperature of HFA-134a, respectively.

The inhaler injection time was 0.1 s, based on the actuation duration of Ventolin® HFA used in the experimental study. The inhaler was injected once. The initial injection velocity magnitude of the pMDI was assumed to be constant at 80 m/s (Ogrodnik et al., 2016) using a solid cone injection type. The particle momentum, as defined by Newton's second law of motion (Huang et al., 2021;

Finlay, 2001), can be expressed as Equation (15). In our analysis, we neglected forces such as Saffman's lift, buoyancy, pressure, Basset's effect, and the virtual mass effect, as the particles have a significantly greater density than air (Finlay, 2001). Furthermore, the thermophoresis force was disregarded because it primarily affects the deposition of sub-micron particles in turbulent aerosol flows. In our study, the predominant particle sizes were larger than 1 μm, and sub-micron particles accounted for only 0.2% of the total, making the influence of thermophoresis force and Brownian motion in relation to drag and gravitational forces negligible.

$$m_p \, \mathrm{d}\overline{\boldsymbol{u}}_{\boldsymbol{p}}/d\mathrm{t} = 18\mu/\rho_p d_p^2 \frac{m_p C_D Re_p}{24}\left(\overline{\boldsymbol{u}} - \overline{\boldsymbol{u}}_{\boldsymbol{p}}\right) + g\left(\rho_p - \rho\right)/\rho_p \tag{6.15}$$

where $\overline{\boldsymbol{u}}_{\boldsymbol{p}}$, ρ_p, d_p, and m_p are the velocity, density, diameter, and mass of the particles, respectively, and $\overline{\boldsymbol{u}}$, μ, and ρ are the velocity, dynamic viscosity, and density of the air, respectively (Narayanan et al., 2022; Ahookhosh et al., 2021). g is gravitational acceleration. The C_D is the drag coefficient for spherical particles (Morsi and Alexander, 1972). Re_p is the Reynolds number of particles (Eq. (4.19)).

The droplet temperature is estimated based on convective and latent heat transfer between the droplet and the continuous phase (air), as described in Eqs. ((4.21)-(4.23)). We considered the trap boundary condition for the airway wall and escape boundary conditions on the airway outlet.

We employed the SIMPLEC (semi-implicit method for pressure-linked equations-consistent) pressure-velocity coupling algorithm. We simulated our models on the Niagara cluster, which features 40 Intel Cascade Lake cores at 2.5 GHz, an 80-core processor, and 20 GiB/202 GB of RAM per node. We also utilized the Intel(R) Xeon(R) Gold 6148 CPU, running at 2.40 GHz with 80 cores available at Lakehead University. The average simulation time was approximately 40-60 hrs.

6.4 Results and Discussion

6.4.1 NGI and CFD Results-Validation

Deposition measurements, including error bars based on standard deviation (SD), are presented in **Fig. 6-4(a)**. The NGI consisted of eight distinct stages (S1-S8), each associated with specific particle size ranges when operating at a 30 L/min flow rate: S1 > 11.72 μm, S2: 6.40-11.72 μm, S3:3.99-6.40 μm, S4: 2.30-3.99 μm, S5: 1.36-2.30 μm, S6: 0.83-1.36 μm, S7: 0.54-0.83 μm, and

S8 < 0.54 μm. The mass fraction shown in this figure was calculated from the actual delivered dose of the pMDI device for each test, which was 114.5 ± 4.51 μg/puff.

The figure also compares the results of our CFD analysis for the mass fraction of deposited particles with our experimental data. The comparison indicates good agreement between the particle deposition in the mouth, pharynx, and trachea from the experimental assessment (43.46%, SD = ±12.2; 3.18%, SD= ±0.2; and 8.79%, SD= ±2.9; respectively) and the results obtained from CFD simulations (36.25%, 5.32%, and 11.8%), as illustrated in **Fig 6-4(a)**. The total deposition on the MT wall for experimental and CFD results was 55.44% (SD = ±9.5) and 53.37%, respectively. The CFD model conditions were carefully set to match the experimental parameters outlined in the Experimental Methods section. This included matching the properties of the airway geometry, airflow temperature, and the MT wall temperature. Specifically, the airflow and the airway MT wall were set at 22°C, and an RH of 50% was considered based on the experimental conditions.

Fig. 6-4(a) also compares our *in-vitro* deposition data for the pMDI and CFD results with the results presented by Dastoorian et al. (2022), Duke et al. (2021), and Cheng et al. (2001). The first two studies employed the USP (United States Pharmacopeia) metal induction port, a simple representative of MT airway geometry, and the same NGI system to assess drug particle deposition. To our knowledge, only a few studies, such as those by Cheng et al. (2001), have utilized realistic MT airway geometry (made of silicon) to obtain regional deposition. In their study, MT, along with five to nine generations of bronchi, were considered, and only the MT region deposition data was compared with our result. This figure confirms the consistency and validity of our results within the broader context of related research. The observed variations may stem from differences in the MT configuration and the specific canister formulation used by Duke et al. (2021). Duke's study used a canister containing a 15% w/w ethanol co-solvent and HFA-134a propellant, with ipratropium bromide as the active pharmaceutical ingredient. The size of the produced particles and their deposition highly depend on these formulation ingredients (Kaviratna et al., 2019; Biswas et al., 2017). We used the impaction parameter, calculated as the square of the aerodynamic diameter multiplied by the volumetric flow rate, to evaluate particles deposited in different studies. This method considers the simultaneous effects of flow rate and particle size on particle deposition.

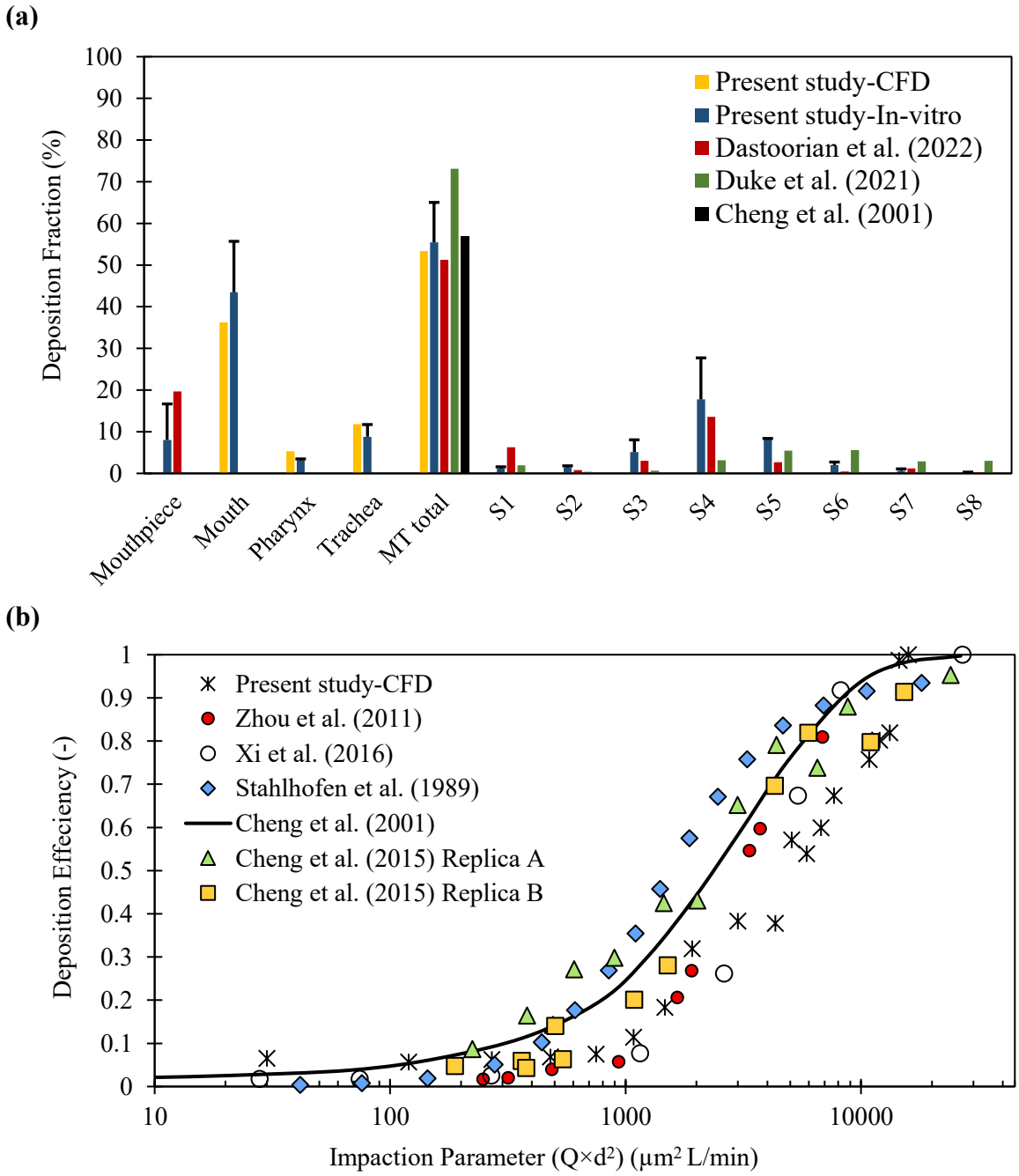

Fig. 6-4: Comparison of **(a)** deposition fraction of particles for pMDI at different regions; and **(b)** deposition efficiency in MT as a function of impaction parameters, with 30 L/min of airflow between the present experimental and CFD study and *in-vitro* and *in-vivo* results (plume temperature: -54°C, inlet air temperature: 22°C, and dry wall model with the temperature of 22°C).

We assessed the effectiveness of our model for particle deposition by comparing it with results from other relevant in-vitro and in-vivo studies (Xi et al., 2016; Cheng et al., 2015; Zhou et al., 2011; Stahlhofen et al., 1989), as shown in **Fig. 6-4(b)**. The deposition efficiency was calculated

based on the ratio of the mass of the deposited particles of a specific size to the total mass of particles ($\frac{\text{mass of the deposited particle with size } i}{\text{mass of deposited particle with size } i + \text{escaped particles with size } i}$) of that size. We had a good agreement between our determined deposition efficiency and the available data based on particle size.

As anticipated, an increase in the impaction parameter (due to larger particles) led to a corresponding rise in deposition efficiency in the MT. Particles smaller than 5 μm in diameter (impaction parameter <750) exhibited minimal deposition in the MT. These fine particles successfully traversed the upper respiratory region, ultimately reaching the lung regions, as reported in numerous deposition investigations in the literature (Kadota et al., 2022; Spasov et al., 2022; Talaat et al., 2022a; Williams et al., 2022; Koullapis et al., 2018; Xu et al., 2017). However, Borojeni et al. (2023) studied particle deposition ranging from 1 to 30 μm in adults' oral airways and found significant variability in oral deposition among individuals. When using a nebulizer for pharmaceutical aerosols with impact parameters of approximately 200 and 400, deposition ranged from 0% to 18% and 1% to 56%, respectively. Furthermore, **Fig. 6-4(b)** shows that particles in the 5-23 μm size range (impaction parameter in the range of 750-15,870) exhibited significantly higher deposition efficiency. As particle size increased beyond 23 μm (impaction parameter >15,870), these particles were deposited entirely on the MT wall and did not pass through the trachea.

6.4.2 Effect of Plume Temperature

Fig. 6-5 shows the effect of the pMDI plume temperature on particle size and deposition on the MT airway wall. Increasing the plume temperature (from C1 to C4 condition - refer to **Table 1**) resulted in a corresponding decrease in particle size. In the C1 condition (i.e., with a plume temperature of - 54°C), the mean particle diameter ($\frac{\text{sum of the diameter of deposited particle}}{\text{number of deposited particles}}$) deposited on the MT wall, was calculated to be 17.1 μm. In contrast, under a slightly higher plume temperature of -20°C (in C2), the mean diameter was 14.6 μm (a reduction of 14.6%). This difference highlights a reduction in the mean particle diameter of approximately 25.0% (from 12.8 μm to 9.6 μm) between the C1 and C3 conditions, and 34.0% (from 12.8 μm to 8.6 μm) between the C1 and C4 conditions, respectively. Decreasing the diameter size by increasing the plume temperature can be attributed to increased evaporation (Rajaraman et al., 2020). As the temperature of the droplet increases, according to the Clausius-Clapeyron expression, the vapor pressure of the

droplet increases. A higher vapor pressure indicates a higher evaporation rate of the droplet (Pal et al., 2021; Speight, 2020). Our simulations showed that the average evaporation rate increased from 3.87×10^{-7} kg/s in the C1 condition to 4.93×10^{-7} kg/s in the C4 condition, representing a 21% rise.

On the other hand, **Fig. 6-5** shows that increasing plume temperature led to a higher deposition fraction ($\frac{\text{deposited particles}}{\text{depoited particles+ escaped particles}}$) in the MT airway. Among the conditions with different plume temperatures, C1 exhibited the lowest deposition fraction (42.55%), while C4 showed the highest (60.61%). Conversely, as discussed earlier, a higher plume temperature (C4) reduced particle diameter; therefore, the deposition amount was expected to be lower due to the finer particle size. Indeed, research has demonstrated that finer particles closely follow the airflow pattern within the airway, thereby tending to pass the MT and deposit in the lower reaches of the respiratory tract (Williams et al., 2022; Feng et al., 2021b; Ke et al., 2020; Zhang et al., 2020; Chen et al., 2018; Sheth et al., 2017). Thus, this result led us to examine the airflow and particle flow pattern through the MT airway under different conditions.

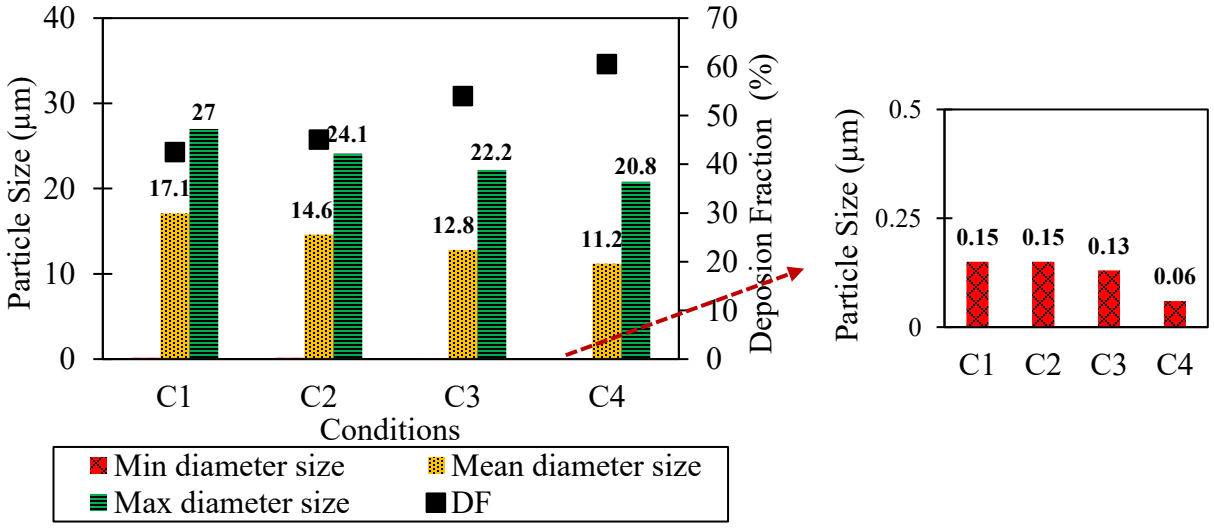

Fig. 6-5: Effect of plume temperature on particle diameter size and deposition fraction at different conditions: (C1: -54°C, C2: -20°C, C3: 0°C, and C4: 10°C, inlet air temperature: 22°C, dry wall model) (refer to **Table 6-1**).

Fig. 6-6(a) illustrates the airflow's velocity magnitude contour and streamlines across the middle plane of MT (at an airflow temperature of 22°C). The different plume temperatures and notable variations among them, especially between C1 (i.e., with a plume temperature of -54°C) and C4 (i.e., with a plume temperature of 10°C), while having a relatively minimal quantitative impact on

airflow velocity, had induced noticeable changes in the flow pattern, mainly in the mouth section, as indicated by the streamlines in **Fig. 6-6(a)**. This phenomenon suggests a complex interplay between plume temperature and the flow field. Thermal gradients between the plume and the airflow induce convective currents, which can influence flow patterns by creating vortices or altering airflow direction. Natural convection is a fundamental example of how thermal gradients can lead to the formation of convective currents (Ting, 2022). In our studies, varying plume temperatures altered the size and intensity of the recirculation regions created.

In **Fig. 6-6(a)**, the flow intensity in the C1 condition was more concentrated at the mouth center, whereas in the C4 condition, it was predominantly nearer to the MT wall (both up and down), with an intense change in the flow direction. Thus, when fine drug particles followed the airflow streamlines, changes in airflow direction influenced particle travel in the MT airway and enhanced inertial impaction. Consequently, the airflow pattern led to a higher particle deposition fraction under the C4 condition.

Fig. 6-6(b) shows the particle tracking results at the midpoint of injection (0.05 s) for the C1 and C4 conditions. For the C1 condition, particles passed through the throat and exhibited shorter residence times. In contrast, particles in the C4 condition were retained in the mouth and pharynx for a longer period. We observed small particles near the palate, likely due to the formation of pronounced recirculation regions in that area, as shown in **Fig. 6-6(a)**. As Sou & Bergström (2021) discussed, factors influencing particles' residence time may increase the probability of particle deposition in MT. Additionally, Cui et al. (2018) noted in their model that the recirculation zone in the trachea is a primary airflow structure, as it causes particle reversal and increases particle residence time in this region, thereby enhancing particle deposition. Thus, in our study, the longer particle residence time in the C4 condition and the location of most particles in the palate area increased the likelihood of particle deposition at this site.

Fig. 6-6(c) shows the mass fraction of the drug in a cross-section of the mouth (this particular cross-section was selected based on our observations made in **Fig. 6-6(a, b)**) for C1 and C4 conditions.

This figure confirms that the greater number of particles seen close to the wall in cross-sections for the C4 condition increased the potential for deposition. **Figs. 6-5** and **6-6** exhibit the impact of two factors, particle size and flow pattern, contributing to distinct deposition behaviors under

different conditions. Although we expected the smaller particles produced in the C4 condition to lead to lower MT particle deposition, the particle flow pattern affected deposition and, hence, resulted in higher deposition in the C4 condition.

These findings suggested that the coldest plume at -54°C showed the highest efficiency in pMDIs. However, patient satisfaction and a comforting experience are crucial in medication adherence. The lower plume temperature (referred to as the "cold Freon effect") in pMDIs may be intolerable for some patients, leading to incorrect usage (McCabe et al., 2012). Human studies on patient preferences and sensory perceptions of different inhalers (Gupta et al., 2019; Roche and Dekhuijzen, 2016; Bunnag et al., 2007; Crompton, 1982) indicate that patients generally prefer a warmer spray. Our results show that changing the plume temperature from -54°C to -20°C decreased device efficiency by 2.55%, but the patient will experience an aerosol 34°C warmer.

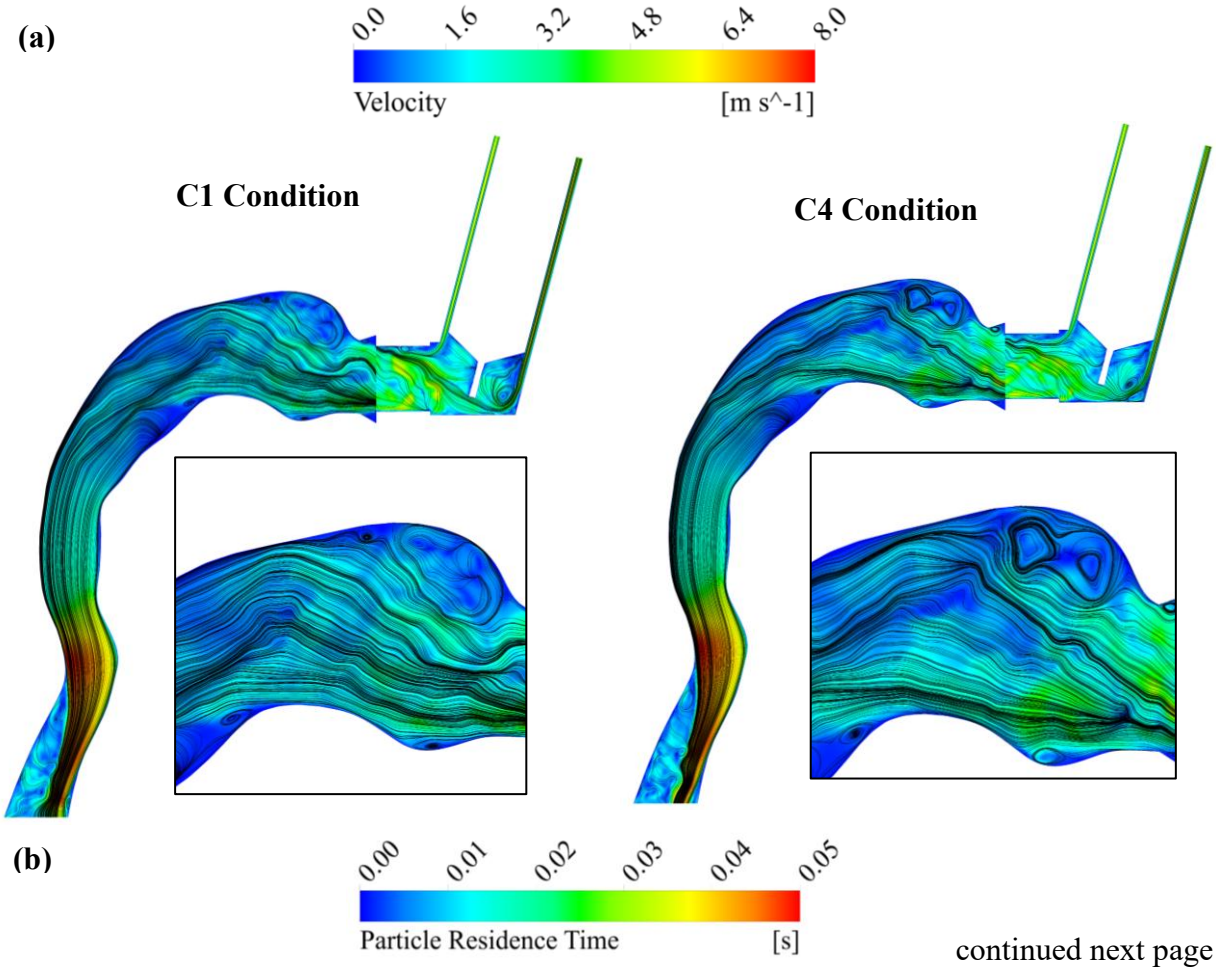

continued next page

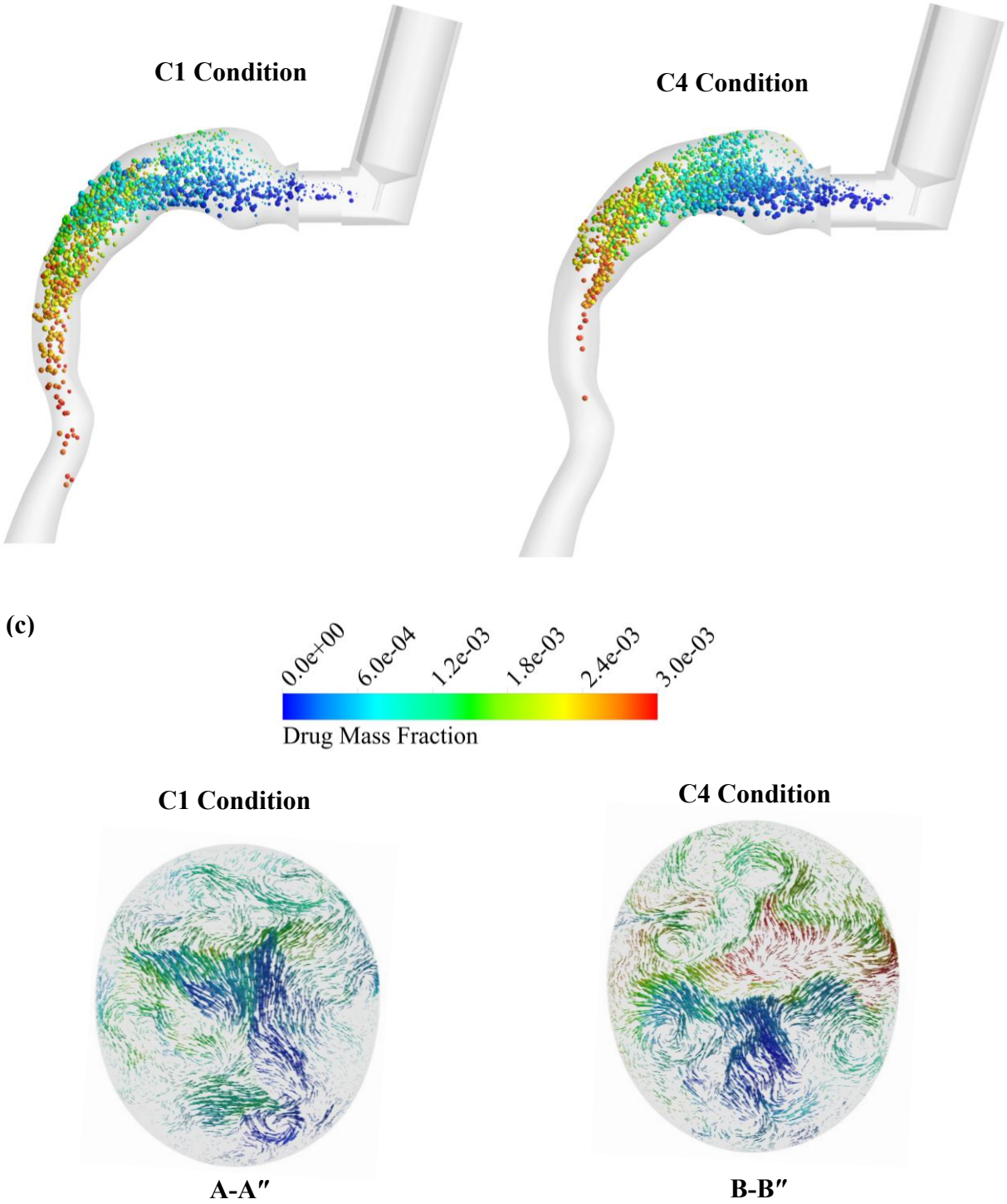

Fig. 6-6: Comparison of **(a)** airflow velocity contour and streamlines across the middle plane of MT; **(b)** residence time of particle; and **(c)** mass fraction of drug across a cross-section of mouth section at the middle of the injection (0.05s) for varying plume temperature, C1: -54°C (left side) and C4: 10°C (right side) (inlet air temperature: 22°C and dry wall model).

6.4.3 Effect of Inlet Air Temperature

Fig. 6-7 explored the impact of inlet air temperature on airflow velocity and temperature distribution within the MT. As detailed in **Table 6-1**, different air temperatures, -15°C, 22°C, and 45°C with 50% RH (referred to as C5, C2, and C6 conditions, respectively), were taken into consideration in **Fig. 6-7**. The plume temperature was maintained at -20°C in this figure. Changes in air temperature had a minimal quantitative influence on the airflow velocity. However, as the inlet airflow temperature increased, we observed a more developed plume, primarily in the mouth and pharynx areas (**Fig. 6-7(a)**). On the other hand, **Fig. 6-7(b)** shows that increasing the inlet air temperature results in a higher temperature distribution within the MT, as expected. The inlet air temperature primarily affected the mouth and pharynx region, increasing the mean temperature at its center from 10°C (C5) to 30°C (C6). Thus, changes in flow behavior in the mouth and pharynx could be attributed to enhanced convective heat transfer mechanisms. As the air temperature increased or decreased, the heat transfer rate also increased, which in turn affected the airflow pattern.

Fig. 6-7 observations are consistent with the research conducted by Narayanan et al. (2022). Their findings showed that increasing the inlet air temperature into MT results in the flow heating or cooling more rapidly, leading to increased flow velocity. Additionally, they noted that regions of recirculation and secondary vortices are more pronounced in high-temperature cases than in low-temperature cases.

Fig. 6-8 demonstrates the effect of inlet air temperature on particle size and deposition fraction within MT. Increasing the inlet air temperature resulted in an increase in particle size. In contrast to the effect of plume temperature on particle size, the magnitude of this effect on particle size and MT deposition was not particularly significant. Changing the air temperature by 37°C, shifting from -15°C to 22°C, resulted in a 0.87% increase in deposition. Conversely, transitioning from 22°C to 45°C resulted in a 4.79% reduction in particle deposition. Wilson et al. (1991) investigated the effects of ambient temperature on particle size and the effectiveness of pMDI at different canister temperatures. Their results indicated that higher canister temperatures led to smaller particle sizes and increased deposition in the lower airways. However, our study did not consider the effect of inlet air temperature on the pMDI canister.

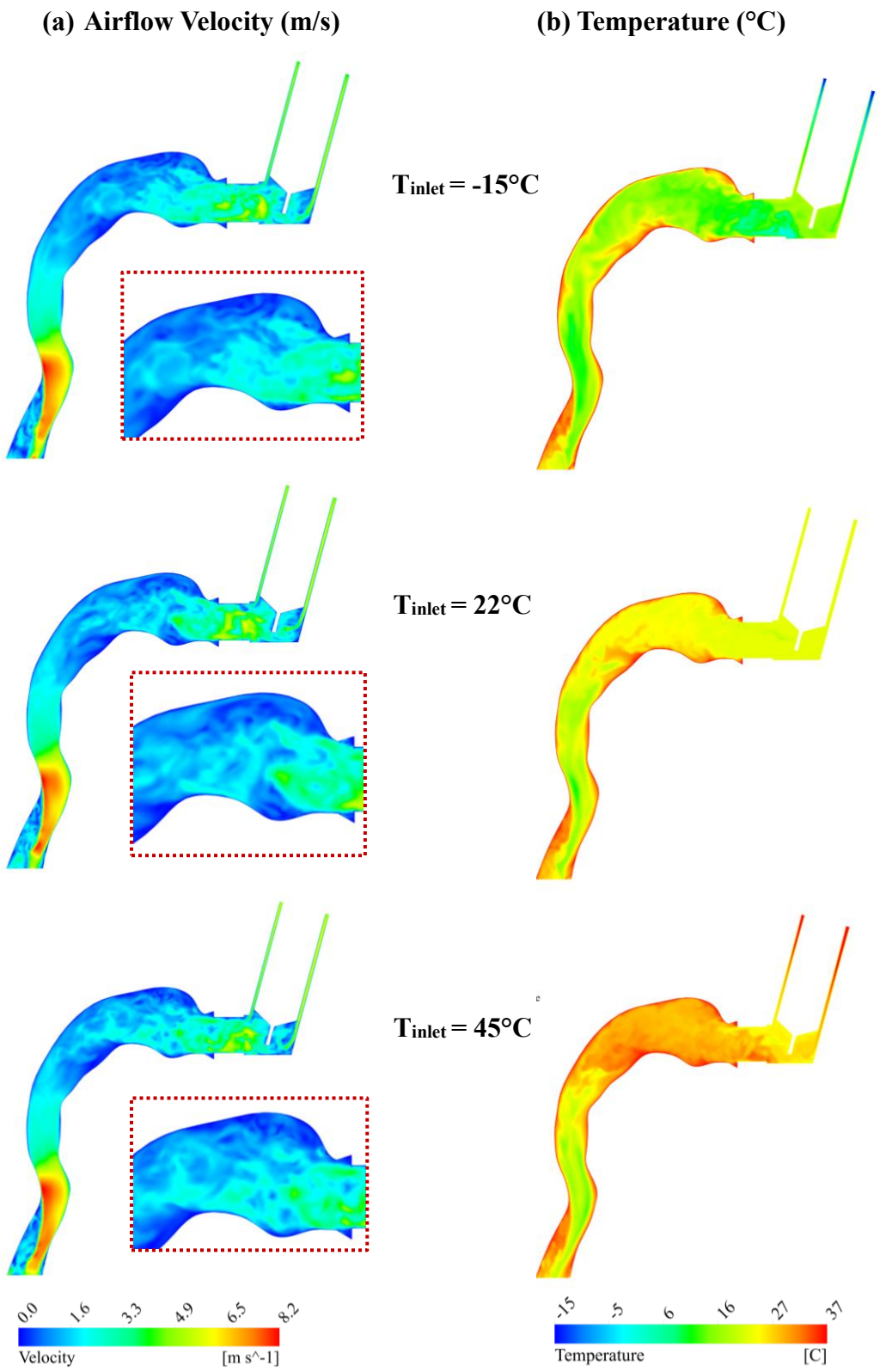

Fig. 6-7: Comparison of **(a)** airflow velocity; and **(b)** temperature distribution within MT at the end of the injection (0.1s) for varying inlet air temperature (C5: -15°C, C2: 22°C, and C6: 45°C, plume temperature: -20°C and dry wall model) (refer to **Table 6-1**).

Narayanan et al. (2022) examined the impact of inlet air temperature (15°C, 26.7°C, and 45°C) on monodisperse particle size in a simplified MT model. Their study indicated that the deposition of small particles (3 µm) was less influenced by changes in inlet air temperature compared to larger particles (5 and 6 µm). It was also found that increasing the inlet air temperature led to higher deposition efficiency. However, our results showed that changing the air temperature by 37°C, shifting from -15°C to 22°C, resulted in a 0.87% increase in deposition. Conversely, transitioning from 22°C to 45°C resulted in a 4.79% reduction in particle deposition. The differences in results may stem from factors such as variations in airway geometry and particle polydispersity, which influence flow behaviour and particle transport.

Additionally, Xu et al. (2017) conducted a study on inhalation injuries caused by exposure to high temperatures of fire smoke. They observed that, for a consistent particle size of 3 µm, the fraction of particle deposition increased with increasing inlet temperature. The study considered the particles to be non-evaporated and monodispersed in size. However, the impact of inlet temperature on particle deposition depends on particle size and flow rate, as these factors influence the evaporation rate (Xu et al., 2017; Yang et al., 2023). According to our findings, given the negligible impact of air temperature on particle size, variations in drug particle deposition were potentially influenced by flow behaviour, as discussed in **Fig 6-7**.

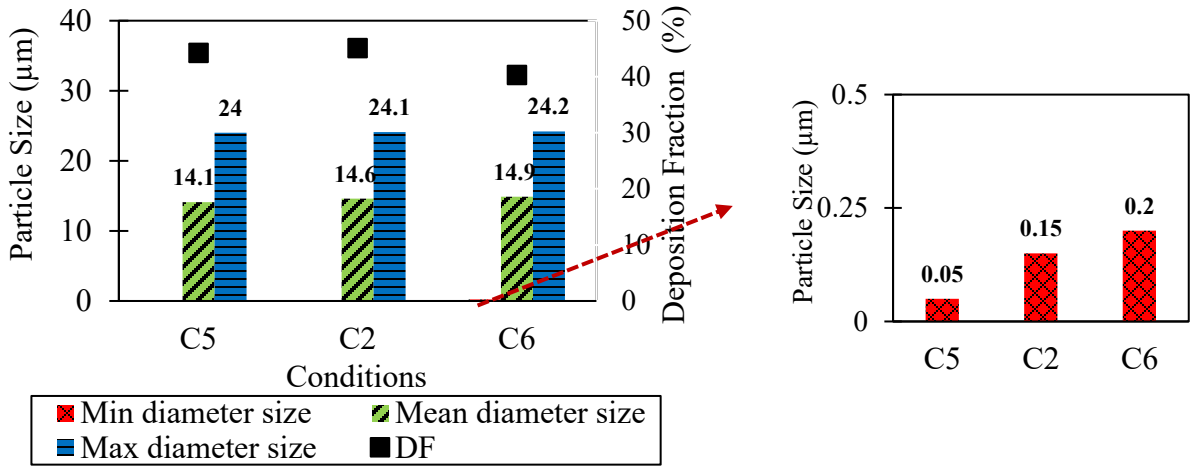

Fig. 6-8: Effect of the inlet air temperature on the particle diameter size and deposition fraction (C5: -15°C, C2: 22°C, and C6: 45°C, plume temperature: -20°C and dry wall model) (refer to **Table 6-1**).

In general, the results suggest that variations in the airflow temperature exerted a minimal influence on particle transport and deposition compared with the plume's temperature. The

differences in the effects of the plume and air temperature became more evident when examining the impact of these two parameters on particle size distribution within the MT, as demonstrated in **Fig. 6-9**. This figure illustrates the impact of the emitted plume and inlet air temperature on the size of deposited particles, showing the mass fraction of particles of a given size relative to the total deposited particles. **Fig. 6-9(a)** illustrates the noticeable impact of plume temperature on particles of almost mid-range sizes. As the number of particles within this specific size range was predominant, any changes were more pronounced in these sizes. **Fig. 6-9(b)** indicates that particle size distribution showed minimal sensitivity to changes in inlet air temperature. In the meantime, both **Figs. 6-9(a,b)** show a narrow and bimodal distribution. The majority of particles were concentrated in a size range of approximately 3 to 13 μm, with a significantly less abundant grouping observed around the particle size of 19 μm. The optimal particle size range for effective respiratory drug delivery is typically reported to be between 1 and 5 μm (Hamishehkar et al., 2012; Millage et al., 2010; Shekunov et al., 2007). This range is often considered suitable for reaching the lower regions of the respiratory system (Jahed et al., 2023). However, particle deposition is highly dependent on the inhalation flow rate. Variations in inhalation flow rate can significantly impact the particle size range delivered to the desired regions of the respiratory system, as thoroughly discussed by Finlay (2001). According to **Fig. 6-9,** on average, less than 20% of particles were less than 5 μm.

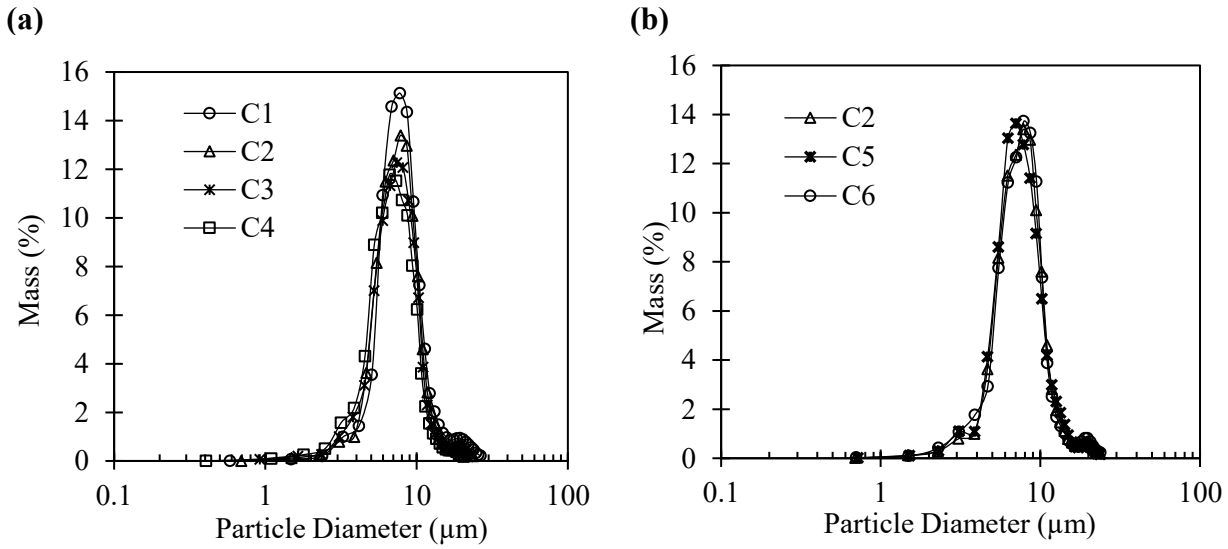

Fig. 6-9: Comparison of deposited particle size distribution on MT wall for different conditions: **(a)** varying plume temperature (C1: -54°C, C2: -20°C, C3: 0°C, and C4: 10°C, inlet air temperature: 22°C); and **(b)** varying inlet air temperature (C5: -15°C, C2: 22°C, and C6: 45°C, plume temperature: -20°C) (dry wall model) (refer to **Table 6-1**).

6.2.1 Effect of Mucus Layer

Three wall structures were explored: a dry MT wall, a wet MT wall, and a mucus-layered wall. The dry MT wall was a solid structure without thickness, and the wet MT wall incorporated water properties with no thickness. As previously mentioned (**Section 6.4.2.2**), the mucus layer, which includes water features, has a certain thickness. Through contour plots (**Fig. 6-10(a,b)**), we compared the RH distribution within MT with and without considering the thickness of the MT wall. The air entering the MT possessed an RH of 50%, regardless of the thickness (see **Fig. 6-10(a)**), causing an almost fully-dry condition near the wall region, and the RH amount increased when approaching the center of the tract. However, as seen in **Fig. 6-10(b),** RH reached about 62% when close to the mucus layer. Due to the thickness of the mucus layer and its thermal impact on the wall, which interacts with the air, the temperature decreased compared to the dry and wet walls in this region. This temperature variation significantly affected the RH levels (Longest and Hindle, 2010), and as this figure shows, it increased near the mucus layer. This localized moisture near the wall contributed to the hygroscopic growth of the particles in the area where they were deposited (**Fig. 6-11**).

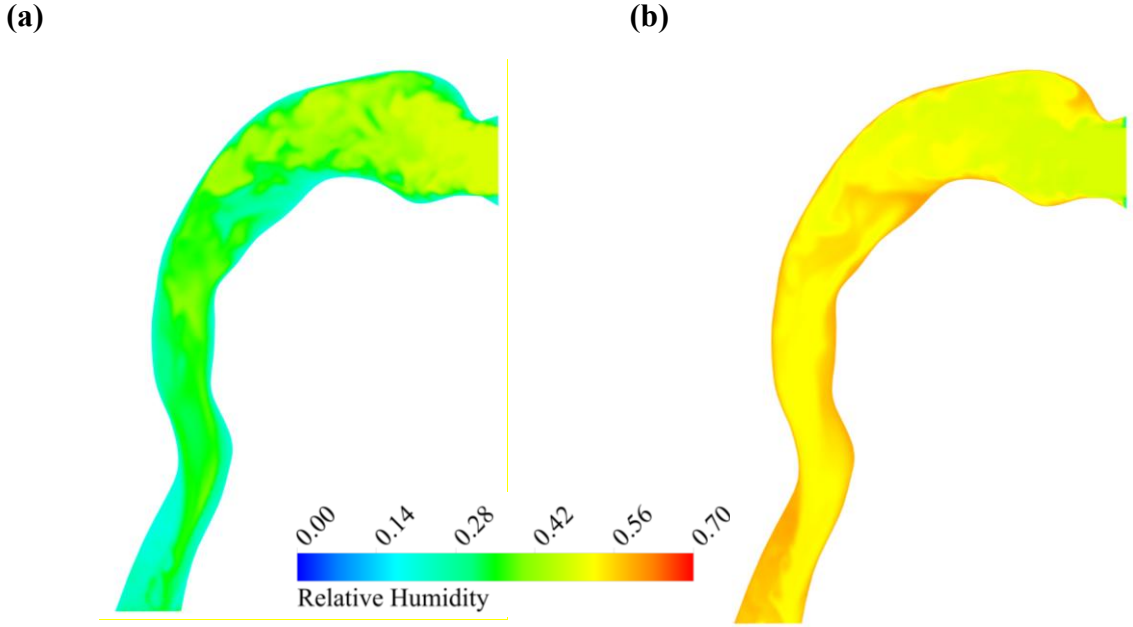

Fig. 6-10: RH distribution within MT for different wall conditions, **(a)** without thickness (dry and wet wall); and **(b)** mucus layer (plume temperature: -20°C and inlet air temperature: 22°C).

Fig. 6-11(a) shows the mass fraction of MT deposited particles normalized by the total deposited mass, while **Fig. 6-11(b)** shows the mass fraction of escaped particles normalized by the total

escaped mass for the drywall and mucus-layered wall models. In **Fig. 6-11(a)**, it is evident that a higher portion of larger particles (14-22 μm in diameter) was deposited in the mucus layer compared to the dry MT wall. The mucus-layered model produced lower temperatures and higher RH near the wall, as indicated in the results of **Fig. 6-10**. This reduced particle evaporation rates and led to larger particle sizes. Meanwhile, this figure shows no substantial difference between the two models for smaller particles. It's important to note that particle heat and mass transfer are strongly affected by their surface area. Smaller particles have a higher surface area-to-volume ratio compared to larger ones. As a result, smaller particles may reach a dynamic equilibrium under these conditions, preventing them from growing. Meanwhile, according to **Fig. 6-11(b)**, escaped particles did not experience the RH near the wall, and the size of escaped particles did not change in the presence of the mucus layer. Thus, we observed the same mass fractions for similar particle diameters in both models.

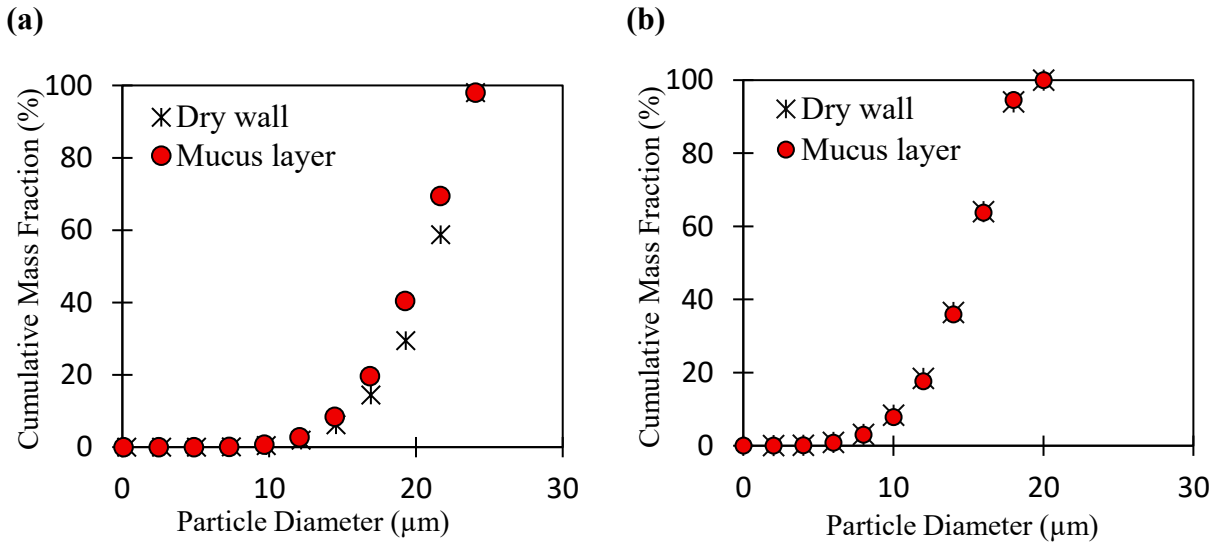

Fig. 6-11: Comparison of mass fraction of different sizes of **(a)** deposited particles on MT wall; and **(b)** escaped particles from the throat outlet for different wall conditions: dry MT wall and mucus-layered MT wall (plume temperature: -20°C and inlet air temperature: 22°C).

Fig. 6-12 compares particles' temperature and size within MT under different wall conditions. The temperature of particles in the dry wall model (**Fig. 6-12(a)**) was higher than that of others, while in the mucus-layered MT model (**Fig. 6-12(c)**), they exhibited the lowest temperature range. In the mucus-layered model, because the outer airway tissue layer was maintained at 37°C and thermal resistance across the wall thickness existed, the interaction temperature between the air and mucus layers was lower than the constant 37°C.

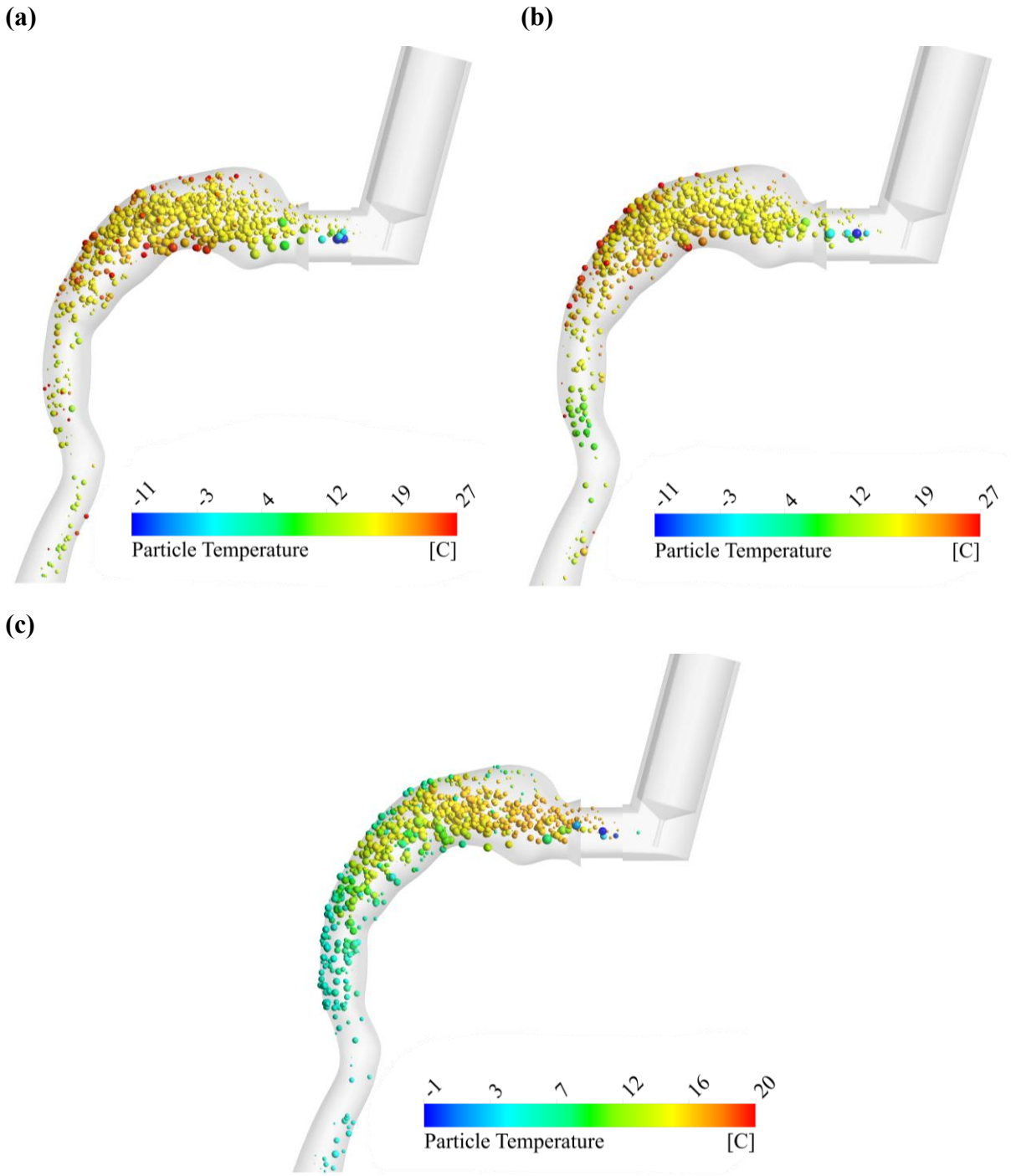

Fig. 6-12: Comparison of particle temperature within MT at 0.1s of injection for different wall conditions: **(a)** dry MT wall; **(b)** wet MT wall; and **(c)** mucus-layered MT wall (plume temperature: -20°C and inlet air temperature: 22°C).

On the other hand, in the wet and dry wall models, air interacted with the wall at a temperature of 37°C. Therefore, the particle temperature near the MT wall for the mucus-layered model was lower than that of the others. This figure confirms the result of **Fig. 6-11(a)**; the lower temperature of

particles in the proximity of the wall region could potentially reduce the evaporation rate, leading to larger particles in the mucus-layered model.

Fig. 6-13 depicts the relationship between the plume temperature, wall properties, and the MT particle depositions. This figure shows that our study's highest MT particle deposition was observed in condition C4, with a plume temperature of 10°C and the dry-wall model. On the other hand, the lowest MT deposition was observed in condition C1, with a plume temperature of -54°C and the mucus-layered model. Notably, the deposition fraction decreased under wet-wall conditions and further decreased in the presence of the mucus layer. The decrease in deposition fraction varied with different plume temperatures. For instance, the largest decrease was observed in the C4 condition, with a 11.05% reduction, while the smallest was observed in the C2 condition, with a 1.30% reduction. Since particles near the wall were observed to enlarge in the presence of a mucus layer (as shown in **Fig. 6-12(c)**), the deposition fraction was also expected to increase. However, the lower temperature near the wall could have influenced particle kinetic energy, causing them to follow the airflow through the MT airway and avoid deposition via impaction. Furthermore, the Stokes number calculated near the wall for the smaller particles was much less than 0.1 ($Stk << 0.1$), confirming that the impaction mechanism had a negligible impact (Finley, 2001).

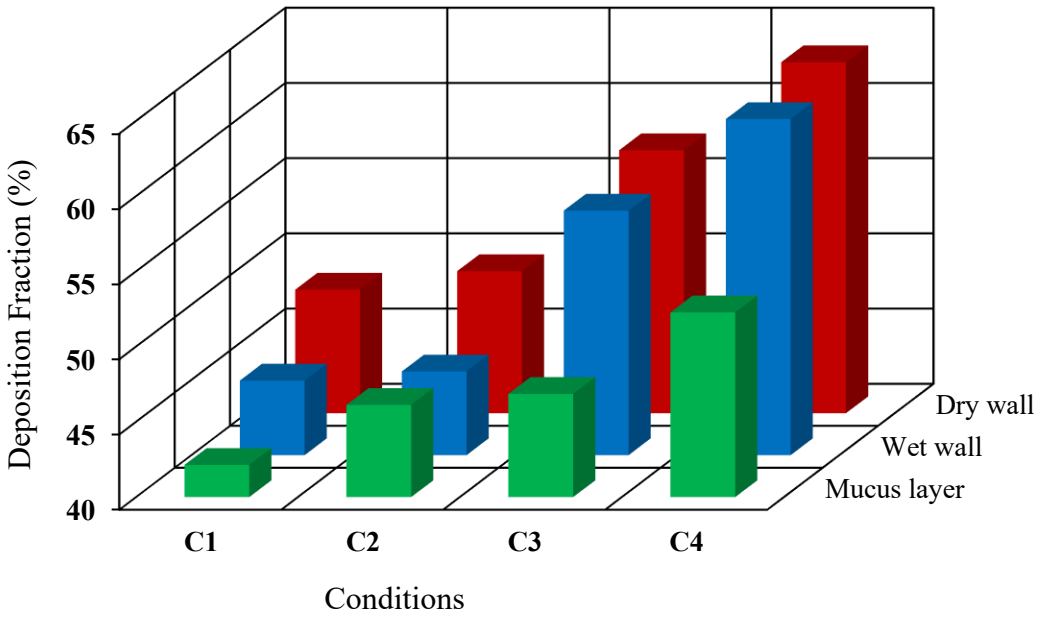

Fig. 6-13: Comparison of the effect of the different wall conditions (dry wall, wet wall, mucus layer) on deposition fraction on MT by considering different plume temperatures (C1: -54°C, C2: -20°C, C3: 0°C, and C4: 10°C, inlet air temperature: 22°C) (refer to **Table 6-1**).

6.3 Conclusions

In this study, we investigated the impact of plume temperature (generated by a pMDI), inlet airflow temperature, and the structure of the MT airway wall on particle dynamics and deposition patterns. Our analysis considered four distinct plume temperatures (-54°C, -20°C, 0°C, and 10°C) and three airflow temperatures (-15°C, 22°C, and 45°C), employing models of the pMDI and realistic MT geometry of the VCU medium-sized MT airway. The simulation using the LES-DPM model effectively captured particle transport and deposition within the airway geometry, along with the airflow. To simulate realistic thermal conditions near the airway wall, we incorporated an airway wall with a thickness of 0.51 mm, including an airway tissue layer of 0.5 mm and a 10 μm mucus layer, with water prperties, into our model.

Our findings revealed that increasing the plume temperature from -54°C to 10°C increased the average evaporation rate of emitted particles by 21% and reduced their size by 34%. Contrary to expectations, this size reduction did not result in a decrease in deposition on the MT and instead led to an increase of up to 18%.

The influence of airflow pattern, driven by different plume temperatures, was more pronounced on particle MT deposition than on particle size. Moreover, while colder plumes improve pMDI efficiency, the "cold Freon effect" may cause patient discomfort. Studies indicate that patients prefer warmer sprays from their inhalers. Our study demonstrates that by raising the plume temperature from -54°C to -20°C, patients can experience a 34°C warmer aerosol while only sacrificing 2.55% in device efficiency.

Conversely, higher air temperature increased upper airway temperature but slightly altered particle size. These changes did not significantly affect the deposition fraction in the airways, which remained less than 5%. Thus, these results demonstrated no concern regarding the impact of ambient air temperature on pMDI performance. We should note that this study did not consider the impact of the inlet air temperature on the pMDI canister, as discussed by Wilson et al. (1991).

The impact of MT wall properties and conditions on drug delivery shows that the mucus layer in the CFD model significantly affects moisture levels, particularly near the MT wall (approximately 62%), leading to particle growth near the wall due to hygroscopic growth. However, it also reduced deposition fractions by about 11% compared to the dry MT wall model. The lower temperature near the mucus layer reduced particles' kinetic energy, leading them to track the airflow and reducing deposition. In contrast, Narayanan et al. (2022) discovered that including the mucus layer increased the deposition fraction. This difference may be attributed to their study not accounting for the interaction between geometric complexity. The noticeable difference in the shape of the respiratory tract can significantly affect airflow patterns, particle movement, and where particles deposit. Due to the significant diversity in upper airway shapes among individuals, there is also a wide range of particle depositions. Additionally, the particle transport and deposition are significantly influenced by pMDI and specific injection features. In our study, we examined polydisperse particle sizes at a high injection velocity and a low plume temperature, yielding results different from theirs.

Incorporating a mucus layer into CFD modeling enhances the accuracy of representing the human airway, particularly when evaluating the effectiveness of inhaler devices, all without significantly increasing computational costs.

6.6 Limitations and Future Directions

- The mucus layer was modeled only as a thermal boundary condition, assuming a smooth, stationary surface. Its natural motion, thickness variation, and undulating structure were not included, which could influence near-wall flow patterns and local deposition.
- The model did not account for shear-driven mucus movement or potential coupling between airflow, droplet temperature, and mucus rheology. Such interactions could affect particle residence time and deposition mechanisms.
- A uniform wall temperature was assumed, whereas airway temperature varies spatially and depends on the breathing cycle, humidity, and individual physiology. Implementing more realistic temperature fields could alter plume cooling and evaporation behavior.
- The DPM evaporation model does not include an explicit Kelvin (curvature) correction for saturation pressure. Instead, droplet evaporation is governed by the temperature-dependent saturation vapor pressure of HFA, as defined in the material properties. This simplification may lead to underprediction of evaporation rates for fine pMDI droplets.

6.7 Nomenclature

Abbreviations

3D	three dimensional
AIT	Alberta idealized throat
ANSYS	analysis of systems
C	condition
CFD	computational fluid dynamics
CPU	central processing unit
DPM	discrete phase model
GB	gigabyte
GHz	gigahertz
GiB	gibibyte
HFA	hydrofluoroalkane
HPLC	high-performance liquid chromatography
LES	large Eddy simulation

MDI	metered-dose inhalers
MT	mouth-throat
NGI	next generation impactor
NSERC	natural sciences and engineering council of Canada
pMDIs	pressurized metered-dose inhalers
PSD	particle size distribution
RAM	random access memory
RDD	respiratory drug delivery
RH	relative humidity
S	stages of NGI
SD	standard deviation
RMSE	root mean squared error
SIMPLEC	semi-implicit method for pressure-linked equations-consistent
USP	United States Pharmacopeia

Notations

$\bar{\boldsymbol{u}}$	filtered velocity (m/s)
t	time
ρ	mixture density (kg/m^3)
$\bar{P}$	filtered pressure (Pa)
$\bar{\sigma}$	stress tensor (N/m^2)
$\bar{\tau}$	subgrid-scale stress (N/m^2)
$\boldsymbol{F}_i$	body force (N)
g	gravitational acceleration
μ	mixture dynamics viscosity (Pa.s)
μ_t	turbulent dynamics viscosity at sub-grid scales (Pa.s)
$\bar{S}$	rate-of-strain tensor (s^{-1})
Δ_f	filter size (m)
V	volume of the computational cell (m^3)
C_k	constant in Equation (6) (-)
C_ε	constant in Equation (7) (-)

k_{sgs}	dynamics kinetic energy (J)
σ_k	turbulent Prandtl number (-)
E	thermal energy (J)
k_{eff}	effective conductivity (W/m.K)
k_t	turbulent thermal conductivity (W/m.K)
T	temperature (K)
T_c	critical temperature (K)
h_s	species enthalpy (J)
$\bar{\tau}_{eff}$	effective shear stress (Pa)
$\vec{J}_s$	diffusion flux of species s (mol/m^2.s)
h	sensible enthalpy (J)
Y_s	species mass fraction (-)
$C_{p,s}$	species-specific heat (J/kg.K)
$D_{m,s}$	mass diffusion coefficients (m^2/s)
$D_{T,s}$	thermal diffusion coefficient (m^2/s)
S_s	rate of creation of species by addition from source (mol/m^3.s)
Sc_t	turbulent Schmidt number
$\boldsymbol{u}_p$	velocity of particle (m/s)
ρ_p	density of particle (kg/m^3)
d_p	diameter of particle (m)
m_p	mass of particle (kg)
C_D	drag coefficient (-)
Re	Reynolds number
Re_p	Reynolds number of particles (-)
Sh	Sherwood number (-)
Stk	Stokes number (-)
Q	fraction of the total mass (-)
$\bar{d}$	mean particle diameter (m)
C_p	particle heat capacity (J/kg.K)

A_p	particle surface area (m^2)
h_c	convective heat transfer (W/m^2K)
h_{fg}	latent heat (J/kg)
B_T	Spalding heat transfer number (-)
$\dot{q}_p$	heat transfer rate (W)
$\dot{m}_p$	particle evaporation rate (kg/s)
a	constant in **Table 6-3** (-)
b	constant in **Table 6-3** (-)
c	constant in **Table 6-3** (-)
d	constant in **Table 6-3** (-)
e	constant in **Table 6-3** (-)

6.8 References

Aghaei, Y., Sajadi, B., Ahmadi, G., 2023. The effect of the mucus layer and the inhaled air conditions on the droplets fate in the human nasal cavity: A numerical study. J. Aerosol Sci. 171, 106163. https://doi.org/10.1016/j.jaerosci.2023.106163

Ahookhosh, K., Saidi, M., Mohammadpourfard, M., Aminfar, H., Hamishehkar, H., Farnoud, A., Schmid, O., 2021. Flow structure and particle deposition analyses for optimization of a pressurized metered dose inhaler (pMDI) in a model of tracheobronchial airway. Eur. J. Pharm. Sci. 164, 105911. https://doi.org/10.1016/j.ejps.2021.105911

Ahookhosh, K., Yaqoubi, S., Mohammadpourfard, M., Hamishehkar, H., Aminfar, H., 2019. Experimental investigation of aerosol deposition through a realistic respiratory airway replica: An evaluation for MDI and DPI performance. Int. J. Pharm. 566, 157–172. https://doi.org/10.1016/j.ijpharm.2019.05.058

Alatrash, A., 2018. Experimental and Numerical Study of Inhaler Spray Characterization (Size Distributions and Velocity). PhD Thesis, Carlt. Univ. Ottawa. Carleton University, Ottawa, Ontario. https://doi.org/10.22215/etd/2018-12966

Alderliesten, M., 2013. Mean Particle Diameters. Part VII. The Rosin-Rammler Size Distribution: Physical and Mathematical Properties and Relationships to Moment-Ratio Defined Mean Particle Diameters. Part. Part. Syst. Charact. 30, 244–257.

https://doi.org/10.1002/ppsc.201200021

ANSYS, 2020. ANSYS FLUENT Theory Guide, 2020 R2. ed. ANSYS, Inc. and Ansys Europe, Ltd. are UL registered ISO 9001: 2015 companies.

Bhardwaj, S., Koullapis, P., Kassinos, S.C., Sznitman, J., 2022. Fate of inhaled aerosols under the influence of glottal motion in a realistic in silico human tracheobronchial tree model. Eur. J. Pharm. Sci. 173. https://doi.org/10.1016/j.ejps.2022.106172

Biswas, R., Hanania, N.A., Sabharwal, A., 2017. Factors determining in vitro lung deposition of albuterol aerosol delivered by ventolin metered-dose inhaler. J. Aerosol Med. Pulm. Drug Deliv. 30, 256–266. https://doi.org/10.1089/jamp.2015.1278

Borojeni, A.A.T., Gu, W., Asgharian, B., Price, O., Kuprat, A.P., Singh, R.K., Colby, S., Corley, R.A., Darquenne, C., 2023. In silico quantification of intersubject variability on aerosol deposition in the oral airway. Pharmaceutics 15, 160. https://doi.org/10.3390/pharmaceutics15010160

Borojeni, A.A.T., Noga, M.L., Vehring, R., Finlay, W.H., 2014. Measurements of total aerosol deposition in intrathoracic conducting airway replicas of children. J. Aerosol Sci. 73, 39–47. https://doi.org/10.1016/j.jaerosci.2014.03.005

Brambilla, G., Church, T., Lewis, D., Meakin, B., 2011. Plume temperature emitted from metered dose inhalers. Int. J. Pharm. 405, 9–15. https://doi.org/10.1016/j.ijpharm.2010.11.037

Bunnag, C., Fuangtong, R., Pothirat, C., Punyaratabandhu, P., 2007. A comparative study of patients' preferences and sensory perceptions of three forms of inhalers among Thai asthma and COPD patients. Asian Pacific J. Allergy Immunol. 25, 99–107.

Calmet, H., Inthavong, K., Eguzkitza, B., Lehmkuhl, O., Houzeaux, G., Vázquez, M., 2019. Nasal sprayed particle deposition in a human nasal cavity under different inhalation conditions. PLoS One 14, 1–27. https://doi.org/10.1371/journal.pone.0221330

Chan, T.L., Lippmann, M., 1980. Experimental measurements and empirical modelling of the regional deposition of inhaled particles in humans. Am. Ind. Hyg. Assoc. J. 41, 399–409. https://doi.org/10.1080/15298668091424942

Charalambidou, A.D., Micheletti, M., Ducci, A., 2023. Study of trailing vortices and impeller jet instabilities of a flat blade impeller in small-scale reactors. AIChE J. 69, 1–18. https://doi.org/10.1002/aic.17842

Chen, X., Feng, Y., Zhong, W., Kleinstreuer, C., 2017. Numerical investigation of the interaction, transport and deposition of multicomponent droplets in a simple mouth-throat model. J. Aerosol Sci. 105, 108–127. https://doi.org/10.1016/j.jaerosci.2016.12.001

Chen, X., Kleinstreuer, C., Zhong, W., Feng, Y., Zhou, X., 2018. Effects of thermal airflow and mucus-layer interaction on hygroscopic droplet deposition in a simple mouth–throat model. Aerosol Sci. Technol. 52, 900–912. https://doi.org/10.1080/02786826.2018.1476751

Chen, X., Zhou, X., Xia, X., Xie, X., Lu, P., Feng, Y., 2021. Modeling of the transport, hygroscopic growth, and deposition of multi-component droplets in a simplified airway with realistic thermal boundary conditions. J. Aerosol Sci. 151. https://doi.org/10.1016/j.jaerosci.2020.105626

Cheng, Y.S., 2003. Aerosol deposition in the extrathoracic region. Aerosol Sci. Technol. 37, 659–671. https://doi.org/10.1080/02786820300906

Cheng, Y.S., Fu, C.S., Yazzie, D., Zhou, Y., 2001. Respiratory Deposition Patterns of Salbutamol pMDI with CFC and HFA-134a Formulations in a Human Airway Replica 14, 255–266. https://doi.org/10.1089/08942680152484180

Cheng, Y.S., Zhou, Y., Chen, B.T., 1999. Particle deposition in a cast of human oral airways. Aerosol Sci. Technol. 31, 286–300. https://doi.org/10.1080/027868299304165

Cheng, Y.S., Zhou, Y., Su, W.C., 2015. Deposition of particles in human mouth-throat replicas and a USP induction port. J. Aerosol Med. Pulm. Drug Deliv. 28, 147–155. https://doi.org/10.1089/jamp.2013.1105

Crompton, G.K., 1982. Problems patients have using pressurized aerosol inhalers. Eur. J. Respir. Dis. Suppl. 119, 101–4.

Cui, X., Wu, W., Gutheil, E., 2018. Numerical study of the airflow structures in an idealized mouth-throat under light and heavy breathing intensities using large eddy simulation. Respir. Physiol. Neurobiol. 248, 1–9. https://doi.org/10.1016/j.resp.2017.11.001

Cui, X.G., Gutheil, E., 2011. Large eddy simulation of the unsteady flow-field in an idealized human mouth-throat configuration. J. Biomech. 44, 2768–2774. https://doi.org/10.1016/j.jbiomech.2011.08.019

Dastoorian, F., Pakzad, L., Kozinski, J., Behzadfar, E., 2022. A CFD Investigation on the Aerosol Drug Delivery in the Mouth–Throat Airway Using a Pressurized Metered-Dose Inhaler Device. Processes 10, 1230. https://doi.org/10.3390/pr10071230

Delvadia, R.R., Longest, P.W., Byron, P.R., 2012. In Vitro Tests for Aerosol Deposition. I: Scaling a Physical Model of the Upper Airways to Predict Drug Deposition Variation in Normal Humans. J. Aerosol Med. Pulm. Drug Deliv. 25, 32–40. https://doi.org/10.1089/jamp.2011.0905

Delvadia, R.R., Wei, X., Longest, P.W., Venitz, J., Byron, P.R., 2016. In Vitro Tests for Aerosol Deposition. IV: Simulating Variations in Human Breath Profiles for Realistic DPI Testing. J. Aerosol Med. Pulm. Drug Deliv. 29, 196–206. https://doi.org/10.1089/jamp.2015.1215

Ding, L., Tang, S., Wyatt, T.A., Knoell, D.L., Oupický, D., 2021. Pulmonary siRNA delivery for lung disease : Review of recent progress and challenges. J. Control. Release 330, 977–991. https://doi.org/10.1016/j.jconrel.2020.11.005

Duke, D.J., Nguyen, D.T., Dos Reis, L.G., Silva, D.M., Neild, A., Edgington-Mitchell, D., Young, P.M., Honnery, D.R., 2021. Increasing the fine particle fraction of pressurised metered dose inhaler solutions with novel actuator shapes. Int. J. Pharm. 597, 120341. https://doi.org/10.1016/j.ijpharm.2021.120341

Duke, D.J., Scott, H.N., Kusangaya, A.J., Kastengren, A.L., Matusik, K., Young, P., Lewis, D., Honnery, D., 2019. Drug distribution transients in solution and suspension-based pressurised metered dose inhaler sprays. Int. J. Pharm. 566, 463–475. https://doi.org/10.1016/j.ijpharm.2019.05.067

Eisner, A.D., Graham, R.C., Martonen, T.B., 1990. Coupled mass and energy transport phenomena in aerosol/vapor-laden gases-I. Theory of the hygroscopic aerosol effects on temperature and relative humidity patterns of inspired air. J. Aerosol Sci. 21, 833–848. https://doi.org/10.1016/0021-8502(90)90156-R

Escudié, R., Liné, A., 2003. Experimental analysis of hydrodynamics in a radially agitated tank. AIChE J. 49, 585–603. https://doi.org/10.1002/aic.690490306

Feng, Y., Zhao, J., Hayati, H., Sperry, T., Yi, H., 2021a. Tutorial : Understanding the transport, deposition, and translocation of particles in human respiratory systems using Computational Fluid-Particle Dynamics and Physiologically Based Toxicokinetic models. J. Aerosol Sci. 151, 105672. https://doi.org/10.1016/j.jaerosci.2020.105672

Feng, Y., Zhao, J., Hayati, H., Sperry, T., Yi, H., 2021b. Tutorial: Understanding the transport, deposition, and translocation of particles in human respiratory systems using Computational Fluid-Particle Dynamics and Physiologically Based Toxicokinetic models. J. Aerosol Sci. 151, 105672. https://doi.org/10.1016/j.jaerosci.2020.105672

Ferron, G.A., Kreyling, W.G., Haider, B., 1988. Inhalation of salt aerosol particles—II. growth and deposition in the human respiratory tract. J. Aerosol Sci. 19, 611–631. https://doi.org/https://doi.org/10.1016/0021-8502(88)90213-3

Ferron, G.A., Oberdörster, G., Henneberg, R., 1989. Estimation of the deposition of aerosolized drugs in the human respiratory tract due to hygroscopic growth. J. Aerosol Med. Depos. Clear. Eff. Lung 2, 271–284. https://doi.org/10.1089/jam.1989.2.271

Finlay, W.H., 2001. The Mechanics of Inhaled Pharmaceutical Aerosols: An Introduction.

Finlay, W.H., Stapleton, K.W., 1995. The effect on regional lung deposition of coupled heat and mass transfer between hygroscopic droplets and their surrounding phase. J. Aerosol Sci. 26, 655–670. https://doi.org/10.1016/0021-8502(94)00132-I

Golshahi, L., Finlay, W.H., 2012. An idealized child throat that mimics average pediatric oropharyngeal deposition. Aerosol Sci. Technol. 46. https://doi.org/10.1080/02786826.2012.667170

Golshahi, L., Noga, M.L., Finlay, W.H., 2012. Deposition of inhaled micrometer-sized particles in oropharyngeal airway replicas of children at constant flow rates. J. Aerosol Sci. 49, 21–31. https://doi.org/10.1016/j.jaerosci.2012.03.001

Golshahi, L., Noga, M.L., Vehring, R., Finlay, W.H., 2013a. An in vitro study on the deposition of micrometer-sized particles in the extrathoracic airways of adults during tidal oral

breathing. Ann. Biomed. Eng. 41, 979–989. https://doi.org/10.1007/s10439-013-0747-0

Golshahi, L., Vehring, R., Noga, M.L., Finlay, W.H., 2013b. In vitro deposition of micrometer-sized particles in the extrathoracic airways of children during tidal oral breathing. J. Aerosol Sci. 57, 14–21. https://doi.org/10.1016/j.jaerosci.2012.10.006

Gupta, M.C., Khanna, J., Chaudhry, D., 2019. Patients' sensory perception and satisfaction with use of metered dose inhalers and dry powder inhalers in moderate persistent asthma. Int. J. Basic Clin. Pharmacol. 8, 1970. https://doi.org/10.18203/2319-2003.ijbcp20193609

Haddrell, A.E., Davies, J.F., Miles, R.E.H., Reid, J.P., Dailey, L.A., Murnane, D., 2014. Dynamics of aerosol size during inhalation: Hygroscopic growth of commercial nebulizer formulations. Int. J. Pharm. 463, 50–61. https://doi.org/10.1016/j.ijpharm.2013.12.048

Hamishehkar, H., Rahimpour, Y., Javadzadeh, Y., 2012. The Role of Carrier in Dry Powder Inhaler, in: Recent Advances in Novel Drug Carrier Systems. InTech, pp. 275–281. https://doi.org/10.5772/51209

He, C., Ahmadi, G., 1998. Particle deposition with thermophoresis in laminar and turbulent duct flows. Aerosol Sci. Technol. 29, 525–546. https://doi.org/10.1080/02786829808965588

Hofmann, W., Martonen, T.B., Graham, R.C., 1989. Predicted Deposition of Nonhygroscopic Aerosols in the Human Lung as a Function of Subject Age. J. Aerosol Med. Depos. Clear. Eff. Lung 2, 49–68. https://doi.org/10.1089/jam.1989.2.49

Huang, F., Zhu, Q., Zhou, X., Gou, D., Yu, J., Li, R., Tong, Z., Yang, R., 2021. Role of CFD based in silico modelling in establishing an in vitro-in vivo correlation of aerosol deposition in the respiratory tract. Adv. Drug Deliv. Rev. https://doi.org/10.1016/j.addr.2020.09.007

ICRP, 1994. Human respiratory tract model for radiological protection. A report of a Task Group of the International Commission on Radiological Protection. Ann. ICRP 24, 1–482.

Iorgulescu, G., 2009. Saliva between normal and pathological. Important factors in determining systemic and oral health. J. Med. Life 2, 303–307.

Jahed, M., Kozinski, J., Pakzad, L., 2023. The impact of actuator nozzle and surroundings condition on drug delivery using pressurized-metered dose inhalers. Biomech. Model.

Mechanobiol. 22, 2117–2133. https://doi.org/10.1007/s10237-023-01754-x

Kadota, K., Matsumoto, K., Uchiyama, H., Tobita, S., Maeda, M., Maki, D., Kinehara, Y., Tachibana, I., Sosnowski, T.R., Tozuka, Y., 2022. In silico evaluation of particle transport and deposition in the airways of individual patients with chronic obstructive pulmonary disease. Eur. J. Pharm. Biopharm. 174, 10–19. https://doi.org/10.1016/j.ejpb.2022.03.010

Kamm, R.D., 1999. Airway wall mechanics. Annu. Rev. Biomed. Eng. 1, 47–72. https://doi.org/10.1146/annurev.bioeng.1.1.47

Kaviratna, A., Tian, G., Liu, X., Delvadia, R., Lee, S., Guo, C., 2019. Evaluation of bio-relevant mouth-throat models for characterization of metered dose inhalers. AAPS PharmSciTech 20, 130. https://doi.org/10.1208/s12249-019-1339-6

Ke, W.R., Wang, W.J., Lin, T.H., Wu, C.L., Huang, S.H., Wu, H.D., Chen, C.C., 2020. In vitro evaluation of aerosol performance and delivery efficiency during mechanical ventilation between soft mist inhaler and pressurized metered-dose inhaler. Respir. Care 65, 1001–1010. https://doi.org/10.4187/respcare.06993

Kim, W.W., Menon, S., 1997. Application of the localized dynamic subgrid-scale model to turbulent wall-bounded flows. 35th Aerosp. Sci. Meet. Exhib. 1–12. https://doi.org/10.2514/6.1997-210

Kleinstreuer, C., Shi, H., Zhang, Z., 2007. Computational Analyses of a Pressurized Metered Dose Inhaler and a New Drug–Aerosol Targeting Methodology. J. Aerosol Med. 20, 294–309. https://doi.org/10.1089/jam.2006.0617

Koullapis, P.G., Hofemeier, P., Sznitman, J., Kassinos, S.C., 2018. An efficient computational fluid-particle dynamics method to predict deposition in a simplified approximation of the deep lung. Eur. J. Pharm. Sci. 113, 132–144. https://doi.org/10.1016/j.ejps.2017.09.016

Lee, B.U., Sub Byun, D., Bae, G.N., Lee, J.H., 2006. Thermophoretic deposition of ultrafine particles in a turbulent pipe flow: Simulation of ultrafine particle behaviour in an automobile exhaust pipe. J. Aerosol Sci. 37, 1788–1796. https://doi.org/10.1016/j.jaerosci.2006.07.006

Lee, C.Y., Cant, S., 2017. Assessment of LES subgrid-scale models and investigation of

hydrodynamic behaviour for an axisymmetrical bluff body flow. Flow, Turbul. Combust. 98, 155–176. https://doi.org/10.1007/s10494-016-9751-4

Lim, S.H., Park, S., Lee, C.C., Ho, P.C.L., Kwok, P.C.L., Kang, L., 2021. A 3D printed human upper respiratory tract model for particulate deposition profiling. Int. J. Pharm. 597. https://doi.org/10.1016/j.ijpharm.2021.120307

Longest, P.W., Hindle, M., 2010. CFD simulations of enhanced condensational growth (ECG) applied to respiratory drug delivery with comparisons to in vitro data. J. Aerosol Sci. 41, 805–820. https://doi.org/10.1016/j.jaerosci.2010.04.006

Longest, P.W., Hindle, M., 2009. Evaluation of the Respimat soft mist inhaler using a concurrent cfd and in vitro approach. J. Aerosol Med. Pulm. Drug Deliv. 22, 99–112. https://doi.org/10.1089/jamp.2008.0708

Longest, P.W., Hindle, M., Das Choudhuri, S., 2009. Effects of Generation Time on Spray Aerosol Transport and Deposition in Models of the Mouth-Throat Geometry. J. Aerosol Med. Pulm. Drug Deliv. 22, 67–83. https://doi.org/10.1089/jamp.2008.0692

Longest, P.W., Hindle, M., Das Choudhuri, S., Xi, J., 2008. Comparison of ambient and spray aerosol deposition in a standard induction port and more realistic mouth-throat geometry. J. Aerosol Sci. 39, 572–591. https://doi.org/10.1016/j.jaerosci.2008.03.008

Longest, P.W., Tian, G., Delvadia, R., Hindle, M., 2012. Development of a stochastic individual path (SIP) model for predicting the deposition of pharmaceutical aerosols: Effects of turbulence, polydisperse aerosol size, and evaluation of multiple lung lobes. Aerosol Sci. Technol. 46, 1271–1285. https://doi.org/10.1080/02786826.2012.708799

Martonen, T.B., 1982. Analytical model of hygroscopic particle behavior in human airways. Bull. Math. Biol. 44, 425–442. https://doi.org/10.1007/BF02462290

McCabe, J.C., Koppenhagen, F., Blair, J., Zeng, X.-M., 2012. ProAir ® HFA Delivers Warmer, Lower-Impact, Longer-Duration Plumes Containing Higher Fine Particle Dose Than Ventolin ® HFA. J. Aerosol Med. Pulm. Drug Deliv. 25, 104–109. https://doi.org/10.1089/jamp.2011.0891

McKiernan, A.P., 2019. Inhaler spray investigation using high-speed phase-contrast X-Ray and

schlieren imaging. Pharm. Res. 36. https://doi.org/10.1007/s11095-019-2657-9

Menon, S., Yeung, P.K., Kim, W.W., 1994. Effect of subgrid models on the computed interscale energy transfer in isotropic turbulence. AIAA Fluid Dyn. Conf. 1994 25. https://doi.org/10.2514/6.1994-2387

Millage, K.K., Bergman, J., Asgharian, B., McClellan, G., 2010. A review of inhalability fraction models: Discussion and recommendations. Inhal. Toxicol. 22, 151–159. https://doi.org/10.3109/08958370903025973

Morrow, P.E., 1986. Factors determining hygroscopic aerosol deposition in airways. Physiol. Rev. 66, 330–376. https://doi.org/10.1152/physrev.1986.66.2.330

Morsi, S.A., Alexander, A.J., 1972. An investigation of particle trajectories in two-phase flow systems. J. Fluid Mech. 55, 193–208. https://doi.org/10.1017/S0022112072001806

Narayanan, J.K., Lin, J., Feng, Y., Cui, X., 2022. Numerical study on the impact of mucus layer and inlet air-temperatures on the particle deposition in a highly idealized mouth-throat model using LES. Powder Technol. 395, 455–475. https://doi.org/10.1016/j.powtec.2021.09.073

Newman, S., 2015. RDD Online Respiratory Drug Delivery, Metered Dose Inhalers [WWW Document]. 2015-08-18. URL http://www.rddonline.com/education/online_training/MDIs/player.html

Ogrodnik, N., Azzi, V., Sprigge, E., Fiset, S., Matida, E., 2016. Nonuniform deposition of pressurized metered-dose aerosol in spacer devices. J. Aerosol Med. Pulm. Drug Deliv. 29, 490–500. https://doi.org/10.1089/jamp.2015.1257

Pal, R., Sarkar, S., Mukhopadhyay, A., 2021. Influence of ambient conditions on evaporation and transport of respiratory droplets in indoor environment. Int. Commun. Heat Mass Transf. 129, 105750. https://doi.org/10.1016/j.icheatmasstransfer.2021.105750

Rahman, M.M., Zhao, M., Islam, M.S., Dong, K., Saha, S.C., 2021. Aging effects on airflow distribution and micron-particle transport and deposition in a human lung using CFD-DPM approach. Adv. Powder Technol. 32, 3506–3516. https://doi.org/10.1016/j.apt.2021.08.003

Rajaraman, P.K., Choi, J., Hoffman, E.A., O'Shaughnessy, P.T., Choi, S., Delvadia, R., Babiskin, A., Walenga, R., Lin, C.L., 2020. Transport and deposition of hygroscopic particles in asthmatic subjects with and without airway narrowing. J. Aerosol Sci. 146, 105581. https://doi.org/10.1016/j.jaerosci.2020.105581

Ranade, V. V., Gupta, D.F., 2014. Computational Modeling of Pulverized Coal Fired Boilers, Phil. Mag. CRC Press. https://doi.org/10.1201/b17752

Roche, N., Dekhuijzen, P.N.R., 2016. The Evolution of Pressurized Metered-Dose Inhalers from Early to Modern Devices. J. Aerosol Med. Pulm. Drug Deliv. 29, 311–327. https://doi.org/10.1089/jamp.2015.1232

Ruzycki, C.A., Martin, A.R., Finlay, W.H., 2019. An Exploration of Factors Affecting In Vitro Deposition of Pharmaceutical Aerosols in the Alberta Idealized Throat. J. Aerosol Med. Pulm. Drug Deliv. 32, 405–417. https://doi.org/10.1089/jamp.2019.1531

Sadeghi, T., Pakzad, L., Fatehi, P., 2023. Evaluation of soft mist inhaler aerosol velocity, size, and deposition inside the mouth - A computational fluid dynamics study. J. Biomech. Eng. 145. https://doi.org/10.1115/1.4056967

Sandberg, T., Blom, H., Caldwell, K.D., 2009. Potential use of mucins as biomaterial coatings. I. Fractionation, characterization, and model adsorption of bovine, porcine, and human mucins. J. Biomed. Mater. Res. - Part A 91, 762–772. https://doi.org/10.1002/jbm.a.32266

Schlesinger, R.B., Bohning, D.E., Chan, T.L., Lippmann, M., 1977. Particle deposition in a hollow cast of the human tracheobronchial tree. J. Aerosol Sci. 8, 429–445. https://doi.org/10.1016/0021-8502(77)90036-2

Shekunov, B.Y., Chattopadhyay, P., Tong, H.H.Y., Chow, A.H.L., 2007. Particle size analysis in pharmaceutics: Principles, methods and applications. Pharm. Res. 24, 203–227. https://doi.org/10.1007/s11095-006-9146-7

Sheth, P., Grimes, M.R., Stein, S.W., Myrdal, P.B., 2017. Impact of droplet evaporation rate on resulting in vitro performance parameters of pressurized metered dose inhalers. Int. J. Pharm. 528, 360–371. https://doi.org/10.1016/j.ijpharm.2017.06.014

Smyth, H., Brace, G., Barbour, T., Gallion, J., Grove, J., Hickey, A.J., 2006. Spray pattern

analysis for metered dose inhalers: Effect of actuator design. Pharm. Res. 23, 1591–1596. https://doi.org/10.1007/S11095-006-0280-Z

Sou, T., Bergström, C.A.S., 2021. Contemporary formulation development for inhaled pharmaceuticals. J. Pharm. Sci. 110, 66–86. https://doi.org/10.1016/j.xphs.2020.09.006

Spasov, G.H., Rossi, R., Vanossi, A., Cottini, C., Benassi, A., 2022. A critical analysis of the CFD-DEM simulation of pharmaceutical aerosols deposition in extra-thoracic airways. Int. J. Pharm. 629, 122331. https://doi.org/10.1016/j.ijpharm.2022.122331

Speight, J.G., 2020. The properties of water, in: Speight, J.G. (Ed.), Natural Water Remediation. Elsevier, pp. 53–89. https://doi.org/10.1016/B978-0-12-803810-9.00002-4

Stahlhofen, W., Rudolf, G., James, A.C., 1989. Intercomparison of Experimental Regional Aerosol Deposition Data. J. Aerosol Med. Depos. Clear. Eff. Lung 2, 285–308. https://doi.org/10.1089/jam.1989.2.285

Stapleton, K.W., Guentsch, E., Hoskinson, M.K., Finlay, W.H., 2000. On the suitability of k-ε turbulence modeling for aerosol deposition in the mouth and throat: A comparison with experiment. J. Aerosol Sci. 31, 739–749. https://doi.org/10.1016/S0021-8502(99)00547-9

Szabová, J., Mišík, O., Fučík, J., Mrázová, K., Mravcová, L., Elcner, J., Lízal, F., Krzyžánek, V., Mravec, F., 2023. Liposomal form of erlotinib for local inhalation administration and efficiency of its transport to the lungs. Int. J. Pharm. 634. https://doi.org/10.1016/j.ijpharm.2023.122695

Talaat, M., Si, X., Liu, X., Xi, J., 2022a. Count- and mass-based dosimetry of MDI spray droplets with polydisperse and monodisperse size distributions. Int. J. Pharm. 623, 121920. https://doi.org/10.1016/j.ijpharm.2022.121920

Talaat, M., Si, X., Xi, J., 2022b. Effect of MDI actuation timing on inhalation dosimetry in a human respiratory tract model. Pharmaceuticals 15, 61. https://doi.org/10.3390/ph15010061

Ting, D., 2022. Natural convection, in: Ting, D. (Ed.), Thermofluids. Elsevier, pp. 295–319. https://doi.org/10.1016/B978-0-323-90626-5.00015-X

Williams, J., Kolehmainen, J., Cunningham, S., Ozel, A., Wolfram, U., 2022. Effect of patient

inhalation profile and airway structure on drug deposition in image-based models with particle-particle interactions. Int. J. Pharm. 612, 121321. https://doi.org/10.1016/j.ijpharm.2021.121321

Wilson, A.F., Mukai, D.S., Ahdout, J.J., 1991. Effect of Canister Temperature on Performance of Metered-Dose Inhalers. Am. Rev. Respir. Dis. 143, 1034–1037. https://doi.org/10.1164/ajrccm/143.5_Pt_1.1034

Winkeljann, B., Bauer, M.G., Marczynski, M., Rauh, T., Sieber, S.A., Lieleg, O., 2020. Covalent Mucin Coatings Form Stable Anti-Biofouling Layers on a Broad Range of Medical Polymer Materials. Adv. Mater. Interfaces 7. https://doi.org/10.1002/admi.201902069

Wu, C., Yan, W., Chen, R., Liu, Y., Li, G., 2022. Numerical study on targeted delivery of magnetic drug particles in realistic human lung. Powder Technol. 397, 116984. https://doi.org/10.1016/j.powtec.2021.11.028

Xi, J., Longest, P.W., 2008. Effects of oral airway geometry characteristics on the diffusional deposition of inhaled nanoparticles. J. Biomech. Eng. 130, 13–17. https://doi.org/10.1115/1.2838039

Xi, J., Yang, T., 2019. Variability in oropharyngeal airflow and aerosol deposition due to changing tongue positions. J. Drug Deliv. Sci. Technol. 49, 674–682. https://doi.org/10.1016/j.jddst.2019.01.006

Xi, J., Yuan, J.E., Yang, M., Si, X., Zhou, Y., Cheng, Y.S., 2016. Parametric study on mouth–throat geometrical factors on deposition of orally inhaled aerosols. J. Aerosol Sci. 99, 94–106. https://doi.org/10.1016/j.jaerosci.2016.01.014

Xu, C., Zheng, X., Shen, S., 2021. A numerical study of the effects of ambient temperature and humidity on the particle growth and deposition in the human airway. Environ. Res. 200, 111751. https://doi.org/10.1016/j.envres.2021.111751

Xu, X.Y., Ni, S.J., Fu, M., Zheng, X., Luo, N., Weng, W.G., 2017. Numerical investigation of airflow, heat transfer and particle deposition for oral breathing in a realistic human upper airway model. J. Therm. Biol. 70, 53–63. https://doi.org/10.1016/j.jtherbio.2017.05.003

Yang, H., Wang, Y., Chen, X., Sun, B., Tao, F., Xie, X., Zhang, Y., 2023. The effects of

temperature and humidity on the deposition of nebulized droplet in an idealized mouth-throat model. Flow Meas. Instrum. 91, 102359. https://doi.org/10.1016/j.flowmeasinst.2023.102359

Yang, M.Y., Ruzycki, C., Verschuer, J., Katsifis, A., Eberl, S., Wong, K., Golshahi, L., Brannan, J.D., Finlay, W.H., Chan, H.K., 2017. Examining the ability of empirical correlations to predict subject specific in vivo extrathoracic aerosol deposition during tidal breathing. Aerosol Sci. Technol. 51, 363–376. https://doi.org/10.1080/02786826.2016.1262532

Zephex®, 2019. HFA 134a Medical Propellant. Koura Zephex, Cheshire.

Zhang, W., Xiang, Y., Lu, C., Ou, C., Deng, Q., 2020. Numerical modeling of particle deposition in the conducting airways of asthmatic children. Med. Eng. Phys. 76, 40–46. https://doi.org/10.1016/j.medengphy.2019.10.014

Zhang, Z., Kim, C.S., Kleinstreuer, C., 2006. Water vapor transport and its effects on the deposition of hygroscopic droplets in a human upper airway model. Aerosol Sci. Technol. 40, 1–16. https://doi.org/10.1080/02786820500461154

Zhou, Y., Sun, J., Cheng, Y.S., 2011. Comparison of deposition in the USP and physical mouth-throat models with solid and liquid particles. J. Aerosol Med. Pulm. Drug Deliv. 24, 277–284. https://doi.org/10.1089/jamp.2011.0882

Chapter 7- Experimental and Numerical Investigation of Drug Delivery in Patient-specific Male and Female Airways: Role of Airway Wall Motion, Breathing Patterns, and Mucus Layer

7.1 Introduction

The human respiratory tract consists of three main segments: the upper airways, known as the extrathoracic (ET) region; the conducting airways within the lungs, referred to as the tracheobronchial region; and the alveolar region. The upper airway prevents particles from entering the lungs via inertial impaction. While this role safeguards our respiratory system, it can also restrict the effectiveness of orally inhaled medications in reaching the deep regions of the lungs (Newman, 2017). Individual differences in airway shape and size can be influenced by factors such as age, gender, genetics, and health conditions (Das et al., 2018; Menache and Grahamt, 1997; Newman, 2017). For instance, the airways of pediatric patients differ significantly from those in adults (Di Cicco et al., 2021; Kolewe et al., 2023), and studies show that females typically have smaller central conducting airways than males (Dominelli and Molgat-Seon, 2022). These differences pose challenges in understanding the details of drug deposition within the airway.

In 1998, Kim & Hu (1998) conducted a study to measure regional lung deposition in healthy adult males and females using a serial bolus aerosol delivery technique. The study compared results based on different monodisperse particle sizes and varying breathing patterns. The results revealed noticeable differences in deposition distribution within the lungs between males and females, with females showing greater deposition in the proximal airways compared to males. A study by Pritchard et al. (1986) suggests that the observed differences in regional particle deposition are influenced by particles that mainly deposit through impaction. Specifically, the smaller size of a female's upper airway compared to that of males leads to stronger turbulent flow into the trachea, potentially enhancing particle deposition in the trachea and downstream airways (Kim and Hu, 1998; Pritchard et al., 1986; Sturm, 2016). Although these studies revealed anatomical differences, they primarily focused on volumetric depth compartments rather than reconstructing airway geometries as computational models.

In a study conducted by Walenga & Longest (2016), mouth-throat (MT) and tracheobronchial models were used to replicate healthy and narrowed airways, reflecting a 30% reduction in airway

diameter associated with asthma. The study examined the delivery of medication through metered-dose inhalers (MDIs) and dry powder inhalers (DPIs) using computational fluid dynamics (CFD) simulations. Their results demonstrated a significant decline in drug deposition within the lower tracheobronchial airways in narrowed airway models, with reductions of 21% for MDI and 25% for DPI. Additionally, Zhang et al. (2002) investigated particle deposition in the conducting airways of 4-year-old children with varying levels of asthma severity. The study focused on evaluating conditions with 30% and 60% reductions in airway diameter. Their numerical findings showed that in healthy children, primarily larger particles (greater than 6 μm) were deposited in the upper airways (Generations G3–G6), whereas in asthmatic children, even smaller particles accumulated in this region. Notably, in cases of severe airway constriction (60%), all particles larger than 4 μm were found to be deposited in the upper airways.

Moreover, the lungs undergo significant deformation even during normal breathing, necessitating that the airways remain highly flexible and capable of substantial changes in length and circumference (Kamm, 1999). Magnetic resonance imaging (MRI) analysis has revealed that the airway expansion and contraction follow a sinusoidal pattern (Bates et al., 2019; Gunatilaka et al., 2020; Sul et al., 2019). This continuous dynamic deformation of airways presents challenges in studying airflow dynamics and particle transport. In an experimental study by Zhao et al. (2020), particle image velocimetry (PIV) was employed to investigate the impact of upper airway wall deformation on airflow. The results revealed that lateral airway deformation, particularly at the level of the soft palate, significantly altered flow patterns throughout the breathing cycle, an effect absent in static airway models.

The CFD modelling conducted by Bates et al. (2019) showed that inspiratory flow resistance decreased by 10.7%, while expiratory flow resistance increased by 19.8% in dynamic versus static airway walls. Similarly, Gunatilaka et al. (2020) investigated airway resistance and pressure drop under static wall conditions across various respiratory phases, end-expiration, peak inspiration, end-inspiration, and peak expiration, along with assessments of dynamic airway walls. Their simulations indicated that airway resistance and pressure drop could vary by up to 200% and 94%, respectively. These variations significantly impact the transport and deposition of drugs, ultimately influencing the effectiveness of inhalers.

Studies on glottis motion during breathing have shown that its size ranges from 1.44 to 2.31 cm^2 in males and from 1.37 to 2.07 cm^2 in females (Rubinstein et al., 1989). Recent studies by Zhao et al. (2020) and Bhardwaj et al. (2022) have highlighted that assuming a static glottis leads to inaccurate predictions of inhaled therapeutic particle delivery, particularly during significant glottal deformations. Gou et al. (2024) investigated how static deformation of the upper airway affects drug delivery from DPIs to the lungs and drug deposition on airway walls. Their findings revealed that as deformation increased, the pharyngeal circulation zone expanded, potentially influencing drug transport. Meanwhile, Li et al. (2023) studied the effects of deforming walls on particle deposition in the pulmonary acinar region. They observed a reduction in deposition fractions across all particle sizes, except for 5 μm particles, which were fully deposited. The extent of the reduction in deposition fraction varied with particle size, reaching up to 65.43%.

The respiratory tract conditions the inhaled air by warming it to body temperature, humidifying it, and filtering out harmful particles (Haut et al., 2021; Kamm, 1999). This physiological air conditioning protects the alveolar membrane from thermal damage and helps maintain adequate moisture levels. This process is facilitated by a thin liquid layer comprising a mucus layer on top and an aqueous layer beneath, with thicknesses ranging from over 5 μm in the trachea to less than 0.3 μm in the alveoli (Fröhlich et al., 2016; Kamm, 1999). Accurate modeling of the airway wall structure and its mechanical properties is essential for simulating the transport and deposition of drug particles. Previous studies have mathematically analyzed the impact of hygroscopic particle characteristics within the human airways (Eisner et al., 1990; Ferron et al., 1989, 1988; Finlay and Stapleton, 1995; Haddrell et al., 2014; Martonen, 1982; Morrow, 1986).

During inhalation, drug particles enter the mouth with a relative humidity (RH) of about 99.8%, which promotes hygroscopic growth. This growth is influenced by factors such as particle quantity, composition, and initial size. Using a simplified MT model, Chen et al. (2021) incorporated a mucus layer into their CFD models to examine the effects of hygroscopic particles, as well as heat and mass transfer, on deposition within the mucus-tissue layer. Their numerical results indicated that these factors could alter the deposition efficiency by up to 10%. In a previous study, Jahed et al. (2023) investigated the impact of interactions between thermally influenced mucus and air on hygroscopic particle deposition in a more anatomically realistic MT model. CFD results showed that the presence of a mucus layer reduced particle deposition fractions by up to approximately 11%, depending on airflow and aerosol plume temperature, compared to a model without

mucus. Conversely, Aghaei et al. (Aghaei et al., 2023) demonstrated that while the nasal mucus layer significantly reduced droplet evaporation, its effect on deposition fraction was minimal.

The literature suggests that the accuracy of CFD simulations for drug delivery and the enhancement of inhaler efficiency depend on both computational precision and the physiological relevance of the respiratory system. While many previous studies have focused primarily on aerosol deposition within the airway, they often overlook the dynamic behavior of the airway and the influence of thermal interactions and mass transfer at the airway wall.

Through experimental and numerical approaches, this study examines the influence of gender-related airway anatomical differences, breathing patterns (steady and transient), airway wall deformation, and the presence of a mucus layer on the transport and regional deposition of drug aerosols from a pressurized metered-dose inhaler (pMDI). To achieve this, we developed two anatomically realistic airway models based on computed tomography (CT) scans of patients with chronic obstructive pulmonary disease (COPD), one male and one female. In line with the findings of Xi and Longest (2008), who conducted a comparative study on micro-aerosol transport in realistic versus simplified oral airway geometries—showing that simplified models fail to capture critical flow features and particle-wall interactions—the present study employs patient-specific geometry to ensure a more accurate representation of airflow dynamics and drug deposition behavior. These models include the trachea and tracheobronchial tree up to the fourth generation (G0–G4) and were integrated with the medium-sized MT model from Virginia Commonwealth University (VCU). The fabricated models, created using rapid prototyping, were used for *in-vitro* experiments to validate computational findings.

Our experiments were conducted with static airway wall features and a constant inhalation flow rate of 30 L/min due to experimental constraints. In our CFD model, validated against *in-vitro* results, we employed the large-eddy simulation (LES) turbulence model to capture transient airflow behaviour and the Lagrangian discrete-phase model (DPM) to track particle motion. To simulate the mucus layer on the airway walls, along with realistic thermal conditions and evaporation effects, we integrated the CFD-DPM framework with the Eulerian wall film (EWF) model (Anzai et al., 2022). Additionally, we developed a user-defined function (UDF) to model the transient sinusoidal deformation of the entire wall, enabling a more physiologically relevant representation of airway dynamics.

7.2 Experimental Setup and Methodology

Fig. 7-1(a) illustrates the experimental setup, which includes a pMDI connected to MT and tracheobronchial tree geometries down to Generation 4 (G4), along with the mouthpiece, collection filter, flow controller, and vacuum pump. We used a 200-metered-dose Salbutamol HFA (Salbutamol sulphate with hydrofluoroalkane propellant) bioequivalent Ventolin® pMDI (SANIS Health, Canada), delivering 100 μg of drug per actuation, as labeled.

Fig. 7-1(b) displays two tracheobronchial airway geometries reconstructed from CT scans of two patients with COPD: a 60-year-old male and a 67-year-old female. These scans were provided by the Iran Imaging Center in Tabriz, Iran. Initially obtained for clinical purposes, the scans were anonymized prior to analysis, retaining only non-identifiable demographic information (age and sex). All personal identifiers were removed to ensure patient confidentiality. The use of these data in this study was approved by the relevant institutional authority, in accordance with local ethical guidelines and institutional policies in effect at the time of data collection.

Evidence of COPD was noted in the G4 bronchi of both patients, with the disease affecting the right lower bronchus in the female patient and the left bronchus in the male patient. In cases of COPD, airway thickening occurs within and beyond the smooth muscle layer, leading to increased airway resistance. The patients' chest CT scans were acquired using a multi-slice scanner, generating 249 slice images with a thickness of 0.5 mm, saved in Digital Imaging and Communications in Medicine (DICOM) format. These images were imported into a medical image processing software (3D Slicer) for airway reconstruction, where segmentation was performed by visually examining each slice to extract the airways. The resulting geometries were then converted into stereolithography (STL) format. The STL files were imported into SOLIDWORKS® CAD Software 2022 (Dassault Systèmes) for further refinement. During this process, the models were smoothed using the Mesh Prep Wizard available in the tools of ScanTo3D add-in for SOLIDWORKS. Although the exact smoothing parameters were not documented, care was taken to preserve the key anatomical features. Subsequently, the distal ends of the bronchi were extended by 10–20 mm beyond their original outlet surfaces to minimize reverse flow and ensure a stable outflow boundary condition (Ahookhosh et al., 2020b; Williams et al., 2022; Zhang et al., 2012; Zhao et al., 2020). Sensitivity analyses indicated that extending beyond this range did not significantly affect the predicted airflow patterns.

Due to the limited availability of high-resolution, full-length airway scans extending from the oral cavity to the G4 bronchi within a single subject, we adopted a composite modeling approach. This strategy combines geometries from different anatomical sources and has been commonly used in previous studies facing similar imaging limitations (Longest et al., 2012b; Tian et al., 2011; Xi et al., 2018). In our case, the medium-sized MT model from VCU was integrated with the CT-derived male tracheobronchial tree, with the MT region volumetrically scaled to match the dimensions of the female geometry. Specifically, the MT model was isotropically scaled using a single volumetric scaling factor to ensure that the overall airway volume was proportionally aligned with the size of the female tracheobronchial tree. It is worth noting that the CT-derived male airway model was approximately twice the size of the female model. As a result, the MT region used for the female case was downscaled isotropically to maintain anatomically realistic proportions between the MT region and the distal airways. While this approach enabled us to construct representative airway models for our simulations, we recognize that combining anatomical segments from different sources may introduce geometric discrepancies and reduce overall anatomical fidelity.

For experimental purposes, hollow models with a 2 mm outer wall thickness were created. The models were segmented into six parts: MT, main trachea, carina, left bronchus, upper right bronchus, and lower right bronchus. This segmentation facilitated regional deposition measurements by allowing easy rinsing of each segment after testing. The final 3D replicas were printed using a Prusa Mk4 printer (Prusa Research, Czech Republic), which offers a dimensional tolerance of approximately ±0.2 mm. The printing process utilized fused deposition modeling technology with polylactic acid (PLA) filament, as shown in **Fig. 7-1(b)**. To ensure manufacturing accuracy, the printed models were compared with their STL counterparts using dimensional measurements and visual inspections at key anatomical points.

A 0.3 μm pore size filter (303 Respirgard II^{TM}, Vital Signs Inc., USA) was connected to the branch outlets via silicone tubing as a collector. A critical flow controller (TPK 2000, Copley Scientific, UK) and a vacuum pump (HCP5, Copley Scientific, UK) were used to generate a constant airflow of 30 L/min during pMDI actuation (see **Fig. 7-1(a)**). Prior to the experiments, leakage testing was conducted separately using a DFM 2000 flow meter (Copley Scientific, UK), which was sequentially connected to different sections of the setup to confirm airtightness. The configuration

shown in **Fig. 7-1(a)** represents the finalized experimental setup used during actuation, following the successful completion of the leakage verification process.

For testing, the inhaler was shaken and securely attached to the airway replica. It was actuated five times at 15-second intervals to ensure adequate delivery of Salbutamol Sulphate to the replica and the collection filter. Experiments were conducted in a controlled environment at a temperature of 22 ± 2 °C and a RH of 50 ± 5%. Each experiment was repeated three times for reliability. After each test, male airway segments were rinsed with 10 mL and 5 mL of high-performance liquid chromatography (HPLC)-grade water containing 0.1% formic acid (Fisher Scientific, US), based on their respective capacities. Female airway segments were rinsed with 5 mL and 2 mL of the same solution. The inhaler mouthpiece, tubing, connectors, and collector filter were rinsed with 5 mL, 2 mL, 1 mL, and 10 mL, respectively. A recovery validation was conducted, confirming that the recovered doses exceeded 96% for the male airway model and 93% for the female model. This indicates minimal particle loss, supporting the reliability of the experimental measurements.

Each collected sample was filtered through a Whatman® nitrocellulose membrane filter with a 0.45 μm pore size before analysis by HPLC. The assay was performed using a ZORBAX Eclipse XDB-C18 (5 μm, 4.6 × 150 mm) OBD column at 40 °C, coupled with a 1525 Binary HPLC pump and a 2489 UV/Visible detector (Waters, US) to quantify the concentration of deposited Salbutamol Sulphate within the airway replicas. The analysis was conducted at room temperature with a mobile phase composed of HPLC-grade water and acetonitrile in a 30:70 ratio. The mobile phase flow rate was maintained at 1 mL/min, with a sample injection volume of 50 μL. Salbutamol Sulphate was detected at a retention time of 1.55 minutes.

7.1 CFD Model Development

7.4.1 Geometry and Mesh

The CAD models of the airway geometries (one male and one female) used in the *in-vitro* study (see **Fig. 7-1(b)**) were also employed in the CFD modeling, as shown in **Fig. 7-2**. The airway geometries were discretized using tetrahedral meshes in the fluid zone and prism meshes along the walls, as shown in **Fig. 7-2** for the inlet, carina, and outlet. The meshing process followed the guidelines in ANSYS Workbench 2020R2 (ANSYS, Inc.), utilizing wall meshes with ten layers

and a thickness transition ratio of 0.27 to effectively capture high-gradient regions (Feng et al., 2021a; Talaat et al., 2022a).

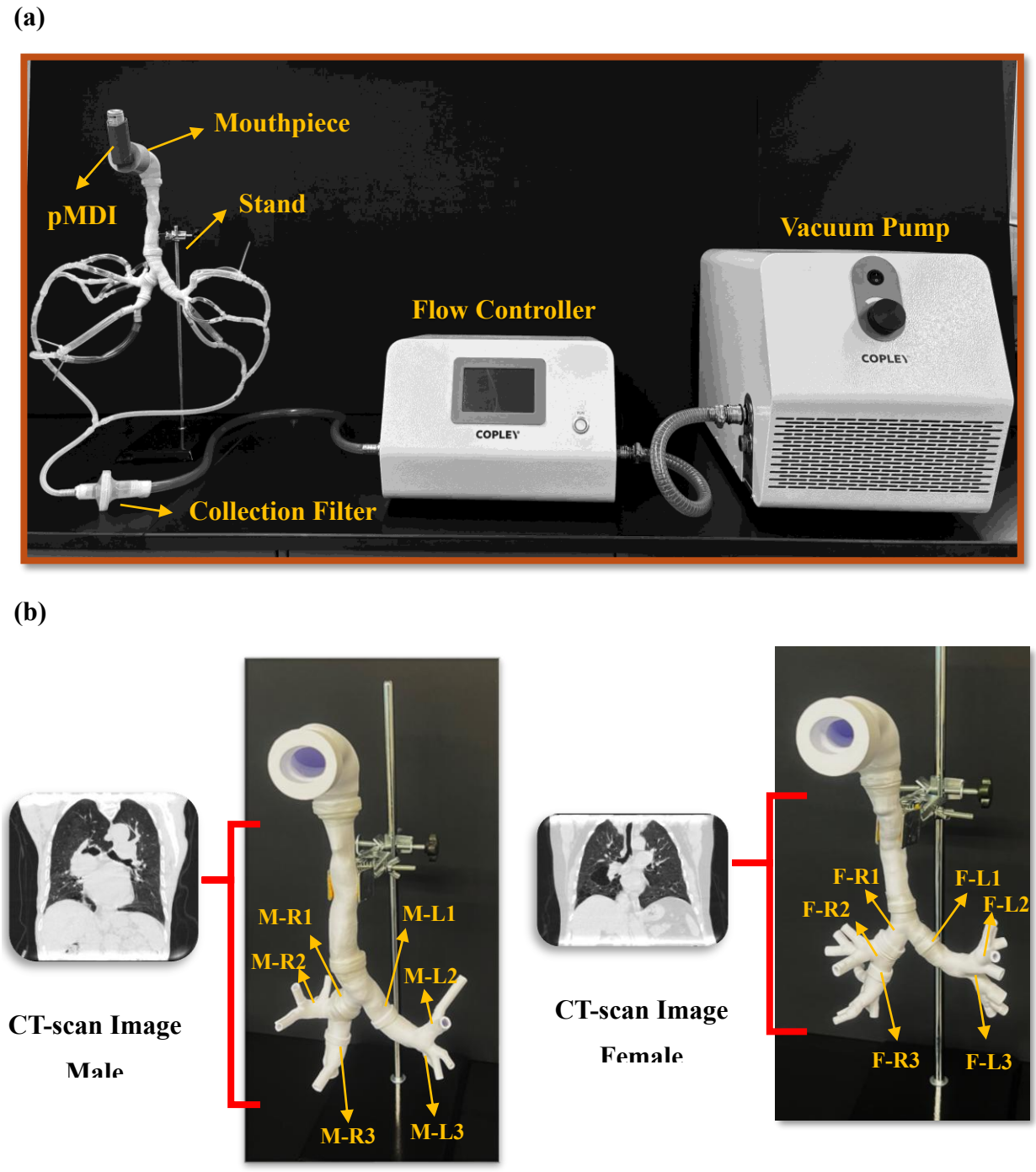

Fig. 7-1: Experimental setup: **(a)** salbutamol HFA pMDI, airway replica, flow controller, and vacuum pump; and **(b)** tracheobronchial tree geometries for male (M) and female (F) extracted from CT-scan images; the male geometry is adapted from (Jahed et al., 2025a). R: right; L: left.

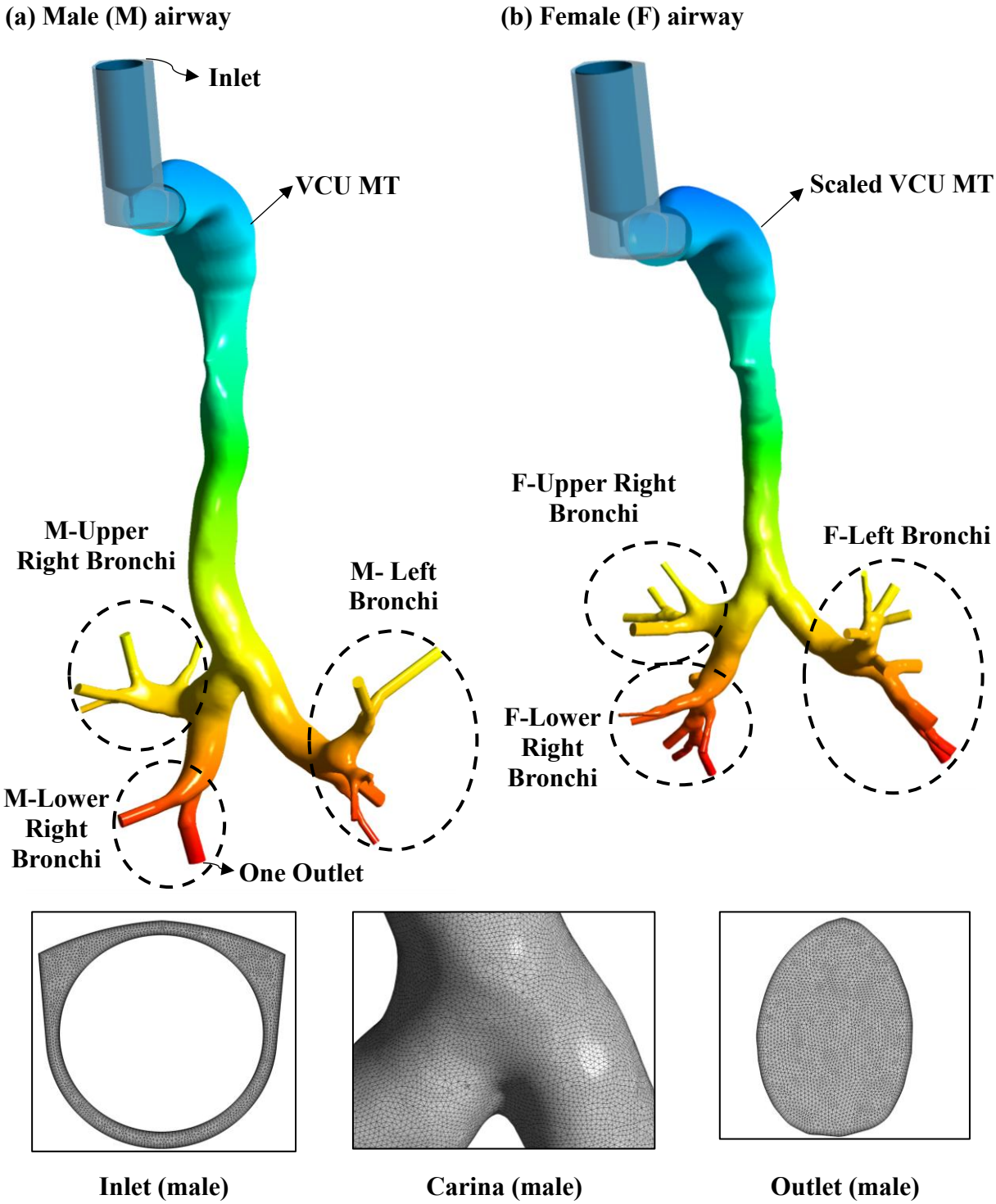

Fig. 7-2: Airway geometry of **(a)** male (M); and **(b)** female (F) patients, along with the mesh structure of different regions in the male airway model.

Mesh independence studies were conducted for both male and female models. The male airway was tested with four mesh resolutions: 1,640,346 (Mesh A), 3,303,011 (Mesh B), 6,584,095 (Mesh C), and 12,944,933 (Mesh D). The female airway was evaluated with five resolutions: 1,144,056 (Mesh A'), 2,116,730 (Mesh B'), 4,469,527 (Mesh C'), 8,297,666 (Mesh D'), and 16,090,064 (Mesh E') (**Fig. 7-3**). Simulations were performed under rigid wall conditions with a constant airflow rate of 30 L/min and 50% RH to assess velocity magnitude at different mesh sizes in the mouth, trachea, and L1 regions (refer to **Fig. 7-1(b)**). The percentage root mean square error (RMSE%), as presented in Section 5.2.1, between Mesh C and Mesh D for the male model and between Mesh D' and Mesh E' for the female model was below 5% in all regions except for the mouth in the female model, where it remained under 10%, as shown in **Fig. 7-3**. The higher RMSE% observed in the female mouth region is likely attributed to its smaller airway volume, which promotes increased turbulence and flow instabilities. These factors make the airflow in this area more sensitive to mesh resolution, impacting mesh independence. However, the overall results confirmed that the differences between Mesh D' and Mesh E' for the female model were within an acceptable range for other key regions. To balance computational cost and accuracy, we selected Mesh C (6,584,095 elements) for the male airway and Mesh D' (8,297,666 elements) for the female airway in our CFD simulations.

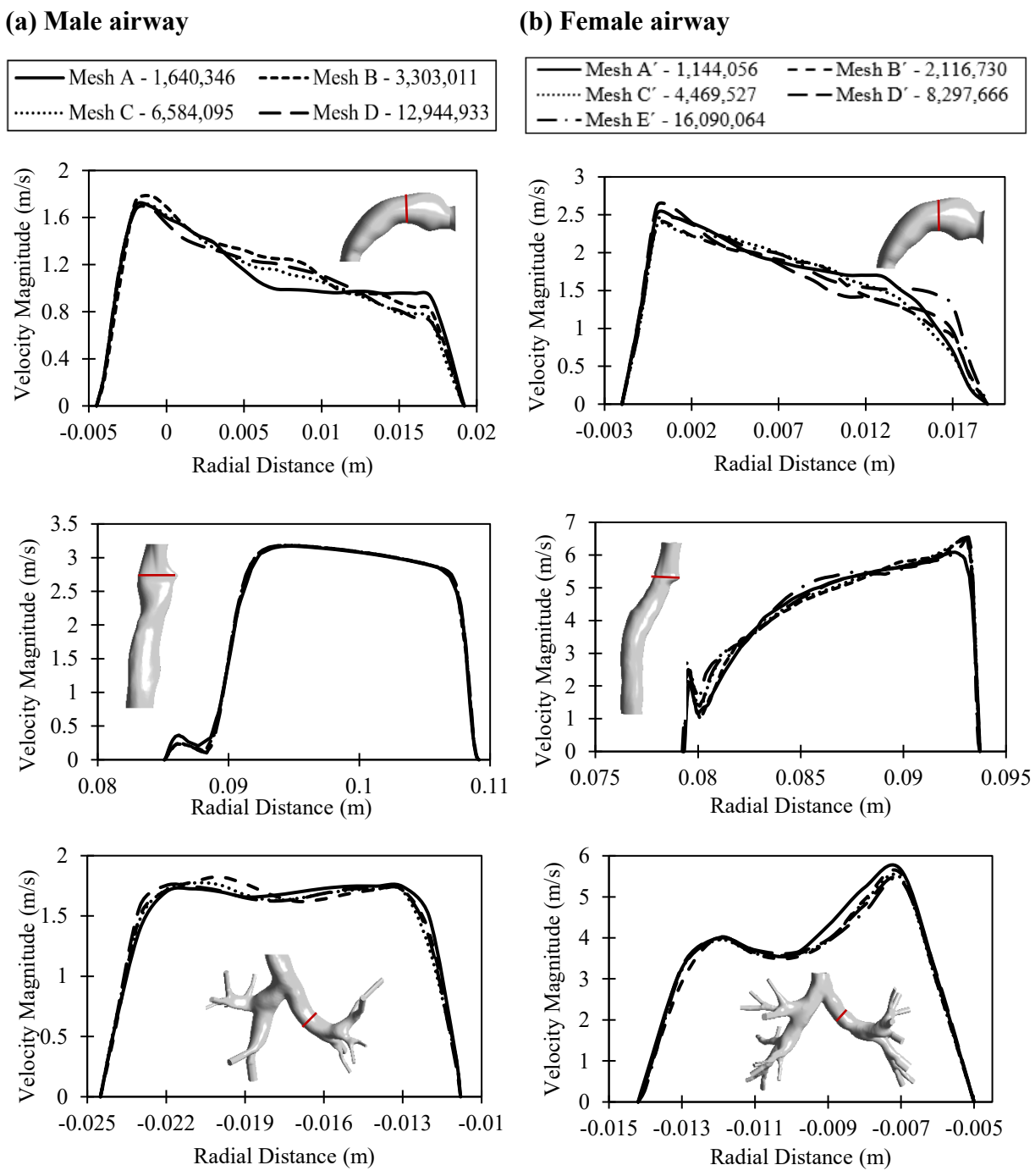

RMSE%	A & B	B & C	C & D
Mouth	11.46%	6.90%	**4.43%**
Trachea	2.10%	2.01%	**1.96%**
L1	5.40%	4.03%	**3.61%**

RMSE%	A′ & B′	B′ & C′	C′ & D′	E′ & D′
Mouth	9.21%	8.84%	12.16%	**9.96%**
Trachea	5.19%	3.98%	4.18%	**3.95%**
L1	6.30%	3.72%	2.74%	**2.63%**

Fig. 7-3: Comparison of mean velocity magnitude along the radial direction of the mouth, trachea, and L1 cross-sections for: **(a)** male; and **(b)** female geometries. The RMSE% between different mesh sizes is also shown. L: left.

7.4.2 Airflow as a Continuous Phase

In our *in-vitro* study, air at a room temperature of 22 ± 2 °C and a relative humidity of 50 ± 5% was inhaled through the airway geometries. We replicated these conditions in our modeling. Due to the complex geometry of the human tracheobronchial airway, airflow transitions from laminar to turbulent, exhibiting transient behavior (Ahookhosh et al., 2020b; Gemci et al., 2022; Shang et al., 2019). In the male model, at a constant flow rate of 30 L/min, the Reynolds number ranged from 1,949 to 3,000. To capture this behavior, we employed the large eddy simulation (LES) model with the wall-adapting local eddy-viscosity (WALE) sub-grid scale model (Eq. (7.6)). The governing equations for airflow under incompressible, Newtonian, and transient conditions, including the conservation of mass (Eq. (7.1)) and momentum (Eq. (7.2)), are as follows (Wilcox, 1993):

$$\nabla.((\overline{\boldsymbol{u}} - u_g) = 0 \tag{7.1}$$

where $\overline{\boldsymbol{u}}$ is the filtered velocity, u_g is the mesh velocity (the velocity of the dynamic boundary), and ρ is the mixture (air and water vapor) density.

$$\rho(\partial/\partial t\,(\overline{\boldsymbol{u}}) + \nabla.((\overline{\boldsymbol{u}} - u_g)\overline{\boldsymbol{u}})) = -\nabla\bar{P} + \nabla.(\bar{\sigma}) - \nabla.(\bar{\tau}) + \boldsymbol{F}_i \tag{7.2}$$

where $\bar{P}$ is filtered pressure, $\bar{\sigma}$ is the stress tensor due to molecular viscosity (Eq. (3)), $\bar{\tau}$ is subgrid-scale stress (Eq. (4)), and $\boldsymbol{F_i}$ is body force, from external forces.

$$\bar{\sigma} = \mu(\nabla\overline{\boldsymbol{u}} + (\nabla\overline{\boldsymbol{u}})^T) - 2/3\ \nabla.\overline{\boldsymbol{u}}I \tag{7.3}$$

$$\bar{\tau} = -2\mu_t\bar{S}_{ij} \tag{7.4}$$

where μ is the mixture of dynamic viscosity, μ_t is the turbulent dynamic viscosity at sub-grid scales, and $\bar{S}_{ij}$ is the filtered rate-of-strain tensor for the resolved scale (Narayanan et al., 2022). The sub-grid-scale WALE model is presented in Eq. (7.4), with its formulation described in Eqs. (4.12)–(4.14).

To predict the temperature distribution in the airway, the following total energy (E) equation (Eq. (7.8)) for airflow is solved (Wilcox, 1993):

$$\rho(\partial/\partial t\,(E) + \nabla.\left(\left(\overline{\boldsymbol{u}} - u_g\right)(E)\right)) = \nabla.\left(k_{eff}\nabla T - \sum_s h_s\vec{J}_s + \left(\bar{\tau}_{eff}.\overline{\boldsymbol{u}}\right)\right) \tag{7.8}$$

where $k_{eff} = k + k_t$ is effective conductivity in which k_t is turbulent thermal conductivity, T is temperature, h_s is the species enthalpy, $\vec{J}_s$ is the diffusion flux of species, and $\bar{\tau}_{eff}$ is the effective shear stress.

The transport equation for species (air and water vapor) is given by (Feng et al., 2021b):

$$\rho(\partial/\partial t\,(Y_s) + \nabla.(\bar{\boldsymbol{u}}Y_s)) = -\nabla.\vec{J}_s + S_s \tag{7.9}$$

where Y_s is the species (air and water vapor) and S_s is the source term arising from the discrete phase due to the evaporation/condensation of water droplets.

7.4.3 Discrete Phase Model (DPM)

The one-way Lagrangian DPM model was utilized to track aerosol particles injected from a pMDI into the airway geometries. Given the highly diluted particle flow (global mass fraction: 0.16%), particle-particle interactions were neglected (Dunbar, 1997; Oliveira et al., 2012; Rahman et al., 2021; Xu et al., 2021). While the global particle volume fraction supports this simplification, localized particle concentration, especially near the nozzle and in recirculation zones, may temporarily exceed this threshold, potentially introducing minor two-way coupling effects. This limitation should be considered when interpreting particle dynamics and interactions with the flow field in these regions. The propellant, primarily hydrofluoroalkane (HFA-134a or HFA-227a), accounts for approximately 99% of the pMDI canister mass (Duke et al., 2019; Sheth et al., 2017; Sou and Bergström, 2021). Therefore, we assumed HFA-134a properties similar to those of inert particles (refer to **Table 6-3**)

The Rosin-Rammler method defined the particle size distribution, spanning 0.1 to 25 μm, with a mean diameter of 5 μm and a spread parameter of 2. This distribution is based on Zhang et al. (2017), who measured the Ventolin pMDI aerosol using laser diffraction at room temperature under two RH conditions: 25%–45% (lower RH) and >90% (higher RH). Given our experimental setup (22°C, RH 50%), we adopted the size distribution corresponding to the lower RH range. The inhaler's injection time was set to 0.1 s, matching the actuation duration of Ventolin® HFA. Particle motion was governed by Newton's second law (Eq. (7.10)), considering drag force, gravitational force, and Brownian motion as primary influences. Saffman's lift force, buoyancy, pressure force, Basset force, and virtual mass effects were excluded due to the higher particle density relative to air (Finlay, 2019). Thermophoresis was also deemed negligible, as the temperature gradients were

insufficient to induce a measurable effect. Additionally, it primarily influences the deposition of sub-micron particles in turbulent aerosol flows (He and Ahmadi, 1998; Lee and Cant, 2017).

$$m_p \, \mathrm{d}\overline{\boldsymbol{u}}_{\boldsymbol{p}}/\mathrm{dt} = 18\mu/\rho_p d_p^2 \frac{m_p C_{Dd} Re_p}{24}\left(\overline{\boldsymbol{u}} - \overline{\boldsymbol{u}}_{\boldsymbol{p}}\right) + \vec{g}\left(\rho_p - \rho\right)/\rho_p + m_p \zeta_i \sqrt{\pi \, S_0/\Delta t} \qquad (7.10)$$

where $\overline{\boldsymbol{u}}_{\boldsymbol{p}}$, ρ_p, d_p, and m_p are the velocity, density, diameter, and mass of the particles, respectively, and $\overline{\boldsymbol{u}}$, μ, and ρ are the velocity, molecular viscosity, and density of the fluid, respectively (Ahookhosh et al., 2021; Narayanan et al., 2022). ζ_i is a stochastic coefficient and $\vec{g}$ is the gravitational acceleration, and C_{Dd} represents the drag force coefficient for spherical particles (Eqs. (4.16)-(4.19)).

And in the Brownian force, noted as the last term on the right side in Eq. (7.10), S_0 is:

$$S_0 = 216\nu k_B T/\pi^2 \rho d_p^5 \left(\rho_p/\rho\right)^2 C_c \qquad (7.15)$$

where k_B is the Boltzmann constant, and ν is the molecular kinematic viscosity of airflow.
The temperature of the particles is estimated based on the convection between the particle and the continuous phase:

$$m_p c_p dT_p/dt = h_c A_p\left(T - T_p\right) \qquad (7.16)$$

where c_p and A_p represent the particle's heat capacity and surface area, respectively. h_c denotes the convective heat transfer coefficient (Aghaei et al., 2023), determined using the following correlation for the Nusselt number (Nu) (Ranz and Marshall, 1952):

$$Nu = h_c d_p/k = 2 + 0.6 \, Re_p^{1/2} Pr^{1/3} \qquad (7.17)$$

where k is the thermal conductivity of the continuous phase, and $Pr = \nu_t/\alpha_t$ is the Prandtl number of the continuous phase, which was set equal to 0.85 (Gessner, 2001), where ν_t is turbulent eddy viscosity, and α_t is turbulent thermal diffusivity.

7.4.4 Mucus Layer Modeling

As illustrated in **Fig. 7-4**, the airway mucus, which interacts with inhaled air and traps particles, consists of both sol and gel components. It is primarily composed of approximately 95% water, with up to 5% lipids, 0.5% mineral salts, 1% free proteins, and various other large macromolecules (Haut et al., 2021; Sosnowski, 2021). In our model, the airway tissue (epithelium) (see **Fig. 7-4**) was represented as a uniform solid layer with a thickness of 0.5 mm, exhibiting properties similar

to those of water (Aghaei et al., 2023; Chen et al., 2018; Narayanan et al., 2022; Xu et al., 2021). This tissue layer introduces thermal resistance due to water's low conductivity, thereby influencing heat transfer between the mucus layer and the outer airway wall, which is maintained at 37°C.

To simulate the mucus layer, which plays a crucial role in conditioning inhaled air, we integrated the Eulerian Wall Film (EWF) model with the CFD-DPM framework. The EWF model in ANSYS Fluent is a widely accepted method for simulating evaporation and heat transfer from thin surface films (Ding et al., 2022; Ferron et al., 2013, 1989; Wang et al., 2016; Xia et al., 2024). Therefore, the mucus layer was modeled as a two-dimensional thin film of water, 10 µm thick, coating the airway tissue surface. Given the thinness of the mucus layer relative to the airway diameter, we assumed that the mucus remains stationary and exhibits uniform temperature, density, and viscosity throughout its thickness. The mucus has a slow average velocity of 5-10 mm/min (Foster et al., 1982), which is negligible compared to the airflow velocity. This study focuses on the role of mucus film in conditioning air and its effect on particle deposition. However, previous studies (Anzai et al., 2022; Paz et al., 2017; Ren et al., 2020) have employed the EWF model to simulate mucus clearance and track droplet formation in the gas phase.

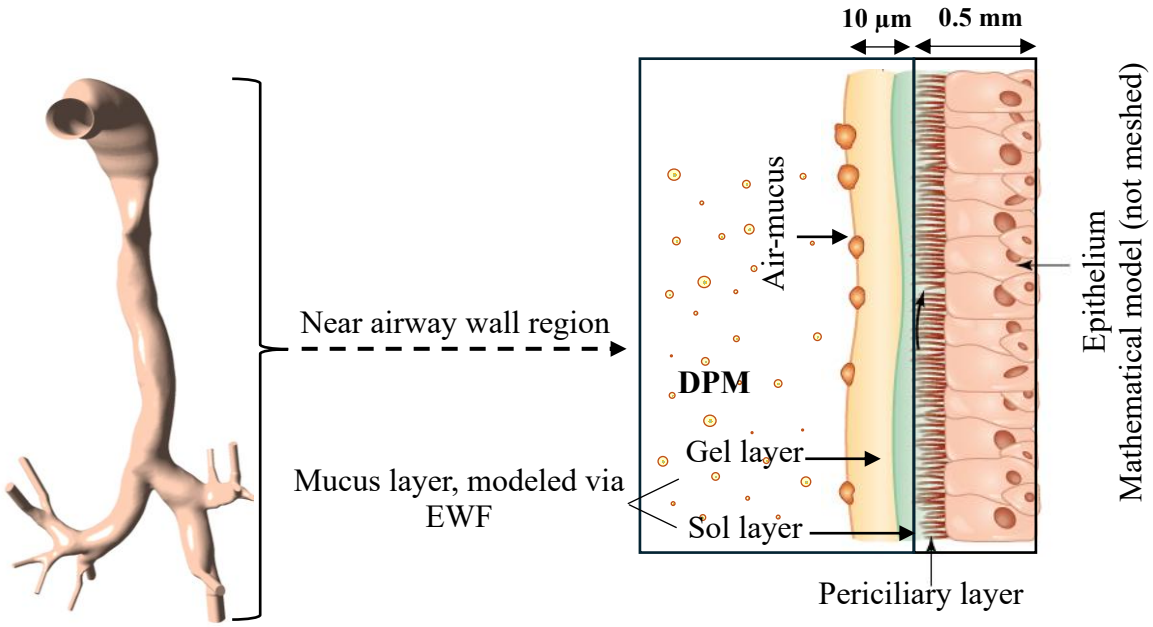

Fig. 7-4: Computational modeling framework, CFD-DPM-EWF, used for simulating particle transport and deposition on the airway wall; the schematic was adapted from (Australia, 2020).

The conservation of mass for a two-dimensional film in a three-dimensional domain is expressed as follows (Kakimpa et al., 2016, 2015):

$$\partial \rho_f H / \partial t = \dot{m}_s \tag{7.18}$$

where ρ_f and H are the film density and height, respectively. $\dot{m}_s$ is a mass source per unit wall area due to particle absorption and phase change. Conservation of film energy is also expressed as follows (O'Rourke and Amsden, 1996):

$$\partial \rho_f H T_f / \partial t = 1/C_p \left[2k_f / H \, (T_s + T_w + 2T_m) + \dot{q}_{imp} + \dot{m}_{vap} L \right] \tag{7.19}$$

where T_f, T_s, T_w, and T_m are the average film temperature, film surface temperature, wall temperature, and film half-depth temperature, respectively. $\dot{q}_{imp}$ is the heat flux source resulting from airflow and particle impingement on the wall. $\dot{m}_{vap}$ is the mass vaporization or condensation rate, and L is the latent heat associated with the phase change. The initial film height was set uniformly at 10 μm across all regions, according to Kamm (1999).

By including the EWF model in our simulation, the predicted trends of RH and temperature within the airway closely matched physiological expectations and aligned well with values reported in previous studies by Ferron et al. (2013 and 1989). These studies provided approximations of the temperature and RH distributions in the upper human airways by solving coupled heat and water vapor transport equations, based on experimental data from the literature.

7.4.5 Boundary Conditions

The inlet boundary condition was set to a mass flow rate of 6.45×10^{-4} kg/s, corresponding to a constant breathing flow rate of 30 L/min. For the COPD inhalation profile, the breathing pattern shown in **Fig. 5(a)** was implemented as a transient table at the model's inlet, based on data from Biswas et al. (2017) for asthma and COPD patients using MDIs. The outlets were assigned to a zero-pressure boundary condition, and all airway walls were modeled with a no-slip boundary condition.

It is essential to note that applying uniform zero-pressure boundary conditions at all outlets may not accurately capture airflow variations in distal regions, particularly in diseased lungs. However, our study focuses on the upper and central airways, using a disease-specific inhalation profile and a patient-specific airway geometry with an obstruction at G4. Although further obstructions may

be present in more distal generations in actual patients, our modeling approach aligns with previous studies that have truncated airway segments (e.g., Ilegbusi et al. (2023) and Yang et al. (2006)), which commonly use zero-pressure outlet conditions.

In the DPM framework, a trap boundary condition was applied to the airway walls to facilitate particle deposition, and an escape boundary condition was set at the outlets to allow particles to exit the domain.

Imaging techniques show that airway cross-sections expand during inhalation, reaching their maximum size at the end of the inhalation cycle (Bates et al., 2019). Using Ciné MRI, Bates et al. (2019) quantified airway wall displacement, enabling the estimation of average airway expansion. Based on these data, we assumed a circular cross-section and determined wall displacement throughout the inhalation cycle, as illustrated in **Fig. 7-5(b)**. A dynamic-mesh approach was used, based on Eq. (7.20), which corresponds to the airway wall displacement curve shown in **Fig. 7-5(b)**. This function was implemented using a user-defined function (UDF) to simulate airway wall deformation throughout the inhalation cycle. The study assumes uniform radial deformation along the airway walls. While this method effectively captures the overall impact of time-dependent airway expansion, it does not consider potential longitudinal displacement or regional variability in wall motion.

This study investigated four combinations of breathing flow rates and wall motion conditions: (1) constant flow with a rigid wall (constant-rigid), (2) constant flow rate with a dynamic wall (constant-dynamic), (3) COPD flow rate with a rigid wall (COPD-rigid), and (4) COPD flow rate with a dynamic wall (COPD-dynamic).

$$\text{Displacement (mm)} = -0.14 + \sum_{i=1}^{5} b_i t^i \tag{7.20}$$

$$b_1 = 2.52, b_2 = -8.58, b_3 = 9.97, b_4 = -4.52, and\ b_5 = 0.68$$

where t is time, and b_1, b_2, b_3, b_4, and b_5 are the constants of polynomial function.

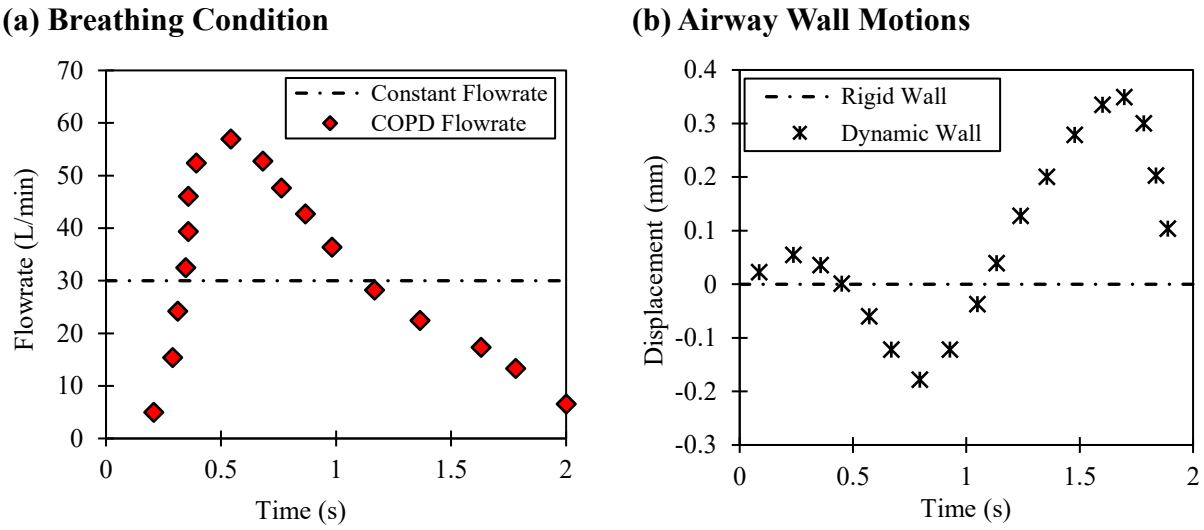

Fig. 7-5: (a) Inhalation flow profiles under constant and COPD breathing conditions; and **(b)** rigid and dynamic airway wall motions (Jahed et al., 2025a).

7.4.6 Simulations

In our simulations, we utilized the SIMPLEC (Semi-Implicit Method for Pressure-Linked Equations-Consistent) algorithm for pressure-velocity coupling. The computations were performed on the Narval cluster, equipped with AMD EPYC Zen2 processors featuring up to 64 cores per processor and 256 GiB of RAM per node. Additionally, we used the Intel® Xeon® Gold 6148 CPU, operating at 2.40 GHz and featuring up to 80 cores per processor, which is available at Lakehead University. The average simulation runtime ranged from 168 to 900 hours, depending on the case.

7.5 Results and Discussion

This section provides a detailed analysis of four factors that influence airflow dynamics and particle deposition within the airways. First, we examine the differences between male and female airways and their impact on particle deposition across various regions of the airways. Next, we analyze the effect of breathing flow rate by comparing deposition trends under different inhalation conditions. We then explore how movements of the airway walls can alter airflow patterns and particle trajectories. Finally, we discuss the influence on airflow dynamics and particle deposition rates.

7.5.1 Effect of the Anatomical Differences on Deposition Fraction

Fig. 7-6 compares deposition fractions (DFs) obtained from CFD simulations and *in-vitro* experiments for both male and female models investigated, thereby validating the simulations. DF represents the ratio of deposited particles in a specific region to the total particles emitted from the pMDI device. In the analysis, rigid airway walls and a consistent flow rate of 30 L/min were maintained to match experimental conditions.

This figure shows that our CFD results are consistent with *in-vitro* data; however, they tend to underestimate deposition in some regions of the male model and overestimate it across all regions of the female model. As shown in the figure, in the case-specific male model, the DF_{CFD} in the main MT region is 13.08% (DF_{Ex}= 17.30%). In contrast, the female model exhibits a higher DF_{CFD} of 20.10% (DF_{Ex}= 19.18%). Similarly, in the trachea, the male model exhibits a DF_{CFD} of 7.25% (DF_{Ex} = 9.18%), whereas the female model shows a significant increase to 23.73% (DF_{Ex} = 20.48%). In the bronchial branches, the DF_{CFD} values in the carina region also follow this pattern: the male model shows a DF_{CFD} of 4.67% (DF_{Ex}= 5.22%), which is lower than the 8.80% (DF_{Ex} = 7.80%) observed in the female model.

However, we noticed that in the male airway used in this study, the DF_{CFD} in the right bronchi is 9.25% (DF_{Ex} = 7.67%), and in the left bronchi, it is 5.06% (DF_{Ex} = 6.65%). On the other hand, the female model shows a DF_{CFD} of 7.77% in the right bronchi (with a DF_{Ex} of 6.63%) and 9.30% in the left bronchi (with a DF_{Ex} of 8.05%). Furthermore, in the female model, the DF in the lower right (LR) bronchi is approximately 50% higher than in the upper right (UR) bronchi. This disparity may indicate a COPD-related symptom, potentially associated with a reduction in bronchial diameter. A similar pattern was observed in the study by Chen et al. (2025), which demonstrated through CFD simulations that airway narrowing and obstructions associated with COPD lead to elevated flow velocities and the formation of recirculatory zones, particularly at bifurcations. These altered flow characteristics result in significantly higher deposition of nanoparticles in localized areas.

Both male and female models received the same aerosol injections while maintaining a consistent breathing flow rate of 30 L/min. The observed deposition differences are primarily due to anatomical variations between their airways. Notably, passages in our female airway model, as indicated in **Table 3-1**, increase the chances of particle-wall collisions.

These findings are consistent with those of Pritchard et al. (1986), who used gamma scintigraphy to study sex differences in the regional deposition of 2.5–7.5 μm particles in healthy volunteers. Their results showed that females had higher deposition fractions than males in the upper respiratory tract, tracheobronchial, and pulmonary regions. Additionally, Sturm (2016) investigated ultrafine particle deposition in the lungs of healthy men and women using both experimental methods and theoretical modeling and also found that females exhibited higher deposition rates.

Fig. 7-6 also compares DFs in our specific male and female airway geometries with two CFD results (Islam et al., 2021; Longest et al., 2012b). Our observed DF in the deep lung for the male airway was 60.69%, which is higher than the 54.50% reported by Longest et al. (2012b) and the 45.09% reported by Islam et al. (2021), while for the female airway, it dropped to 30.30%. Notable differences were also identified in the regional deposition patterns. Longest et al. (2012b) reported that approximately 44% of the inhaled dose was deposited in the MT region, with only 0.6% deposited in the upper generations of the conducting airways (up to G3). In our airway models, however, 26.23% and 49.60% of the particles were deposited in the upper bronchial generations (G0-G4) in the male and the female airways, respectively. It's worth noting that differences in airway region definitions between the studies may have slightly impacted these deposition comparisons. Longest et al. (2012b) studied the DFs of MDI particles from the mouth up to the third generation of the airway in healthy males, while Islam et al. (2021) extended their deposition data to G5 of Weibel's airway model. For a direct comparison with our findings, we used only data from Islam et al. up to G4. Notably, Longest et al. (2012b) simplified the airway branches in their model to lower geometric complexity, whereas our models include more anatomical detail to improve physiological relevance. Both studies referenced employed an airflow rate of 30 L/min. This discrepancy suggests that variations in patient-specific anatomy and modeling assumptions may have contributed to the differences in results and could affect treatment effectiveness.

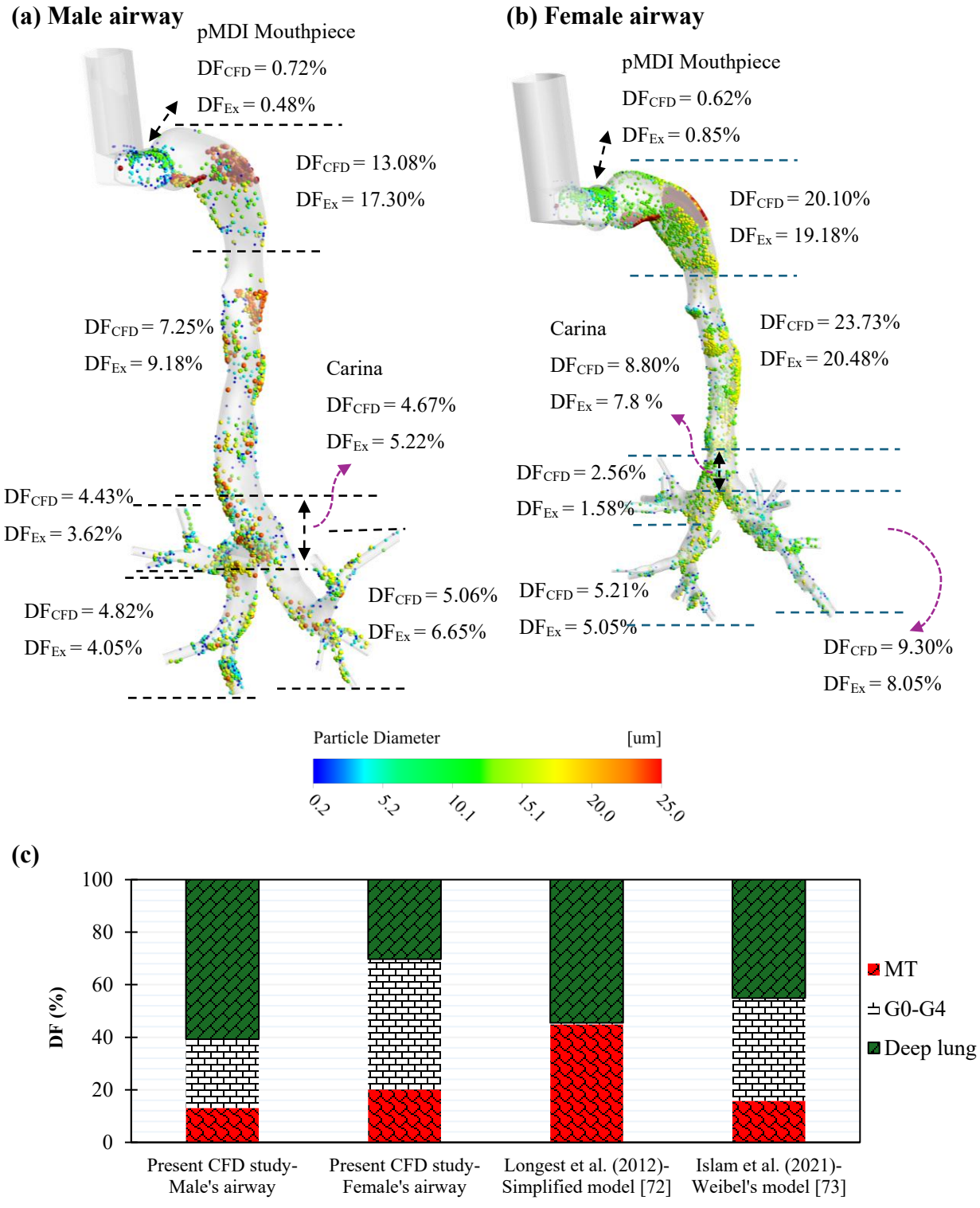

Fig. 7-6: Regional deposition fractions from the CFD model (DF_{CFD}) and experimental (Ex) data (DF_{Ex}) for **(a)** male; and **(b)** female airways, at an inhalation flow rate of 30 L/min with rigid airway walls. The CFD-predicted particle size distribution is also shown; and **(c)** comparison of deposition fractions between the CFD models in (Islam et al., 2021; Longest et al., 2012b) and the present study.

Fig. 7-6 also illustrates the size of the deposited particles and the patterns of their deposition within the male and female airway geometries investigated in this study. The figure signifies that larger particles traverse the trachea and carina regions of the male airway, whereas in the female airway, only particles smaller than 15 μm reach the bronchial region. To further illustrate these trends, **Table 7-1** presents regional deposition ratios based on the number of deposited particles.

Table 7-1: Deposition ratios of particles in different size ranges across various regions of the male and female airways in CFD models. MT: mouth-throat.

Particle Size	**Deposition Ratio (%)**					
(μm)	Case	MT	Trachea	Carina	Left Bronchi	Right Bronchi
< 1	**Male**	8.03	12.89	8.25	29.99	40.85
	Female	3.36	18.04	7.32	35.10	36.19
1-5	**Male**	10.75	12.91	8.36	27.35	40.63
	Female	4.58	22.63	8.90	33.05	30.84
5-10	**Male**	15.43	19.09	10.38	18.67	36.42
	Female	8.94	38.49	14.95	20.23	17.39
10-15	**Male**	19.44	25.18	17.63	13.62	24.13
	Female	41.15	32.74	14.57	5.33	6.21
15-20	**Male**	99.40	0.45	0.08	0.02	0.04
	Female	100	0	0	0	0
> 20	**Male**	100	0	0	0	0
	Female	100	0	0	0	0

In this study, the deposition ratio is defined as the number of particles within a specific size range that deposit in a given region, relative to the total number of particles of the same size range that deposit across the entire airway. This table indicates that 41.15% of particles with a diameter of 10-15 μm were deposited in the MT region of the female airway, compared to 19.44% in the male airway. Thus, a smaller portion of particles in this range of size reached the lower regions of the female airway. For mid-size particles (5-10 μm), 38.49% were deposited in the female trachea, compared to only 19.09% in the male trachea. Moreover, a higher proportion of smaller particles

was retained in the female trachea, indicating greater overall deposition in this region. It is essential to note that this study focuses on spherical particles, which are representative of aerosols generated by pMDIs. However, this assumption limits the generalizability of our findings. A recent study by Prinz et al. (2025) demonstrates that non-spherical particles, such as fibres, exhibit distinct aerodynamic behaviors. These differences often lead to deeper lung penetration due to orientation-dependent drag and inertia. Consequently, the deposition patterns reported in this study should be interpreted with caution for spherical aerosols. Future studies that include a broader range of particle shapes would provide a more comprehensive understanding of inhaled drug delivery.

Fig. 7-7 compares the mean velocity magnitude across the airway cross-sections of the specific male and female anatomies used in this study, demonstrating consistently higher airflow velocity in the female airway from the main trachea to the bronchial branches. In the female trachea, airflow velocity is approximately 5 m/s, whereas in the male trachea it is approximately 2 m/s. The female airway's narrower geometry restricts airflow, increasing velocity and turbulence, especially in the trachea region. This elevated airflow velocity amplifies the inertial impaction mechanism (Finlay, 2019), contributing to higher deposition fractions throughout all regions of the female airway. In addition, **Fig. 7-7** highlights the profound impact of airway geometry on airflow dynamics, which in turn affects particle deposition patterns, as illustrated in **Fig. 7-6.** Anatomical asymmetries between the left and right bronchi, particularly the longer, narrower left bronchus due to the heart's position, further influence airflow behaviour (Moore et al., 2006). In the analyzed female airway, the mean velocity in the left bronchus ranges from approximately 3 to 4 m/s, whereas in the right bronchus it is lower, at approximately 1.5 to 2.5 m/s. This observation aligns with the findings of Kadota et al. (2022), who demonstrated that variations in airway structure among COPD patients lead to significant differences in airflow distribution between lung lobes. These variations are primarily due to changes in bronchial diameters and branching angles.

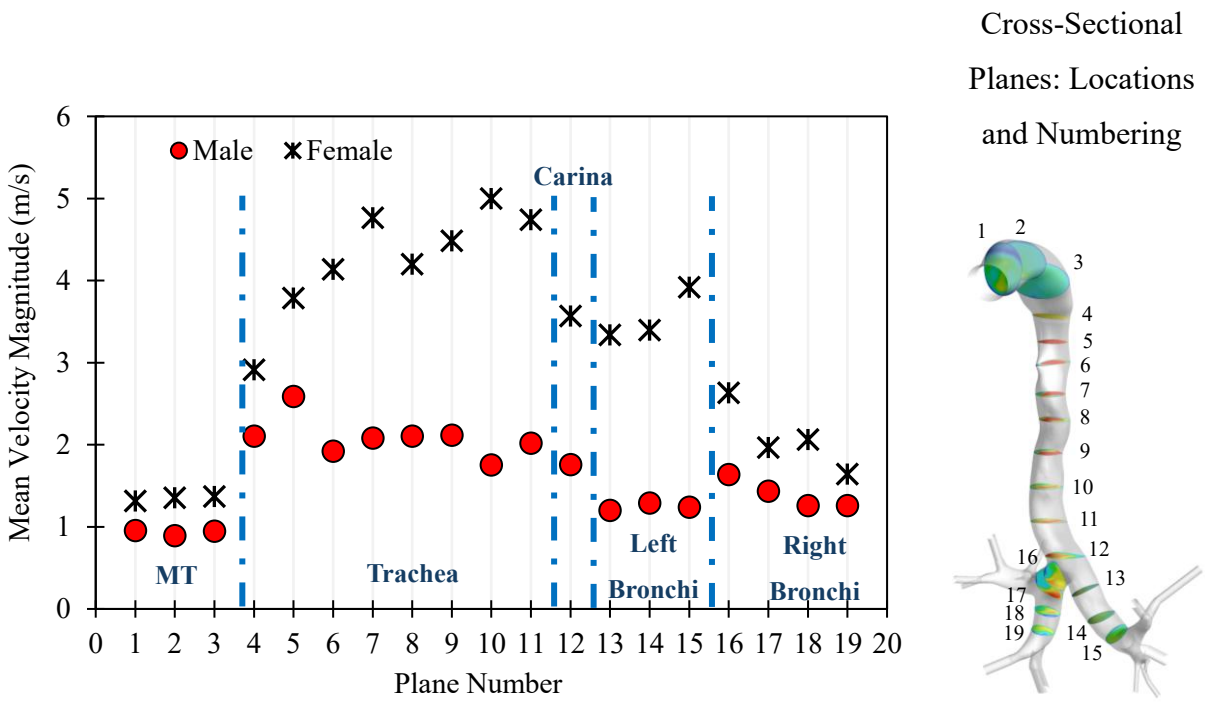

Fig. 7-7: CFD-predicted mean velocity magnitude for male and female airway geometries across different cross-sections (planes) in different airway regions, at an inhalation flow rate of 30 L/min with rigid airway walls. MT: mouth-throat.

7.5.2 Effect of the Breathing Flowrate on Deposition Fraction

Fig. 7-8 illustrates the effects of constant and COPD flow rates on particle deposition within the airways, with a particular focus on the rigid airway walls. In both the male and female airway models used in this study, the deposition fraction in the upper airways—specifically the mouth, trachea, and carina regions—decreases under COPD conditions. During the initial inhaler injection period (0 to 0.1 s), when a constant flow rate of 30 L/min is applied, particles experience a higher flow rate and slight irregularities in the mouth and carina regions, as shown in the airflow streamlines in **Fig. 7-9(a).** This leads to greater deposition in the upper airways. In contrast, during the same period, in COPD patients, the flow rate remains below 10 L/min, thereby reducing turbulence, as demonstrated in **Fig. 7- 9(b)**.

The slower airflow, which persists until approximately 0.3 s, eventually reaches approximately 30 L/min (similar to the constant-flow rate condition), as illustrated in Fig. 7-- **9(c)**, allowing particles to gently enter the airways. Consequently, the Stokes number increases progressively. At low

Stokes numbers, particles tend to closely follow the airflow streamlines due to weak inertial effects, leading to minimal deposition in the upper airways. In contrast, when models use mean or maximum flow rates, the Stokes number remains consistently high, leading to greater deposition in the upper airways than in more realistic breathing conditions (Mirzaaghaian et al., 2024). By 0.6 s, the COPD flow rate peaks at approximately 60 L/min (**Fig. 7-9(d)**), facilitating the transport of particles initially injected at 0.1 s deeper into the airways, ultimately reaching the distal lung regions.

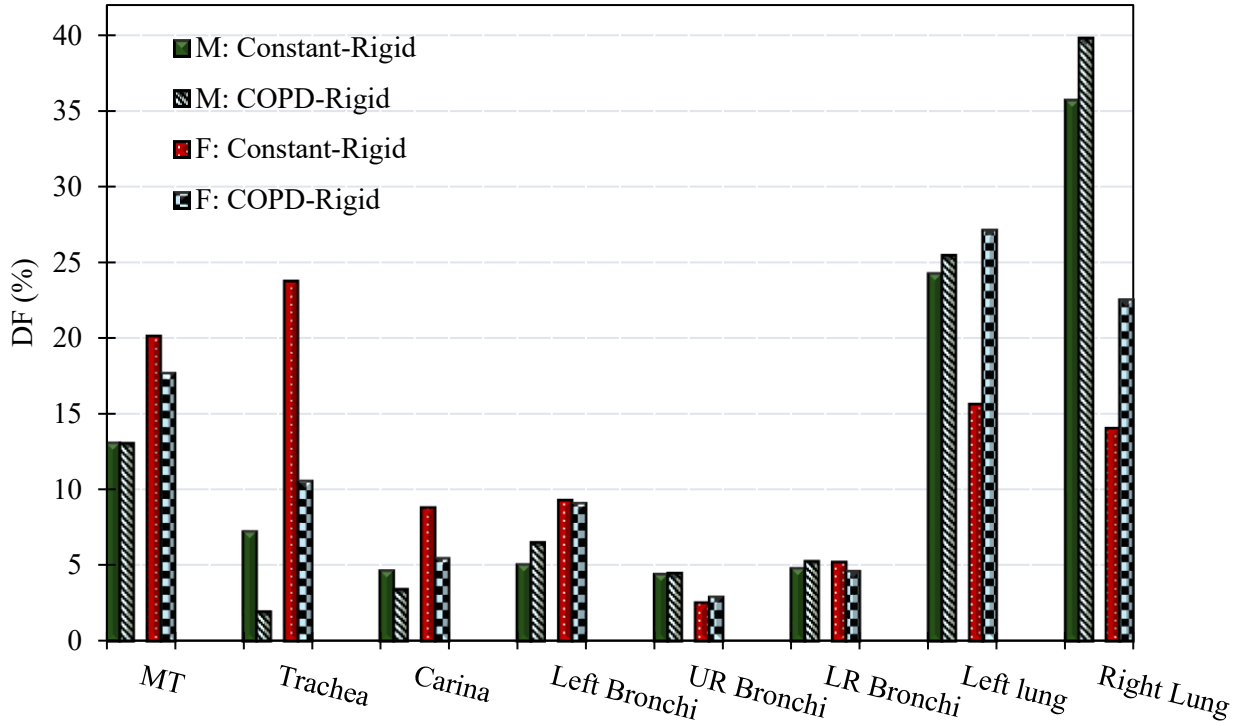

Fig. 7-8: Deposition fraction (DF) in the male (M) and female (F) airways under constant and COPD flow rate conditions, with rigid walls. MT: mouth-throat, UR: upper-right, LR: lower-right.

These findings are consistent with those reported by Kadota et al. (2020), Chen et al. (2023), and Mirzaaghaian et al. (2024), all of whom emphasized the influence of breathing patterns on particle transport and deposition. Kadota et al. (2020) conducted CFD simulations to compare constant and patterned airflows within a patient's airway. They found that, at a constant flow rate of 28.3 L/min, most particles were deposited in the mouth, throat, and trachea. In contrast, patterned airflow resulted in reduced deposition in the mouth and throat while enhancing deposition in the lungs. Similarly, Chen et al. (2023) studied dust transport in the respiratory tracts of coal workers using

CFD. Their research revealed that during non-steady breathing, particle deposition in regions before the bronchus was lower than during steady-state breathing at 30 L/min. Mirzaaghaian et al. (2024) further demonstrated that total particle deposition for particle sizes ranging from 3 to 9 μm was consistently lower under realistic breathing patterns than under constant-flow-rate conditions, applicable to both male and female lung models. Complementing these findings, Mišík et al. (2025) demonstrated that inhalation through high-resistance nebulizer systems results in a slower, deeper breathing pattern. Their CFD studies, along with experimental evidence, showed that this breathing pattern enhances aerosol deposition in the lower airways.

In our study, illustrated in **Fig. 7-8**, we observed gender-specific differences in particle deposition when comparing the COPD flow rate to a constant flow rate of 30 L/min. In the male model and under the COPD flow rate, particle deposition in the MT region slightly decreased by 0.1%. However, we noted significant reductions in the trachea (73.0%) and carina (26.2%) regions. These reductions demonstrate that fewer particles were lost in the upper airway at the COPD flow rate, allowing 16.35% more particles to reach the lungs successfully. The female model shows more pronounced reductions in particle deposition at the COPD flow rate, with decreases of 12.0% in the MT region, 55.4% in the trachea, and 37.7% in the carina. The COPD breathing condition led to greater particle delivery efficiency in the female upper airway model compared to the male model. Consequently, drug delivery to the deep lungs significantly increased in the female model, with 73.45% more particles reaching the left lung and 60.4% more reaching the right lung. In line with this, Farkas et al. (2020) employed both experimental and computational methods to demonstrate that the breathing patterns of asthma patients differ from those of healthy individuals. Their findings indicated that these disease-specific breathing profiles contribute to uneven airflow distribution across the lung lobes, leading to ventilation heterogeneity. As a result, some lobes receive a higher concentration of aerosol particles than others.

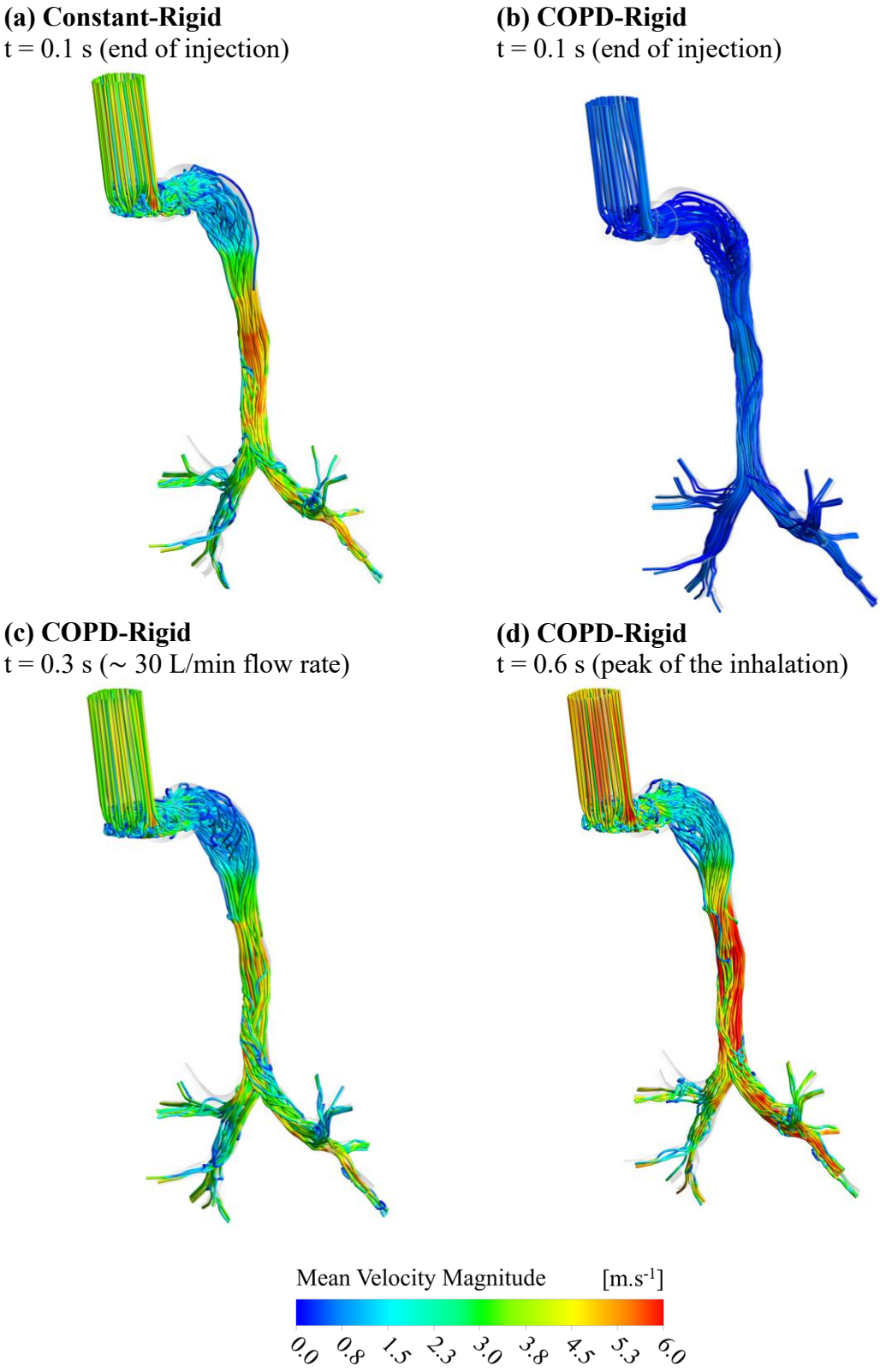

Fig. 7-9: Streamlines of airflow in the female airway under **(a)** constant flow rate of 30 L/min; **(b)** COPD flow rate at t = 0.1 s (end of injection); **(c)** COPD flow rate at t = 0.3 s (~ 30 L/min flow rate); and **(d)** COPD flow rate at t = 0.6 s (peak inhalation), with the rigid wall condition.

Fig. 7-10 presents iso-surfaces of swirling strength (λ_{ci}), colored by turbulent kinetic energy (TKE), for both male and female airway models under constant and COPD flow conditions. These images capture the moment corresponding to the peak inhalation flow rate. All simulations were performed under rigid wall conditions in the mouth and trachea regions. A normalized swirling strength threshold of 0.05 was employed, meaning that only regions where the swirling strength reached or exceeded 5% of the maximum value in the domain were visualized. This threshold was selected because it was the lowest level at which coherent vortex structures could still be distinctly identified, ensuring consistent and interpretable comparisons across all cases. This figure illustrates areas of significant vortical activity. Notably, the COPD-Rigid cases, both male and female, exhibit more extensive and intense swirling structures compared to their counterparts with constant flow.

When comparing the male and female airway geometries, it is observed that the female airway exhibits greater swirling strength and higher localized TKE in the trachea region under COPD conditions (minimum swirling strength of about 728 s^{-1} compared to 1046 s^{-1}, respectively). This may be attributed to sharper airway curvatures and a reduced lumen diameter, both of which promote flow instability and an earlier transition to turbulence. From a theoretical perspective, this observation is consistent with the classic understanding of turbulence onset. Smaller airway diameters and sharper bends increase the local Reynolds number, generating stronger velocity gradients that promote flow separation, recirculation, and the development of coherent vortical structures (Wilcox, 1993). The increased TKE in the female model under COPD conditions supports this, indicating enhanced energy content in the turbulent eddies and stronger secondary flows. These findings highlight how anatomical differences and pathological breathing patterns combine to increase flow complexity and turbulence, significantly impacting particle transport and deposition during respiratory drug delivery.

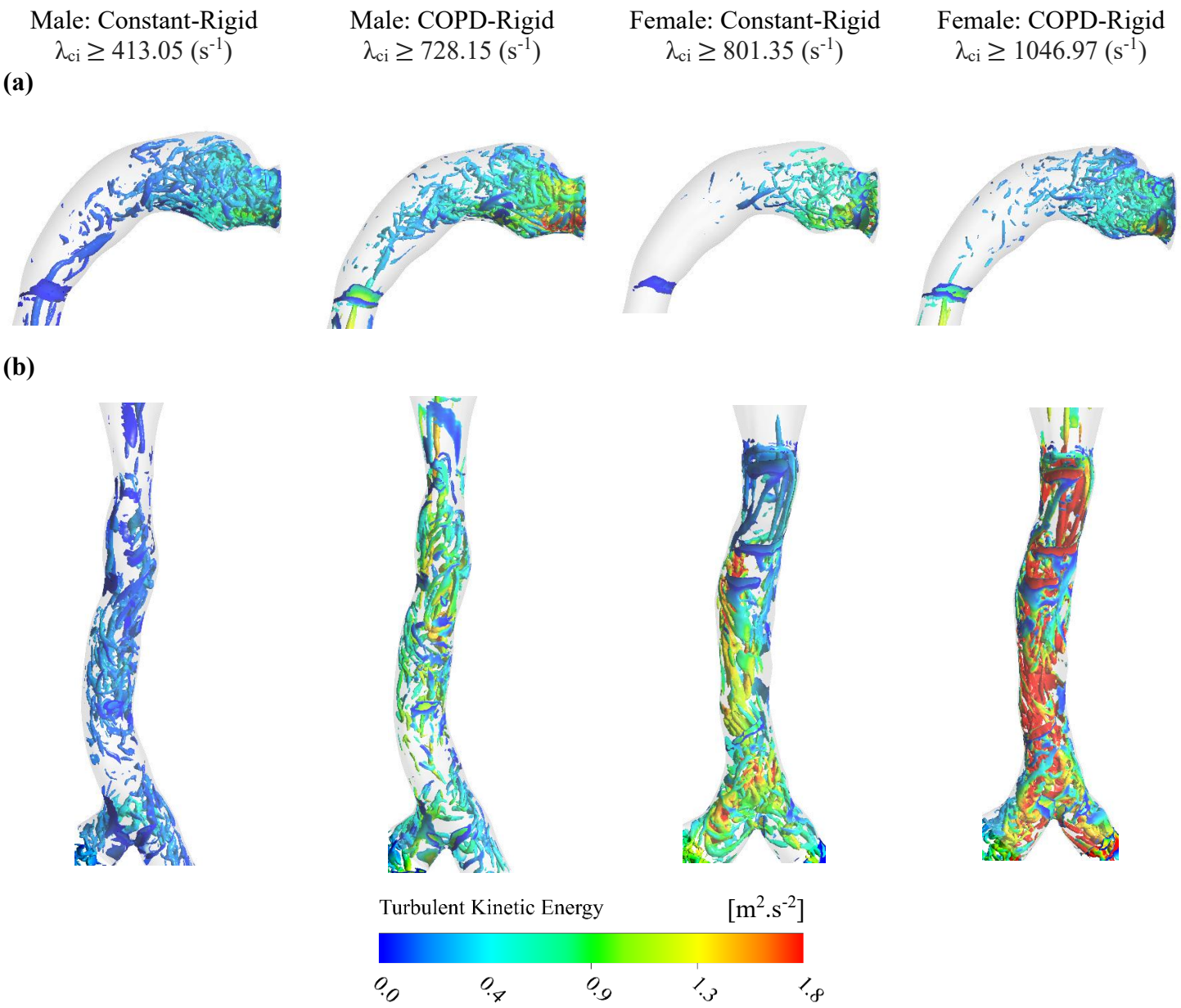

Fig. 7-10: Iso-surfaces of swirling strength (λ_{ci}) at a normalized threshold of 0.05, colored by turbulent kinetic energy (TKE), for male and female airway models under constant and COPD flow profiles with rigid wall conditions at: **(a)** the mouth region; and **(b)** the trachea and carina regions.

Fig. 7-11 shows the effect of flow rate on particle transport within the specific male airway during an inhalation cycle. As shown in **Figs. 7-11(a)** and **11(b)**, at 0.2 s, which is 0.1 s after injection is completed, 8.7% of the total injected particles (100 μg) reach the lung in the constant-rigid case. In contrast, in the COPD-rigid case, nearly 90% of the particles remain suspended in the MT region and trachea, with only a few passing beyond the trachea. **Figs. 7-11(c)** and **11(d)** show particle

positions at this stage. By 0.3 s, in the constant-rigid case, 20.87% of the total particle mass remains in the airflow, while 35.9% deposits on the airway walls and 43.23% escapes to the deep lung. Conversely, in the COPD-rigid case, where airflow reaches 30 L/min at 0.3 s, 80.97% of the particles remain suspended, and only 4.38% of the particles reach the lung. At 0.4 s, as the airflow increases in the COPD profile, the proportion of suspended particles decreases to 14.56%, while 55.23% of particles reach the lung. Beyond this time, the remaining particles in the COPD case travel deeper into the lung at a faster rate than in the constant-rigid case.

These results indicate that gradually increasing the breathing rate in patients with COPD initially slows particle transport. However, as inhalation continues, this increased flow rate enhances deposition in the deeper regions of the lung. Any interruption in the inhalation process, such as pausing, coughing, or changing the breathing patterns, can adversely affect the efficiency of drug delivery. Imai et al. (2012) demonstrate that holding one's breath increases particle deposition on airway walls by reducing fluid velocity, thereby making gravitational sedimentation the dominant mechanism of deposition.

Furthermore, this improvement in deep lung deposition, as demonstrated by a representative COPD breathing profile, highlights a key advantage of pMDIs. Aerosol generation in pMDIs is independent of the patient's inspiratory effort. However, it is important to interpret these results carefully, especially in relation to the type of inhaler used. Notably, Farkas et al. (2019) demonstrated that patients with more severe COPD often have reduced inspiratory capacity when using DPIs. This reduction can lead to lower flow rates and significantly decreased drug delivery to the lungs. While slower inhalation may enhance deep lung deposition with pMDIs, it can be detrimental for DPI use, where effective drug dispersion relies on a high inspiratory flow rate. Therefore, it is essential to consider the complex relationship between disease severity, inhalation patterns, and inhaler mechanics when assessing therapeutic outcomes in COPD.

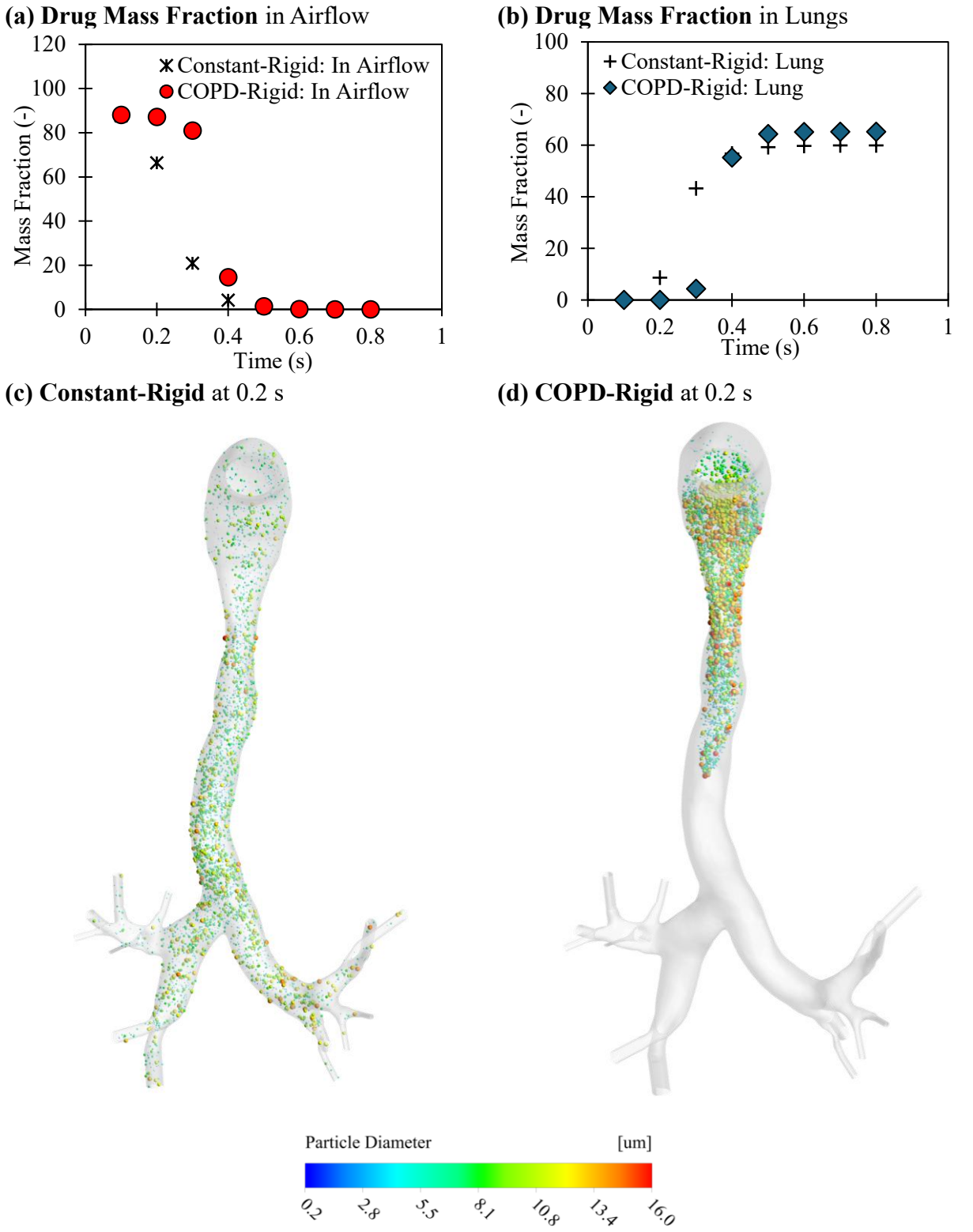

Fig. 7-11: Particle transport during inhalation between constant-rigid and COPD-rigid cases: **(a, b)** temporal variation of particle mass fraction suspended in the airflow and deposited in the lungs; and **(c, d)** spatial distribution of particles at 0.2 s.

7.5.1 Effect of the Dynamic Wall on Deposition Fraction

Figs. 7-12(a) and **12(b)** show the impact of airway wall motion on regional particle deposition and particle transport to the lungs at both constant and COPD flow rates in the specific male airway geometry analyzed. The results indicate that dynamic wall motion reduces particle deposition on airway walls across most regions compared with rigid wall conditions. Specifically, the overall deposition reduction in dynamic wall conditions is 4.15% at a constant flow rate of 30 L/min and 3% at a COPD flow rate.

However, particle deposition in the MT region increases at a constant flow rate of 30 L/min, rising from 13.08% to 16.74%, as shown in **Fig. 7-12(a)**. Meanwhile, **Fig. 7-12(b)** indicates that wall motion has minimal effect on particle transport to the left lung. In contrast, dynamic wall motion increases the number of particles reaching the deeper regions of the right lung by 4.38% at the constant flow rate and by 4.82% at the COPD flow rate. During one inhalation cycle, wall motion analysis shows a minor expansion around $t \approx 0.2$ s, followed by a contraction at $t \approx 0.8$ s, and a major expansion at $t \approx 1.7$ s, as illustrated in **Fig. 7-5(b)**. According to **Fig. 7-11(a)**, under the constant flow condition, 66.32% of total particles within the airway are influenced by the minor expansion phase. Still, most of these particles exit the airway before encountering the contraction phase. In contrast, under the COPD flow rate, 87.25% of the total particles at the first expansion peak accumulate in the MT region and the upper tracheal section. Following this, before reaching the second phase (contraction), only 0.01% of the particles remain in the airflow.

These findings highlight the potential interplay among inhalation duration, injection timing, and airway wall motion in particle deposition and transport. It is worth mentioning that in pMDIs, where injection time is short (0.1 s), most particles pass through the upper airway before wall motion significantly influences their trajectory. As a result, wall motion has a minimal impact on particle deposition. Inhaler devices with longer injection times, such as the Respimat soft mist inhaler (Mohammadkhani et al., 2025; Sadeghi et al., 2024, 2023), may be more susceptible to airway wall motion. This influence is particularly noticeable during wall contraction (approximately 0.8 s) and maximum wall expansion (around 1.7 s). During these times, particles are more likely to interact with the wall's dynamic movements.

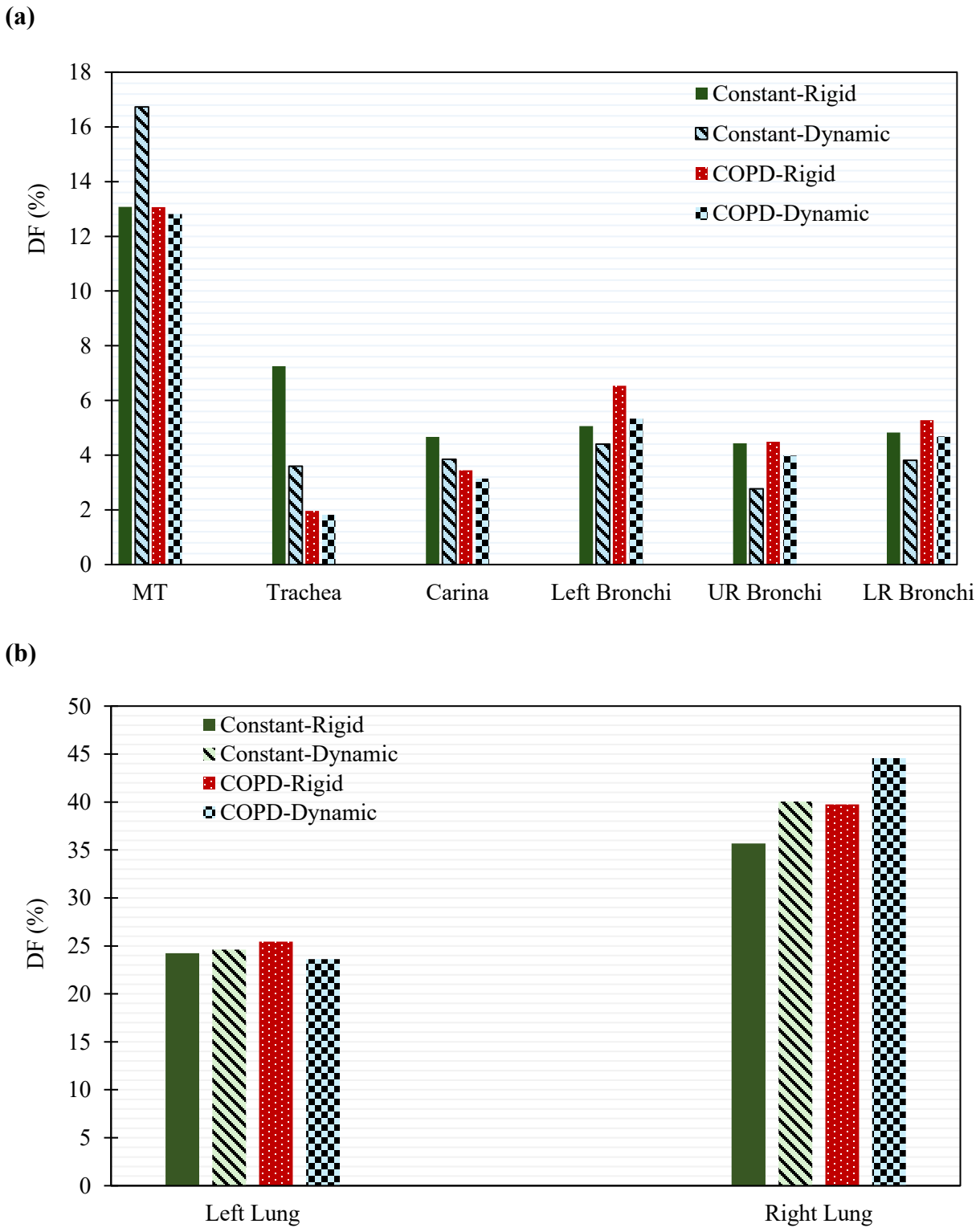

Fig. 7-12: Deposition fraction (DF) in the male **(a)** airway segments; and **(b)** lungs under different conditions. MT: mouth-throat, UR: upper-right, LR: lower-right.

Fig. 7-13 illustrates the effect of wall motion on airflow dynamics in the male airway's glottis region at the peak displacement times (t = 0.2 s and t = 0.8 s). The velocity contours and secondary flow vectors highlight key differences between rigid and dynamic wall conditions. At t = 0.2 s, during the initial maximum expansion, the wall moves outward by 0.05 mm. Under the constant-rigid wall condition, the velocity distribution remains relatively symmetric, with peak velocities concentrated near the center of the cross-section. The secondary flow vectors indicate limited circulatory motion within the glottis, suggesting a stable and predictable flow pattern. In contrast, at t = 0.8 s, the velocity slows slightly but becomes more complex and asymmetrical. The secondary flow vectors exhibit circulatory motion, with vortices forming near the center of the cross-section and increasing flow mixing. However, dynamic wall motion redistributes velocity, creating additional secondary flow structures.

In the COPD-rigid case, the early stage of an inhalation cycle exhibits relatively smooth, uniform airflow, as shown in **Fig. 7-9(b)**. However, wall motion during this stage introduces significant instability, as highlighted in the COPD-dynamic case at t = 0.2 s in **Fig. 7-13**, where pronounced vorticity develops in the region. At the peak of contraction (t = 0.8 s), the wall moved inward toward the glottal center, merging a symmetric vortex pair into a single, strong central vortex. In contrast, this central vortex splits into two distinct vortices under the COPD flow rate.

Airway motion exhibits subject-specific and regionally variable behavior, particularly in patients with respiratory conditions, due to differences in lung mechanics and airway elasticity (Armstrong et al., 2006; Gunatilaka et al., 2020; Schwab et al., 1993; Xiao et al., 2024). For instance, pulmonary fibrosis alters tidal volume and induces bronchiectasis, which significantly affects particle transport and deposition patterns. As demonstrated by Qin et al. (2022), changes in pulmonary fibrosis lead to a shift in microsphere deposition from the bronchial regions to the upper respiratory tract, thereby reducing the efficiency of deep lung delivery. Also, Xiao et al. (2024) used cine-MRI data to quantify airway movement in children's upper airways during breathing. They found that certain regions exhibited motion ranges exceeding 50% compared to adjacent areas. Although the overall velocity field remained similar between dynamic and static walls, notable differences were observed in the positioning of airflow jets and the size of recirculation regions. Similarly, Gunatilaka et al. (2020) examined inter-subject variability in airway motion and its impact on airflow dynamics. Their study, comparing static and dynamic airway models in healthy and tracheomalacia patients, revealed that anatomical changes and displacement variability

affect key parameters, including pressure drop, work of breathing, and tracheal resistance. In our study, the dynamic airway motion data were obtained from healthy individuals. While airway compliance may differ in patients with COPD, the applied motion patterns still represent physiologically relevant deformation and offer valuable insights into the effects of wall motion on particle transport and deposition.

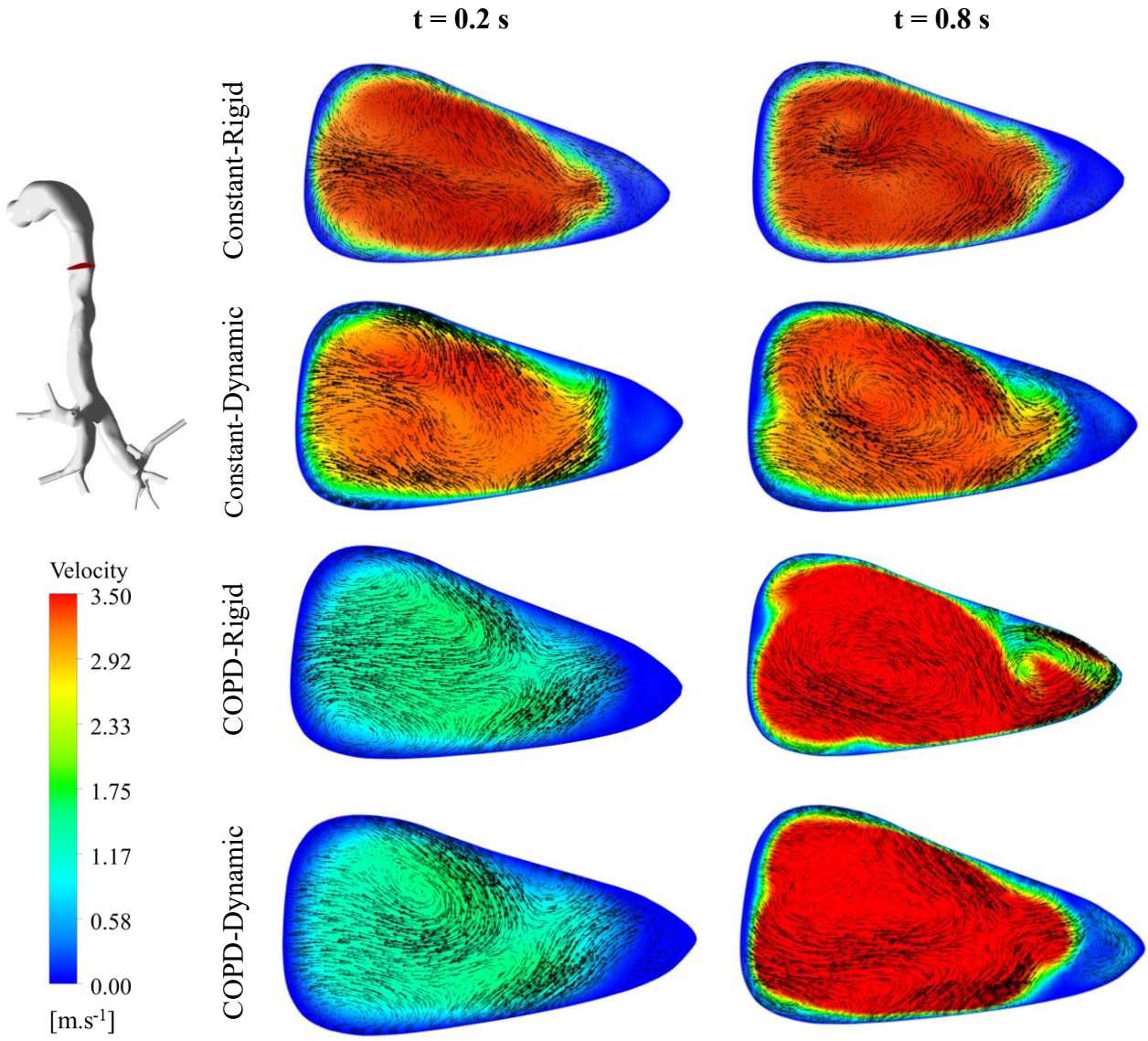

Fig. 7-13: Cross-sectional contour and vector plots of the flow field within the glottis region at displacement peaks (t = 0.2 s and t = 0.8 s) under different conditions (Jahed et al., 2025a).

7.5.2 Effect of Mucus Layer on Airflow Dynamics and Deposition Fraction

Fig. 7-14 illustrates the deposition fraction of inhaled particles across different airway regions under the COPD flow rate and both rigid and dynamic wall conditions. The analysis compares two scenarios: dry walls (no mucus layer) and walls with a mucus layer. The results indicate a small increase in deposition fraction in the deeper lung regions (left and right lungs) when a mucus layer is present, but the overall difference remains minimal. In the rigid wall case, approximately 0.5% more particles pass through the carina when the mucus layer is included. In the dynamic wall case, this increase is around 1.5% compared to the dry wall condition.

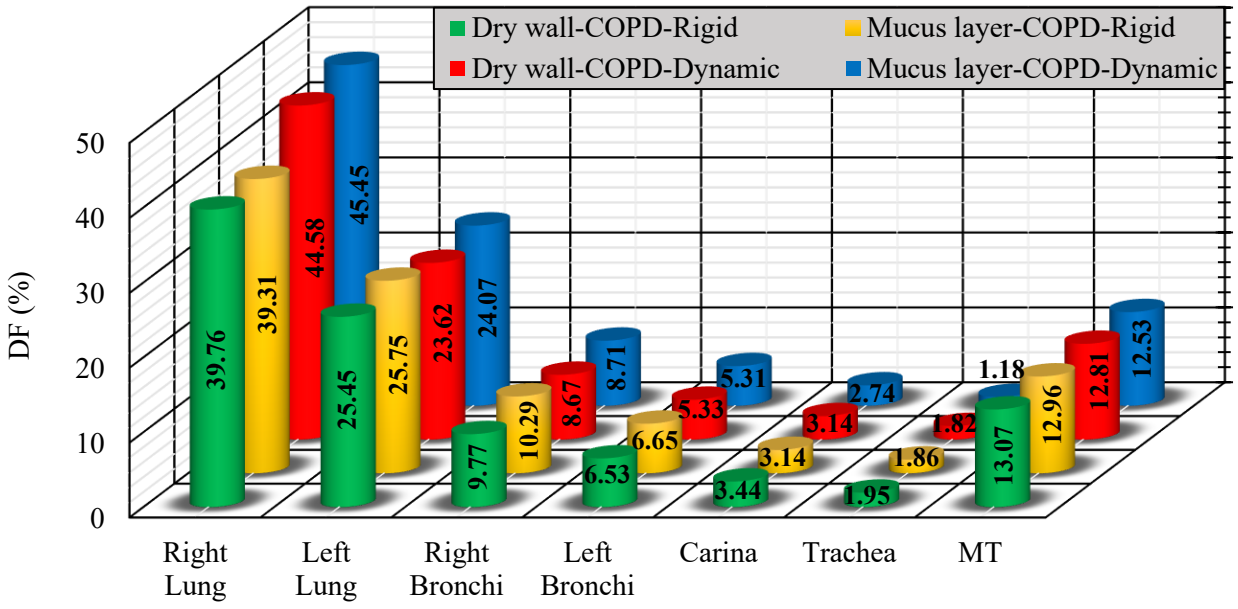

Fig. 7-14: Comparison of deposition fractions (DFs) in the male airway under different conditions, with and without a mucus layer. MT: mouth-throat.

In this study, we modeled the mucus layer but did not account for the hygroscopic properties of aerosolized particles. On the other hand, Longest et al. (2008) examined deposition fractions in models that both included and excluded hygroscopic properties. They found only minor differences attributable to hygroscopicity. However, their models did not account for a mucus layer. Jahed et al. (2024) found that droplet deposition in the MT region decreased when a mucus layer was present in the model, with this effect being highly dependent on droplet temperature. Similarly,

Chen et al. (2021) observed reduced droplet deposition when both mucus and hygroscopic effects were considered, although they noted that the inhalation flow rate had a more significant impact than realistic wall boundary conditions.

Although the mucus layer did not significantly alter the deposition fraction of inert particles, it substantially altered airflow conditions, as shown in **Fig. 7-15**. This figure shows the effect of the mucus layer on RH within the airway under COPD flow rate and dynamic wall conditions. Without a mucus layer (**Fig. 7-15(a)**), the RH distribution varies along the airway, with core flow maintaining high humidity (around 50%), but RH decreases near the walls. Since the wall temperature (37°C) does not contribute additional moisture, the air near the walls warms without absorbing water vapor, resulting in a drop in RH. In contrast, the presence of a mucus layer (**Fig. 7-15(b)**) significantly alters the RH distribution. RH levels near the airway walls increase to 90%–100%, particularly around the glottis, while core regions of the carina and left bronchi exceed 80%. This increase occurs because the mucus layer serves as a moisture source, releasing water vapor through evaporation and elevating local RH levels.

In addition to the effects of COPD flow rate (**Fig. 7-9**) and airway wall expansion and contraction (**Fig. 7-13**) on airflow patterns, **Fig. 7-16** illustrates how the mucus layer further modifies airflow dynamics. In the dry airway (**Fig. 7-16(a)**), greater mixing occurs, particularly in the upper airway region, indicating higher turbulence intensity. In contrast, when a mucus layer is present (**Fig. 7-16(b)**), the velocity field becomes more uniform with reduced fluctuations. The impact of the mucus layer is particularly evident at the carina and in the left bronchus.

Beyond airflow modulation, these changes influence wall shear stress (WSS), a key factor in maintaining airway epithelial integrity. Studies show that WSS is highest at airway bifurcations, reaching approximately 0.4185 Pa during peak airflow (Koombua and Pidaparti, 2008). During quiet breathing, WSS typically ranges from 0.05 to 0.3 Pa (Button and Boucher, 2008). However, during physical activity, increased airflow causes a notable increase in WSS. For instance, during high-intensity exercise like running, peak WSS can be approximately 5.9 times higher than during walking, at around 32.45 Pa (Tsega, 2022). Such variations in WSS, influenced by airway geometry, airflow rate, and tissue compliance, can contribute to airway disease progression when WSS deviates significantly, whether excessively high or low (Bilek et al., 2003; Huh et al., 2007; Sidhaye et al., 2008).

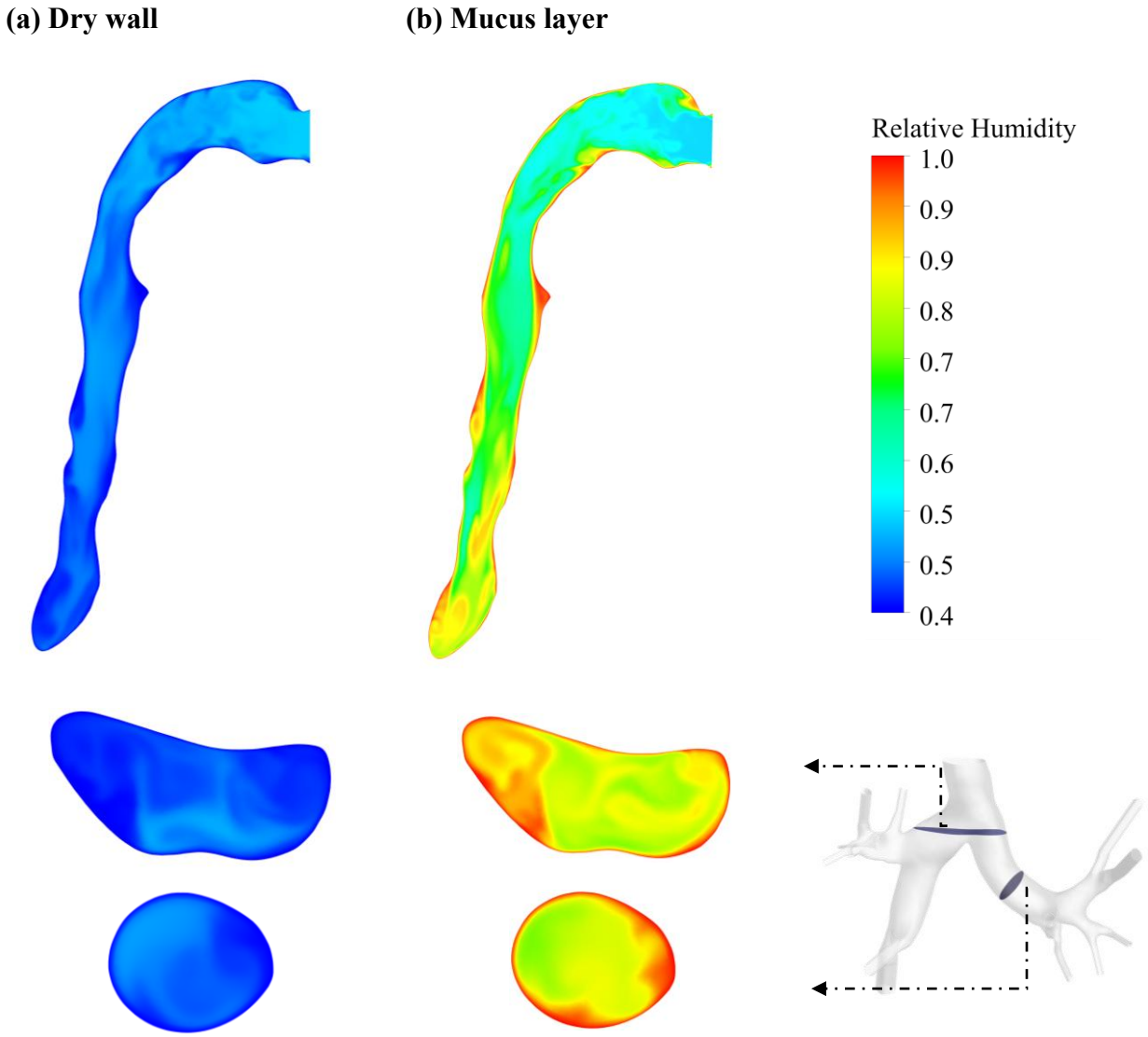

Fig. 7-15: Relative humidity (RH) contours on the middle plane and cross-sectional planes in the male airway (carina and left bronchus) under the COPD-dynamic condition. Comparison between **(a)** dry wall (without mucus); and **(b)** wall with a mucus layer.

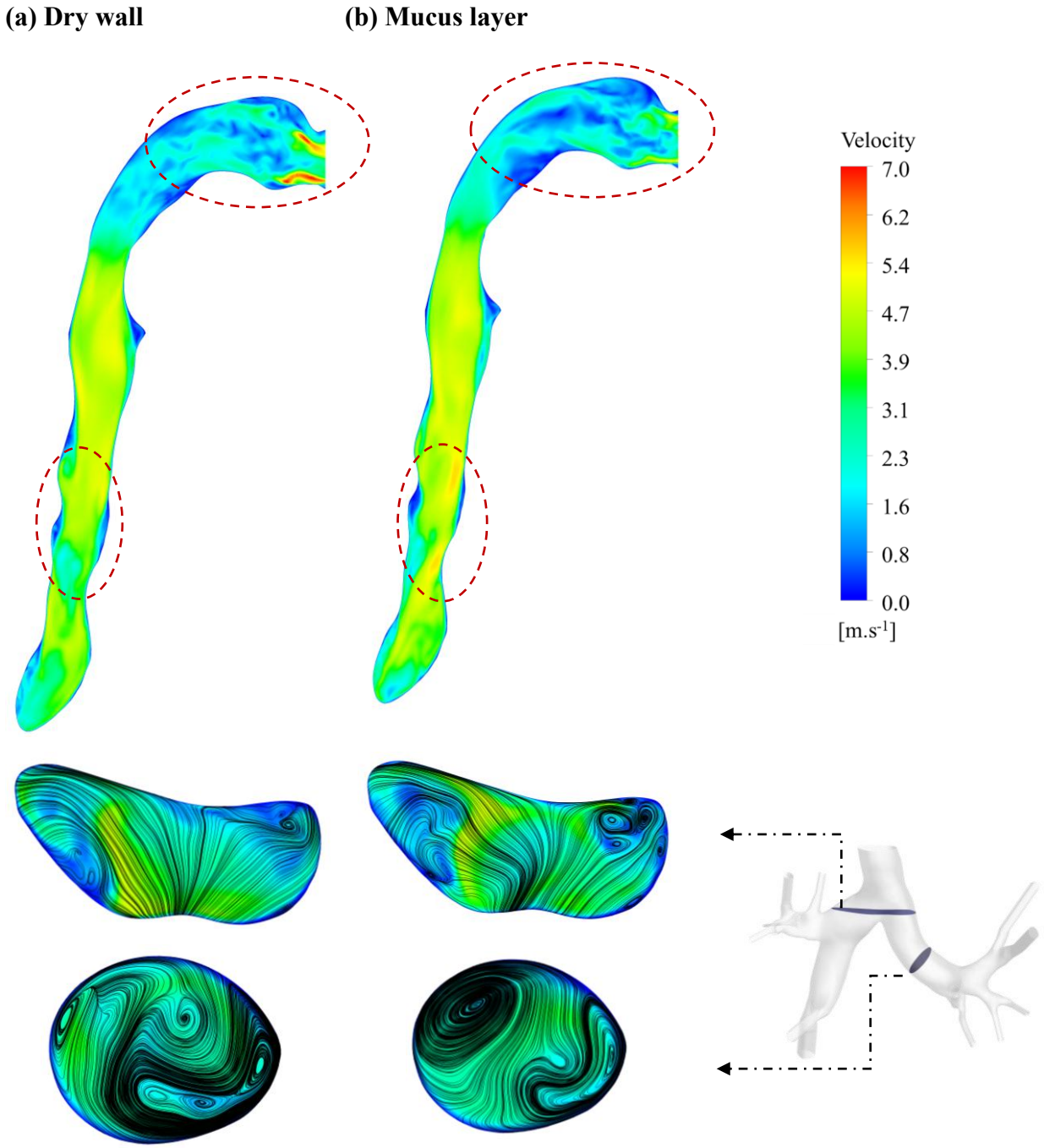

Fig. 7-16: Air velocity contours and streamlines on the middle plane and cross-sectional planes in the male airway (carina and left bronchus) under the COPD-dynamic condition. Comparison between **(a)** dry wall (without mucus); and **(b)** wall with a mucus layer.

Fig. 7-17 shows the effect of the mucus layer on WSS distribution across different regions of the male airway under the COPD-dynamics condition, both with and without a mucus layer, at a peak flow rate (t = 0.6 s). The results indicate that the presence of a mucus layer alters the distribution of shear stress, particularly in high-curvature regions and at bifurcations. Across all regions, the mucus layer generally reduces WSS intensity and smooths sharp variations (indicated by red dashed circles), particularly in areas of peak shear stress, thereby creating a smoother, more uniform flow along the airway walls. These findings emphasize the importance of accounting for airway surface conditions when evaluating shear stress effects, as regions of elevated WSS may correspond to disease-prone areas and provide insights into disease progression, severity, and treatment response (Evans et al., 2014; Huh et al., 2007; Nucci et al., 2003).

This study models the mucus layer as uniform and does not consider its rheological properties. In a healthy, well-hydrated mucus layer, local humidity is enhanced, which reduces velocity gradients and, consequently, the WSS. However, in pathological conditions such as COPD, cystic fibrosis, or asthma, mucus can become thick, exhibiting increased viscosity and elasticity (Dawson et al., 2003; Nielsen et al., 2004). This alteration can disrupt airflow and increase localized WSS by narrowing the airways (Erken et al., 2023; Haut et al., 2021).

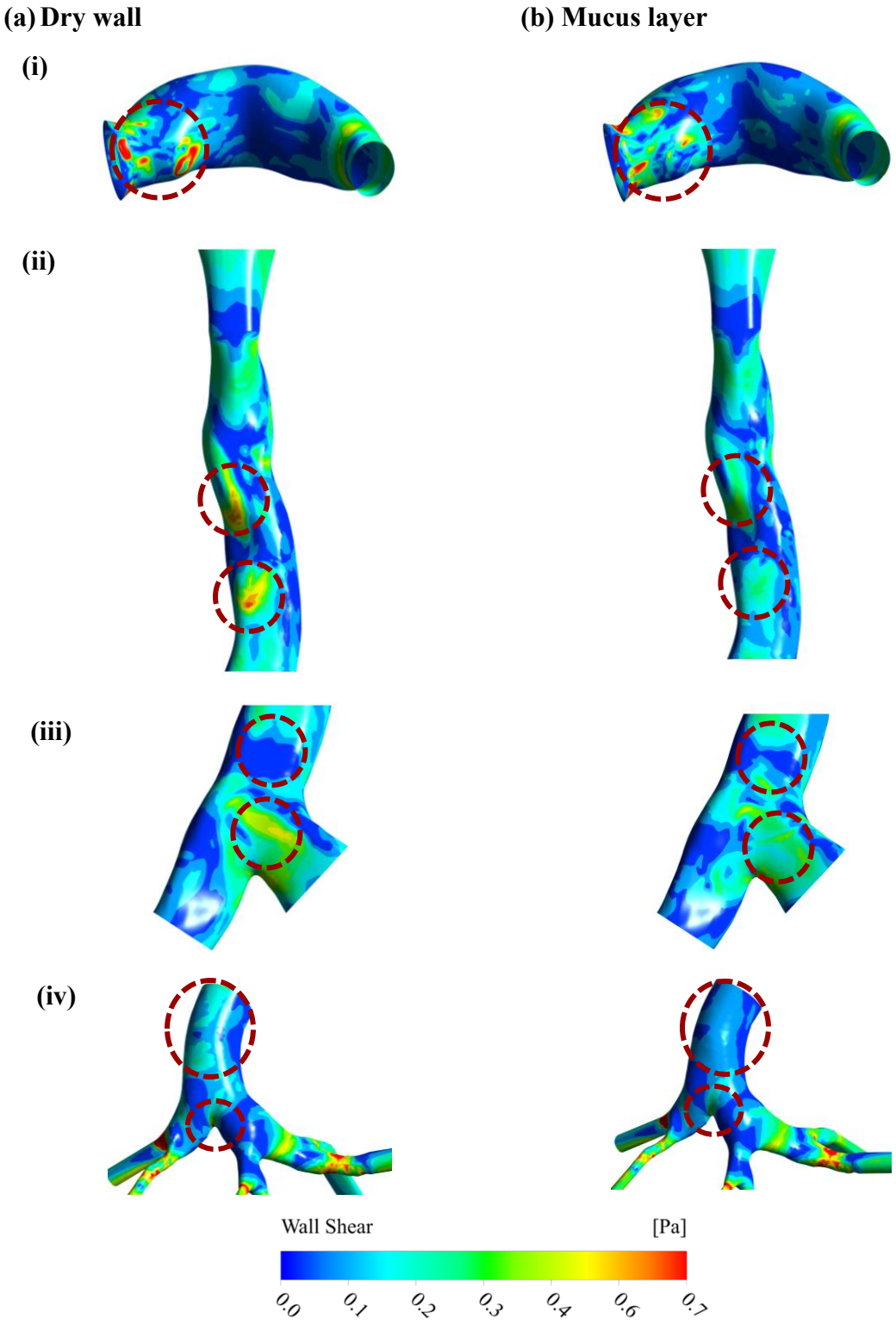

Fig. 7-17: Wall shear stress (WSS) contours in different regions of the male airway—(i) MT, (ii) trachea, (iii) carina, and (iv) left bronchi—under the COPD-dynamic condition. Comparison between **(a)** dry wall (without mucus); and **(b)** wall with a mucus layer.

In extreme cases, severe mucus buildup may even cause airway closure, creating high-shear stress regions upon reopening that can damage the epithelium and exacerbate disease progression. Erken et al. (2023) demonstrated that in COPD-affected airways, the viscoelastic properties of mucus, particularly its non-Newtonian, shear-thinning behavior, can result in higher WSS peaks during airway closure events. Their findings indicate that more viscous, elastic mucus increases resistance to airway reopening after collapse, leading to localized regions of high shear stress.-Although this study does not explicitly address airway closure, both studies emphasize the significant impact of airway surface conditions on WSS distribution and their implications for the progression and treatment of COPD.

7.6 Conclusions

This study explores the intricate relationship between airway wall dynamics, transient breathing patterns, and the thermophysical and transport properties of the mucus layer, with a focus on their impact on airflow behaviour, drug aerosol transport, and deposition from a pMDI. We analyzed these interactions by accounting for realistic anatomical differences between male and female airways. This allowed for a more detailed understanding of airflow and particle deposition, reflecting the complexity of actual anatomy compared to simplified models.

The results demonstrate that anatomical differences in the airway geometries of the specific male and female subjects studied significantly impact aerosol deposition patterns. The narrower female airway generated higher airflow velocities and turbulence, particularly in the trachea, leading to increased upper-airway deposition, with approximately 48% of particles being lost before reaching the bronchi. In contrast, the wider male airway model used in this study allowed more particles to penetrate deeper into the bronchial tree, with only 32% of the particles lost in the upper airway. Comparisons between constant and COPD flow rates revealed that the gradual increase in flow associated with COPD initially reduces turbulence and upper airway deposition, thereby facilitating deeper particle transport. In our male airway model, this effect resulted in a 16.35% increase in the amount of drug reaching the lungs. Notably, the female model exhibited a more pronounced 55.4% reduction in tracheal deposition under COPD flow conditions.

Airway wall motion decreased overall deposition by 4.15% and 3% under constant and COPD flow conditions, respectively. However, due to the short injection duration of pMDIs (0.1 s), the impact of wall motion on deposition patterns was limited, as most particles passed through the

upper airway before significant wall displacement occurred. Devices with longer injection durations, such as soft-mist inhalers, may exhibit more pronounced effects of airway motion on deposition patterns. The mucus layer did not significantly alter overall particle deposition, but it did influence airflow dynamics through heat- and mass-transfer interactions. Changes in airflow dynamics altered velocity gradients, which, in turn, affected WSS. Both factors (airflow dynamics and WSS) safeguard the integrity of the airway epithelium. In fact, abnormal levels of WSS, whether extremely high or low, can contribute to worsening airway diseases.

This study analyzes drug delivery through pMDIs using gender-specific airway models with enhanced anatomical detail. Although the analysis focuses on only two patients, it provides valuable insights for pharmaceutical companies seeking to optimize inhaler devices tailored to different genders. By tailoring the aerosol plume characteristics to gender-specific needs, these inhalers can enhance drug delivery efficiency and improve therapeutic outcomes.

7.7 Limitations and Future Directions

- Only one male and one female airway model were analyzed. While these geometries provide valuable gender-related insights, they cannot fully represent the variability across the population. Future work will incorporate multiple patient-specific models with diverse anatomical features.
- Dynamic wall motion was prescribed using an upper airway displacement profile. Real airway deformation is heterogeneous and may vary along the bronchial tree. More realistic motion patterns obtained from imaging or physiological models could improve prediction accuracy.
- The simulations used representative breathing patterns, including COPD-like conditions, but did not include individualized flow rate profiles for each patient. Future studies should integrate patient-specific inhalation data to capture realistic inter-individual variability.
- The mucus layer was assumed to be stationary with uniform thickness and temperature-dependent properties. Its complex rheology, spatially varying thickness, and potential movement during inhalation were not included. Incorporating mucus dynamics would allow more accurate prediction of near-wall deposition and drug retention.

- Droplets did not significantly influence the airflow field due to low mass loading. In reality, dense pMDI sprays may alter local turbulence and mixing. Including fully coupled two-way or four-way interactions would improve modeling accuracy.
- Deposition in deeper lung regions was not examined, even though therapeutic outcomes depend heavily on distal airway delivery. Extending the model into several bronchial generations would allow assessment of total system efficiency.
- Aerosol droplets were assumed to retain their initial size. Evaporation, hygroscopic growth in humid airways, and potential interactions with mucus could significantly modify droplet diameter and deposition patterns.

7.8 Nomenclature

3D	three dimensional
CAD	computer-aided design
CFD	computational fluid dynamics
COPD	chronic obstructive pulmonary disease
CPU	central processing unit
CT	computed tomography
DF	deposition fraction
DICOM	digital imaging and communication in medicine
DPI	dry powder inhaler
DPM	discrete phase model
ET	extrathoracic
EWF	Eulerian wall film
EX	experimental
F	female
G	generation
GHz	gigahertz

GiB	gibibyte
HFA	hydrofluoroalkane
HPLC	high-performance liquid chromatography
LES	large eddy simulation
LR	lower-right
M	male
MDI	metered-dose inhaler
MRI	magnetic resonance imaging
MT	mouth-throat
PIV	particle image velocimetry
PLA	polylactic acid
RAM	random access memory
RH	relative humidity
RMSE	root mean square error
SD	standard deviation
SIMPLEC	semi-implicit method for pressure-linked equations-consistent
STL	stereolithography
TB	tracheobronchial
TKE	turbulent kinetic energy
UDF	user-defined function
UR	upper-right
VCU	Virginia Common-wealth University
WALE	wall-adapting local eddy viscosity
WSS	wall shear stress

Notations

$\vec{J}_s$	diffusion flux of species ($kg/m^2.s$)
$\bar{S}_{ij}$	filtered rate-of-strain tensor ($1/s$)
$\dot{m}_s$	mass source ($kg/m^2.s$)
$\dot{m}_{vap}$	mass vaporization or condensation rate ($kg/m^2.s$)
$\dot{q}_{imp}$	source term due to airflow and particle impingement on the wall (W/m^2)
$\overline{\boldsymbol{u}}_{\boldsymbol{p}}$	particle velocity (m/s)
$\bar{\tau}_{eff}$	effective shear stress (Pa)
h_c	convective heat transfer coefficient ($W/m^2.K$)
h_s	species enthalpy (J/kg)
A_p	particle surface area (m^2)
C_{Dd}	drag force coefficient (-)
C_w	WALE constant (-)
Re_p	particle Reynolds number (-)
S_{ij}^d	modified rate-of-strain tensor ($1/s$)
S_s	source term ($kg/m^2.s$)
T_f	film temperature (K)
T_m	film half-depth temperature (K)
T_s	film surface temperature (K)
T_w	wall temperature (K)
Y_s	species mass fraction (-)
b_i	constants of polynomial function (-)
c_p	particle heat capacity ($J/kg\,.K$)
$\vec{g}$	gravitational acceleration (m/s^2)

k_B	Boltzmann constant (-)
k_K	Von Kármán constant (-)
k_{eff}	effective conductivity ($W/m.K$)
k_t	turbulent thermal conductivity ($W/m.K$)
v_t	turbulent eddy viscosity (m^2/s)
$\overline{\boldsymbol{P}}$	filtered pressure (Pa)
$\overline{\boldsymbol{u}}$	filtered velocity (m/s)
α_t	turbulent thermal diffusivity (m^2/s)
ζ_i	stochastic coefficient (-)
μ_t	turbulent dynamic viscosity ($Pa.s$)
ρ_f	film density (kg/m^3)
$\bar{\bar{\sigma}}$	stress tensor (Pa)
$\bar{\bar{\tau}}$	subgrid-scale stress (Pa)
λ_{ci}	swirling strength
C_c	Cunningham correction (-)
C_D	drag coefficient (-)
d_p	particle diameter (m)
E	thermal energy (J)
$\boldsymbol{F_i}$	body force (N)
H	film height (m)
m_p	particle mass (kg)
T	temperature (K)
λ	molecular mean free path (m)
μ	mixture dynamic viscosity ($Pa.s$)

ρ_p	particle density (kg/m^3)
L	latent heat (J/kg)
Nu	Nusselt number (-)
Pr	Prandtl number (-)
V	computational cell volume (m^3)
d	distance (m)
k	thermal conductivity ($W/m.K$)
v	molecular kinematic viscosity (m^2/s)
μ	molecular viscosity of fluid ($Pa.s$)
ρ	fluid density (kg/m^3)
$\boldsymbol{\rho}$	mixture density (kg/m^3)

7.9 References

Aghaei, Y., Sajadi, B., Ahmadi, G., 2023. The effect of the mucus layer and the inhaled air conditions on the droplets fate in the human nasal cavity: A numerical study. J. Aerosol Sci. 171, 106163. https://doi.org/10.1016/j.jaerosci.2023.106163

Ahookhosh, K., Saidi, M., Aminfar, H., Mohammadpourfard, M., Hamishehkar, H., Yaqoubi, S., 2020. Dry powder inhaler aerosol deposition in a model of tracheobronchial airways: Validating CFD predictions with in vitro data. Int. J. Pharm. 587, 119599. https://doi.org/10.1016/j.ijpharm.2020.119599

Ahookhosh, K., Saidi, M., Mohammadpourfard, M., Aminfar, H., Hamishehkar, H., Farnoud, A., Schmid, O., 2021. Flow structure and particle deposition analyses for optimization of a pressurized metered dose inhaler (pMDI) in a model of tracheobronchial airway. Eur. J. Pharm. Sci. 164, 105911. https://doi.org/10.1016/j.ejps.2021.105911

Anzai, H., Shindo, Y., Kohata, Y., Hasegawa, M., Takana, H., Matsunaga, T., Akaike, T., Ohta, M., 2022. Coupled discrete phase model and Eulerian wall film model for numerical simulation of respiratory droplet generation during coughing. Sci. Rep. 12.

https://doi.org/10.1038/s41598-022-18788-3

Armstrong, J.J., Leigh, M.S., Sampson, D.D., Walsh, J.H., Hillman, D.R., Eastwood, P.R., 2006. Quantitative upper airway imaging with anatomic optical coherence tomography. Am. J. Respir. Crit. Care Med. 173, 226–233. https://doi.org/10.1164/rccm.200507-1148OC

Australia, A., n.d. Smoke Doesn't Cause Asthma Attacks; It Causes Respiratory Attacks [WWW Document]. URL https://airphysioaustralia.com.au/smoke-doesnt-cause-asthma-attacks-it-causes-respiratory-attacks/

Bates, A.J., Schuh, A., Amine-Eddine, G., McConnell, K., Loew, W., Fleck, R.J., Woods, J.C., Dumoulin, C.L., Amin, R.S., 2019. Assessing the relationship between movement and airflow in the upper airway using computational fluid dynamics with motion determined from magnetic resonance imaging. Clin. Biomech. 66, 88–96. https://doi.org/10.1016/j.clinbiomech.2017.10.011

Bhardwaj, S., Koullapis, P., Kassinos, S.C., Sznitman, J., 2022. Fate of inhaled aerosols under the influence of glottal motion in a realistic in silico human tracheobronchial tree model. Eur. J. Pharm. Sci. 173. https://doi.org/10.1016/j.ejps.2022.106172

Bilek, A.M., Dee, K.C., Gaver, D.P., 2003. Mechanisms of surface-tension-induced epithelial cell damage in a model of pulmonary airway reopening. J. Appl. Physiol. 94, 770–783. https://doi.org/10.1152/japplphysiol.00764.2002

Biswas, R., Hanania, N.A., Sabharwal, A., 2017. Factors determining in vitro lung deposition of albuterol aerosol delivered by ventolin metered-dose inhaler. J. Aerosol Med. Pulm. Drug Deliv. 30, 256–266. https://doi.org/10.1089/jamp.2015.1278

Button, B., Boucher, R.C., 2008. Role of mechanical stress in regulating airway surface hydration and mucus clearance rates. Respir. Physiol. Neurobiol. 163, 189–201. https://doi.org/10.1016/j.resp.2008.04.020

Chen, L., Ma, H., Liu, G., Cui, X., Xu, Q., 2023. Dust transport law and deposition characteristic in coal workers' respiratory tract based on CFD simulations. Powder Technol. 427, 118760. https://doi.org/10.1016/j.powtec.2023.118760

Chen, W.-H., Chen, C.-H., Chang, M.-H., 2025. Exploring nanoparticles in lungs under COPD

conditions for nanospray drug flow and deposition: CFD simulations and AI predictions. Int. J. Pharm. 678, 125740. https://doi.org/10.1016/j.ijpharm.2025.125740

Chen, X., Kleinstreuer, C., Zhong, W., Feng, Y., Zhou, X., 2018. Effects of thermal airflow and mucus-layer interaction on hygroscopic droplet deposition in a simple mouth–throat model. Aerosol Sci. Technol. 52, 900–912. https://doi.org/10.1080/02786826.2018.1476751

Chen, X., Zhou, X., Xia, X., Xie, X., Lu, P., Feng, Y., 2021. Modeling of the transport, hygroscopic growth, and deposition of multi-component droplets in a simplified airway with realistic thermal boundary conditions. J. Aerosol Sci. 151. https://doi.org/10.1016/j.jaerosci.2020.105626

Das, P., Nof, E., Amirav, I., Kassinos, S.C., Sznitman, J., 2018. Targeting inhaled aerosol delivery to upper airways in children: Insight from computational fluid dynamics (CFD). PLoS One 13. https://doi.org/10.1371/journal.pone.0207711

Dawson, M., Wirtz, D., Hanes, J., 2003. Enhanced viscoelasticity of human cystic fibrotic sputum correlates with increasing microheterogeneity in particle transport. J. Biol. Chem. 278, 50393–50401. https://doi.org/10.1074/jbc.M309026200

Di Cicco, M., Kantar, A., Masini, B., Nuzzi, G., Ragazzo, V., Peroni, D., 2021. Structural and functional development in airways throughout childhood: Children are not small adults. Pediatr. Pulmonol. 56, 240–251. https://doi.org/10.1002/ppul.25169

Ding, H., Zhang, Y., Sun, C., Yang, Y., Wen, C., 2022. Numerical simulation of supersonic condensation flows using Eulerian-Lagrangian and Eulerian wall film models. Energy 258, 124833. https://doi.org/10.1016/j.energy.2022.124833

Dominelli, P.B., Molgat-Seon, Y., 2022. Sex, gender and the pulmonary physiology of exercise. Eur. Respir. Rev. 31. https://doi.org/10.1183/16000617.0074-2021

Duke, D.J., Scott, H.N., Kusangaya, A.J., Kastengren, A.L., Matusik, K., Young, P., Lewis, D., Honnery, D., 2019. Drug distribution transients in solution and suspension-based pressurised metered dose inhaler sprays. Int. J. Pharm. 566, 463–475. https://doi.org/10.1016/j.ijpharm.2019.05.067

Dunbar, C.A., 1997. Atomization mechanisms of the pressurized metered dose inhaler. Part. Sci.

Technol. 15, 253–271. https://doi.org/10.1080/02726359708906771

Eisner, A.D., Graham, R.C., Martonen, T.B., 1990. Coupled mass and energy transport phenomena in aerosol/vapor-laden gases-I. theory of the hygroscopic aerosol effects on temperature and relative humidity patterns of inspired air. J. Aerosol Sci. 21, 833–848. https://doi.org/10.1016/0021-8502(90)90156-R

Erken, O., Fazla, B., Muradoglu, M., Izbassarov, D., Romanò, F., Grotberg, J.B., 2023. Effects of elastoviscoplastic properties of mucus on airway closure in healthy and pathological conditions. Phys. Rev. Fluids 8, 1–26. https://doi.org/10.1103/PhysRevFluids.8.053102

Evans, D.J., Green, A.S., Thomas, N.K., 2014. Wall shear stress distributions in a model of normal and constricted small airways. Proc. Inst. Mech. Eng. Part H J. Eng. Med. 228, 362–370. https://doi.org/10.1177/0954411914527586

Farkas, Á., Lizal, F., Jedelsky, J., Elcner, J., Horváth, A., Jicha, M., 2019. Simulation of airway deposition of an aerosol drug in COPD patients. Pharmaceutics 11, 1–10. https://doi.org/10.3390/pharmaceutics11040153

Farkas, Á., Lizal, F., Jedelsky, J., Elcner, J., Karas, J., Belka, M., Misik, O., Jicha, M., 2020. The role of the combined use of experimental and computational methods in revealing the differences between the micron-size particle deposition patterns in healthy and asthmatic subjects. J. Aerosol Sci. 147. https://doi.org/10.1016/j.jaerosci.2020.105582

Feng, Y., Zhao, J., Hayati, H., Sperry, T., Yi, H., 2021a. Tutorial : Understanding the transport , deposition , and translocation of particles in human respiratory systems using Computational Fluid-Particle Dynamics and Physiologically Based Toxicokinetic models. J. Aerosol Sci. 151, 105672. https://doi.org/10.1016/j.jaerosci.2020.105672

Feng, Y., Zhao, J., Hayati, H., Sperry, T., Yi, H., 2021b. Tutorial: Understanding the transport, deposition, and translocation of particles in human respiratory systems using Computational Fluid-Particle Dynamics and Physiologically Based Toxicokinetic models. J. Aerosol Sci. 151, 105672. https://doi.org/10.1016/j.jaerosci.2020.105672

Ferron, G.A., Kreyling, W.G., Haider, B., 1988. Inhalation of salt aerosol particles—II. growth and deposition in the human respiratory tract. J. Aerosol Sci. 19, 611–631.

https://doi.org/https://doi.org/10.1016/0021-8502(88)90213-3

Ferron, G.A., Oberdörster, G., Henneberg, R., 1989. Estimation of the deposition of aerosolized drugs in the human respiratory tract due to hygroscopic growth. J. Aerosol Med. Depos. Clear. Eff. Lung 2, 271–284. https://doi.org/10.1089/jam.1989.2.271

Ferron, G.A., Upadhyay, S., Zimmermann, R., Karg, E., 2013. Model of the deposition of aerosol particles in the respiratory tract of the rat. II. hygroscopic particle deposition. J. Aerosol Med. Pulm. Drug Deliv. 26, 101–119. https://doi.org/10.1089/jamp.2011.0965

Finlay, W.H., 2019. The Mechanics of Inhaled Pharmaceutical Aerosols: An Introduction. Elsevier Science.

Finlay, W.H., Stapleton, K.W., 1995. The effect on regional lung deposition of coupled heat and mass transfer between hygroscopic droplets and their surrounding phase. J. Aerosol Sci. 26, 655–670. https://doi.org/10.1016/0021-8502(94)00132-I

Foster, W.M., Langenback, E.G., Bergofsky, E.H., 1982. Lung mucociliary function in man: interdependence of bronchial and tracheal mucus transport velocities with lung clearance in bronchial asthma and healthy subjects, in: WALTON, W.H. (Ed.), Inhaled Particles V. Pergamon, pp. 227–244. https://doi.org/https://doi.org/10.1016/B978-0-08-026838-5.50020-9

Fröhlich, E., Mercuri, A., Wu, S., Salar-Behzadi, S., 2016. Measurements of deposition, lung surface area and lung fluid for simulation of inhaled compounds. Front. Pharmacol. 7, 1–10. https://doi.org/10.3389/fphar.2016.00181

Gemci, T., Ponyavin, V., Collins, R., Corcoran, T.E., Saha, S.C., Islam, M.S., 2022. CFD study of dry pulmonary surfactant aerosols deposition in upper 17 generations of human respiratory tract. Atmosphere (Basel). 13, 1–18. https://doi.org/10.3390/atmos13050726

Gessner, T., 2001. Dynamic mesh adaption for supersonic combustion waves modeled with detailed reaction mechanisms. Freiburg (Breisgau), Univ., Diss.

Gou, D., Zhu, Q., Chan, H., Kourmatzis, A., Cheng, S., Yang, R., 2024. Effects of the deformation and size of the upper airway on the deposition of aerosols. Int. J. Pharm. 124165. https://doi.org/10.1016/j.ijpharm.2024.124165

Gunatilaka, C.C., Schuh, A., Higano, N.S., Woods, J.C., Bates, A.J., 2020. The effect of airway motion and breathing phase during imaging on CFD simulations of respiratory airflow. Comput. Biol. Med. 127, 104099. https://doi.org/10.1016/j.compbiomed.2020.104099

Haddrell, A.E., Davies, J.F., Miles, R.E.H., Reid, J.P., Dailey, L.A., Murnane, D., 2014. Dynamics of aerosol size during inhalation: Hygroscopic growth of commercial nebulizer formulations. Int. J. Pharm. 463, 50–61. https://doi.org/10.1016/j.ijpharm.2013.12.048

Haut, B., Nonclercq, A., Buess, A., Rabineau, J., Rigaut, C., Sobac, B., 2021. Comprehensive analysis of heat and water exchanges in the human lungs. Front. Physiol. 12. https://doi.org/10.3389/fphys.2021.649497

He, C., Ahmadi, G., 1998. Particle deposition with thermophoresis in laminar and turbulent duct flows. Aerosol Sci. Technol. 29, 525–546. https://doi.org/10.1080/02786829808965588

Huh, D., Fujioka, H., Tung, Y.C., Futai, N., Paine, R., Grotberg, J.B., Takayama, S., 2007. Acoustically detectable cellular-level lung injury induced by fluid mechanical stresses in microfluidic airway systems. Proc. Natl. Acad. Sci. U. S. A. 104, 18886–18891. https://doi.org/10.1073/pnas.0610868104

Ilegbusi, O.J., Islam, A., Santhanam, A.P., 2023. Computational modelling of airflow in distal airways using hybrid lung model. Math. Comput. Model. Dyn. Syst. 29, 186–207. https://doi.org/10.1080/13873954.2023.2243087

Imai, Y., Miki, T., Ishikawa, T., Aoki, T., Yamaguchi, T., 2012. Deposition of micrometer particles in pulmonary airways during inhalation and breath holding. J. Biomech. 45, 1809–1815. https://doi.org/10.1016/j.jbiomech.2012.04.017

Islam, M.S., Larpruenrudee, P., Hossain, S.I., Rahimi-Gorji, M., Gu, Y., Saha, S.C., Paul, G., 2021. Polydisperse aerosol transport and deposition in upper airways of age-specific lung. Int. J. Environ. Res. Public Health 18. https://doi.org/10.3390/ijerph18126239

Jahed, M., Kozinski, J., Pakzad, L., 2025. Airway wall dynamics during inhalation on drug delivery via pMDIs using patient-specific airway models, in: Respiratory Drug Delivery Europe. Respiratory Drug Delivery 2025, pp. 120–123.

Jahed, M., Kozinski, J., Pakzad, L., 2024. Mucus, airway and plume temperature effects on

pMDI-drug delivery in a mouth-throat airway: Experimental and numerical studies. J. Aerosol Sci. 181, 106436. https://doi.org/10.1016/j.jaerosci.2024.106436

Jahed, M., Kozinski, J., Pakzad, L., 2023. The impact of actuator nozzle and surroundings condition on drug delivery using pressurized-metered dose inhalers. Biomech. Model. Mechanobiol. 22, 2117–2133. https://doi.org/10.1007/s10237-023-01754-x

Kadota, K., Inoue, N., Matsunaga, Y., Takemiya, T., Kubo, K., Imano, H., Uchiyama, H., Tozuka, Y., 2020. Numerical simulations of particle behaviour in a realistic human airway model with varying inhalation patterns. J. Pharm. Pharmacol. 72, 17–28. https://doi.org/10.1111/jphp.13195

Kadota, K., Matsumoto, K., Uchiyama, H., Tobita, S., Maeda, M., Maki, D., Kinehara, Y., Tachibana, I., Sosnowski, T.R., Tozuka, Y., 2022. In silico evaluation of particle transport and deposition in the airways of individual patients with chronic obstructive pulmonary disease. Eur. J. Pharm. Biopharm. 174, 10–19. https://doi.org/10.1016/j.ejpb.2022.03.010

Kakimpa, B., Morvan, H., Hibberd, S., 2016. The depth-averaged numerical simulation of laminar thin-film flows with capillary waves. J. Eng. Gas Turbines Power 138. https://doi.org/10.1115/1.4033471

Kakimpa, B., Morvan, H.P., Hibberd, S., 2015. Solution strategies for thin film rimming flow modelling, in: Volume 5C: Heat Transfer. American Society of Mechanical Engineers, pp. 1–9. https://doi.org/10.1115/GT2015-43503

Kamm, R.D., 1999. Airway wall mechanics. Annu. Rev. Biomed. Eng. 1, 47–72. https://doi.org/10.1146/annurev.bioeng.1.1.47

Kim, C.S., Hu, S.C., 1998. Regional deposition of inhaled particles in human lungs; comparison between men and women. J. Appl. Physiol. 84, 1834–1844. https://doi.org/10.1152/jappl.1998.84.6.1834

Kolewe, E.L., Padhye, S., Woodward, I.R., Feng, Y., Briddell, J.W., Fromen, C.A., 2023. A pediatric upper airway library to evaluate interpatient variability of in silico aerosol deposition. AAPS PharmSciTech 1–13. https://doi.org/10.1208/s12249-023-02619-3

Koombua, K., Pidaparti, R.M., 2008. Inhalation induced stresses and flow characteristics in

human airways through fluid-structure interaction analysis. Model. Simul. Eng. 2008. https://doi.org/10.1155/2008/358748

Lee, C.Y., Cant, S., 2017. Assessment of LES subgrid-scale models and investigation of hydrodynamic behaviour for an axisymmetrical bluff body flow. Flow, Turbul. Combust. 98, 155–176. https://doi.org/10.1007/s10494-016-9751-4

Li, P., Guo, W., Fan, J., Su, C., Zhao, X., Xu, X., 2023. Aerosol deposition in the pulmonary acinar region : Influence of wall motion and interparticle collisions. J. Aerosol Sci. 167, 106077. https://doi.org/10.1016/j.jaerosci.2022.106077

Longest, P.W., Hindle, M., Das Choudhuri, S., Xi, J., 2008. Comparison of ambient and spray aerosol deposition in a standard induction port and more realistic mouth-throat geometry. J. Aerosol Sci. 39, 572–591. https://doi.org/10.1016/j.jaerosci.2008.03.008

Longest, P.W., Tian, G., Walenga, R.L., Hindle, M., 2012. Comparing MDI and DPI aerosol deposition using in vitro experiments and a new stochastic individual path (SIP) model of the conducting airways. Pharm. Res. 29, 1670–1688. https://doi.org/10.1007/s11095-012-0691-y

Martonen, T.B., 1982. Analytical model of hygroscopic particle behavior in human airways. Bull. Math. Biol. 44, 425–442. https://doi.org/10.1007/BF02462290

Mary, I., Sagaut, P., 2001. Large eddy simulation of flow around a high lift airfoil, Direct and Large-Eddy Simulation IV.

Menache, M.G., Grahamt, R.C., 1997. Conducting airway geometry as a function of age. Ann. Occup. Hyg. 41, 531–536. https://doi.org/10.1093/annhyg/41.inhaled_particles_viii.531

Mirzaaghaian, A., Zhao, M., Rahman, M.M., Dong, K., 2024. Numerical simulation of targeted drug delivery to different regions of realistic human lung model under realistic aerosol breathing condition. Powder Technol. 444, 120039. https://doi.org/10.1016/j.powtec.2024.120039

Mišík, O., Prinz, F., Elcner, J., Cabalka, M., Bělka, M., Lízal, F., 2025. Influence of nebulizer pressure drop on breathing profiles and aerosol deposition in human airways. J. Aerosol Sci. 188, 106620. https://doi.org/10.1016/j.jaerosci.2025.106620

Mohammadkhani, M., Kozinski, J., Pakzad, L., 2025. Atomization characteristics of soft mist inhaler (SMI) devices: aerosolized particle delivery through the respiratory tract—an innovative numerical and experimental study. J. Aerosol Sci. 106593. https://doi.org/10.1016/j.jaerosci.2025.106593

Moore, K.L., Dalley, A.F., Agur, A.M.R., 2006. Clinically Oriented Anatomy, Clinically Oriented Anatomy. Lippincott Williams & Wilkins.

Morrow, P.E., 1986. Factors determining hygroscopic aerosol deposition in airways. Physiol. Rev. 66, 330–376. https://doi.org/10.1152/physrev.1986.66.2.330

Morsi, S.A., Alexander, A.J., 1972. An investigation of particle trajectories in two-phase flow systems. J. Fluid Mech. 55, 193–208. https://doi.org/10.1017/S0022112072001806

Narayanan, J.K., Lin, J., Feng, Y., Cui, X., 2022. Numerical study on the impact of mucus layer and inlet air-temperatures on the particle deposition in a highly idealized mouth-throat model using LES. Powder Technol. 395, 455–475. https://doi.org/10.1016/j.powtec.2021.09.073

Newman, S.P., 2017. Drug delivery to the lungs: challenges and opportunities. Ther. Deliv. 8, 647–661. https://doi.org/10.4155/tde-2017-0037

Nicoud, F., Ducros, F., 1999. Subgrid-scale stress modelling based on the square of the velocity. Flow Meas. Instrum. 62, 183–200. https://doi.org/https://doi.org/10.1023/A:1009995426001

Nielsen, H., Hvidt, S., Sheils, C.A., Janmey, P.A., 2004. Elastic contributions dominate the viscoelastic properties of sputum from cystic fibrosis patients. Biophys. Chem. 112, 193–200. https://doi.org/10.1016/j.bpc.2004.07.019

Nucci, G., Suki, B., Lutchen, K., 2003. Modeling airflow-related shear stress during heterogeneous constriction and mechanical ventilation. J. Appl. Physiol. 95, 348–356. https://doi.org/10.1152/japplphysiol.01179.2001

O'Rourke, P.J., Amsden, A.A., 1996. A particle numerical model for wall film dynamics in port-injected engines, in: SAE Technical Papers. https://doi.org/10.4271/961961

Oliveira, R.F., Teixeira, S., Teixeira, J.C., Silva, L.F., Antunes, H., 2012. pMDI sprays: theory,

experiment and numerical simulation, in: Liu, C. (Ed.), Advances in Modeling of Fluid Dynamics. IntechOpen, Rijeka. https://doi.org/10.5772/46099

Paz, C., Suárez, E., Parga, O., Vence, J., 2017. Glottis effects on the cough clearance process simulated with a CFD dynamic mesh and Eulerian wall film model. Comput. Methods Biomech. Biomed. Engin. 20, 1326–1338. https://doi.org/10.1080/10255842.2017.1360872

Prinz, F., Kánská, J., Elcner, J., Hájek, O., Kummerländer, A., Krause, M.J., Jícha, M., Lízal, F., 2025. Transport and deposition of inhaled fibers in a realistic female airway model: A combined experimental and numerical study. Comput. Biol. Med. 194, 110473. https://doi.org/10.1016/j.compbiomed.2025.110473

Pritchard, J.N., Jane Jefferies, S., Black, A., 1986. Sex differences in the regional deposition of inhaled particles in the 2.5–7.5 μm size range. J. Aerosol Sci. 17, 385–389. https://doi.org/10.1016/0021-8502(86)90110-2

Qin, Z., Shi, Y., Qiao, J., Lin, G., Tang, B., Li, X., Zhang, J., 2022. CFD simulation of porous microsphere particles in the airways of pulmonary fibrosis. Comput. Methods Programs Biomed. 225, 107094. https://doi.org/10.1016/j.cmpb.2022.107094

Rahman, M.M., Zhao, M., Islam, M.S., Dong, K., Saha, S.C., 2021. Aging effects on airflow distribution and micron-particle transport and deposition in a human lung using CFD-DPM approach. Adv. Powder Technol. 32, 3506–3516. https://doi.org/10.1016/j.apt.2021.08.003

Ranz, W.E., Marshall, W.R., 1952. Evaporation from drops : Part II. Chem. Eng. Prog. 48, 173–180.

Ren, S., Li, W., Wang, L., Shi, Y., Cai, M., Hao, L., Luo, Zihao, Niu, J., Xu, W., Luo, Zujin, 2020. Numerical analysis of airway mucus clearance effectiveness using assisted coughing techniques. Sci. Rep. 10, 1–10. https://doi.org/10.1038/s41598-020-58922-7

Rubinstein, I., England, S.J., Zamel, N., Hoffstein, V., 1989. Glottic dimensions in healthy men and women. Respir. Physiol. 77, 291–299. https://doi.org/10.1016/0034-5687(89)90117-5

Sadeghi, T., Fatehi, P., Pakzad, L., 2024. Effect of nasal inhalation on drug particle deposition and size distribution in the upper airway: with soft mist inhalers. Ann. Biomed. Eng. https://doi.org/10.1007/s10439-023-03423-7

Sadeghi, T., Pakzad, L., Fatehi, P., 2023. Evaluation of soft mist inhaler aerosol velocity, size, and deposition inside the mouth - A computational fluid dynamics study. J. Biomech. Eng. 145. https://doi.org/10.1115/1.4056967

Schwab, R.J., Gefter, W.B., Pack, A.I., Hoffman, E.A., 1993. Dynamic imaging of the upper airway during respiration in normal subjects. J. Appl. Physiol. 74, 1504–1514. https://doi.org/10.1152/jappl.1993.74.4.1504

Shang, Y., Dong, J., Tian, L., Inthavong, K., Tu, J., 2019. Detailed computational analysis of flow dynamics in an extended respiratory airway model. Clin. Biomech. 61, 105–111. https://doi.org/10.1016/j.clinbiomech.2018.12.006

Sheth, P., Grimes, M.R., Stein, S.W., Myrdal, P.B., 2017. Impact of droplet evaporation rate on resulting in vitro performance parameters of pressurized metered dose inhalers. Int. J. Pharm. 528, 360–371. https://doi.org/10.1016/j.ijpharm.2017.06.014

Sidhaye, V.K., Schweitzer, K.S., Caterina, M.J., Shimoda, L., King, L.S., 2008. Shear stress regulates aquaporin-5 and airway epithelial barrier function. Proc. Natl. Acad. Sci. U. S. A. 105, 3345–3350. https://doi.org/10.1073/pnas.0712287105

Sosnowski, T.R., 2021. Inhaled aerosols: Their role in COVID-19 transmission, including biophysical interactions in the lungs. Curr. Opin. Colloid Interface Sci. 54, 101451. https://doi.org/10.1016/j.cocis.2021.101451

Sou, T., Bergström, C.A.S., 2021. Contemporary formulation development for inhaled pharmaceuticals. J. Pharm. Sci. 110, 66–86. https://doi.org/10.1016/j.xphs.2020.09.006

Sturm, R., 2016. Total deposition of ultrafine particles in the lungs of healthy men and women: experimental and theoretical results. Ann. Transl. Med. 4, 1–10. https://doi.org/10.21037/atm.2016.06.05

Sul, B., Altes, T., Ruppert, K., Qing, K., Hariprasad, D.S., Morris, M., Reifman, J., 2019. Dynamics of the tracheal airway and its influences on respiratory airflows: An exemplar study. J. Biomech. Eng. 141, 1–12. https://doi.org/10.1115/1.4043723

Talaat, M., Si, X., Liu, X., Xi, J., 2022. Count- and mass-based dosimetry of MDI spray droplets with polydisperse and monodisperse size distributions. Int. J. Pharm. 623, 121920.

https://doi.org/10.1016/j.ijpharm.2022.121920

Tian, G., Longest, P.W., Su, G., Hindle, M., 2011. Characterization of respiratory drug delivery with enhanced condensational growth using an individual path model of the entire tracheobronchial airways. Ann. Biomed. Eng. 39, 1136–1153. https://doi.org/10.1007/s10439-010-0223-z

Tsega, E.G., 2022. CFD simulations of respiratory airflow in human upper airways response to walking and running for oral breathing condition. Heliyon 8, e10039. https://doi.org/10.1016/j.heliyon.2022.e10039

Walenga, R.L., Longest, P.W., 2016. Current inhalers deliver very small doses to the lower tracheobronchial airways: Assessment of healthy and constricted lungs. J. Pharm. Sci. 105, 147–159. https://doi.org/10.1016/j.xphs.2015.11.027

Wang, X., Chang, H., Corradini, M., Cong, T., Wang, J., 2016. Prediction of falling film evaporation on the AP1000 passive containment cooling system using ANSYS FLUENT code. Ann. Nucl. Energy 95, 168–175. https://doi.org/10.1016/j.anucene.2016.05.014

Wilcox, D.C., 1993. Turbulence Modelling for CFD 3rd Edition, Turbulence Modeling for CFD.

Williams, J., Kolehmainen, J., Cunningham, S., Ozel, A., Wolfram, U., 2022. Effect of patient inhalation profile and airway structure on drug deposition in image-based models with particle-particle interactions. Int. J. Pharm. 612, 121321. https://doi.org/10.1016/j.ijpharm.2021.121321

Xi, J., April Si, X., Dong, H., Zhong, H., 2018. Effects of glottis motion on airflow and energy expenditure in a human upper airway model. Eur. J. Mech. B/Fluids 72, 23–37. https://doi.org/10.1016/j.euromechflu.2018.04.011

Xi, J., Longest, P.W., 2008. Effects of oral airway geometry characteristics on the diffusional deposition of inhaled nanoparticles. J. Biomech. Eng. 130, 13–17. https://doi.org/10.1115/1.2838039

Xia, Y., Ali, A.B.H., Khaware, A., Cao, J., 2024. Numerical simulation of liquid film evaporation and condensation for water reactors. Proc. World Congr. Momentum, Heat Mass Transf. 1–12. https://doi.org/10.1115/icmfht24.148

Xiao, Q., Gunatilaka, C., McConnell, K., Bates, A., 2024. The effect of including dynamic imaging derived airway wall motion in CFD simulations of respiratory airflow in patients with OSA. Sci. Rep. 14, 1–11. https://doi.org/10.1038/s41598-024-68180-6

Xu, C., Zheng, X., Shen, S., 2021. A numerical study of the effects of ambient temperature and humidity on the particle growth and deposition in the human airway. Environ. Res. 200, 111751. https://doi.org/10.1016/j.envres.2021.111751

Yang, X.L., Liu, Y., Luo, H.Y., 2006. Respiratory flow in obstructed airways. J. Biomech. 39, 2743–2751. https://doi.org/10.1016/j.jbiomech.2005.10.009

Zhang, R., Song, X., Zhan, S., Hu, J., Tan, W., 2017. Investigation of influence factors on particle size measurement with pMDI. Biomed. Res. 28, 9582–9588.

Zhang, Z., Kleinstreuer, C., Hyun, S., 2012. Size-change and deposition of conventional and composite cigarette smoke particles during inhalation in a subject-specific airway model. J. Aerosol Sci. 46, 34–52. https://doi.org/10.1016/j.jaerosci.2011.12.002

Zhang, Z., Kleinstreuer, C., Kim, C.S., 2002. Micro-particle transport and deposition in a human oral airway model. J. Aerosol Sci. 33, 1635–1652. https://doi.org/10.1016/S0021-8502(02)00122-2

Zhao, J., Feng, Y., Fromen, C.A., 2020. Glottis motion effects on the particle transport and deposition in a subject-specific mouth-to-trachea model: A CFPD study. Comput. Biol. Med. 116, 103532. https://doi.org/10.1016/j.compbiomed.2019.103532

Chapter 8 - How Breathing Interruptions Influence pMDI Aerosol Delivery: A CFD Study in a Realistic Airway

8.1 Introduction

Effective drug delivery to the lungs remains a substantial challenge in the treatment of respiratory diseases, despite the long-standing use of inhalers. Among the various devices available, pressurized metered-dose inhalers (pMDIs) are commonly prescribed for managing conditions such as asthma and chronic obstructive pulmonary disease (COPD) (Biswas et al., 2017; Kaviratna et al., 2019; Kunda et al., 2017; Sheth et al., 2017). However, their effectiveness is highly dependent on the patient's inhalation technique and breathing pattern during use (Dolovich and Dhand, 2011; Kadota et al., 2020; P. G. Koullapis et al., 2018).

Misuse of pMDIs is a widespread issue, with reported error rates ranging from 14% to as high as 90% (Giraud and Roche, 2002; McFadden, 1995). Giraud and Roche (2002) demonstrated that even after prior education and technique checks, over 66% of patients still misused their pMDIs, highlighting concerns surrounding improper use and its impact on inhaler efficiency. One of the most critical errors is poor coordination, specifically failing to synchronize actuation with inhalation. This issue affects all age groups but is particularly common among children, older adults, and individuals with severe respiratory distress (Bell and Newman, 2007; Crompton, 1982; Giraud and Roche, 2002; McFadden, 1995).

Talaat et al. (2022b) developed an MDI–mouth–lung model extending to generation 9 (G9) to investigate the effects of actuation timing on drug delivery. They found that late actuation increased drug loss in the mouth and reduced deposition in the pharynx, larynx, and lungs, although the reduction in lung dose itself was not noticeable. In contrast, early actuation, occurring before inhalation, reduced drug loss in the mouth, pharynx, and larynx, nearly doubling deposition in the tracheobronchial region. Despite a slightly higher loss within the device itself, early actuation remarkably enhanced lung drug delivery. On the other hand, Biswas et al. (2017) reported, in an *in-vitro* study using an idealized mouth-throat (MT) model, that optimal delivery occurred when the pMDI was actuated during the first half of inhalation at higher flow rates.

A serious issue arises from errors in inhalation technique. Studies indicate that most patients commit multiple errors; for instance, 24% either stop inhalation upon actuation or unintentionally

breathe through the nose. Such errors are often linked to the so-called "cold Freon" effect from the propellant, which can trigger coughing and, in some cases, paradoxical bronchospasm (Bell and Newman, 2007; Bunnag et al., 2007; Crompton, 1982; Giraud and Roche, 2002). Furthermore, Giraud and Roche (2002) reported that the frequency of pMDI misuse increases with age, with 61.0% of patients aged 15–30 years misusing their inhalers, compared to 85.9% among those aged 75 years or older. These findings raise critical concerns about whether sufficient medication actually reaches the intended site, potentially undermining the treatment's therapeutic effectiveness.

Most *in-silico* studies (Ahookhosh et al., 2021; Borojeni et al., 2023; Cui et al., 2018; Sadeghi et al., 2025, 2024; Williams et al., 2022) and *in-vitro* experiments (Golshahi et al., 2013a; Lewis et al., 2016) have focused on how patient-specific inhalation and exhalation flow patterns influence particle transport and deposition within the respiratory airways. For instance, Koullapis et al. (2018) simulated particle deposition over a complete breathing cycle in a simplified deep lung model extending from generation 10 to the pulmonary acinar region. Their results showed that particles larger than 5 μm exhibited high deposition rates (up to 82%), primarily in the bronchial airways during inhalation. In contrast, submicron particles (those smaller than 1 μm) showed minimal retention, with up to 90% being exhaled. Notably, particles ranging from 1 to 5 μm showed greater deposition in both the conducting airways and the acinar region during exhalation than during inhalation. Similarly, Biswas et al. (2017) conducted *in-vitro* experiments to evaluate the effects of inspiratory flow rate, inhalation duration, and MDI actuation timing on lung deposition using an albuterol HFA-MDI (Ventolin). Their results highlighted that proper synchronization of inhaler actuation with inhalation was the most critical factor for maximizing lung drug delivery. Additionally, higher inspiratory flow rates and longer inhalation durations further improved deposition efficiency.

While previous studies have advanced our understanding of aerosol behavior under ideal or controlled breathing conditions, the effects of irregular or disrupted inhalation patterns, often caused by patient errors during inhaler use, remain largely unexplored. In practice, patients rarely breathe in perfectly controlled patterns. Instead, unexpected events, such as holding the breath immediately after actuation, premature exhalation, or coughing during inhalation, can significantly alter airflow dynamics and drug deposition profiles.

This study investigates the impact of the aforementioned irregular inhalation patterns on aerosol transport and deposition from pMDIs. A realistic male airway model, extending from the oral cavity to the fourth bronchial generation, was used to simulate airflow and particle dynamics. Large-eddy simulation combined with the discrete phase model (LES–DPM) in ANSYS Fluent was employed to analyze the effects of a single, timed pause in inhalation, as well as premature exhalation and coughing. To ensure the reliability of the computational results, an experimental study was conducted under controlled conditions to validate the simulation outputs. In both computational and experimental studies, the airflow rate was maintained at 30 L/min, with ambient conditions set to a temperature of 22 °C and a relative humidity (RH) of 50%.

8.2 Experimental Setup and Methodology

The geometry of the tracheobronchial tree, including branches up to the fourth generation (G4), was reconstructed from computed tomography (CT) data of a 60-year-old male patient with COPD. The scans were obtained from the Iran Imaging Center (Tabriz, Iran) and anonymized prior to analysis, retaining only age and sex. Use of the data was approved by the institutional authority in accordance with local ethical guidelines. The CT dataset consisted of 249 slices, each 0.5 mm thick, stored in the Digital Imaging and Communications in Medicine (DICOM) format. These images were imported into the medical imaging software 3D Slicer for segmentation and 3D reconstruction of the airway. The resulting geometry was then exported in stereolithography (STL) format and imported into SOLIDWORKS® 2022 (Dassault Systèmes) for surface smoothing (see **Fig. 8-1(a)**).

Given the limited availability of high-resolution, full-length scans extending from the oral cavity to G4 in a single subject, we adopted a composite modeling approach, a strategy previously established in the literature (Longest et al., 2012b; Tian et al., 2011; Xi et al., 2018). Specifically, we combined the medium-sized MT model from Virginia Commonwealth University (VCU) with the CT-derived tracheobronchial tree to create a complete airway geometry. This airway geometry (from the oral cavity to G4) was then physically replicated with a wall thickness of 2 mm using fused deposition modeling (FDM) and polylactic acid (PLA) filament on an UltiMaker S3 3D printer (Netherlands). **Fig. 8-1(a)** illustrates the experimental setup, which includes a pMDI connected to the airway replica and fitted with a mouthpiece. A commercially available Salbutamol HFA pMDI (Ventolin® bioequivalent, produced by SANIS Health, Canada) was used, delivering

100 µg of Salbutamol Sulphate per actuation across 200 metered doses.

To collect the deposited particles, the branch outlets were connected to 0.3 µm pore size filters (303 Respirgard II™, Vital Signs Inc., USA) using silicone tubing. Airflow was generated by a vacuum pump (HCP5, Copley Scientific, UK) and regulated through a critical flow controller (Copley Scientific, UK), as illustrated in **Figs. 8-1(c)** and **1(d)**. A flow meter (Copley Scientific, UK) ensured a steady flow rate of 30 L/min and verified the system's integrity by confirming the absence of leaks.

All experiments were conducted in a controlled environment, maintaining a temperature of 22 ± 2 °C and a RH of 50 ± 5%. Before each test, the inhaler was shaken and securely attached to the airway replica. It was actuated five times at 15-second intervals to ensure adequate drug delivery to both the airway model and the collection filters. After each run, the airway segments were rinsed with high-performance liquid chromatography (HPLC)-grade water containing 0.1% formic acid (Fisher Scientific, US). Drug quantification was performed using a ZORBAX Eclipse XDB-C18 column (5 µm, 4.6 × 150 mm) maintained at 40 °C, together with a 1525 Binary HPLC pump and a 2489 UV/Visible detector (Waters, US). Additional experimental details are available in Jahed et al. (2025).

8.3 CFD Model Development

8.3.1 Geometry and Mesh

The airway geometry, depicted in **Fig. 8-1(e)**, was discretized using a hybrid mesh consisting of tetrahedral elements in the fluid domain with prism layers near the walls, as illustrated in **Fig. 8-1(f)** for the lower right bronchi and at the inlet. Meshing was performed in ANSYS Workbench 2020R2 (ANSYS, Inc.), utilizing ten inflation layers applied to the walls. A thickness transition ratio of 0.27 was employed to ensure adequate near-wall resolution.

Mesh independence for this airway model was previously evaluated in section 7.4.1. In that study, four mesh resolutions were tested: 1,640,346 elements (Mesh A), 3,303,011 elements (Mesh B), 6,584,095 elements (Mesh C), and 12,944,933 elements (Mesh D). Convergence was assessed by comparing velocity magnitudes across different regions of the airway. Based on those results, Mesh C was selected for all simulations reported here, as it provided sufficient resolution without incurring unnecessary computational costs.

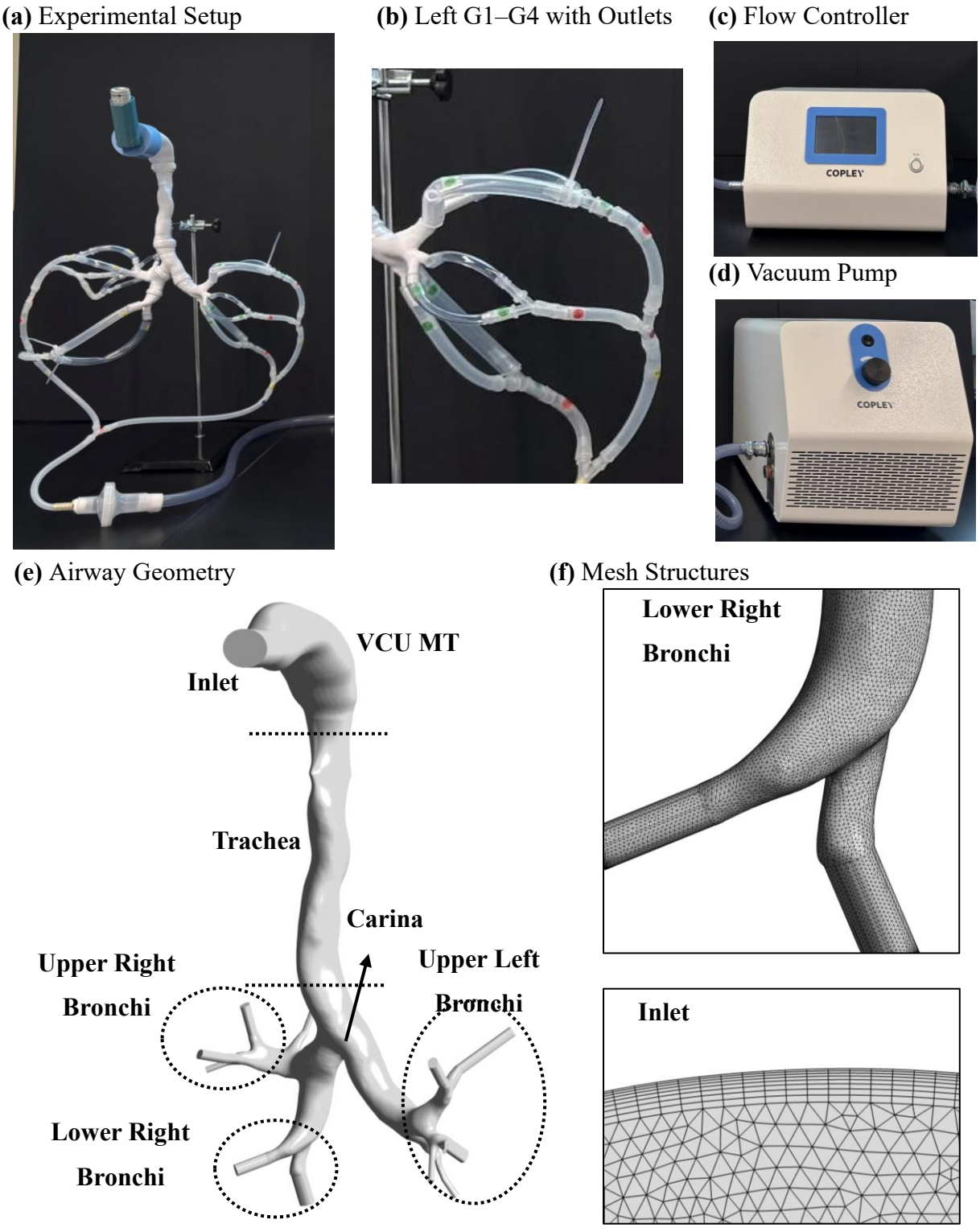

Fig. 8-1: **(a)** Experimental setup comprising a Salbutamol HFA pMDI connected to a composite airway replica with the medium-sized VCU MT model; **(b)** left bronchial branches (G1-G4) with outlets; **(c)** flow controller (TPK 2000, Copley Scientific, UK); **(d)** vacuum pump (HCP5, Copley Scientific, UK); **(e)** CAD representation of the airway geometry; and **(f)** sample mesh structure in the lower right bronchi with prismatic inflation layers at the inlet.

8.3.2 Governing Equations

We utilized the large eddy simulation (LES) model, incorporating the wall-adapting local eddy-viscosity (WALE) subgrid-scale model, to capture the transitional and turbulent airflow characteristics within the airway (Gemci et al., 2022; Shang et al., 2019). The airflow was treated as incompressible, Newtonian, and unsteady. The governing equations for the fluid phase consist of the continuity equation (Eq. (4.1)) and the Navier–Stokes momentum equation (Eq. (4.2)). The subgrid-scale (SGS) stress tensor is defined in Eqs. (4.12)–(4.14).

To model aerosol transport, the Lagrangian discrete phase model (DPM) was used to track individual particles injected from the pMDI into the airway geometry. Given the highly dilute nature of the aerosol, with a mass loading of only 0.16%, particle–particle interactions were considered negligible (Dunbar, 1997; Oliveira et al., 2012; Rahman et al., 2021; Xu et al., 2021). The particle size distribution followed the Rosin-Rammler formulation, with diameters ranging from 0.1 to 25 μm (Jahed et al., 2025). Particle dynamics were governed by Newton's second law (Eqs. (7.10)-(7.15)), which accounted for drag, gravitational, and Brownian forces as the primary mechanisms influencing motion.

At the model inlet, a COPD-specific inhalation profile was imposed, as shown in **Fig. 8-2(a)**. This time-dependent profile was derived from Biswas et al. (2017), who characterized the inhalation behavior of asthma and COPD patients using MDIs. To reflect real-world variability and interruptions during inhalation, three alternative profiles were also examined: (i) an inhalation with a pause (**Fig. 8-2(b)**), (ii) unintentional exhalation (**Fig. 8-2(c)**), and (iii) a cough-induced airflow disturbance, based on Particle Image Velocimetry (PIV) measurements reported by Oh et al. (2022) (shown in **Fig. 8-2(d)**), all occurring before peak flow. These profiles were implemented in the model as transient tables.

For the boundary conditions, we applied a zero-pressure condition at all outlets, while the airway walls were set as no-slip boundaries. In the DPM, particle–wall interactions were assigned a trap condition, and an escape condition was defined at all outlets. The pressure-velocity coupling was managed using the SIMPLEC (Semi-Implicit Method for Pressure-Linked Equations Consistent) algorithm. All numerical simulations were conducted on the Narval high-performance computing (HPC) cluster, equipped with AMD EPYC Zen2 processors with up to 64 cores and 256 GB of RAM per node. The average simulation runtime was approximately 96 hours.

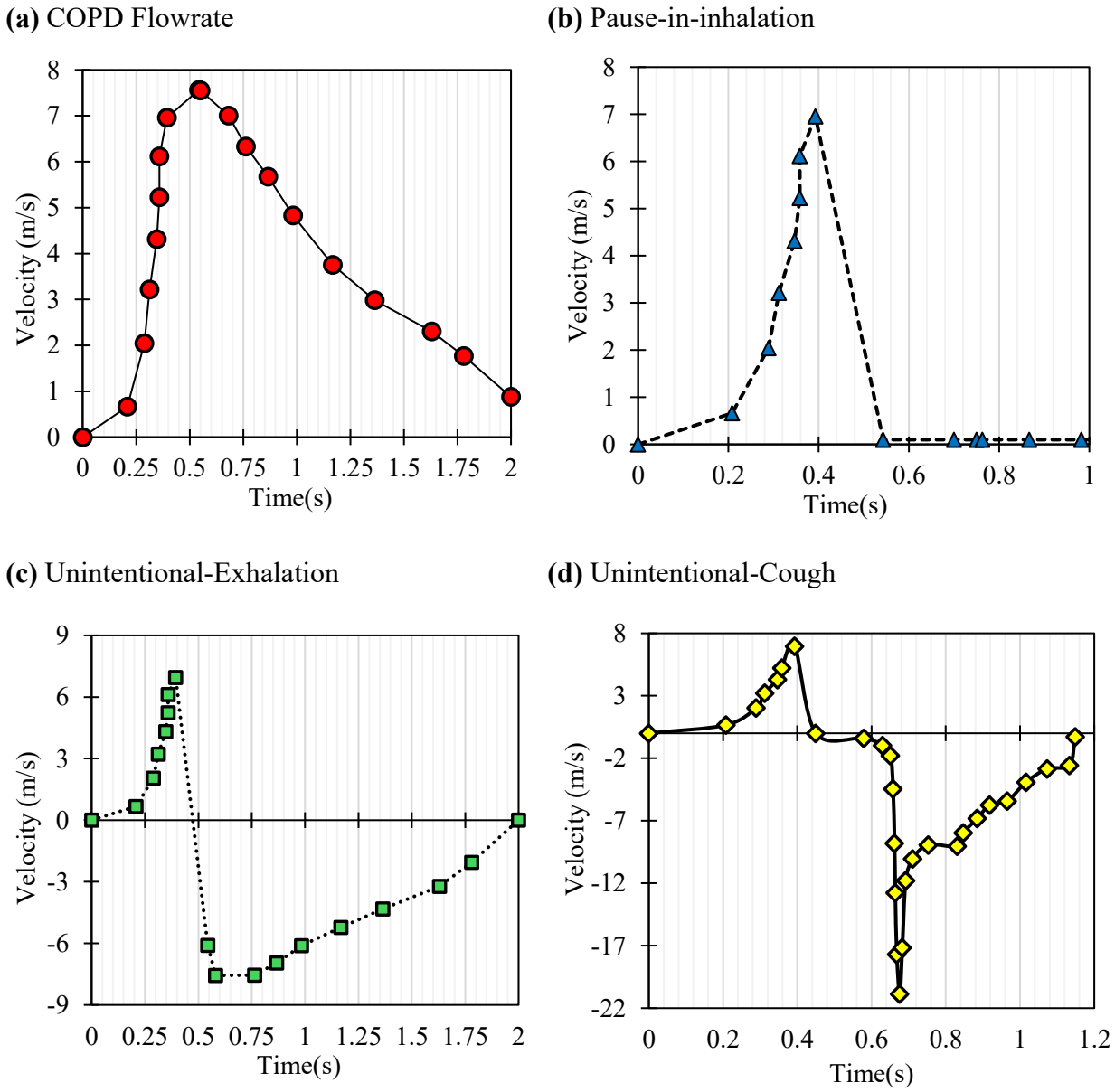

Fig. 8-2: Inhalation flow profiles illustrating different breathing scenarios: **(a)** a standard COPD inhalation profile (Biswas et al., 2017); **(b)** inhalation followed by a pause; **(c)** inhalation followed immediately by exhalation; and **(d)** inhalation interrupted by a coughing event before reaching peak flow (Oh et al., 2022).

8.4 Results and Discussion

Fig. 8-3 compares the deposition fractions (DFs) predicted by CFD simulations with those measured in *in-vitro* experiments for the airway model, thereby supporting the validity of the numerical simulations. The deposition fraction is the proportion of particles deposited in a specific region relative to the total number emitted from the pMDI. To replicate experimental conditions, a constant airflow rate of 30 L/min was maintained in the simulations.

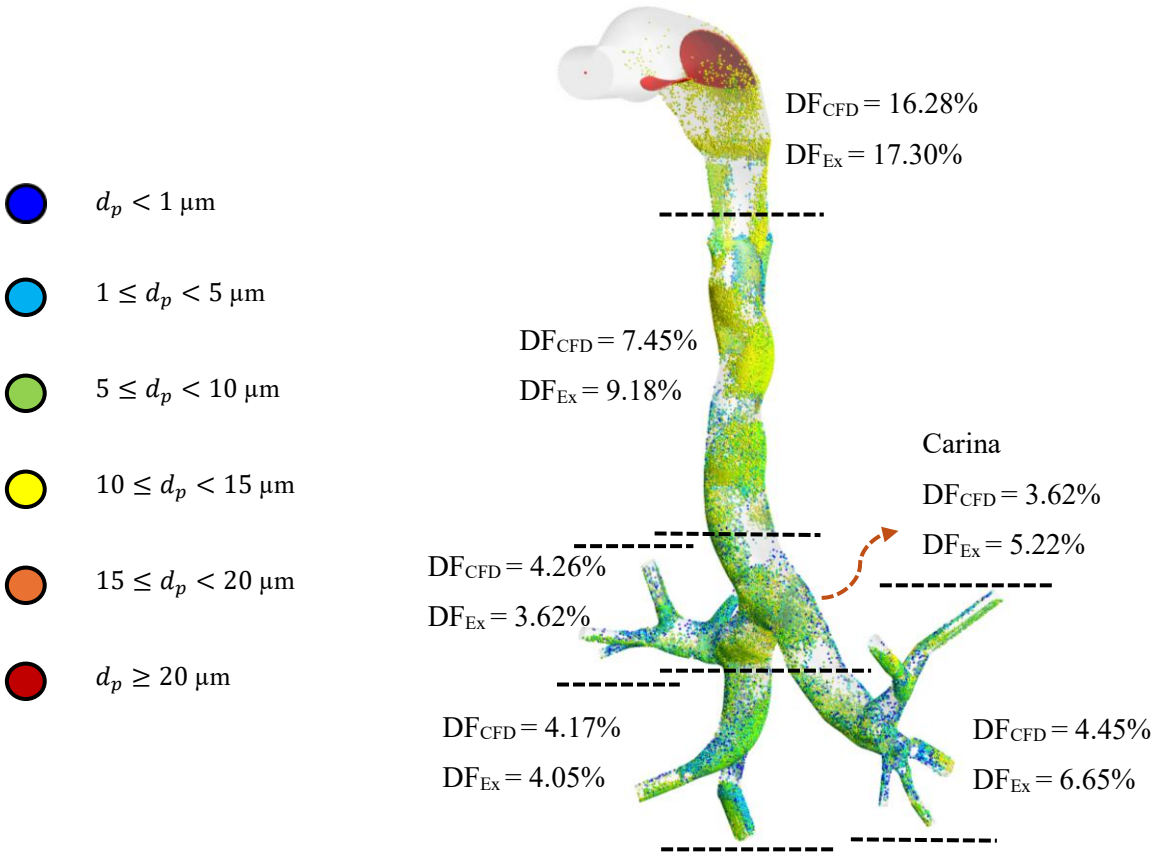

Fig. 8-3: Regional deposition fractions from CFD simulations (DF_{CFD}) and experimental measurements (DF_{Ex}) at a constant inhalation flow rate of 30 L/min. The corresponding particle size distribution predicted by the CFD model is also presented.

The CFD results demonstrate a strong agreement with experimental measurements across various airway regions. In the MT region, the predicted DF is 16.28%, closely matching the experimental value of 17.30%. For the trachea, the CFD prediction is 7.45%, compared to the experimental value of 9.18%. At the carina, the simulated DF is 3.62%, while the measured value is 5.22%. In the right bronchus, CFD predicts a DF of 8.44%, while experiments report 7.67%. For the left bronchus, the CFD yields a DF of 4.45%, slightly lower than the experimental value of 6.65%.

Additionally, the figure presents the particle size distribution and deposition patterns throughout the airway, as predicted by CFD. Consistent with the findings of Yousefi et al. (Yousefi et al., 2017), particles larger than 20 µm are almost entirely trapped within the MT. Their simulations showed that droplets in the 20–30 µm and 30–45.6 µm size ranges primarily deposited in the MT, with minimal penetration beyond the laryngeal inlet. In contrast, smaller particles (less than 20 µm) managed to traverse the MT, with some depositing in the trachea and the first generations of

branching airways. Lambert et al. (Lambert et al., 2011) also noted that 10 μm particles, although partly lost in the oral cavity, frequently impinged on the carinal ridges and branching points further downstream.

From **Fig. 8-3**, we noted that before any irregular breathing patterns occurred, approximately 10% of the particles escaped through the outlets, while about 20% had already deposited on the airway walls. The remaining majority, nearly 70%, remained suspended within the airway, making them highly susceptible to redistribution during disrupted inhalation events such as pauses, premature exhalation, or coughing. This observation raises important questions about the eventual fate of this suspended fraction and its potential impact on downstream deposition patterns.

To investigate the mechanisms governing particle transport and deposition, we examined airflow dynamics across various breathing scenarios. **Fig. 8-4** illustrates the iso-surfaces of the Q-criterion, which indicate coherent vortical structures during representative events: the COPD flow rate, unintentional exhalation, and unintentional cough. These surfaces are colored by TKE, thereby visualizing both vortex formation and turbulence intensity.

Among the three conditions, the unintentional cough produces the most extensive and energetic vortical structures, with widespread regions of elevated TKE, particularly concentrated in the upper trachea and central bronchial branches. This observation suggests that intense turbulent mixing and flow instability are driven by the rapid, forceful reversal of airflow during coughing. In contrast, the COPD flow condition is characterized by weaker, more localized vortices with lower TKE, reflecting relatively mild flow disturbances. The unintentional exhalation scenario falls between these two extremes, displaying moderate vortex activity and TKE levels. Vortical structures are most pronounced in the central and lower bronchi, where TKE is higher than in the COPD condition; however, it remains lower than in the coughing case due to weaker flow reversal.

(a) COPD Flowrate **(b)** Unintentional-Exhalation **(c)** Unintentional-Cough

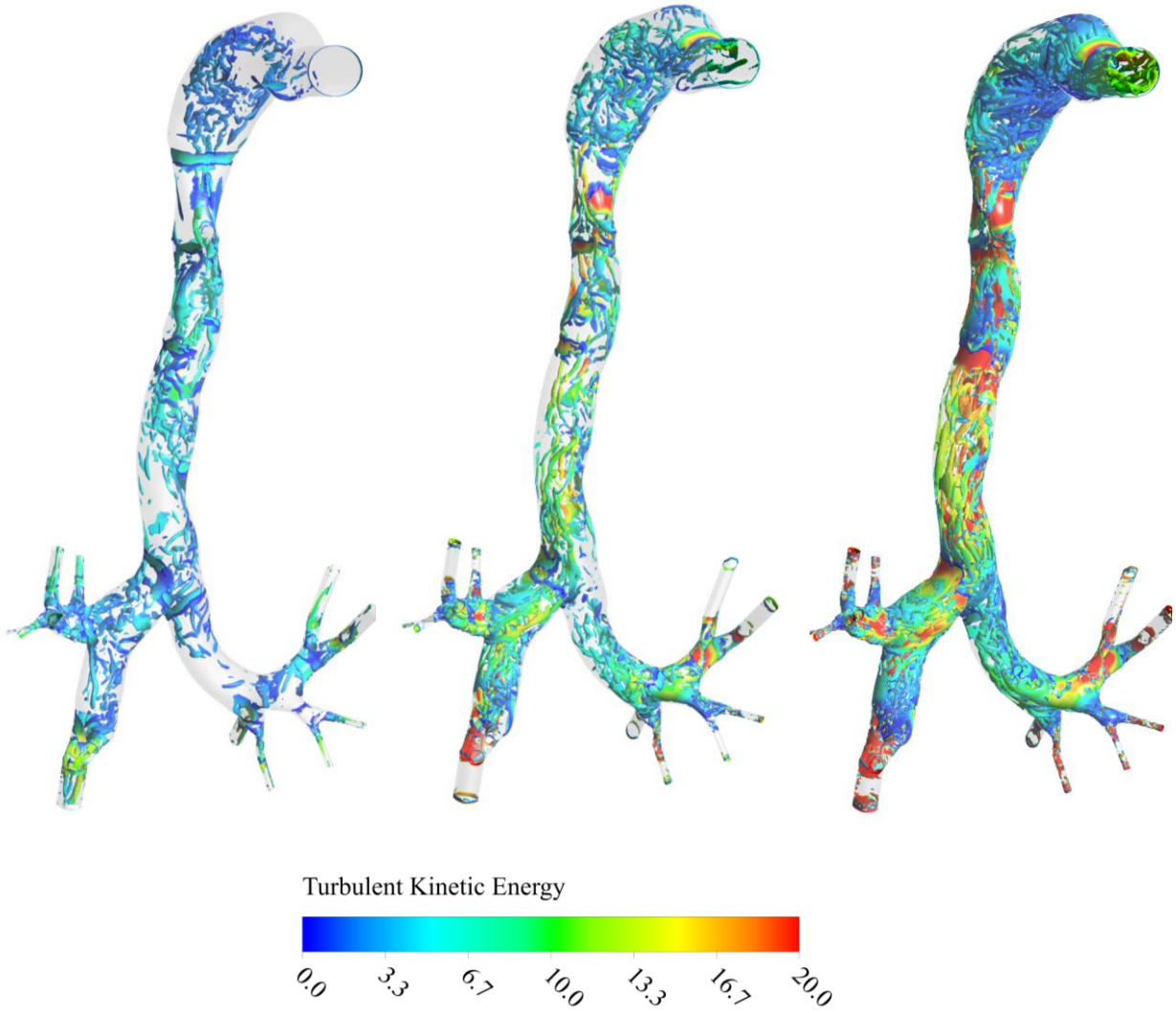

Fig. 8-4: Iso-surfaces of the Q-criterion colored by turbulent kinetic energy (TKE) under three breathing conditions: **(a)** standard COPD profile; **(b)** unintentional exhalation; and **(c)** unintentional cough, each shown at peak flow rate, refer to **Fig. 8-2**.

An examination of the airflow distribution at G1 reveals that vortical structures are more pronounced in the right bronchus than in the left, leading to higher TKE on the right. This asymmetry is linked to the larger anatomical diameter of the right bronchus, which allows for greater airflow under similar pressure conditions. Consistent with this, Kadota et al. (2020) found that the airflow rate in the right bronchus exceeded that in the left, regardless of whether the inhalation profile was constant or time-varying. In contrast, studies by Qin et al. (2022) and Koombua and Pidaparti (2008) reported nearly symmetrical velocity distributions between the left

and right bronchi, which likely resulted from their use of simplified airway geometries derived from the Weibel model. These findings underscore that simplified airway models fail to capture essential asymmetries in bronchial curvature, bifurcation angles, and diameters, all of which affect local flow dynamics and turbulence generation.

Fig. 8-5 presents the midplane of the MT region, along with cross-sectional views, illustrating the velocity magnitude and streamlines under different inhalation maneuvers. These results highlight how breathing patterns strongly influence near-wall flow and the formation of recirculation zones. In particular, the velocity contours and streamlines in the mouth region (top row of **Fig. 8-5**) reveal clearly the differences in airflow patterns across the various breathing scenarios. Among them, unintentional exhalation generates a smooth, organized reversal of streamlines, producing a gentle backflow that gradually expels air from the trachea. In contrast, the unintentional cough produces a much stronger outward flow, characterized by sharply deflected and irregular streamlines. This disturbed flow pattern illustrates the greater force and turbulence associated with coughing, which can enhance particle clearance from the airways but also disrupts the stability of airflow within the MT region.

In the cross-sectional views in **Fig. 8-5**, airflow under the COPD profile remains relatively smooth and organized, reflecting the low and stable inspiratory effort characteristic of this condition. During the pause-in-inhalation scenario, the flow nearly stagnates; however, small recirculation zones persist due to airway geometry. By contrast, unintentional exhalation reverses the flow and triggers the formation of complex vortical structures, notably increasing instability throughout the airway. This effect is most pronounced in the bronchial branches, where abrupt geometric changes intensify the formation of large, strong vortices. The most intense and chaotic patterns occur during unintentional coughs, characterized by high-velocity jets and vigorous vortex formation. Overall, while the COPD airflow produces steady and minimally disturbed flow, the pause-in-inhalation scenario introduces localized stagnation and recirculation. Both exhalation and cough scenarios produce markedly greater flow disturbances, turbulence, and recirculation, features with implications for particle transport and deposition.

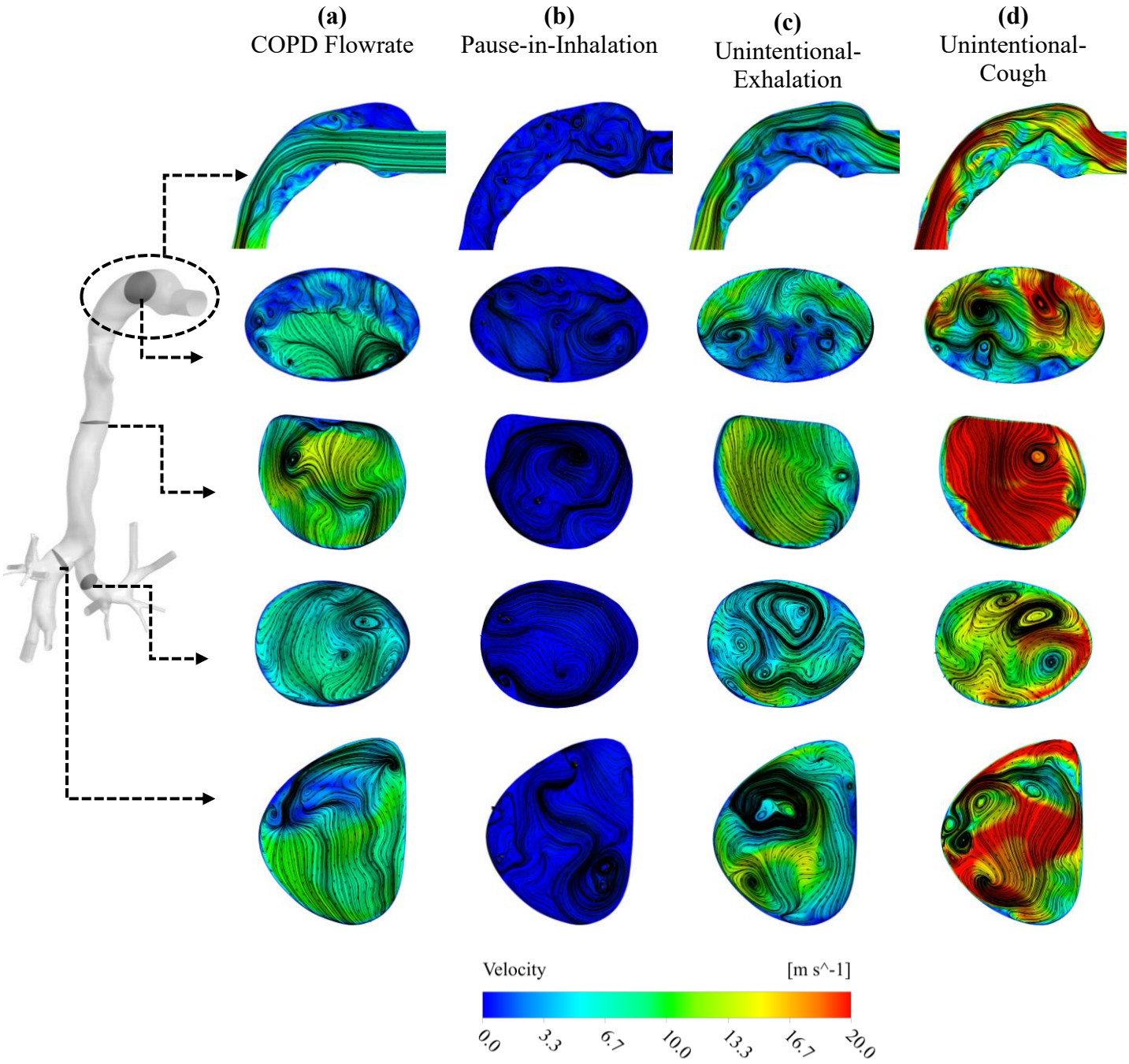

Fig. 8-5: Middle plane of the MT region and cross-sectional planes in the mouth, trachea, left bronchus, and right bronchus, showing airflow velocity contours and streamlines under different breathing conditions: **(a)** standard COPD profile; **(b)** pause-in-inhalation; **(c)** unintentional exhalation; and **(d)** unintentional cough (see **Fig. 8-2**).

Fig. 8-6 shows the distribution of aerosol particles suspended in airflow during different types of breathing irregularities. Under normal COPD inhalation, particles can penetrate deeply into the bronchial branches. During the pause-in-inhalation scenario, however, particles that pass through

the MT region tend to accumulate at the bifurcations of the central airways and within the left and right bronchi. This accumulation is beneficial because the recirculation zones that form during the pause occur only after the particles have already passed through the MT. As a result, their residence time is limited, reducing interactions with the airway walls and preventing excessive deposition, as illustrated by the flow features in **Fig. 8-5**.

In cases of unintentional exhalation, particles are primarily redirected toward the upper airway, leading to a marked accumulation in the trachea and MT region. Unlike the pause-in-inhalation scenario, these particles remain trapped in the MT, where localized recirculation zones form. This increases the likelihood of particle deposition through interactions with vortical structures (see **Fig. 8-5**) (Cui et al., 2018; Sou and Bergström, 2021). By contrast, an unintentional cough provides the most effective clearance, with only a small fraction of particles remaining shortly after the coughing event. The rapid, high-momentum airflow generated during a cough expels the majority of particles from the airway system. It is clear that, in addition to the type of abnormal respiratory event, the timing of the event is crucial in determining how aerosol particles distribute and deposit efficiently throughout the respiratory tract.

Fig. 8-7 illustrates the regional and lung (outlets: left and right lungs) deposition fractions under four different inhalation scenarios. The results show that abnormal breathing patterns notably shift deposition from the distal to the proximal regions of the airway. Among all scenarios, the unintentional cough produced the highest deposition in the MT region, reaching 35.2%, compared to 14.5% for the COPD baseline. The MT consistently exhibited high deposition across all conditions, due to its complex geometry and elevated flow velocities, with deposition considerably increasing during coughing and exhalation events.

Lung deposition, particularly in the left lung, was strongly affected by altered breathing conditions. Under the COPD flow rate, the left lung deposition reached 19.9%, but it dropped sharply to 2.1% during unintentional exhalation and further reduced to 0.9% during coughing. The right lung also experienced a notable decrease, falling from 30.5% under COPD conditions to 7.9% during coughing. These results highlight that unintentional respiratory maneuvers can severely impair drug delivery to the lower airways, potentially limiting therapeutic effectiveness.

(a) COPD Flowrate **(b)** Pause-in-Inhalation

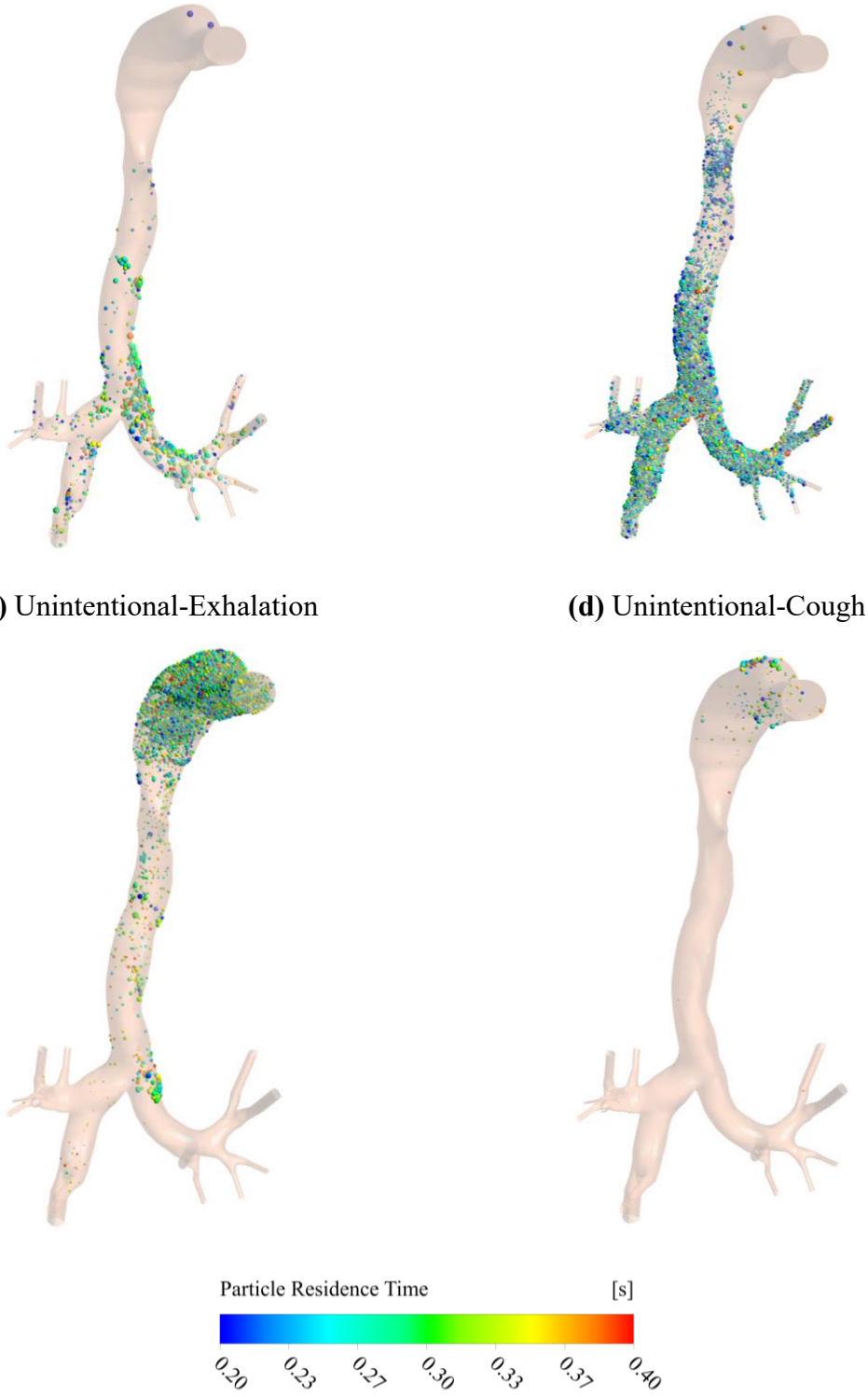

(c) Unintentional-Exhalation **(d)** Unintentional-Cough

Fig. 8-6: Particle distributions at 0.6 s within the airway under four different breathing conditions: **(a)** standard COPD profile; **(b)** pause-in-inhalation; **(c)** unintentional exhalation; and **(d)** unintentional cough.

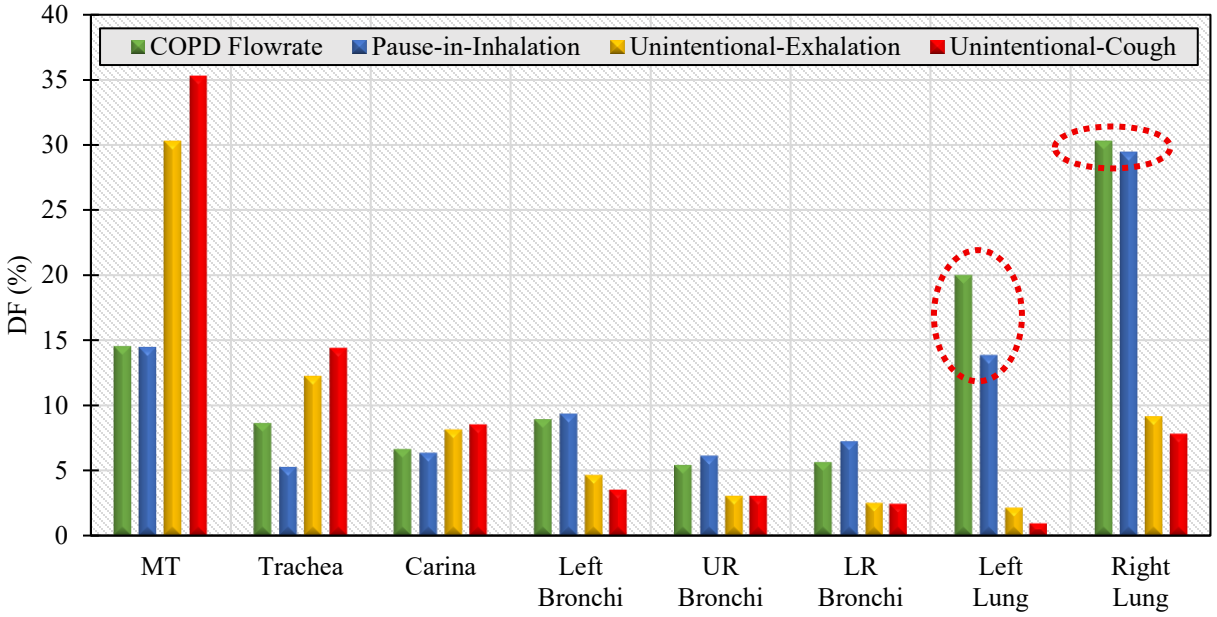

Fig. 8-7: Regional deposition fraction (DF, %) of inhaled particles under four breathing conditions: COPD baseline, pause-in-inhalation, unintentional exhalation, and unintentional cough. Deposition regions include the mouth–throat (MT), trachea, carina, upper right (UR), lower right (LR), upper left (UL), and lower left (LL) bronchial branches.

Among these irregular patterns, the inhalation pause had the least detrimental impact, as it caused limited disturbance to particle transport (as highlighted by red dashed circles). It is essential to note that our findings are specific to the timing of each irregularity; changes in the onset or duration of these events may result in different deposition outcomes.

Fig. 8-8 illustrates the relationship between particle residence time and the Stokes (*Stk*) number under various breathing conditions. The *Stk* number quantifies a particle's tendency to deviate from streamlines due to inertia and is defined as:

$$Stk = \rho_p d_p^2 U / 18\mu D \tag{11}$$

where U is the characteristic velocity of the flow, and D is the diameter of the airway.

Under the COPD flow rate, particles predominantly exhibit low *Stk* numbers (< 0.1) and short residence times across almost all regions, reflecting the steady and streamlined flow pattern that minimizes recirculation (refer to **Fig. 8-5**). Nevertheless, deposition in the upper airway, particularly in the MT and trachea, remains notable due to strong inertial impaction at geometric contractions in the glottis region, as well as abrupt curvatures and rapid directional changes in the pharynx and trachea. This effect becomes more pronounced under conditions characterized by

higher airflow velocities and complex vortical structures, as observed in **Figs. 8-5(c)** and **8-5 (d)**, where flow disturbances further increase the likelihood of particle impaction and proximal deposition.

These findings align with those of Longest and Vinchurkar (2009), who showed that both the *Stk* and Dean numbers ($De = Re\sqrt{D/2R_c}$, where *Re* is the Reynolds number, *D* is the airway diameter, and R_c is the radius of curvature of the airway, affect particle deposition during exhalation. The *De* number indicates the strength of curvature-induced secondary flow structures, which can guide particles toward the airway walls. At higher *De* numbers (≥100), these secondary flows become more effective at transporting particles to the walls, thereby increasing deposition.

Additionally, tracheal deposition was higher during coughing (14.3%) and exhalation (12.2%) than the baseline of 8.6% in COPD. As demonstrated in **Fig. 8-8**, the majority of particles depositing in the trachea under coughing and exhalation conditions exhibited longer residence times (t > 0.2 s) than those in the COPD case. This indicates that reverse airflow facilitates tracheal deposition by preventing particles from traveling deeper into the airway and instead redirecting them back toward the upper regions. Moreover, particles in the trachea exhibited significantly higher Stk numbers, reaching up to 0.4 during coughing, highlighting the prominent role of inertial impaction in deposition under these transient, forceful conditions. Although both coughing and exhalation involve airflow reversal, particle deposition during coughing is higher, likely due to the more abrupt flow acceleration and the higher particle velocities generated during coughing, as shown in **Figs. 8-4** and **8-5**.

In contrast, the pause-in-inhalation scenario results in a more moderate redistribution of particles, leading to a roughly 39% reduction in tracheal deposition compared to the complete COPD inhalation profile, while deposition in the left and right bronchial branches (G1–G4) remains elevated. This outcome suggests that although particle residence time increases during the pause in inhalation (refer to **Fig. 8-8**), the absence of continuous airflow (*Stk* < 0.008) allows a greater fraction of particles to migrate toward the distal lung regions. Notably, around 9% of the particles remain suspended in the airway flow even after 1.5 s, indicating prolonged residence and delayed deposition compared to other scenarios. This observation aligns with the findings of Imai et al. (2012), who reported that post-inhalation breath-holding can enhance particle deposition in lower

airway generations. However, unlike their study, the pause in our study occurs during inhalation rather than after its completion. Similarly, Sadeghi et al. (2025) demonstrated that stepped pulsatile inhalation (2-step and 3-step profiles) with short pauses between phases reduces turbulence in the pediatric upper airway and throat, decreases impaction, and improves distal delivery.

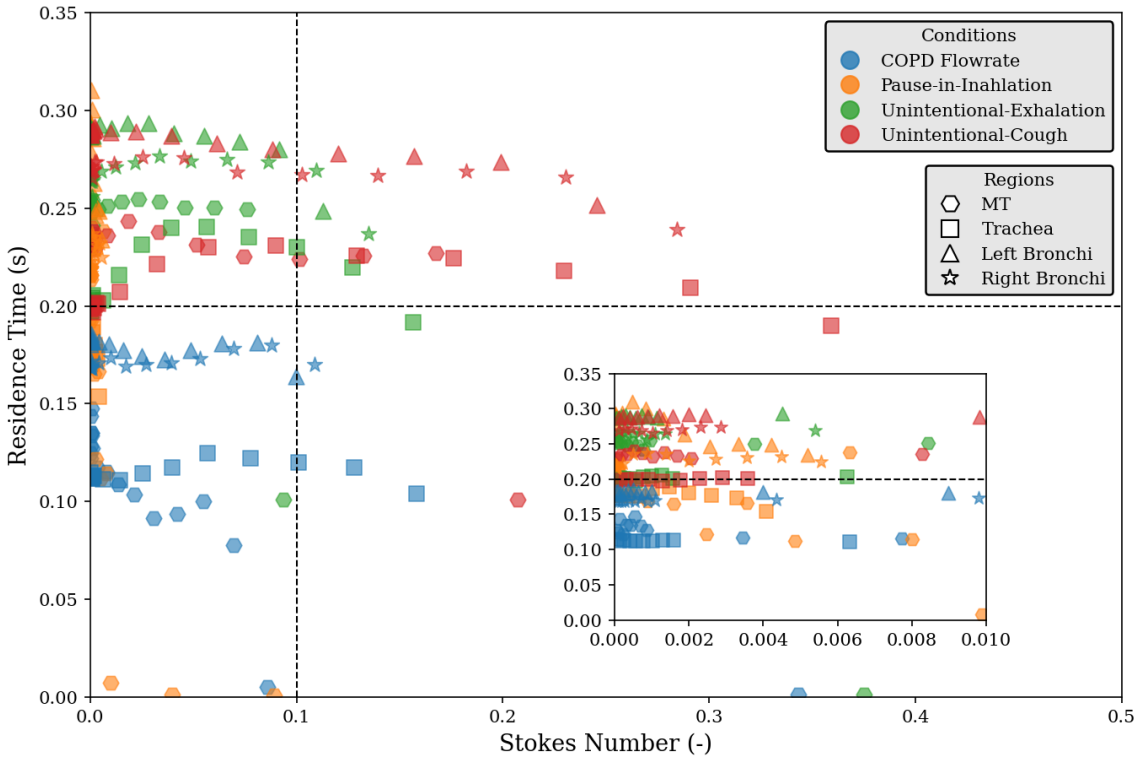

Fig. 8-8: Comparison of deposited particle residence time and Stokes number across airway regions, MT (mouth-throat), trachea, left and right bronchi, under four breathing conditions: COPD flow rate, pause-in-inhalation, unintentional exhalation, and unintentional cough.

Deposition in the left and right bronchi is approximately 50% lower during reversal flows associated with unintentional cough and exhalation (see **Fig. 8-7**) compared to full breathing and pause-in-inhalation scenarios. As shown in **Fig. 8-8**, coughing induces higher Stk numbers in these regions, reaching values of up to 0.3, thereby enhancing inertial impaction —a mechanism typically more prominent in the upper airway. During exhalation, this effect becomes more pronounced for larger particles, which are particularly sensitive to flow reversal and abrupt directional changes. However, despite the presence of strong recirculation (as shown in **Fig. 8-5**) and increased *Stk* numbers, total bronchial deposition under these conditions does not exceed that observed during the pause-in-inhalation and COPD scenarios. In the latter case, the combination

of lower *Stk* numbers and prolonged residence times suggests a mixed deposition mechanism, primarily governed by gravitational settling and weak inertial impaction rather than the strong inertial effects seen during reversal flows.

To further explore how breathing patterns affect the dynamics of particle transport, **Fig. 8-9** shows the deposition fraction of pMDI particles by diameter across various airway regions and under four different inhalation patterns. In the MT region, deposition under COPD and pause-in-inhalation conditions clearly favors larger particles (greater than 12 μm), with a notable peak at approximately 16–18 μm. This pattern is anticipated, as larger particles are more prone to inertial impaction in the upper airway (Finlay, 2019). However, under the unintentional exhalation and coughing, the fraction of larger particles slightly decreases, while the proportion of smaller particles (less than 12 μm) increases. Consequently, even particles that initially avoid deposition in the upper airway may ultimately deposit there during flow reversals, particularly during forceful coughing.

In the trachea, particle deposition primarily shifts toward mid-sized particles (6–12 μm) across all breathing conditions, with inertial impaction as the primary mechanism of deposition. However, during the pause-in-inhalation, the peak deposition of these particles is distinctly reduced due to lower particle velocity and decreased inertial momentum. As a result, although the particles remain within the impaction-dominated size range, their forward momentum is not strong enough to cause significant deposition compared to conditions of COPD, exhalation, and coughing airflow. Across various scenarios, particle size distributions are generally similar, except for the 12 μm particles in the carina, where deposition appears relatively unaffected by changes in inhalation patterns. However, the left bronchi exhibited two distinct deposition peaks at approximately 7 μm and 12 μm, with the pause-in-inhalation condition producing the highest values, clearly exceeding those under the COPD baseline. In the upper right bronchi, deposition fractions remained lower overall, peaking at approximately 2% at a diameter of around 8 μm for both pause-in-inhalation and COPD flow rate conditions. In the lower right bronchi, deposition showed a sharp peak at approximately 14 μm (5.8%) during the pause-in-inhalation condition. In contrast, the deposition for other conditions remained notably lower and relatively flat across most particle sizes. This enhanced deposition of larger particles during the pause-in-inhalation condition highlights the role of gravitational settling, which becomes more prominent for heavier particles under reduced-flow conditions, as illustrated in **Fig. 8-8**.

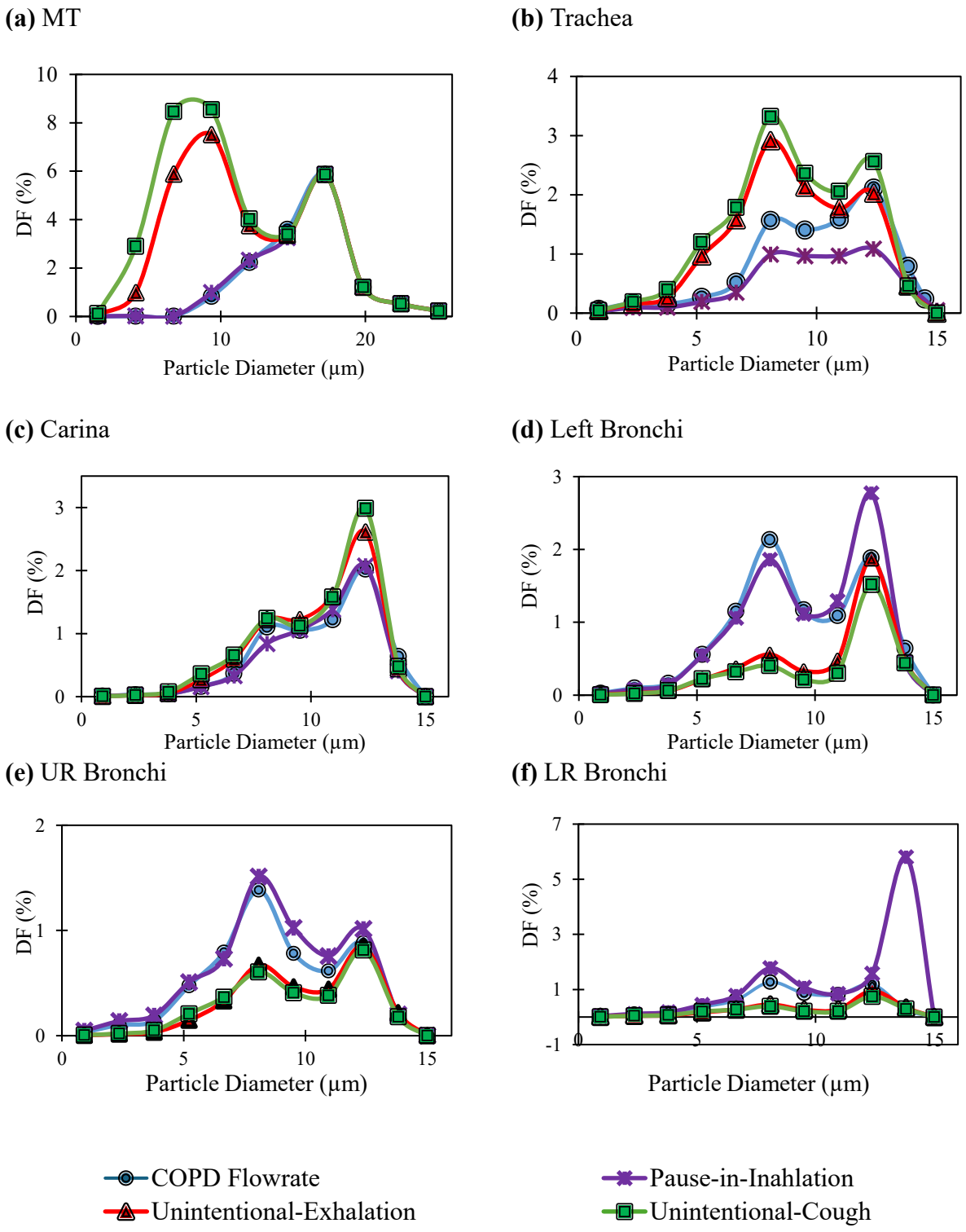

Fig. 8-9: Deposition fraction (%) of pMDI particles as a function of particle size across different airway regions **(a)** MT; **(b)** Trachea; **(c)** Carina; **(d)** Left Bronchi; **(e)** UR Bronchi; and **(f)** LR Bronchi, under four breathing conditions. UR: upper right, LR: lower right.

Fig. 8-10 compares the mass fraction of injected particles escaped from the mouth during two unintentional breathing events: exhalation and coughing. As shown in **Fig. 8-10(a)**, unintentional exhalation results in a higher exhaled particle fraction (27.95%) compared to coughing (24.11%). This indicates that, unlike the rapid and forceful reversal flow seen during coughing, the slower, more sustained reverse flow during exhalation promotes the outward transport of particles, particularly smaller ones. In contrast, coughing, with its stronger but shorter expiratory burst, enhances inertial impaction, thereby limiting particle escape while increasing deposition in the upper airways, as previously shown in **Fig. 8-5**. From a therapeutic perspective, although more particles are lost during exhalation, reducing overall lung delivery, this may also be beneficial as it reduces undesirable deposition in the upper airway.

Fig. 8-10(b) displays the mass fractions of exhaled particles by size for both unintentional exhalation and coughing. In both scenarios, particles smaller than 5 μm make up the majority of the exhaled mass. Notably, approximately 80% of particles in the <1 μm and 1–2 μm size ranges are expelled through the mouth. Although both breathing scenarios show similar trends, coughing produces a slightly higher proportion of small particles (<2 μm). Conversely, in the 5–10 μm range, unintentional exhalation results in a higher exhaled mass fraction (approximately 35%) compared to coughing (around 26.8%). This suggests that under milder flow conditions, even larger particles can be expelled due to a reduced influence of inertial impaction.

These findings are consistent with those of Koullapis et al. (2018), who simulated aerosol transport in the deep lung (G10–G19) over a complete inhalation–exhalation cycle. Their study demonstrated that particles smaller than 2 μm are primarily exhaled, with 75–89% of these particles leaving the system. This supports our observations and reinforces the idea that low-inertia particles closely follow airflow streamlines, making them highly susceptible to reversal and exhalation, whether this occurs after a full inhalation from the deep lung or prematurely from the proximal airways. A key difference emerges for particles in the 2–5 μm size range. While Koullapis et al. (2018) reported a greater deposition within this size range due to deeper lung penetration and prolonged residence time, with only about 44% of particles being exhaled, our study found a markedly higher exhalation fraction of approximately 70%. This discrepancy highlights the disruptive impact of unintentional flow reversal, where particles that would typically deposit in the lower airways are prematurely redirected and exhaled, thereby reducing the efficiency of drug delivery to the target regions.

(a)

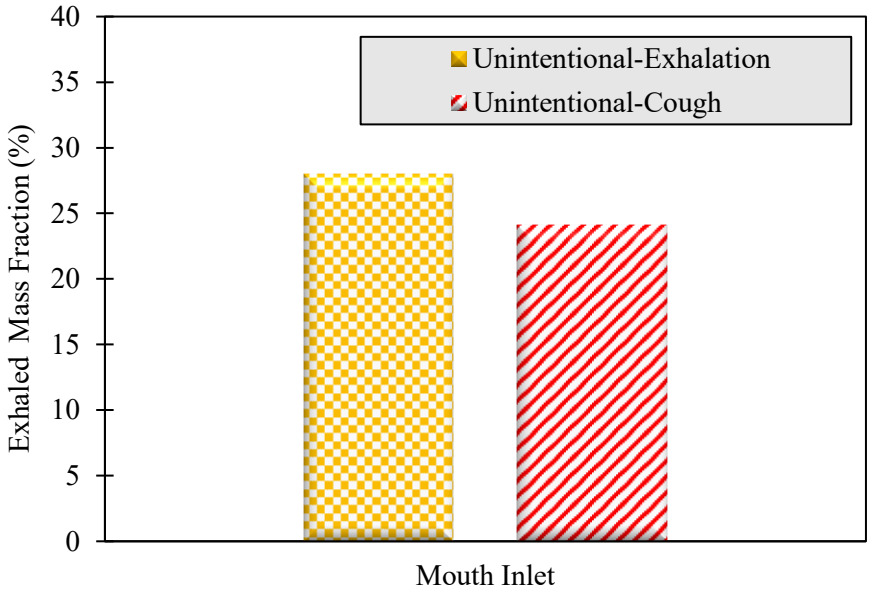

(b)

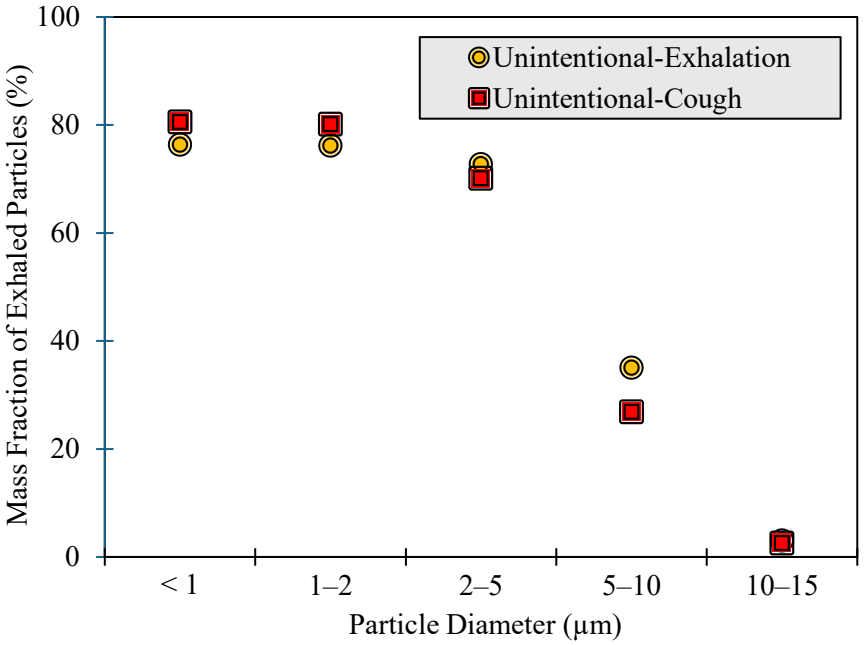

Fig. 8-10: **(a)** Exhaled mass fraction (%) at the mouth inlet; and **(b)** mass fraction (%) of exhaled particles as a function of particle diameter, comparing unintentional exhalation and cough scenarios.

If successful delivery is defined as particles passing beyond the trachea, our results in **Table 8-1** show that a pause during inhalation has only a minimal impact on device efficiency compared to COPD complete cycle breathing (65.93% vs. 70.20%), suggesting that this error alone is unlikely to require repeating a puff. In contrast, when a patient coughs or exhales during inhalation, a substantial portion of the drug is lost, either expelled or deposited in the upper airway, with losses reaching about 78% during exhalation and 82% during coughing, compared to only around 30% during a complete COPD inhalation. Such conditions necessitate the use of a second puff.

The concern, however, is that these events result in a substantial fraction of the medication being deposited in the upper airways, as shown in **Table 8-1**. Even when the second puff is administered correctly, approximately 30% more drug is deposited in this region, particularly under COPD flow conditions. While such increased upper-airway deposition may be acceptable for rescue inhalers, where ensuring immediate relief outweighs potential side effects, it is more troubling for maintenance therapy, where excessive deposition in the upper airways can be a serious concern. These findings may provide valuable insights for physicians, helping them determine the appropriate number of puffs and the optimal interval between them, thereby balancing effective drug delivery with the minimization of side effects.

Table 8-1: Fraction of inhaled drug lost and successfully delivered to the lower airway (G1–G4) and beyond, under different breathing conditions.

Conditions	Drug Lost (%)	Delivered Drug (%)	
		G1-G4	Beyond G4 (Lungs)
COPD Flowrate	29.76	19.95	50.25
Pause-in-Inhalation	26.01	22.67	43.26
Unintentional-Exhalation	78.56	10.16	11.28
Unintentional-Cough	82.30	8.97	8.73

8.5 Conclusions

This study evaluated the effect of irregular inhalation patterns, specifically pause-in-inhalation, unintentional exhalation, and cough, on aerosol transport and deposition from pMDIs. LES coupled with the DPM (LES-DPM) was employed in a realistic male airway geometry, supported by *in-vitro* experimental validation, to analyze airflow dynamics and particle behavior under both normal and disturbed breathing conditions.

Our results indicate that unintentional breathing maneuvers remarkably decrease the efficiency of drug delivery. This reduction occurs due to disruption of vortex formation, increased TKE, and a shift in particle deposition toward the upper airways. Among the scenarios studied, coughing generated the strongest vortical structures and the highest TKE, resulting in the lowest lung deposition and an increased accumulation of particles in the MT and trachea, approximately 58.8% and 40% more, respectively, compared to uninterrupted COPD inhalation. Although premature exhalation was less turbulent, it still redirected particles away from the lungs, yielding only 2.1% lung deposition in the left lung and a higher exhaled particle fraction of 27.95%, compared to 24.11% observed during coughing.

Particle size analysis revealed that submicron and fine particles (<2 μm) were particularly prone to exhalation, with up to 80% escaping through the mouth during both exhalation and coughing. Additionally, approximately 70% of particles with diameters of 2–5 μm were exhaled during irregular breathing (unintentional exhalation and cough). This highlights the disruptive impact of premature flow reversal, which hinders deeper lung deposition and considerably reduces delivery efficiency to the intended target regions.

Overall, the findings indicate that pausing during inhalation has a minimal impact on successful drug delivery. However, actions such as coughing or exhaling while inhaling can result in substantial drug loss and increased deposition in the upper airway, sometimes exceeding 80%. This redistribution reduces the amount of medication reaching the lower airways and increases local drug deposition in the oropharynx. These results highlight the clinical importance of proper inhalation techniques. This knowledge allows physicians to guide patients on the appropriate number of puffs, the ideal timing between them, and whether a dose should be repeated, thus maximizing therapeutic effectiveness while reducing side effects.

8.6 Limitations and Future Directions

- The analysis was conducted using a single anatomically realistic airway model. Although this geometry captures key anatomical features, inter-individual variability in airway dimensions, curvature, and localized obstructions may influence how breathing interruptions affect aerosol transport and deposition. Future studies should consider multiple patient-specific airway models.

- While the cough waveform was derived from measured physiological data, the pause-in-inhalation and early-exhalation breathing profiles were constructed based on the qualitative characteristics of these events rather than direct patient recordings. This idealization may influence the predicted aerosol dynamics under irregular breathing conditions.
- Coughing was modeled as a high-velocity reverse flow at the airway outlet. In reality, coughing involves complex physiological processes, including glottal closure, thoracic compression, rapid airway reopening, and the formation of highly turbulent jets. Incorporating these mechanisms could further refine predictions of aerosol transport and deposition.
- The effects of breathing interruptions were evaluated only within the upper airway region. Deposition in the deeper lung was not considered, despite its critical importance for therapeutic efficacy. Extending the computational domain to include multiple bronchial generations would enable assessment of distal aerosol delivery under irregular breathing conditions.

8.7 Nomenclature

3D	three dimensional
CAD	computer-aided design
CFD	computational fluid dynamics
COPD	chronic obstructive pulmonary disease
CPU	central processing unit
CT	computed tomography
DF	deposition fraction
DICOM	digital imaging and communication in medicine
DPM	discrete phase model
Ex	experimental
FDM	fused deposition modeling
G	generation

GiB	gibibyte
HFA	hydrofluoroalkane
HPLC	high-performance liquid chromatography
LES	large eddy simulation
LR	lower-right
MT	mouth-throat
PIV	particle image velocimetry
PLA	polylactic acid
PMDI	pressurized metered-dose inhaler
RAM	random access memory
RH	relative humidity
RMSE	root mean square error
SGS	subgrid-scale
SIMPLEC	semi-implicit method for pressure-linked equations-consistent
STL	stereolithography
TKE	turbulent kinetic energy
UR	upper-right
VCU	Virginia Commonwealth University
WALE	wall-adapting local eddy viscosity

Notations

$\bar{S}_{ij}$	filtered rate-of-strain tensor $(1/s)$
$\overline{\boldsymbol{u}}_{\boldsymbol{p}}$	particle velocity (m/s)
C_D	drag coefficient (-)
C_{Dd}	drag force coefficient (-)

C_c	Cunningham correction factor (-)
L_s	subgrid-scale mixing length (m)
Re_p	particle Reynolds number (-)
S_{ij}^d	modified rate-of-strain tensor $(1/s)$
a_1, a_2, a_3	empirical constants (-)
$\vec{g}$	gravitational acceleration (m/s^2)
k_B	Boltzmann constant (-)
$\overline{\boldsymbol{P}}$	filtered pressure (Pa)
$\overline{\boldsymbol{u}}$	filtered velocity (m/s)
ζ_i	stochastic coefficient (-)
μ_t	turbulent dynamic viscosity $(Pa.s)$
$\bar{\bar{\sigma}}$	stress tensor (Pa)
$\bar{\bar{\tau}}$	subgrid-scale stress (Pa)
D	airway diameter (m)
De	Dean number (-)
d_p	particle diameter (m)
$\boldsymbol{F_i}$	body force (N/m^3)
m_p	particle mass (kg)
R_c	radius of curvature of the airway (m)
Re	Reynolds number (-)
T	temperature (K)
U	characteristic velocity of the flow
μ	mixture dynamic viscosity $(Pa.s)$
ρ_p	particle density (kg/m^3)

stk	Stokes number (-)
v	kinematic viscosity (m^2/s)
λ	molecular mean free path (m)
μ	molecular viscosity of fluid ($Pa.s$)
ρ	fluid density (kg/m^3)
$\boldsymbol{\rho}$	mixture density (kg/m^3)

8.8 References

Ahookhosh, K., Saidi, M., Mohammadpourfard, M., Aminfar, H., Hamishehkar, H., Farnoud, A., Schmid, O., 2021. Flow structure and particle deposition analyses for optimization of a pressurized metered dose inhaler (pMDI) in a model of tracheobronchial airway. Eur. J. Pharm. Sci. 164, 105911. https://doi.org/10.1016/j.ejps.2021.105911

Bell, J., Newman, S., 2007. The rejuvenated pressurised metered dose inhaler. Expert Opin. Drug Deliv. 4, 215–234. https://doi.org/10.1517/17425247.4.3.215

Biswas, R., Hanania, N.A., Sabharwal, A., 2017. Factors determining in vitro lung deposition of albuterol aerosol delivered by ventolin metered-dose inhaler. J. Aerosol Med. Pulm. Drug Deliv. 30, 256–266. https://doi.org/10.1089/jamp.2015.1278

Borojeni, A.A.T., Gu, W., Asgharian, B., Price, O., Kuprat, A.P., Singh, R.K., Colby, S., Corley, R.A., Darquenne, C., 2023. In silico quantification of intersubject variability on aerosol deposition in the oral airway. Pharmaceutics 15, 160. https://doi.org/10.3390/pharmaceutics15010160

Bunnag, C., Fuangtong, R., Pothirat, C., Punyaratabandhu, P., 2007. A comparative study of patients' preferences and sensory perceptions of three forms of inhalers among Thai asthma and COPD patients. Asian Pacific J. Allergy Immunol. 25, 99–107.

Crompton, G.K., 1982. Problems patients have using pressurized aerosol inhalers. Eur. J. Respir. Dis. Suppl. 119, 101–4.

Cui, X., Wu, W., Gutheil, E., 2018. Numerical study of the airflow structures in an idealized mouth-throat under light and heavy breathing intensities using large eddy simulation.

Respir. Physiol. Neurobiol. 248, 1–9. https://doi.org/10.1016/j.resp.2017.11.001

Dolovich, M.B., Dhand, R., 2011. Aerosol drug delivery: Developments in device design and clinical use. Lancet 377, 1032–1045. https://doi.org/10.1016/S0140-6736(10)60926-9

Dunbar, C.A., 1997. Atomization mechanisms of the pressurized metered dose inhaler. Part. Sci. Technol. 15, 253–271. https://doi.org/10.1080/02726359708906771

Finlay, W.H., 2019. The Mechanics of Inhaled Pharmaceutical Aerosols: An Introduction. Elsevier Science.

Gemci, T., Ponyavin, V., Collins, R., Corcoran, T.E., Saha, S.C., Islam, M.S., 2022. CFD study of dry pulmonary surfactant aerosols deposition in upper 17 generations of human respiratory tract. Atmosphere (Basel). 13, 1–18. https://doi.org/10.3390/atmos13050726

Giraud, V., Roche, N., 2002. Misuse of corticosteroid metered-dose inhaler is associated with decreased asthma stability. Eur. Respir. J. 19, 246–251. https://doi.org/10.1183/09031936.02.00218402

Golshahi, L., Noga, M.L., Vehring, R., Finlay, W.H., 2013. An in vitro study on the deposition of micrometer-sized particles in the extrathoracic airways of adults during tidal oral breathing. Ann. Biomed. Eng. 41, 979–989. https://doi.org/10.1007/s10439-013-0747-0

Imai, Y., Miki, T., Ishikawa, T., Aoki, T., Yamaguchi, T., 2012. Deposition of micrometer particles in pulmonary airways during inhalation and breath holding. J. Biomech. 45, 1809–1815. https://doi.org/10.1016/j.jbiomech.2012.04.017

Jahed, M., Kozinski, J., Pakzad, L., 2025a. Experimental and Numerical Investigation of Drug Delivery in Patient-Specific Male and Female Airways: Role of Airway Wall Motion, Breathing Patterns, and Mucus Layer. J. Drug Deliv. Sci. Technol. 107409. https://doi.org/https://doi.org/10.1016/j.jddst.2025.107409

Jahed, M., Kozinski, J., Pakzad, L., 2025b. Airway wall dynamics during inhalation on drug delivery via pMDIs using patient-specific airway models, in: Respiratory Drug Delivery Europe. Respiratory Drug Delivery 2025, pp. 120–123.

Kadota, K., Inoue, N., Matsunaga, Y., Takemiya, T., Kubo, K., Imano, H., Uchiyama, H., Tozuka, Y., 2020. Numerical simulations of particle behaviour in a realistic human airway

model with varying inhalation patterns. J. Pharm. Pharmacol. 72, 17–28. https://doi.org/10.1111/jphp.13195

Kaviratna, A., Tian, G., Liu, X., Delvadia, R., Lee, S., Guo, C., 2019. Evaluation of bio-relevant mouth-throat models for characterization of metered dose inhalers. AAPS PharmSciTech 20, 130. https://doi.org/10.1208/s12249-019-1339-6

Koombua, K., Pidaparti, R.M., 2008. Inhalation induced stresses and flow characteristics in human airways through fluid-structure interaction analysis. Model. Simul. Eng. 2008. https://doi.org/10.1155/2008/358748

Koullapis, P., Kassinos, S.C., Muela, J., Perez-Segarra, C., Rigola, J., Lehmkuhl, O., Cui, Y., Sommerfeld, M., Elcner, J., Jicha, M., Saveljic, I., Filipovic, N., Lizal, F., Nicolaou, L., 2018. Regional aerosol deposition in the human airways: The SimInhale benchmark case and a critical assessment of in silico methods. Eur. J. Pharm. Sci. 113, 77–94. https://doi.org/10.1016/j.ejps.2017.09.003

Koullapis, P.G., Hofemeier, P., Sznitman, J., Kassinos, S.C., 2018. An efficient computational fluid-particle dynamics method to predict deposition in a simplified approximation of the deep lung. Eur. J. Pharm. Sci. 113, 132–144. https://doi.org/10.1016/j.ejps.2017.09.016

Kunda, N.K., Hautmann, J., Godoy, S.E., Marshik, P., Chand, R., Krishna, S., Muttil, P., 2017. A novel approach to study the pMDI plume using an infrared camera and to evaluate the aerodynamic properties after varying the time between actuations. Int. J. Pharm. 526, 41–49. https://doi.org/10.1016/j.ijpharm.2017.04.051

Lambert, A.R., O'Shaughnessy, P.T., Tawhai, M.H., Hoffman, E.A., Lin, C.L., 2011. Regional deposition of particles in an image-based airway model: Large-eddy simulation and left-right lung ventilation asymmetry. Aerosol Sci. Technol. 45, 11–25. https://doi.org/10.1080/02786826.2010.517578

Lewis, D.A., O'Shea, H., Church, T.K., Brambilla, G., Traini, D., Young, P.M., 2016. Exploring the impact of sample flowrate on in vitro measurements of metered dose inhaler performance. Int. J. Pharm. 514, 420–427. https://doi.org/10.1016/j.ijpharm.2016.05.025

Longest, P.W., Tian, G., Walenga, R.L., Hindle, M., 2012. Comparing MDI and DPI aerosol deposition using in vitro experiments and a new stochastic individual path (SIP) model of

the conducting airways. Pharm. Res. 29, 1670–1688. https://doi.org/10.1007/s11095-012-0691-y

Longest, P.W., Vinchurkar, S., 2009. Inertial deposition of aerosols in bifurcating models during steady expiratory flow. J. Aerosol Sci. 40, 370–378. https://doi.org/10.1016/j.jaerosci.2008.11.007

McFadden, E.R., 1995. Improper patient techniques with metered dose inhalers: Clinical consequences and solutions to misuse. J. Allergy Clin. Immunol. 96, 278–283. https://doi.org/10.1016/S0091-6749(95)70206-7

Morsi, S.A., Alexander, A.J., 1972. An investigation of particle trajectories in two-phase flow systems. J. Fluid Mech. 55, 193–208. https://doi.org/10.1017/S0022112072001806

Narayanan, J.K., Lin, J., Feng, Y., Cui, X., 2022. Numerical study on the impact of mucus layer and inlet air-temperatures on the particle deposition in a highly idealized mouth-throat model using LES. Powder Technol. 395, 455–475. https://doi.org/10.1016/j.powtec.2021.09.073

Nicoud, F., Ducros, F., 1999. Subgrid-scale stress modelling based on the square of the velocity. Flow Meas. Instrum. 62, 183–200. https://doi.org/https://doi.org/10.1023/A:1009995426001

Oh, W., Ooka, R., Kikumoto, H., Han, M., 2022. Numerical modeling of cough airflow: Establishment of spatial–temporal experimental dataset and CFD simulation method. Build. Environ. 207, 108531. https://doi.org/10.1016/j.buildenv.2021.108531

Oliveira, R.F., Teixeira, S., Teixeira, J.C., Silva, L.F., Antunes, H., 2012. pMDI sprays: theory, experiment and numerical simulation, in: Liu, C. (Ed.), Advances in Modeling of Fluid Dynamics. IntechOpen, Rijeka. https://doi.org/10.5772/46099

Qin, Z., Shi, Y., Qiao, J., Lin, G., Tang, B., Li, X., Zhang, J., 2022. CFD simulation of porous microsphere particles in the airways of pulmonary fibrosis. Comput. Methods Programs Biomed. 225, 107094. https://doi.org/10.1016/j.cmpb.2022.107094

Rahman, M.M., Zhao, M., Islam, M.S., Dong, K., Saha, S.C., 2021. Aging effects on airflow distribution and micron-particle transport and deposition in a human lung using CFD-DPM approach. Adv. Powder Technol. 32, 3506–3516. https://doi.org/10.1016/j.apt.2021.08.003

Sadeghi, T., Fatehi, P., Pakzad, L., 2025. Aerosol drug delivery in pediatric airways: in vitro and CFD insights into tongue position and inhalation patterns using soft mist inhalers. Int. J. Pharm. 683, 126059. https://doi.org/10.1016/j.ijpharm.2025.126059

Sadeghi, T., Fatehi, P., Pakzad, L., 2024. Effect of nasal inhalation on drug particle deposition and size distribution in the upper airway: with soft mist inhalers. Ann. Biomed. Eng. https://doi.org/10.1007/s10439-023-03423-7

Shang, Y., Dong, J., Tian, L., Inthavong, K., Tu, J., 2019. Detailed computational analysis of flow dynamics in an extended respiratory airway model. Clin. Biomech. 61, 105–111. https://doi.org/10.1016/j.clinbiomech.2018.12.006

Sheth, P., Grimes, M.R., Stein, S.W., Myrdal, P.B., 2017. Impact of droplet evaporation rate on resulting in vitro performance parameters of pressurized metered dose inhalers. Int. J. Pharm. 528, 360–371. https://doi.org/10.1016/j.ijpharm.2017.06.014

Sou, T., Bergström, C.A.S., 2021. Contemporary formulation development for inhaled pharmaceuticals. J. Pharm. Sci. 110, 66–86. https://doi.org/10.1016/j.xphs.2020.09.006

Talaat, M., Si, X., Xi, J., 2022. Effect of MDI actuation timing on inhalation dosimetry in a human respiratory tract model. Pharmaceuticals 15, 61. https://doi.org/10.3390/ph15010061

Tian, G., Longest, P.W., Su, G., Hindle, M., 2011. Characterization of respiratory drug delivery with enhanced condensational growth using an individual path model of the entire tracheobronchial airways. Ann. Biomed. Eng. 39, 1136–1153. https://doi.org/10.1007/s10439-010-0223-z

Wilcox, D.C., 1993. Turbulence Modelling for CFD 3rd Edition, Turbulence Modeling for CFD.

Williams, J., Kolehmainen, J., Cunningham, S., Ozel, A., Wolfram, U., 2022. Effect of patient inhalation profile and airway structure on drug deposition in image-based models with particle-particle interactions. Int. J. Pharm. 612, 121321. https://doi.org/10.1016/j.ijpharm.2021.121321

Xi, J., April Si, X., Dong, H., Zhong, H., 2018. Effects of glottis motion on airflow and energy expenditure in a human upper airway model. Eur. J. Mech. B/Fluids 72, 23–37. https://doi.org/10.1016/j.euromechflu.2018.04.011

Xu, C., Zheng, X., Shen, S., 2021. A numerical study of the effects of ambient temperature and humidity on the particle growth and deposition in the human airway. Environ. Res. 200, 111751. https://doi.org/10.1016/j.envres.2021.111751

Yousefi, M., Inthavong, K., Tu, J., 2017. Effect of pressurized metered dose inhaler spray characteristics and particle size distribution on drug delivery efficiency. J. Aerosol Med. Pulm. Drug Deliv. 30, 359–372. https://doi.org/10.1089/jamp.2016.1299.

Chapter 9- CFD-Based Investigation of Mouth-Throat Transport and Deposition of Realistic Active Pharmaceutical Ingredients from pMDI Aerosols

9.1 Introduction

Pressurized metered-dose inhalers (pMDIs) deliver aerosols in which the active pharmaceutical ingredient (API) is either dissolved or suspended in a hydrofluoroalkane (HFA) propellant before being released from the valve. The total formulation volume within the canister typically ranges from 8.5 to 19 mL, depending on the specific formulation. Each actuation delivers an API dose of approximately 25–100 μg, representing roughly 1% of the total formulation mass (Stein et al., 2014; Versteeg et al., 2017).

Aerosol delivery within the respiratory tract is a complex multiphase flow phenomenon that can be effectively analyzed using computational fluid dynamics (CFD). The airflow in the human respiratory system exhibits transitions between laminar and turbulent regimes, depending on the geometry and local flow conditions. As air passes through the glottis and enters the trachea, the flow shifts from laminar to turbulent. Further along its path, as the airflow moves from the trachea into the bronchi and bronchioles, it gradually reverts toward a laminar regime (Feng et al., 2021a; Zhao et al., 2020; Longest et al., 2012). Accurately capturing these transitions is essential for predicting the dynamics of inhaled particle transport. Selecting an appropriate turbulence model is therefore crucial to balance accuracy and computational efficiency. Three primary approaches are commonly employed to resolve turbulent flow: Direct Numerical Simulation (DNS), Reynolds-Averaged Navier-Stokes (RANS), and Large Eddy Simulation (LES). DNS offers the highest accuracy by resolving all turbulence scales through the full unsteady Navier–Stokes equations; however, its extreme computational cost makes it impractical for modeling aerosol transport in realistic airway geometries (Feng et al., 2021a; Huang et al., 2021).

The RANS k-ω turbulence model has demonstrated strong predictive capability for airflow and aerosol deposition within the upper respiratory tract, particularly in the nasopharyngeal and extrathoracic regions (Sadeghi et al., 2023; Dastoorian et al., 2022; Longest and Hindle, 2009; Ball et al., 2008; Xi and Longest, 2008; Zhang et al., 2002). In this framework, all turbulent fluctuations are represented through empirical correlations derived from standard flow configurations. In

contrast, Large Eddy Simulation (LES) resolves the large-scale turbulent eddies while modeling only the sub-grid scales using approaches similar to those employed in RANS. Because LES explicitly captures instantaneous turbulent fluctuations, it better represents turbulence anisotropy, particularly in near-wall regions, enhancing the accuracy of particle trajectory and deposition predictions (Huang et al., 2021).

In 2008, Jayaraju et al. simulated airflow in a mouth-throat (MT) model using both the RANS k-ω (without near-wall corrections) and LES frameworks, validating their predictions against Particle Image Velocimetry (PIV) measurements. The LES model reproduced the velocity and turbulent kinetic energy distributions with excellent agreement with the experimental data, whereas the RANS k-ω model showed larger deviations. Regarding particle dynamics, LES demonstrated a clear advantage in predicting deposition for particles smaller than 5 μm, while both models exhibited comparable accuracy for larger particle sizes.

Similarly, Koullapis et al. (2018) performed a comprehensive comparison of the RANS k-ω and LES models to evaluate airflow and regional aerosol deposition in the upper airways. Their study examined several modeling parameters, including particle-tracking schemes, acting forces, injection timing, particle number, numerical methods, and mesh resolution. The LES model produced more accurate mean flow fields and better captured turbulent structures than the RANS k-ω approach. In contrast, RANS k-ω simulations using coarse meshes and mean-flow tracking underestimated turbulence intensity, whereas those employing turbulent tracking tended to overpredict deposition for small and intermediate particle sizes.

Overall, the LES model demonstrated superior accuracy in predicting regional deposition, particularly for larger particles, owing to its capability to explicitly resolve instantaneous velocity fluctuations. In addition to models that treat airflow as a continuous phase, the accuracy of aerosol transport and deposition predictions also depends on how the discrete phase (particles or droplets) is represented. Two primary modeling frameworks are commonly used: the Eulerian or two-fluid model (TFM) and the Lagrangian approach. TFM treats both the fluid and particulate phases as continuous systems, making it computationally efficient for large-scale simulations. However, this formulation limits the ability to resolve individual particle characteristics, such as size, density, and shape, which are critical when particle–particle interactions or non-spherical geometries significantly influence flow dynamics and deposition behavior (Ariyaratne et al., 2018; Chen and

Wang, 2014).

The Lagrangian framework can be further categorized according to whether interactions among discrete particles are included. When particle-particle interactions are neglected, the approach is known as the Discrete Phase Model (DPM); when such interactions are included, it is referred to as the Discrete Element Method (DEM) (Chen and Wang, 2014; Cristea and Conti, 2018; Huang et al., 2021). The DPM is widely used in one-way coupled CFD simulations (Borojeni et al., 2023; Islam et al., 2019; Liu et al., 2023; Rahman et al., 2021; Sarkar et al., 2017; Xi and Longest, 2007; Zhang et al., 2006). This approach assumes that the aerosol phase is sufficiently dilute, allowing particle–particle interactions and feedback effects on the continuous phase to be neglected. While this simplification reduces computational cost, it may compromise predictive accuracy in regions with high aerosol concentrations, where mechanisms such as coalescence and agglomeration become important (Feng and Kleinstreuer, 2014; Islam et al., 2020).

Furthermore, Longest and Hindle (2010) demonstrated that enhanced condensational growth (ECG) can substantially improve drug deposition efficiency in the respiratory tract. Their findings revealed that aerosol concentration strongly influences the final droplet size, whereas the initial aerosol size has a comparatively minor effect. The limitations of the DPM in capturing particle-particle interactions can be addressed by the DEM, which tracks the motion and collisions of individual particles in detail. However, DEM simulations are computationally intensive, particularly for inhaler applications where the number of generated particles is extremely large. DEM is more suitable for granular systems where particle interactions dominate, and fluid effects are relatively weak (Burman et al., 1980).

To bridge this gap, the Dense Discrete Phase Model (DDPM) was developed as a hybrid framework integrating Eulerian-Eulerian and Eulerian-Lagrangian approaches. DDPM effectively accounts for droplet-droplet interactions in dense aerosol flows (Ariyaratne et al., 2018; Cristea and Conti, 2018). Adamczyk et al. (2014) demonstrated that DDPM provides superior accuracy compared to conventional models when simulating polydisperse particle systems, as it enables interaction modeling across both dense and dilute regions and yields improved pressure drop predictions relative to the Euler-Euler method. More recently, Wu et al. (2023) applied the DDPM framework to study coal-sludge co-combustion in a full-loop circulating fluidized bed, successfully capturing gas-solid flow and combustion behavior. On the other hand, a study by

Chen and Wang (2014) compared the TFM, DDPM, and CFD-DEM approaches for impinging gas–solid flow and found that DDPM struggled to accurately simulate dual-jet interactions under certain conditions.

Furthermore, Feng and Kleinstreuer (2014) employed a coupled DDPM-DEM framework to simulate the transport and deposition of interacting particles in a triple-bifurcation bronchial airway. In this approach, DDPM modeled the continuous phase while DEM tracked individual particle dynamics. Their results demonstrated that the hybrid DDPM-DEM model improved the accuracy of fluid-particle interaction predictions compared to the conventional DPM, particularly under dense aerosol inhalation conditions characterized by high inlet particle volume fractions and elevated Stokes numbers. More recently, Williams et al. (2025) investigated coupling effects in simulating drug aerosol inhalation within patient-specific airway geometries. They modeled monodisperse particle injection with a total mass of 100 μg, representing a typical API dose, and found that under two-way coupling, particle motion became decorrelated from the carrier airflow, resulting in a more uniform spatial distribution and a higher total deposition fraction.

In most numerical studies of aerosol generation from pMDIs, the system is simplified by modeling only the API mass, assuming a highly dilute aerosol flow. This simplification, however, neglects the volumetric and dynamic influence of the HFA propellant, which can significantly affect aerosol transport and deposition. Given the high injection velocity of pMDIs (approximately 100 m/s) (Ahookhosh et al., 2021; Duke et al., 2021; Versteeg et al., 2017), particle-particle interactions become non-negligible, as they can alter droplet size distribution and aerodynamic characteristics (Balachandar and Eaton, 2010; Elghobashi, 1994; Williams et al., 2025).

This study aims to address the following research question: How do propellant-induced dense-phase interactions and particle-particle dynamics influence aerosol transport and API deposition in pMDI sprays compared with the conventional dilute-phase CFD assumption? To address this, a more realistic numerical model of inhaled drug transport and deposition in the human airway was developed using a pMDI device model. A four-way coupled DDPM was implemented to simulate a two-phase aerosol mixture comprising the API (100 μg per actuation) and HFA propellant (0.05 mL per actuation). Simulations were performed in ANSYS Fluent employing the k-ω turbulence model for airflow prediction, selected for its superior near-wall resolution and compatibility with DDPM (which currently does not support LES; Huang et al., 2021). The computational domain

was based on a medium-sized Virginia Commonwealth University (VCU) MT geometry. LES-DPM (dilute phase), k-ω-DPM (dilute phase), and k-ω-DDPM (dense phase) were compared to evaluate predictive accuracy and computational efficiency. Simulation results were validated against Next Generation Impactor (NGI) experimental data obtained under identical flow conditions. Both numerical and experimental analyses were conducted at an airflow rate of 30 L/min, a temperature of 22 °C, and a relative humidity (RH) of 50%.

9.2 Experimental Setup and Methodology

We utilized the medium-sized VCU MT geometry (Delvadia et al., 2016, 2012; Longest et al., 2008; Xi and Longest, 2008), obtained from the Respiratory Drug Delivery Online (RDD Online) database (Newman, 2015), for both experimental and computational investigations. The stereolithography (STL) file of the MT model was first imported into SOLIDWORKS® CAD software to create a hollow geometry with an outward wall thickness of 3 mm for experimental fabrication. To facilitate cleaning and rinsing, the MT model was divided into three detachable sections: mouth, pharynx, and trachea. The MT model was then fabricated using an UltiMaker S3 3D printer (Netherlands) employing fused deposition modeling (FDM) technology with a polylactic acid (PLA) filament, as shown in **Fig. 9-1(a)**. The three segments were assembled and sealed with Teflon tape to ensure airtight connections and prevent leakage. For the experiments, a 200-dose Ventolin® pMDI (SANIS Health, Canada) containing salbutamol sulphate (100 μg of active drug per actuation, as labeled) was used. The inhaler was directly connected to the 3D-printed realistic MT model, and aerosol deposition was quantified using an NGI equipped with an eight-stage impactor (see **Fig. 9-1(b))**, a critical flow controller (Copley Scientific, UK), and a vacuum pump (HCP5, Copley Scientific, UK). To maintain consistent environmental conditions, both the MT replica and the impactor were housed inside a temperature-controlled chamber maintained at 22 ± 2 °C and 50 ± 5% RH. The vacuum pump was calibrated to sustain a constant flow rate of 30 L/min, representative of adult resting tidal breathing (Biswas et al., 2017; Worth Longest and Hindle, 2009; Wu et al., 2022).

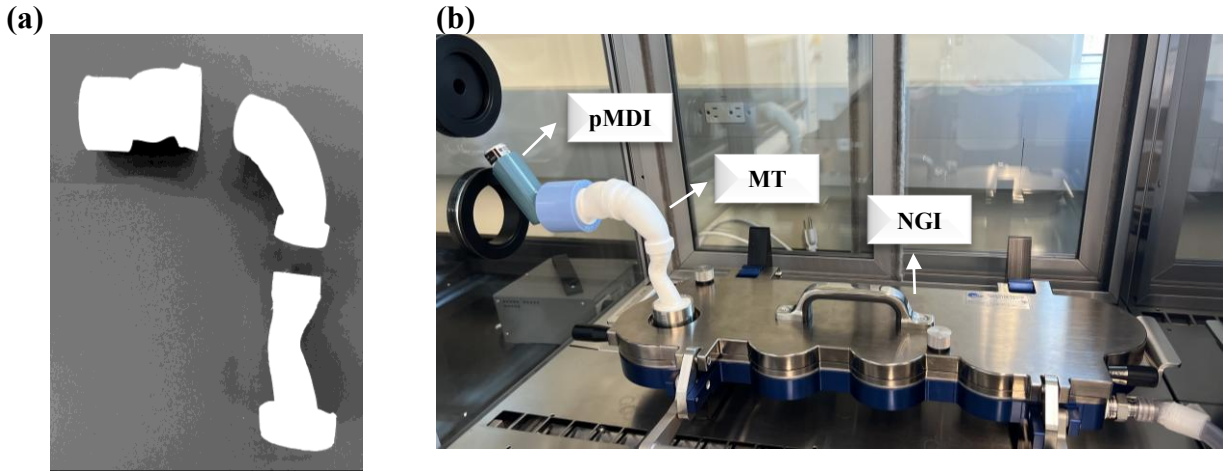

Fig. 9-1: Experimental setup: **(a)** 3D-printed MT replica; and **(b)** salbutamol HFA pMDI connected to the MT model and NGI, housed in the temperature-controlled chamber.

High-performance liquid chromatography (HPLC) analysis was conducted to quantify the amount of salbutamol sulphate deposited on the inhaler mouthpiece, MT replica and the cups of the NGI. The assay utilized an XSelect CSH Prep C18 5 µm OBD 19 × 150 mm column (Waters, US) maintained at 40 °C, connected to a Waters 1525 Binary HPLC pump and a 2489 UV/Visible detector. The calibration curve ranged from 0.2 to 20 ppm, showing a strong linear relationship (R2 = 0.998) with a limit of quantification (LOQ) of 1.7 ppm. The mobile phase consisted of HPLC-grade water and acetonitrile (65:35 v/v), operated at a flow rate of 1 mL/min with an injection volume of 100 µL. Detection was carried out at a wavelength of 254 nm, with a retention time of approximately 4.5 min for salbutamol sulphate. Before each test, the inhaler was shaken, then actuated and connected to the MT model. The device was actuated 5 times at 10-s intervals to ensure adequate drug deposition on the MT and NGI cups above the detection threshold. Each experiment was repeated three times for reproducibility. Following each test, the MT replica segments, inhaler mouthpiece, and NGI cups were rinsed with 15 mL, 10 mL, and 10 mL of HPLC-grade water containing 0.1% formic acid (Fisher Scientific, US), respectively. The collected samples were then filtered through Whatman® nitrocellulose membrane filters with 0.45 µm pore size prior to HPLC analysis.

9.3 CFD Model Development

9.3.1 Geometry and Mesh

The geometries of the pMDI, MT airway model, and the integrated computational mesh structure are depicted in **Fig. 9-2**. Mesh generation was performed using ANSYS Workbench 2024R1 (ANSYS Inc., USA), incorporating polyhedral elements in the fluid domain and poly-prism layers near the walls. The near-wall mesh consisted of eight prism layers with a thickness growth ratio of 0.272, enabling accurate resolution of steep velocity and turbulence gradients in the near-wall region (Feng et al., 2021b; Talaat et al., 2022). The meshing approach and mesh type employed in this study have been previously validated in our prior studies (Jahed et al., 2025).

To ensure mesh-independent predictions of airflow and particle transport within the MT geometry, a mesh sensitivity analysis was conducted using the LES-DPM framework, which generally requires a finer spatial resolution than the k-ω-DPM model. Six different grid resolutions: Mesh A (1,198,640), Mesh B (1,764,833), Mesh C (2,513,892), Mesh D (3,732,088), Mesh E (5,341,060), and Mesh F (8,443,328) elements. All simulations were performed at a constant airflow rate of 30 L/min and 50% RH. **Figs. 9-3(a)** and **(b)** display the mean velocity magnitude at cross sections in the mouth (AA′) and trachea (BB′) regions for each mesh size. The differences in mean velocity magnitude between meshes D and E, as well as between meshes E and F, in both regions, were below 3% and 2%, respectively. Additionally, the effect of mesh resolution on the collision rate in the DDPM simulations was investigated, as illustrated in **Fig. 9-3(c)**. The results demonstrate a significant dependence of the collision rate on mesh refinement, with only minor differences between Meshes E and F. Therefore, Mesh E was selected as the optimal resolution for subsequent simulations.

9.3.2 Governing Equations

9.3.2.1 Airflow as a Continuous phase

To simulate airflow within the MT model and inhaler, the unsteady, three-dimensional, incompressible Navier-Stokes equations were solved using ANSYS Fluent 2024 R1 (ANSYS Inc., USA). Under a constant flow rate of 30 L/min, the Reynolds number in the VCU MT geometry ranged from 1,600 to 4,400, indicating a transition from laminar to turbulent flow. To accurately capture this transitional behavior, both LES with the Wall-Adapting Local Eddy (WALE) sub-grid

model and the k-ω Shear Stress Transport (SST) turbulence model were employed. These models have been extensively applied in respiratory airflow studies (Dastoorian et al., 2022; Feng et al., 2021a; Mohammadkhani et al., 2026, 2025a; Sadeghi et al., 2025; Worth Longest and Hindle, 2009; Xi et al., 2016; Xi and Longest, 2007), demonstrating strong predictive capability for capturing flow separation, vortex structures, and aerosol transport in upper airway geometries.

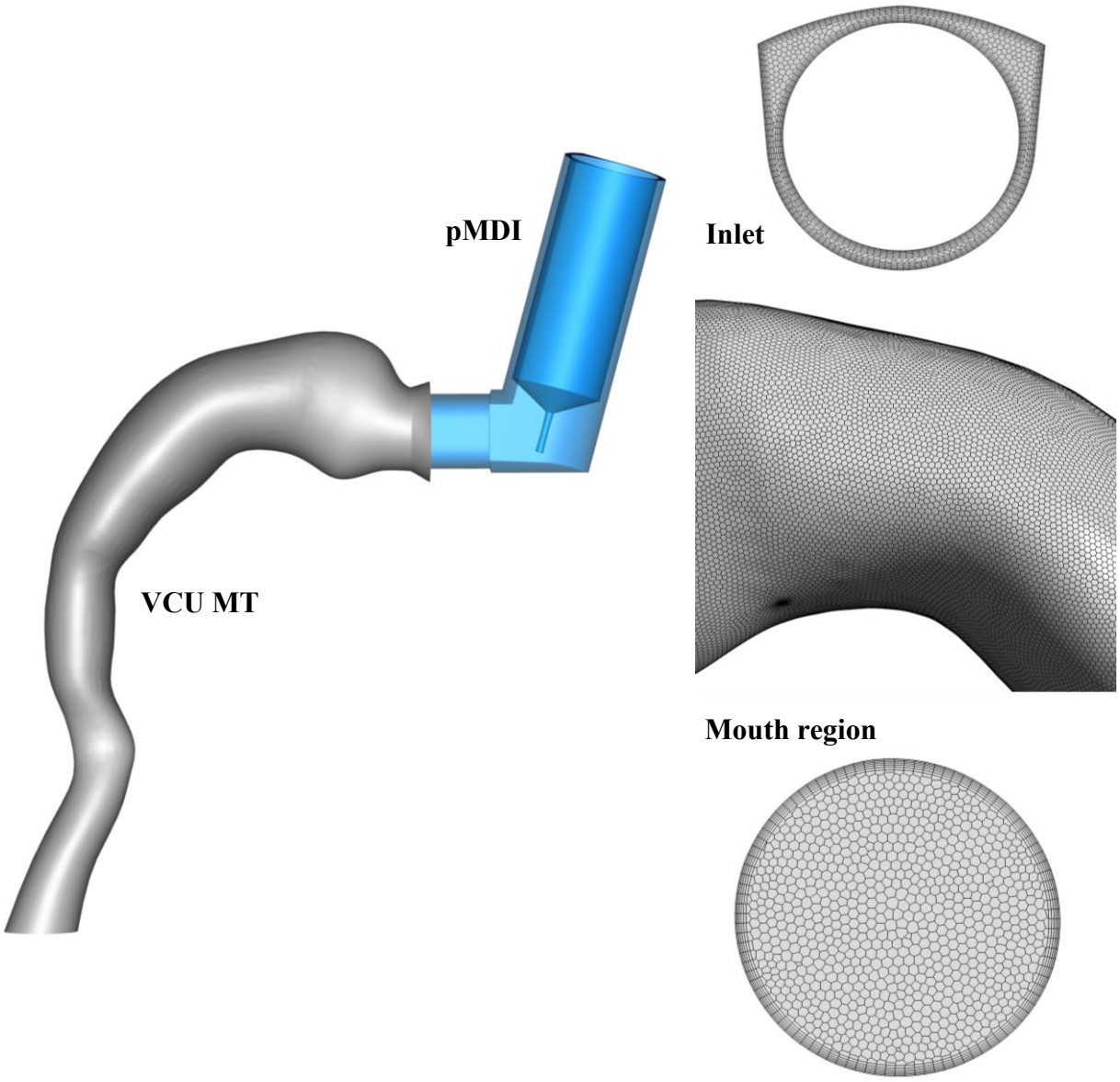

Fig. 9-2: Geometry of the MT model integrated with the pMDI device, along with the computational mesh shown at the inlet, mouth region and outlet.

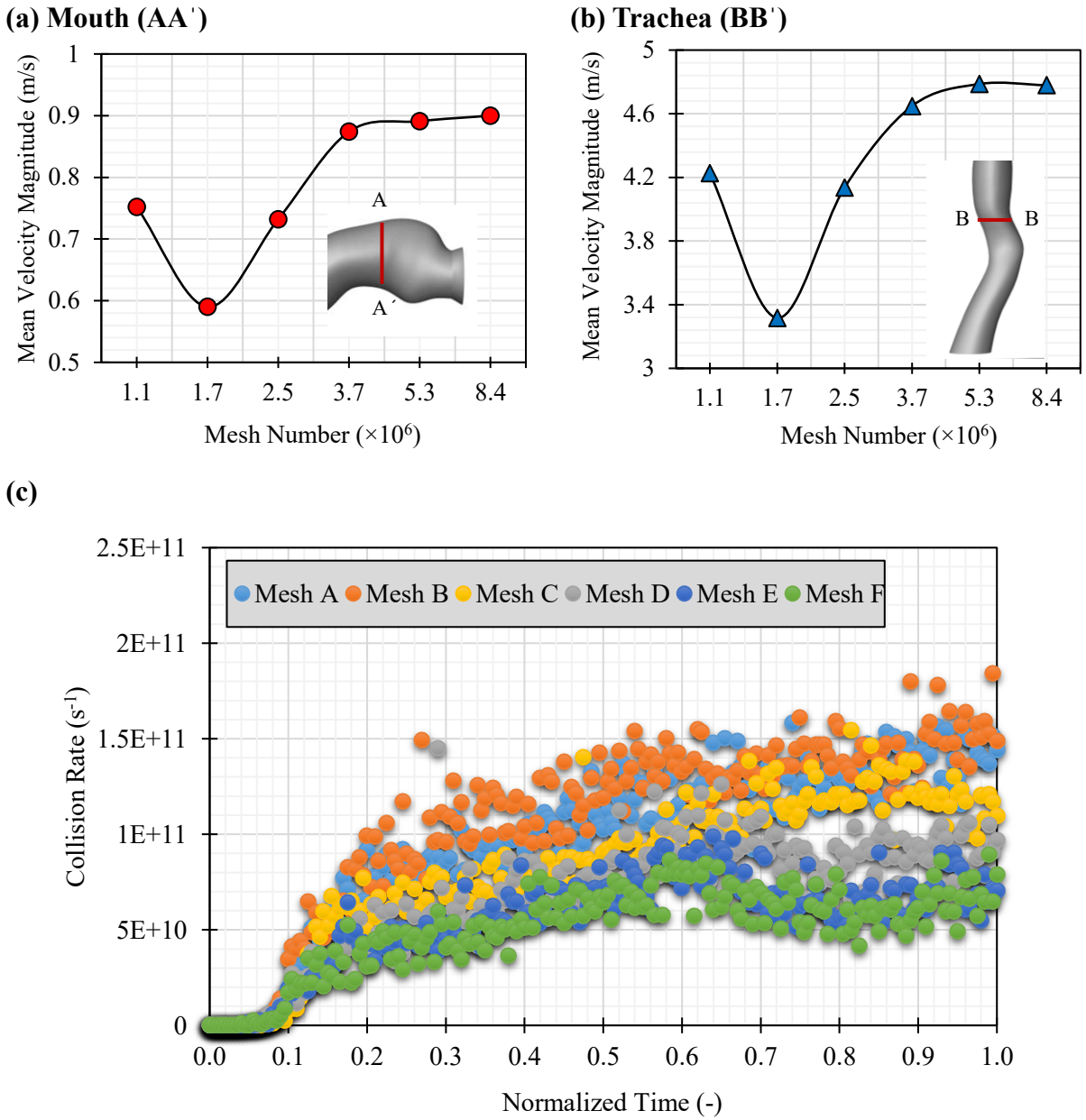

Fig. 9-3: Comparison of mean velocity magnitude at the cross-section of **(a)** the mouth (AA'), and **(b)** the trachea (BB') for different mesh sizes; and **(c)** droplet collision rate across various meshes within the MT model.

Table 9-1 summarizes the turbulence models applied for both dilute and dense aerosol phases. For the dilute phase, airflow was simulated using both LES-WALE and k-ω SST frameworks, along with the corresponding transport equations for turbulent kinetic energy and specific dissipation rate. For the dense aerosol phase, the k-ω SST model was employed. This approach enabled a comparative evaluation of how different turbulence-discrete phase model combinations influence predictions of airflow dynamics, droplet dispersion, and deposition efficiency.

Table 9-1: Governing equations and sub-models employed in the simulation, the dilute and dense phase formulations.

Dilute phase (Wilcox, 1993)	
$\nabla.(\overline{\boldsymbol{u}}) = 0$ (9.1)	ρ: density of mixture (air, water vapor, and droplet vapor) $\overline{\boldsymbol{u}}$ **:** filtered velocity S_{DPM}: mass transfer from the discrete to the continuous phase $\bar{P}$: filtered pressure $\bar{\sigma}$: stress tensor due to molecular viscosity $\bar{\tau}$: subgrid-scale stress $\boldsymbol{F}_i$: body force μ: dynamic viscosity of mixture μ_t: turbulent dynamic viscosity at sub-grid scales $\bar{S}$: filtered rate-of-strain tensor $\bar{S}_{ij}$: filtered rate-of-strain tensor componenet L_s: mixing length for sub-grid scales k_K: von Kármán constant d: distance to the closest wall C_w: WALE constant ($= 0.325$) V: computational cell volume k: turbulent kinetic energy ω: specific dissipation rate P_k: production of turbulent kinetic energy β^*, β: empirical constants σ_k, σ_ω: turbulent Prandtl numbers for k and ω F_l: Blending function to switch between k−ω (near-wall) and k−ϵ (far-field) y: distance to the nearest wall $CD_{k\omega}$: cross-diffusion term
$\rho(\partial/\partial t\,(\overline{\boldsymbol{u}}) + \nabla.(\overline{\boldsymbol{u}}\overline{\boldsymbol{u}})) = -\nabla\bar{P} + \nabla.(\bar{\sigma}) - \nabla.(\bar{\tau}) + \boldsymbol{F}_i$ (9.2)	
$\bar{\sigma} = \mu(\nabla\overline{\boldsymbol{u}} + (\nabla\overline{\boldsymbol{u}})^T) - 2/3\,\nabla.\overline{\boldsymbol{u}}I$ (9.3)	
$\bar{\tau} = -2\mu_t\bar{S}$ (9.4)	
$\bar{S} = 1/2(\nabla\overline{\boldsymbol{u}} + (\nabla\overline{\boldsymbol{u}})^T)$ (9.5)	
LES-WALE (Nicoud and Ducros, 1999)	
$\mu_t = \rho L_s^2 \left(S_{ij}^d S_{ij}^d\right)^{3/2} / \left(\bar{S}_{ij}\bar{S}_{ij}\right)^{5/2} + \left(S_{ij}^d S_{ij}^d\right)^{5/4}$ (9.6)	
$L_s = min\left(k_K d, C_w V^{1/3}\right)$ (9.7)	
$S_{ij}^d = \partial\bar{u}_i/\partial x_j$ (9.8)	
k-ω SST (Wilcox, 1993)	
$\mu_t = \rho k/\omega$ (9.9)	
$\rho(\partial/\partial t\,(k) + \nabla.(\overline{\boldsymbol{u}}_p)) = P_k - \beta^*\rho\omega k + \nabla.[(\mu + \sigma_k\mu_t)\nabla k]$ (9.10)	
$\rho(\partial/\partial t\,(\omega) + \nabla.(\overline{\boldsymbol{u}}_p\omega)) = P_k\omega/k - \beta\rho\omega^2 + +\nabla.[(\mu + \sigma_\omega\mu_t)\nabla\omega] + 2(1 - F_l)\rho\sigma_{\omega 2}1/\omega\nabla k.\nabla\omega$ (9.11)	
$F_l = \tanh(\min(\max(\sqrt{k}/\beta^*\omega y, 500\mu/y^2\rho\omega), 4\rho\sigma_{\omega 2}k/CD_{k\omega}y^2))$ (9.12)	

Dense phase (k-ω SST) (Anderson and Jackson, 1967)

$$\partial(\alpha_p\rho_p)/\partial t + \nabla.(\alpha_p\rho_p\overline{\boldsymbol{u}}_p) = \sum_{q=1}^{nphases}(\dot{m}_{qp} - \dot{m}_{pq}) \quad (9.13)$$

$$\partial/\partial t\left(\alpha_p\rho_p\overline{\boldsymbol{u}}_p\right) + \nabla.\left(\alpha_p\rho_p\overline{\boldsymbol{u}}_p\overline{\boldsymbol{u}}_p\right) = -\alpha_p\nabla\bar{P} + \nabla.\left(\alpha_p\bar{\bar{\sigma}}\right) - \nabla.\left(\alpha_p\bar{\bar{\tau}}\right) + \boldsymbol{F}_i + \sum_{q=1}^{nphases}(\dot{m}_{pq}\overline{\boldsymbol{u}}_{pq} - \dot{m}_{qp}\overline{\boldsymbol{u}}_{qp}) + K_{DPM}(\bar{v}_{DPM} - \overline{\boldsymbol{u}}_p) + S_{DPM,explicit} \quad (9.14)$$

$$\mu_t = \alpha_p\rho_p k/\omega \quad (9.15)$$

$$\partial/\partial t\left(\alpha_p\rho_p k\right) + \nabla.\left(\alpha_p\rho_p\overline{\boldsymbol{u}}_p\right) = P_k - \alpha_p\beta^*\rho_p\omega k + \nabla.[(\mu_p + \sigma_k\mu_t)\nabla k] \quad (9.16)$$

$$\partial/\partial t\left(\alpha_p\rho_p\omega\right) + \nabla.\left(\alpha_p\rho_p\overline{\boldsymbol{u}}_p\omega\right) = P_k\omega/k - \alpha_p\beta\rho_p\omega^2 + +\nabla.[(\mu_p + \sigma_\omega\mu_t)\nabla\omega] + 2(1 - F_l)\rho_p\sigma_{\omega 2}1/\omega\nabla k.\nabla\omega \quad (9.17)$$

α_p: volume fraction of phase p (airflow)

$\overline{\boldsymbol{u}}_p$: time-averaged velocity of phase p (airflow)

ρ_p: mixture density of phase p

$\dot{m}_{pq}$: mass transfer from phase q (droplets) to p (airflow)

$\dot{m}_{qp}$: mass transfer from phase p (airflow) to q (droplets)

$\overline{\boldsymbol{u}}_{pq}$: velocity of mass transfer from phase q to p

$\overline{\boldsymbol{u}}_{qp}$: velocity of mass transfer from phase p to q

K_{DPM}: drag coefficient

$S_{DPM,explicit}$: explicit source term for DPM

$\bar{v}_{DPM}$: velocity of the discrete phase

To estimate the temperature distribution within the MT during dense-phase simulations, the enthalpy equation for the airflow was solved:

$$\partial/\partial t\left(\alpha_p\rho_p\left(e_p+\frac{\overline{\boldsymbol{u}}_p^2}{2}\right)\right)+\nabla.\left(\alpha_p\rho_p\overline{\boldsymbol{u}}_p\left(h_p+\frac{\overline{\boldsymbol{u}}_p^2}{2}\right)\right) \tag{9.18}$$
$$=\nabla.\left(\alpha_p k_{eff}\nabla T_p-\sum_s h_s\vec{J}_s+\left(\alpha_p\bar{\tau}_{eff}.\overline{\boldsymbol{u}}_p\right)\right)+\overline{P}\partial\alpha_p/\partial t$$
$$+\sum_{q=1}^{nphases}\left(\dot{m}_{pq}h_{pq}-\dot{m}_{qp}h_{qp}\right)+Q_{DPM}+S_{DPM,explicit}$$

where e_p is the internal energy of the airflow, $k_{eff}=k+k_t$ denotes the effective thermal conductivity with k_t representing the turbulent thermal conductivity, T_p is the airflow temperature, h_s refers to the enthalpy of a specific species, $\vec{J}_s$ is the species diffusion flux, and $\bar{\tau}_{eff}$ is the effective shear stress tensor. The airflow enthalpy (h_p) is defined as:

$$h_p=\sum_s Y_s h_s+\bar{P}/\rho \tag{9.19}$$

where Y_s denotes the mass fraction of species (e.g., air and water vapor). The enthalpy of species (h_s) is defined as:

$$h_s=\int c_{P,s}dT \tag{9.20}$$

where $c_{P,s}$ is the specific heat capacity of the species. The diffusion flux of species ($\vec{J}_s$) is defined as:

$$\vec{J}_s=-(\rho D_{s,m}+\mu_t/Sc_t)\nabla Y_s-D_{T,s}\nabla T/T \tag{9.21}$$

where $D_{s,m}$ and $D_{T,s}$ are the mass and thermal diffusion coefficients, respectively (Xu et al., 2021). The turbulent Schmidt number (Sc_t) was determined using the Sherwood number correlation $Sh=0421(ReSc_t)^{0.446}$, as reported by Zhang et al. (2006). The terms h_{pq} and h_{qp} represent enthalpy associated with mass transfer between the airflow and droplets. Q_{DPM} denotes the convective heat transfer between droplets and the airflow, which is defined as:

$$Q_{DPM}=h_{DPM}A_i(T_{DPM}-T_p) \tag{9.22}$$

where h_{DPM} is the particle-averaged interphase heat exchange coefficient, A_i is the interfacial area between the droplets and the airflow, and T_{DPM} is the particle-averaged temperature. The transport

equation for the species, which accounts for air, water vapor, and droplet vapor, is provided by Feng et al. (2021a) as follows:

$$\partial/\partial t\,(\alpha_p \rho_p Y_s) + \nabla.\left(\alpha_p \rho_p \overline{\boldsymbol{u}} Y_s\right) = -\nabla.\vec{J}_s + S_s \tag{9.23}$$

where S_s denotes the source term contributed by the discrete phase as a result of droplet evaporation or condensation. In the dilute phase, DPM simplifies Eqs. (9.18-23) by assuming that the discrete-phase volume fraction is negligible, i.e., $\alpha_p = 1$. This simplification treats droplets as point entities that occupy no volume within the continuous phase (Crowe et al., 2011; Sommerfeld, 2001). Consequently, local volume fraction corrections to the source terms in the energy equation, Eq. (9.18), are omitted. The DPM also does not explicitly account for enthalpy transfer associated with mass exchange between phases in the energy equation for the continuous phase. Instead, phase-change processes, such as evaporation and condensation, are directly modeled via Lagrangian particle tracking, without requiring modifications to the governing equations of the continuous phase (ANSYS, 2024).

9.3.2.2 Discrete Phase Model (DPM)

The Lagrangian DPM model was employed to track diluted aerosol droplets, which were one-way coupled and injected into the MT geometry via a pMDI. The propellant, primarily hydrofluoroalkane (HFA-134a or HFA-227a), constitutes approximately 99% of the pMDI canister mass (Duke et al., 2019; Sheth et al., 2017; Sou and Bergström, 2021). For this study, we focused on multi-component droplets made up of 99% HFA-134a by mass, with properties outlined in **Table 6-3**, and 1% non-evaporating API with a density of 1,230 kg/m³. The droplet size distribution was defined using the Rosin-Rammler method, capturing a polydisperse range of droplet sizes, as detailed in section 6.3.2.3. The inhaler's injection time was set to 0.1 s, matching the actuation time of Ventolin® HFA.

Droplet motion was governed by Newton's second law, accounting for drag, gravitational, and stochastic forces. Other forces, including the Saffman lift force, buoyancy, pressure, Basset force, and virtual mass effects, were excluded because of the high droplet density relative to air (Finlay, 2019).

The governing equation for droplet motion is expressed as:

$$m_d \, \mathrm{d}\overline{\boldsymbol{u}}_{\boldsymbol{d}}/dt = 18\mu/\rho_d d_d^2 \frac{m_d C_{Dd} Re_d}{24}(\overline{\boldsymbol{u}} - \overline{\boldsymbol{u}}_{\boldsymbol{d}}) + g(\rho_d - \rho)/\rho_d \quad (9.24)$$

where $\overline{\boldsymbol{u}}_{\boldsymbol{d}}$, ρ_d, d_d, and m_d denote the velocity, density, diameter, and mass of the droplets, respectively, and $\overline{\boldsymbol{u}}$, μ, and ρ represent the velocity, molecular viscosity, and density of the inhaled airflow, respectively (Ahookhosh et al., 2021; Narayanan et al., 2022).

$$C_{Dd} = C_D/C_c \quad (9.25)$$

$$C_D = a_1 + a_2/Re_d + a_2/{Re_d}^2 \quad (9.26)$$

$$C_c = 1 + 2\lambda/d_d\left(1.257 + 0.4e^{-(11d_d/2\lambda)}\right) \quad (9.27)$$

$$Re_d = \rho_d d_d|\overline{\boldsymbol{u}} - \overline{\boldsymbol{u}}_{\boldsymbol{d}}|/\mu \quad (9.28)$$

where C_D represents the drag coefficient, C_c denotes the Cunningham correction factor, a_1, a_2, a_3 are constants (Morsi and Alexander, 1972), λ indicates the molecular mean free path, and Re_d refers to the Reynolds number of droplets.

The droplet temperature is calculated by accounting for convective heat transfer, latent heat effects, and the multi-component vaporization rate between the droplets and the continuous phase:

$$m_d c_d dT_d/dt = h_c A_d(T - T_d) + \sum_i dm_i/dt(h_{vap,i}) \quad (9.29)$$

where c_d and A_d represent the particle heat capacity and surface area, respectively. m_i is the mass of component *i* within the droplet, and $h_{vap,i}$ is the latent heat of vaporization of component *i.* h_c denotes the convective heat transfer coefficient (Aghaei et al., 2023), determined using the Nusselt (Nu) number correlation (Eq. 30) proposed by Ranz and Marshall, (1952):

$$Nu = h_c d_p/k = (\ln(1 + B_T)/B_T)\,(2 + 0.6\, Re_d^{1/2} Pr^{1/3}) \quad (9.30)$$

where k is the thermal conductivity of the continuous phase (airflow), and B_T is the Spalding heat transfer number. The Prandtl number of the continuous phase, $Pr = v_t/\alpha_t$, was set equal to 0.85 (Gessner, 2001), where v_t is the turbulent eddy viscosity, and α_t is the turbulent thermal diffusivity.

The vaporization rate of component *i* is expressed as:

$$\frac{dm_i}{dt} = -A_d k_{c,i} \rho \ln(1 + B_{m,i}) \tag{9.31}$$

where $k_{c,i}$ and $B_{m,i}$ are the mass transfer coefficient and the Spalding mass number, for species i., respectively.

9.3.2.3 Dense Discrete Phase Model (DDPM)

The DDPM model employed in this study represents a hybrid that integrates both Eulerian-Eulerian and Eulerian-Lagrangian to simulate dense aerosol injection and its influence on airflow. This four-way coupled model explicitly accounts for the effects of dense aerosols on the continuous phase (airflow) within the MT geometry, as well as droplet-droplet interactions, including coalescence and bouncing due to collisions. The DDPM follows the general Lagrangian DPM formulation for particle motion described in Eqs. (9-24-31), with the key distinction that droplet feedback on the continuous phase is incorporated through the local volume fraction distribution (ANSYS, 2024), as summarized in **Table 9-1**. Additionally, to resolve droplet-droplet interactions, the O'Rourke algorithm (O'Rourke, 1981) was employed.

In this method, collisions can occur only when two droplet parcels occupy the same computational cell of the continuous phase. Once a collision is detected, the algorithm evaluates its outcome, either coalescence or bouncing, based on the collisional (We_c) number:

$$We_c = \rho U_{rel}^2 \overline{D} / \sigma \tag{9.32}$$

where U_{rel} is the relative velocity between the two parcels, $\overline{D}$ is the arithmetic mean diameter of the droplets represented by the two parcels, and σ is the surface tension. The outcome of a collision determines how the states of the interacting droplets are updated: coalescence typically occurs during direct collisions, whereas oblique impacts tend to result in bouncing (ANSYS, 2024). The offset distance between droplet centers and the trajectory of the smaller droplet influences the likelihood of coalescence. This critical offset depends on both the collisional Weber number (We_c) and the size ratio between the collector droplet and the smaller droplet. O'Rourke (1981) quantified the critical offset using the following equation:

$$b_{crit} = (r_1 + r_2)\sqrt{\min(1.0, 2.4f/We_c)} \tag{9.33}$$

where r_1 and r_2 are the radii of the collector (larger) and smaller droplets, respectively, and f is a function that accounts for the size ratio between the two droplets:

$$f(r_1/r_2) = (r_1/r_2)^3 - 2.4\,(r_1/r_2)^2 + 2.7(r_1/r_2) \quad (9.34)$$

The actual collision parameter b is given by:

$$b = (r_1 + r_2)\sqrt{Y} \quad (9.35)$$

where Y is a random number between 0 and 1. A collision is deemed to result in coalescence if b is less than b_{crit}; otherwise, the droplets bounce apart (O'Rourke, 1981).

9.3.3 Boundary Conditions and Simulation

The inlet boundary condition was specified as a mass flow inlet of 6.45×10^{-4} kg/s, corresponding to a constant breathing flow rate of 30 L/min at room temperature (22°C) and 50% RH. A zero-pressure outlet condition was applied at the airway exit, while no-slip conditions were enforced on all airway walls. For both the DPM and DDPM frameworks, a trap boundary condition was assigned to the MT walls, and an escape condition was applied to droplets leaving through the airway outlet. Simulations employed the Phase-Coupled SIMPLEC (Semi-Implicit Method for Pressure-Linked Equations-Consistent) algorithm for pressure-velocity coupling. All computations were carried out on the Narval cluster, which features AMD EPYC Zen2 processors with up to 256 cores and 256 GiB of RAM per node. The average runtime for simulations ranged from 72 to 168 hours.

9.4 Results and Discussion

Fig. 9-4(a) compares deposition efficiency across a range of impaction parameters (μm²·L/min), revealing consistent trends between the present computational models and previously published experimental datasets (Cheng et al., 2015, 2001; Golshahi et al., 2013; Stahlhofen et al., 1989; Xi et al., 2016; Zhou et al., 2011). As expected, the deposition rate increased with increasing impaction parameters, in agreement with well-established in-vitro observations reported by Zhou et al. (2011) and Xi et al. (2016).

Among the modeling approaches, the RANS-based k-ω-DPM predictions most closely followed the experimental curve across the full range of impaction parameters. The LES-DPM model also captured the overall trend but slightly underpredicted deposition in the mid-to-high impaction region. In contrast, the k-ω-DDPM model underestimated deposition at impaction parameters below 10^3 μm²·L/min. **Fig. 9-4(b)** further quantifies these observations by comparing the total deposition fractions across all models and validation datasets. The LES-DPM and k-ω-DPM

models predicted deposition fractions of approximately 52.30% and 53.26%, respectively, which closely matched the in-vitro results (55.44%) and previously published values reported by Cheng et al. (2001) (56.84%) and Mohammadkhani et al. (2025b) (56.30%).

In contrast, the DDPM approach underpredicted deposition (48.40%), highlighting differences in dense-phase behavior compared with dilute-phase models. These results indicate that dense-phase modeling can affect deposition predictions in ways that differ from dilute-phase assumptions, representing an essential first step toward assessing whether four-way-coupled dense-phase modeling can more accurately capture pMDI spray behavior. Similar trends have been reported in previous studies; for instance, the CFD study by Cui (2011) on airflow and particle dispersion in the human upper respiratory system demonstrated that incorporating two-way coupling resulted in lower deposition efficiencies for submicron and micron particles compared with one-way DPM, highlighting the critical role of interphase and interparticle interactions in aerosol transport dynamics.

Fig. 9-5 compares the relative velocity vectors between the aerosol phase and the airflow for three simulation frameworks: LES-DPM, k-ω-DPM, and k-ω-DDPM, alongside the propellant flow visualized in the 2D MT geometry using Schlieren imaging, as reported by McKiernan (2019). PIV software was employed to track the transient plume features (McKiernan, 2019) (**Fig. 9-5(a)**). The vectors represent the local relative velocity as $u_{rel} = u_d - u_f$, capturing the slip between droplet and fluid velocities. In the LES-DPM case (**Fig. 9-5(b)**), strong fluctuations in both magnitude and direction are observed, particularly near the oral cavity and along the central jet, where unsteady eddies intermittently accelerate or decelerate particles relative to the airflow. These fluctuations reflect one-way coupling under large-eddy turbulence, capturing localized inertial decoupling and secondary flows. In contrast, the k-ω-DPM model (**Fig. 9-5(c)**) produces a smoother relative velocity field, consistent with the time-averaged nature of RANS-based turbulence modeling. Although the slip vector directions resemble those in LES, fine-scale fluctuations are suppressed, and the flow in the pharynx follows the expected curvature toward the trachea. A marked deviation is observed in the k-ω-DDPM case (**Fig. 9-5(d)**), where four-way coupling alters the flow topology. Here, relative velocity vectors exhibit reduced magnitude and directional divergence at the mouth entrance, and the airflow is redirected by the momentum of the dense particle phase.

(a)

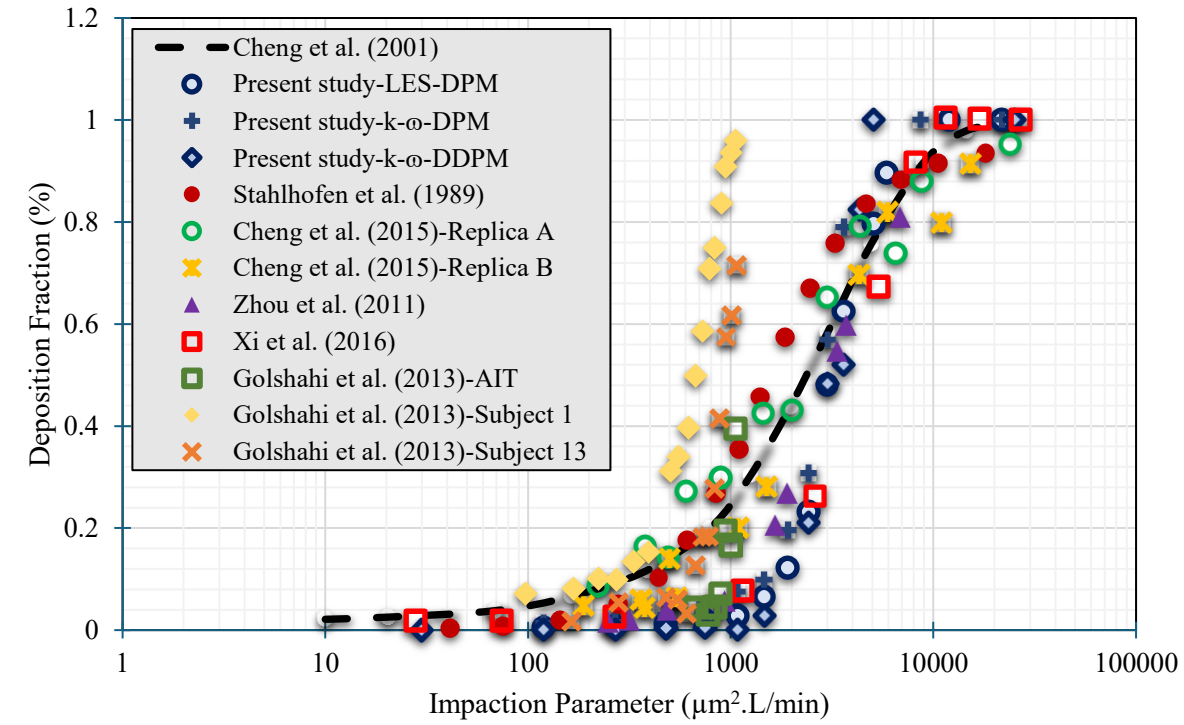

(b)

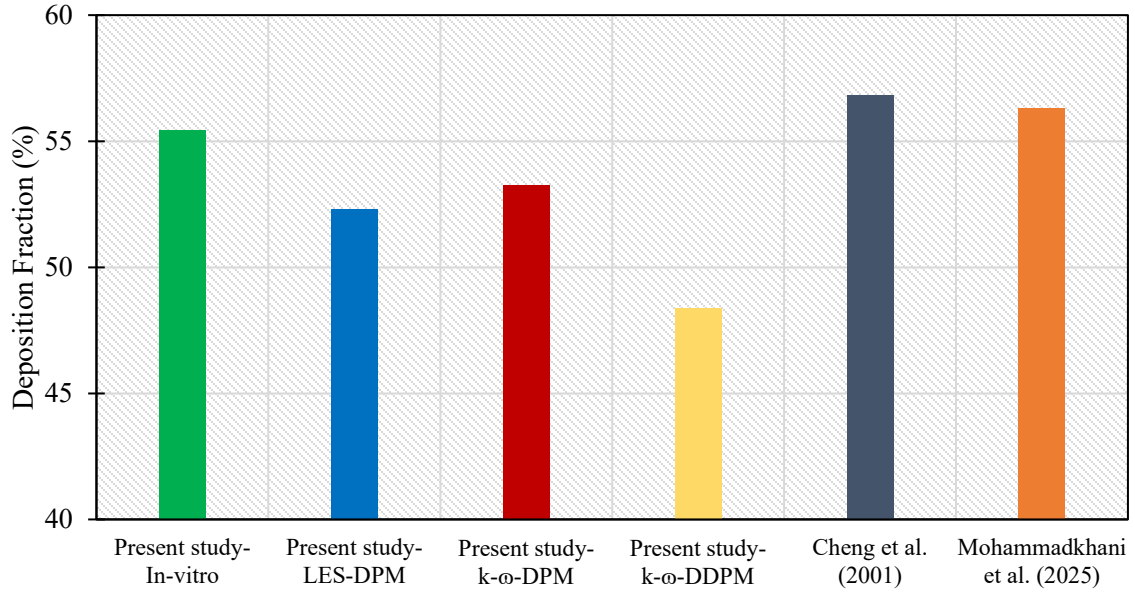

Fig. 9-4: **(a)** Comparison of deposition rate as a function of the impaction parameter; **(b)** total deposition fraction between the present CFD models (LES–DPM, k–ω–DPM, k–ω–DDPM) in comparison with in-vitro measurements and experimental data from previous studies.

The dashed box highlights a region where, in the one-way coupled cases (LES-DPM and k-ω-DPM), the main flow bends downward toward the tracheal axis. In contrast, in the four-way coupled DDPM model, the flow remains straighter and aligns with the aerosol jet direction, closely matching McKiernan's (2019) experimental observations (**Fig. 9-5(a)**). This realignment indicates that the aerosol phase influences airflow through two-way momentum exchange, thereby entraining the surrounding flow and causing it to move with the particles.

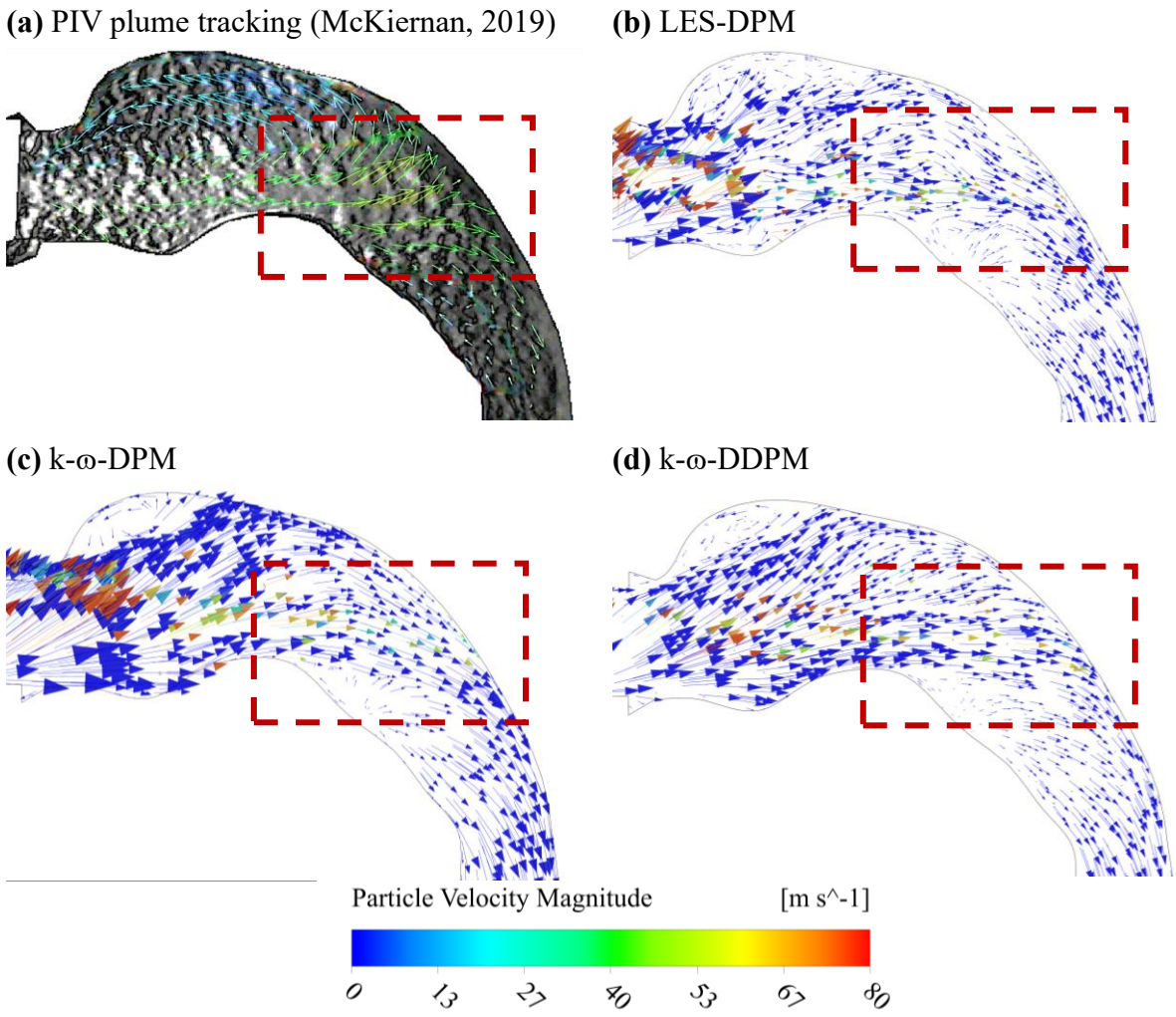

Fig. 9-5: Relative velocity vectors of the aerosol phase in the mid-sagittal plane for: **(a)** PIV plume tracking (McKiernan, 2019); **(b)** LES-DPM; **(c)** k-ω-DPM; and **(d)** k-ω-DDPM.

Overall, the DDPM model exhibits smoother gradients, lower relative velocities, and reduced slip, providing a more physically realistic representation of dense aerosol-air interactions (Cui, 2011; Feng and Kleinstreuer, 2014). This also explains its tendency to underpredict deposition fractions: stronger particle-air entrainment suppresses inertial impaction. LES-DPM captures unsteady,

turbulence-driven slip that promotes dispersion, while DDPM highlights interphase momentum coupling that governs plume alignment in dense pMDI sprays.

Following the relative velocity analysis, airflow characteristics were further examined using both secondary flow streamlines (**Fig. 9-6**) and velocity magnitude profiles (**Fig. 9-7**) across multiple cross-sections of the MT region. The cross-sectional streamlines (**Fig. 9-6**) illustrate the development of secondary flow structures induced by the high-speed pMDI jet and airway curvature. While all three frameworks, LES-DPM, k-ω-DPM, and k-ω-DDPM, capture the main jet penetration, their predictions of secondary vortices differ substantially. As shown in **Fig. 9-6,** LES-DPM resolves fine-scale, asymmetric, and unsteady vortices, reflecting the rich turbulence characteristics of large-eddy simulations. In contrast, the RANS-based k-ω models predict smoother, more symmetric patterns with reduced small-scale structures due to time averaging. Similar observations were reported by Cui (2011), who compared SST k-ω and LES turbulence models at a flow rate of 30 L/min in an MT model. Their result showed that although both approaches reproduced the main laryngeal jet and overall recirculation zones, the secondary vortical structures differed noticeably. The k-ω-DDPM model, which incorporates four-way coupling, shows modified vortex structures and a reshaped jet core, as shown in **Fig. 9-6**. The presence of a dense aerosol phase and droplet collisions facilitates momentum exchange between particles and the continuous phase, redistributing flow momentum toward the periphery and altering the overall flow field.

These differences are further quantified in **Fig. 9-7**, which presents velocity magnitude profiles along three lines: MM' (mouth), PP' (pharynx), and TT' (trachea). At MM', just downstream of the jet origin (**Fig. 9-7(b)**), LES-DPM predicts a peaked velocity profile with pronounced near-wall gradients, capturing shear-layer instabilities (Cui and Gutheil, 2011; Koullapis et al., 2018). The k-ω-DPM model underpredicts peak velocities and shows a flatter distribution, whereas the k-ω-DDPM model predicts higher velocities, particularly near the jet core, where strong particle–air interactions accelerate the local flow. This behavior highlights the influence of interphase momentum exchange in the dense aerosol region injected at 80 m/s, enhancing jet diffusion and modifying the flow structure, effects absent in one-way coupled simulations.

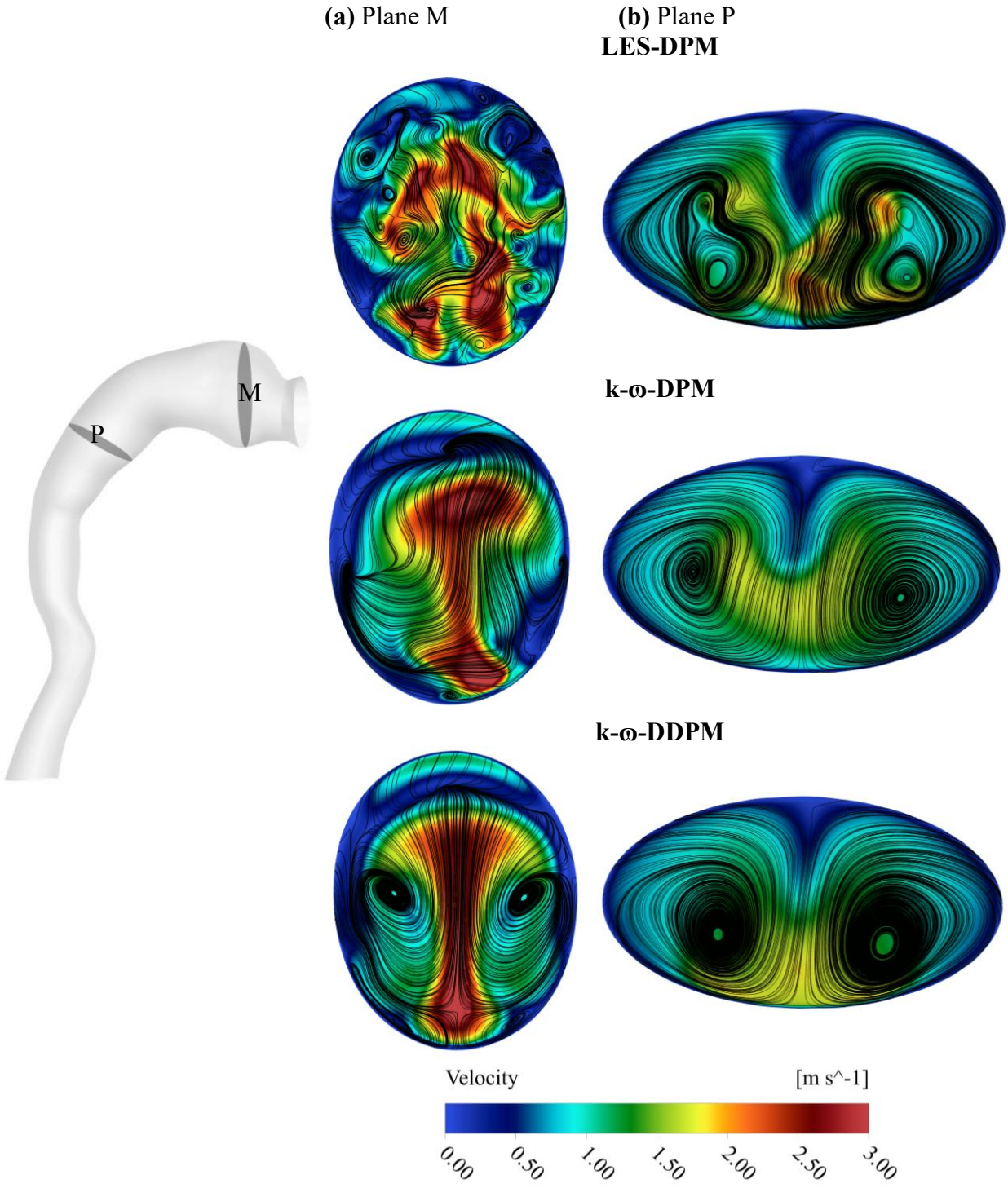

Fig. 9-6: Secondary flow streamlines overlaid on velocity magnitude contours across cross-sections in the **(a)** mouth (M); and **(b)** pharynx (P) regions, comparing predictions from LES-DPM, k–ω-DPM, and k–ω-DDPM frameworks.

At the PP' section (**Fig 9-7(b)**), LES captures local velocity fluctuations likely associated with secondary vortices. Notably, the DDPM model closely follows the LES trend at the secondary

peak, whereas the one-way k-ω-DPM model significantly underpredicts the velocity in this region. By the TT' line (**Fig 9-7(c)**), the velocity field approaches a quasi-fully developed state in all models, though minor differences remain at the centerline. These results demonstrate that both turbulence modeling and interphase coupling influence the development of secondary flows and the axial velocity field, especially in upstream regions where flow curvature, jet dynamics, and shear interactions dominate.

(a) MM'

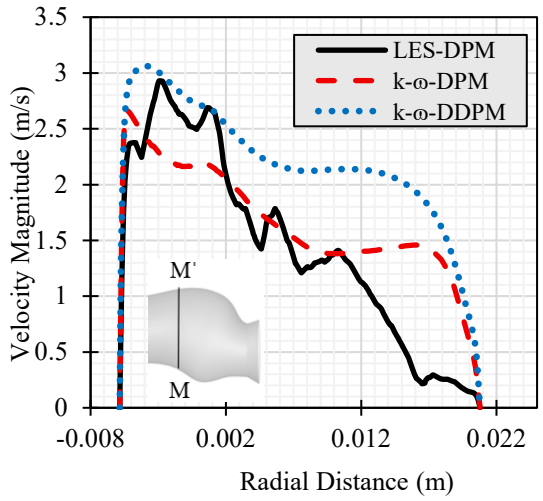

(b) PP'

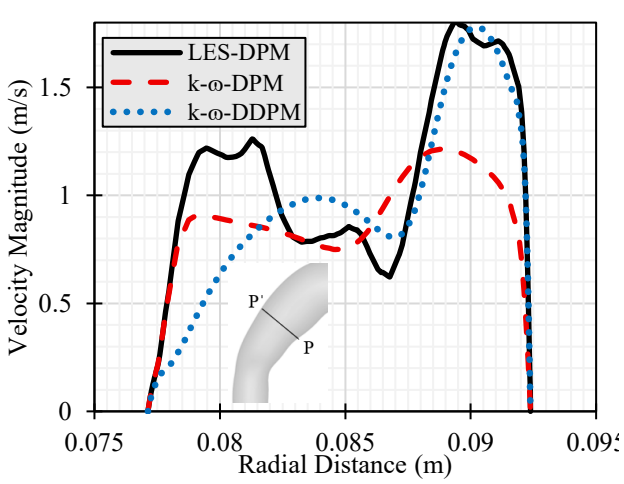

(c) TT'

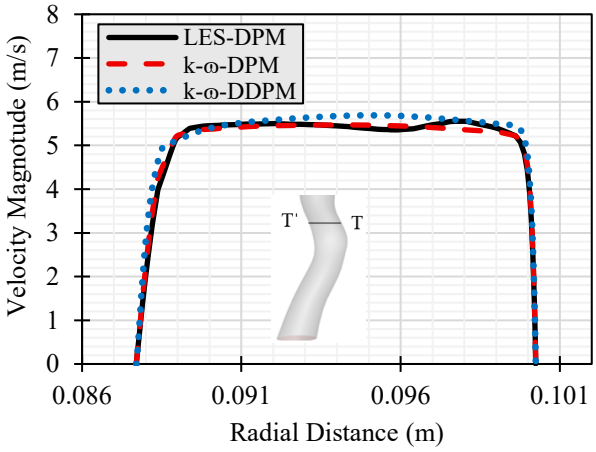

Fig. 9-7: Velocity magnitude profiles along radial lines at three cross-sectional locations in the MT geometry: **(a)** MM' (mouth); **(b)** PP' (pharynx); and **(c)** TT' (trachea), comparing predictions from LES-DPM, k–ω-DPM, and k–ω-DDPM frameworks.

Fig. 9-8 compares particle deposition patterns within the MT geometry with the corresponding particle-size distributions predicted by the three modeling frameworks. As shown in **Fig. 9-8(a)**, all three models identify similar primary deposition regions along the posterior wall of the oropharynx and at the laryngeal jet impaction zone, consistent with the dominant inertial impaction mechanism characteristic of pMDI sprays. However, the extent and distribution of deposition vary across models. LES-DPM predicts a slightly broader deposition pattern, with dispersed particles reaching deeper into the tracheal region. This broader distribution reflects the higher turbulent mixing and secondary vortical motions captured by LES, which promote particle dispersion and wall re-entrainment.

In contrast, the k-ω-DPM model predicts a more localized deposition pattern, concentrated near the central jet path and posterior pharyngeal wall, due to its smoother, time-averaged representation of turbulence. The observed variability in regional deposition among these frameworks aligns with the findings of Koullapis et al. (2018), who conducted a multi-group benchmark study comparing aerosol deposition across different computational models in a standardized airway geometry. They reported substantial variability in regional deposition, particularly within the extrathoracic and upper tracheal regions, despite comparable total deposition. They attributed these differences to turbulence resolution, particle-tracking accuracy, and mesh refinement, which influence local flow fluctuations that govern particle impaction and dispersion. In their analysis, RANS-based models generally predicted more localized, upstream deposition, whereas higher-fidelity LES approaches captured broader, more distributed deposition patterns extending toward the distal airways.

Introducing interphase and interparticle coupling in the k-ω-DDPM framework markedly alters the deposition pattern. Deposition in the oral cavity decreases, and accumulation occurs near the upper trachea. This shift indicates that particle-particle and particle-fluid interactions reduce jet momentum and modify local airflow, consistent with the dense-phase effects discussed earlier. The corresponding deposited particle size distributions in **Fig. 9-8(b)** show similar peaks around 15-17 μm across all models. However, the DDPM curve shows a narrower, higher peak with a distinct tail extending beyond 25 μm, suggesting that collisions and coalescence in the dense-phase model promote the formation of larger agglomerates. The DDPM framework also predicts slightly higher mid-sized droplet fractions, about 6% and 4% higher than k-ω-DPM and LES-DPM, respectively, and a small population of larger particles (0.3% larger than 25 μm), reflecting additional physical processes absent in dilute DPM models.

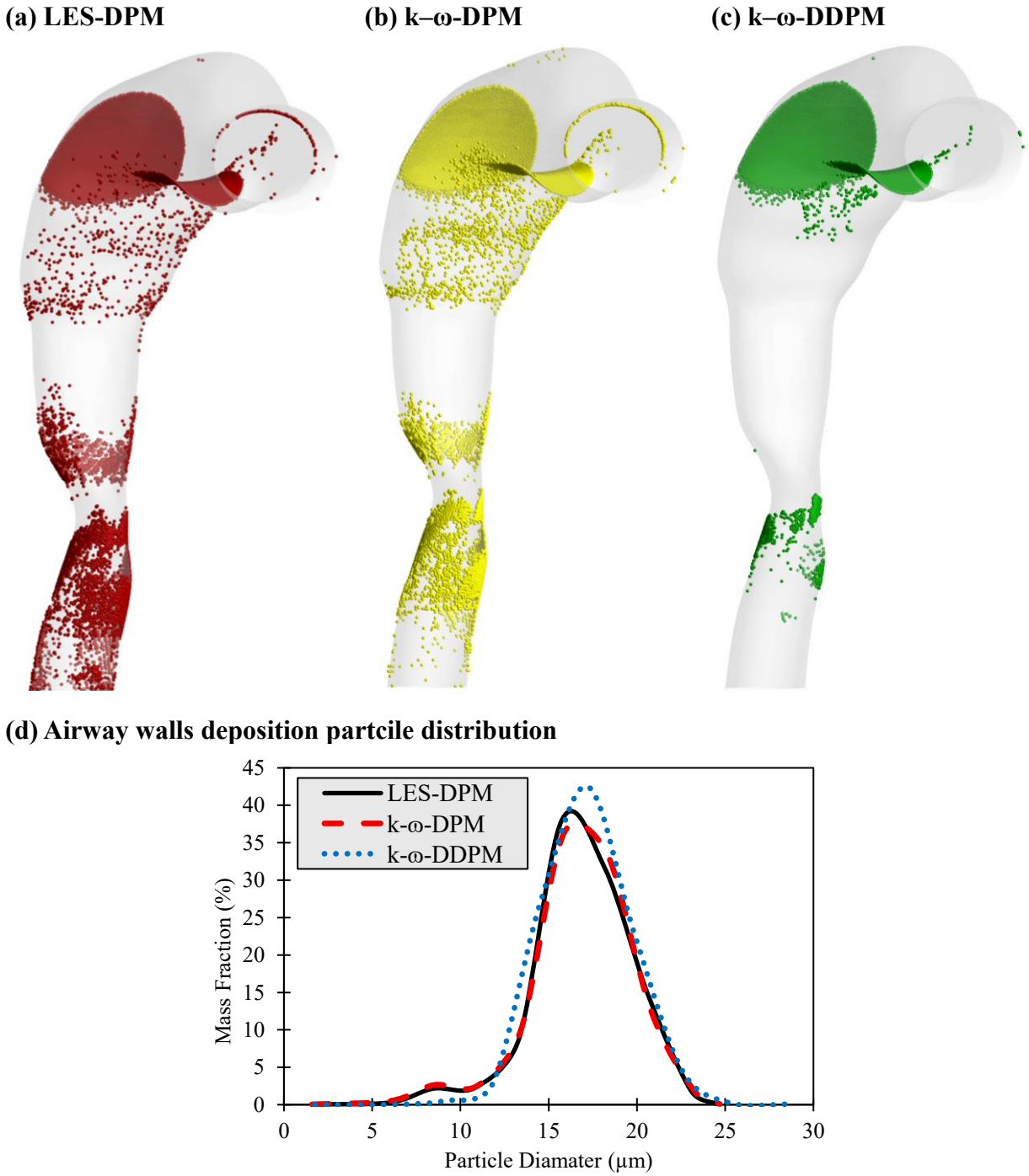

Fig. 9-8: Comparison of particle deposition patterns within the MT geometry predicted by **(a)** LES-DPM; **(b)** k–ω-DPM; and **(c)** k–ω-DDPM frameworks; and **(d)** corresponding deposited particle size distributions.

Although these interactions influence droplet growth and dispersion, their overall impact on total deposition remains moderate. The DDPM framework underpredicts total deposition by approximately 7% relative to in-vitro data (**Fig. 9-4(b)**), indicating a modest reduction in overall

MT deposition due to interphase and interparticle momentum exchange. Nevertheless, the deposited particle size distributions (**Fig. 9-8(d)**) remain consistent across all models, while the spatial deposition patterns differ substantially, highlighting the influence of dense-phase dynamics on local deposition behavior. Following the evaluation of velocity and flow patterns, the analysis proceeds to the thermal characteristics governing heat and mass transfer. The thermal behavior of the airflow and its influence on droplets were analyzed using the mean airflow temperature, the Jakob number (Ja), and the evaporation rate along the nozzle centerline at the midpoint of the injection time (t = 0.05 s), as shown in **Fig. 9-9**.

As shown in **Fig. 9-9(a)**, the mean airflow temperature decreases after the nozzle exit and gradually recovers downstream for all three models. The magnitude of this cooling varies among the three models. In this study, droplets were injected at 219.15 K (Ventolin plume initial injection temperature; Brambilla et al., 2011) into ambient air at 295.15 K, generating a strong initial thermal gradient. The k-ω-DDPM predicts the most pronounced drop, reaching a minimum of approximately 286 K within 5 mm of the nozzle, whereas LES-DPM and k-ω-DPM predict milder cooling (approximately 291-293 K). This discrepancy results directly from the energy sink term, which is active only in the DDPM.

Energy transport in the airflow phase is governed by the enthalpy conservation equation (Eq. (9-18)). The last two source terms, Q_{DPM} and $S_{\mathrm{DPM,\,explicit}}$, account for energy coupling between droplets and the carrier airflow and are included only in the DDPM formulation. Their presence introduces latent heat feedback from droplet evaporation directly into the airflow energy balance, whereas these terms are neglected in the one-way coupled DPM simulations. In one-way coupled DPM simulations, droplets absorb heat from the airflow without thermal feedback, leaving the airflow temperature largely unchanged.

The Jakob number (Ja) quantifies the ratio of available sensible heat in the gas phase (airflow) to the latent heat required for droplet vaporization (Shi et al., 2019), defined as:

$$Ja = c_{d,g}(T_p - T_{DPM})/h_{fg} \tag{9.36}$$

Where $c_{d,g}$ is the specific heat capacity of the airflow, and h_{fg} is the latent heat of vaporization of the droplet. Near the nozzle (0-5 mm), k-ω-DPM predicts the highest Ja (approximately 1.3), due to one-way and weak thermal coupling, which allows the airflow to remain relatively warm (as shown in **Fig. 9-9(a)**) while the droplets remain cold. In contrast, k-ω-DDPM predicts a lower

initial Ja (around 1.0), as two-way energy exchange and droplet-droplet interactions enhance evaporative cooling of the airflow, reducing $\Delta T = T_p - T_{DPM}$ within the dense spray core.

As the plume evolves downstream, *Ja* decreases monotonically in all models due to thermal equilibration between the airflow and droplets. The sharpest decline occurs in DPM, where droplets warm rapidly while the gas remains largely unaffected due to the uncoupled formulation. In contrast, DDPM maintains a higher downstream *Ja* (approximately 0.46 at 25 mm), as the dense spray preserves a significant interphase temperature gradient through ongoing vaporization and delayed droplet heating. Mirzaei et al. (2023) demonstrated in their CFD and experimental study of multiphase flow in industrial cyclone preheaters that the DDPM model effectively captures thermal features and dense particle effects, making it a reliable approach for simulating coupled momentum-energy transport in dense particulate systems. Their results confirmed that DDPM can accurately predict both gas-phase cooling and the delayed thermal response of particles in clustered regimes, phenomena that one-way coupled DPM models fail to resolve.

The evaporation rate profile (**Fig. 9-9(c)**) along the axial direction further elucidates the coupling between thermal gradients, droplet dynamics, and interphase heat and mass transfer. In both LES-DPM and k-ω-DPM frameworks, the evaporation rate increases steadily up to approximately 20 mm, despite the declining *Ja* number. This trend is attributed to the transition from sensible heating near the nozzle to latent-heat-driven vaporization downstream, where droplets reach their wet-bulb temperature and evaporation becomes more efficient (Sazhin, 2022; Yu and Chen, 2021). The progressive droplet shrinkage also enhances the surface-area-to-volume ratio, thereby intensifying local heat and mass transfer.

In the k-ω-DDPM framework, however, the evaporation rate exceeds those of both DPM models between 15 and 20 mm, reflecting dense-spray effects. First, droplet–droplet collisions within this dense region trigger secondary breakup, increasing the total droplet surface area available for vaporization (Kropotova and Strizhak, 2021). Second, the two-way energy coupling maintains favorable thermal gradients between the droplets and the surrounding gas, promoting continued evaporation. This behaviour is also reflected in the slightly higher Ja number observed at these distances (**Fig. 9-9(b)**) compared to that of the one-way-coupled DPM model. Beyond 20 mm, the DDPM-predicted evaporation rate drops sharply, even though the *Ja* number remains relatively high. This indicates the onset of a diffusion-limited regime, where vapor accumulation reduces the

vapor pressure gradient and, combined with gas-phase cooling and inter-droplet shielding, suppresses further mass transfer. Such behavior is typical of dense sprays and has been shown in detailed Eulerian-Lagrangian and DDPM simulations (Sazhin, 2022). In contrast, the DPM models do not capture this suppression due to the absence of vapor accumulation and energy feedback mechanisms.

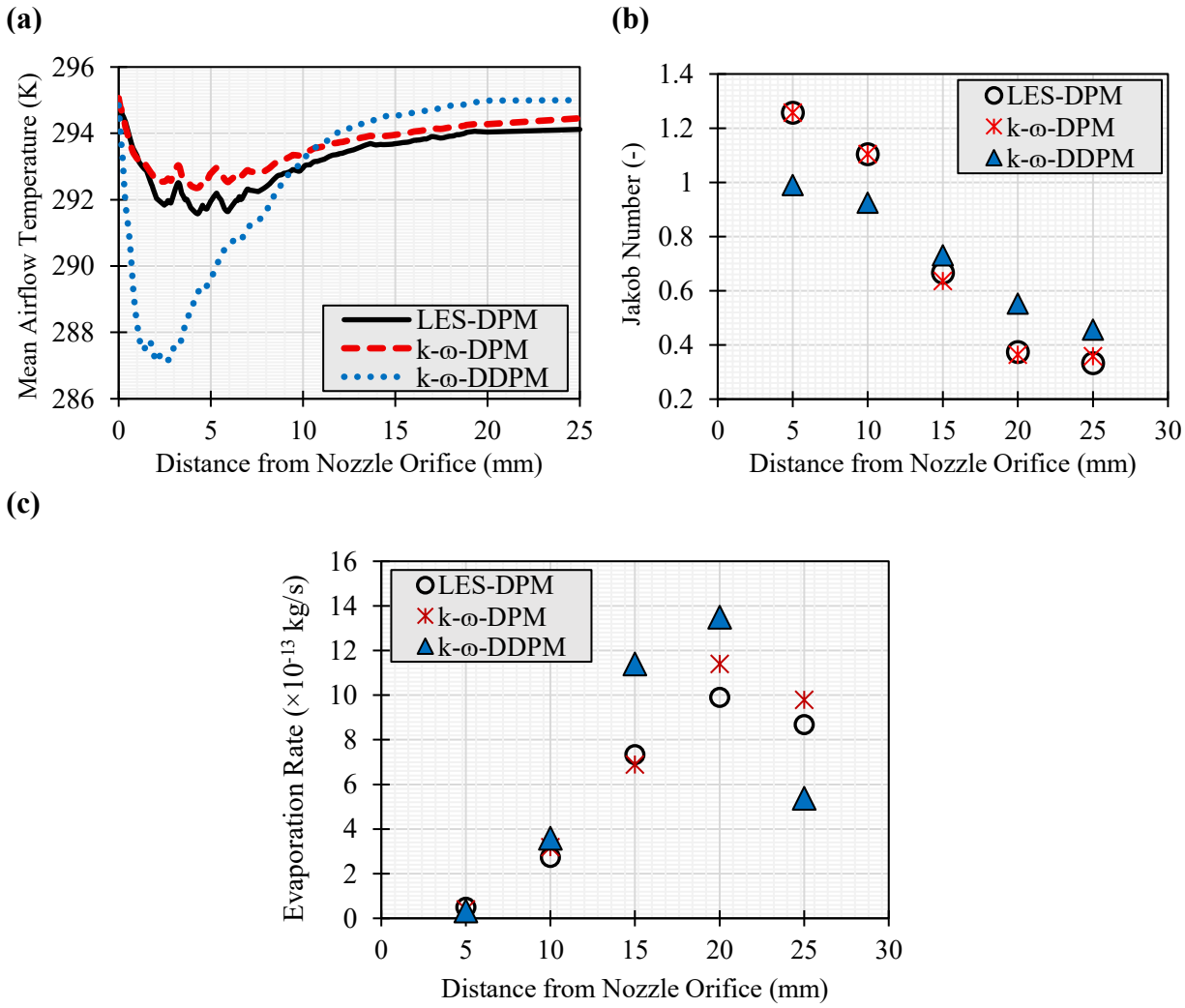

Fig. 9-9: **(a)** Mean airflow temperature; **(b)** Jakob number; and **(c)** evaporation rate along the axial direction, comparing predictions from the LES-DPM, k-ω-DPM, and k-ω-DDPM frameworks.

The variations in airflow temperature and evaporation rate along the spray axis influence the evolution of droplet size within the MT geometry. **Fig. 9-10** demonstrates the axial variation of mean droplet size predicted by the dilute and dense spray models, which are governed by local evaporation dynamics, droplet interactions, and interphase thermal feedback. Across all models,

the mean droplet size decreases progressively downstream due to continuous evaporation. However, the DDPM framework predicts overall larger droplets, despite showing the highest total evaporation rate between 15-20 mm. Overall, the k-ω-DDPM model predicted mean droplet sizes approximately 15% larger than those obtained from the LES-DPM and k-ω-DPM models. This outcome arises from dense-spray effects, frequent droplet–droplet collisions and coalescence, and energy redistribution, which maintain a broader size distribution. These findings indicate that local evaporation rates do not solely control mean droplet size but are also influenced by droplet population dynamics and two-way thermal coupling, effects uniquely captured in dense-spray modeling using DDPM. While the three models predict MT deposition within a comparable range, DDPM provides a more physically consistent and mechanistically complete description of dense spray behavior, particularly in capturing airflow cooling, inter-particle interactions, and downstream droplet evolution. These features are essential for realistic modeling of inhaler performance, patient-specific aerosol transport, and heat- or humidity-sensitive drug delivery systems. Nevertheless, further experimental validation is required to confirm the predictive capability and reliability of the DDPM approach.

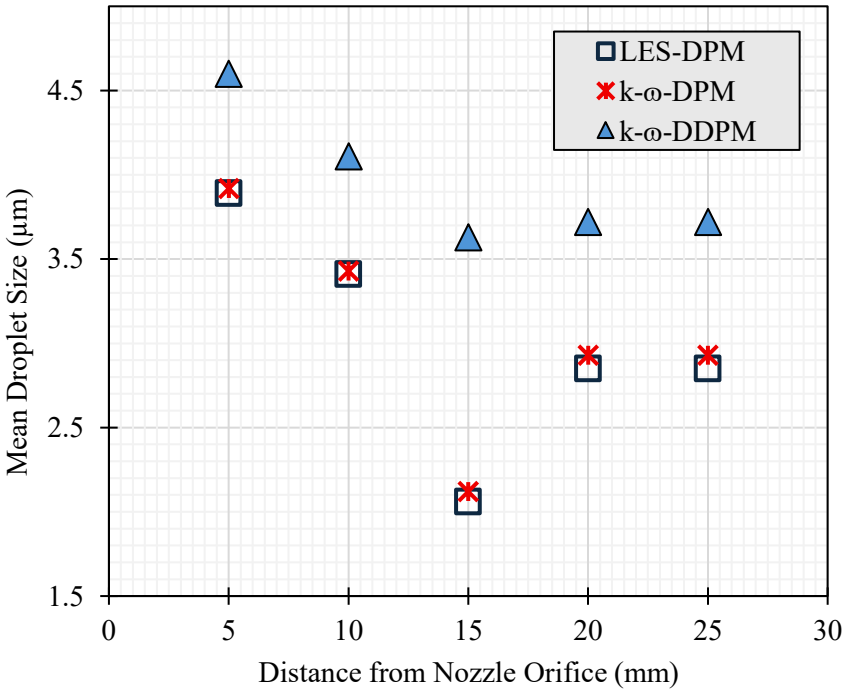

Fig. 9-10: Comparison of mean droplet size along the axial direction predicted by LES-DPM, k-ω-DPM, and k-ω-DDPM models.

9.5 Conclusions

This study aimed to evaluate the impact of different turbulence and phase-interaction models on simulating dense aerosol flow from pMDI by explicitly accounting for the HFA propellant, in addition to the API, a factor often neglected under the conventional dilute-phase assumption. To achieve this, three transient, three-dimensional two-phase flow simulations were conducted: k-ω-DPM and LES-DPM, both based on a dilute-phase, one-way-coupled assumption, and k-ω-DDPM, which adopts a dense-phase, four-way-coupled approach to account for droplet–airflow, droplet–droplet, and thermal interactions. These models were compared in terms of their ability to capture key physical phenomena, including plume structure, droplet evaporation, and regional deposition. Validation was performed against experimental deposition data under standardized flow conditions. Our results indicate that although the LES and k-ω frameworks exhibit distinct airflow structures, their overall deposition distributions remain comparable, as most pMDI particles are inertia-dominated and primarily influenced by impaction geometry rather than by small-scale turbulence. In contrast, the DDPM framework incorporates additional physics through interphase momentum exchange and particle-particle interactions, which directly modify the local jet dynamics. These dense-phase effects reduce the plume momentum and shift deposition downstream, resulting in lower impaction within the oral cavity and greater accumulation near the upper trachea. Consequently, the observed variations in regional deposition arise predominantly from interphase and interparticle coupling rather than differences in turbulence resolution. From a thermal perspective, the DDPM model demonstrates enhanced capability to resolve the coupled heat transfer between the airflow and droplet phases. Two-way energy exchange preserves realistic thermal gradients between droplets and the surrounding air, sustaining vaporization even in downstream regions where temperature differentials typically diminish. Furthermore, the DDPM framework captures the local airflow cooling induced by dense-spray interactions, an effect absent in one-way coupled DPM formulations. These coupled thermal interactions influence droplet size evolution and momentum, thereby reinforcing the downstream shift in deposition predicted by DDPM.

The DDPM framework bridges the gap between idealized dilute-phase models and the realistic dense-aerosol dynamics characteristic of pMDI sprays. In this study, DDPM was implemented alongside the k-ω turbulence model due to software constraints in *ANSYS Fluent*; however, future integration of DDPM with LES could enable more accurate predictions of aerosol–air interactions

and localized deposition, particularly in regions dominated by transient vortical structures and rapid jet-driven mixing.

Overall, the selection of a suitable modeling framework for simulating aerosol transport in pMDIs ultimately depends on the primary objective of the study. Based on our results, if the focus is on upper airway deposition fractions, the difference between models was relatively small, suggesting that lower-cost frameworks such as k-ω-DPM or LES-DPM can be sufficiently accurate. However, if the aim is to resolve complex, transitional, and turbulent airflow dynamics, the LES model is essential for its enhanced ability to capture unsteady vortical structures. For applications where detailed plume behavior and near-nozzle evaporation are of critical importance, particularly in dense sprays, the DDPM framework offers superior predictive capability by accounting for droplet–droplet and thermal interactions. Ultimately, this study provides a comparative framework to guide model selection based on simulation goals, balancing accuracy and computational efficiency.

9.6 Limitations and Future Directions

- The simulations were limited to the mouth–throat (MT) region, and aerosol transport and deposition in the downstream bronchial airways were not considered.
- In the dense-phase framework, the dense discrete phase model (DDPM) was coupled only with the k–ω turbulence model due to software constraints; coupling DDPM with large eddy simulation (LES) was not feasible in the present study.
- Airflow dynamics were not directly validated against experimental measurements; validation was performed through comparison of predicted deposition fractions with available in vitro and numerical studies.
- Inter-particle interactions were modeled at the continuum level within the DDPM framework, and detailed microscale collision and agglomeration effects were not explicitly resolved.

9.7 Nomenclature

3D	three dimensional
API	active pharmaceutical ingredient

CAD	computer-aided design
CFD	computational fluid dynamics
DDPM	dense discrete phase model
DEM	discrete element method
DNS	direct numerical simulation
DPM	discrete phase model
ECG	enhanced condensational growth
GiB	gibibyte
HFA	hydrofluoroalkane
HPLC	high-performance liquid chromatography
LES	large eddy simulation
MT	mouth-throat
NGI	next generation impactor
PIV	particle image velocimetry
PLA	polylactic acid
PMDI	pressurized metered-dose inhaler
RAM	random access memory
RANS	Reynolds-averaged Navier-Stokes
RDD	respiratory drug delivery
RH	relative humidity
SIMPLEC	semi-implicit method for pressure-linked equations-consistent
SST	shear stress transport
STL	stereolithography
TFM	two-fluid model
URANS	unsteady Reynolds-averaged Navier-Stokes
VCU	Virginia Commonwealth University
WALE	wall-adapting local eddy viscosity

Notations

$\bar{S}_{ij}$	filtered rate-of-strain tensor (1/s)
$\vec{J}_s$	species diffusion flux ($kg/m^2.s^1$)
$\dot{m}_{pq}$	mass transfer from phase q (droplets) to p (airflow) (kg/s)
$\dot{m}_{qp}$	mass transfer from phase p (airflow) to q (droplets) (kg/s)

$\bar{v}_{DPM}$	velocity of discrete phase (m/s)
$\overline{\boldsymbol{u}}_p$	time-averaged velocity of phase p (airflow) (m/s)
$\overline{\boldsymbol{u}}_{pq}$	velocity of mass transfer from phase q to p (m/s)
$\overline{\boldsymbol{u}}_{qp}$	velocity of mass transfer from phase p to q (m/s)
$\overline{\boldsymbol{u}}_{\boldsymbol{d}}$	velocity of droplet (m/s)
$\bar{\tau}_{eff}$	effective shear stress tensor (Pa)
h_{DPM}	particle-averaged interphase heat exchange coefficient (W/m^2.K)
h_c	convective heat transfer coefficient (W/m^2.K)
h_{pq}, h_{qp}	enthalpy associated with mass transfer between the airflow and droplets (J/kg)
h_s	enthalpy of a specific species (J/kg)
A_d	droplet surface area (m^2)
A_i	interfacial area between the droplets and the airflow (m^2)
B_T	Spalding heat transfer number (-)
$B_{m,i}$	Spalding mass number for species (-)
C_w	WALE constant ($= 0.325$) (-)
$\overline{D}$	arithmetic mean diameter of the droplets (m)
$D_{T,s}$	thermal diffusion coefficients (m^2/s)
$D_{s,m}$	mass diffusion coefficients (m^2/s)
F_l	Blending function to switch between k−ω (near-wall) and k−ϵ (far-field) (-)
K_{DPM}	drag coefficient (-)
L_s	mixing length for sub-grid scales (m)
$\bar{P}$	filtered pressure (Pa)
P_k	production of turbulent kinetic energy (W/m^3)
Q_{DPM}	convective heat transfer between droplets and the airflow (W/m^3)
Re_d	Reynolds number of droplets (-)
$\bar{S}$	rate-of-strain tensor for resolved scale (1/s)
$S_{DPM,explicit}$	explicit source term for DPM (kg/m^3.s)
S_{DPM}	mass transfer from discrete to continuous phase (kg/m^3.s)
Sc_t	turbulent Schmidt number (-)
S_s	source term as a result of droplet evaporation or condensation (kg/m^3.s)

T_{DPM}	particle-averaged temperature (K)
T_p	airflow temperature (K)
U_{rel}	relative velocity between two parcels (m/s)
We_c	collisional Weber number (-)
Y_s	mass fraction of species (-)
b_{crit}	critical offset (m)
$c_{P,s}$	specific heat capacity of the species (J/kg.K)
c_d	droplet heat capacity (J/kg.K)
e_p	internal energy of the airflow (J/kg)
k_K	von Kármán constant (-)
$k_{c,i}$	mass transfer coefficient of component (m/s)
k_{eff}	effective thermal conductivity (W/m.K)
k_t	turbulent thermal conductivity (W/m.K)
r_1, r_2	radii of the collector (larger) and smaller droplets (m)
v_t	turbulent eddy viscosity (m^2/s)
$\overline{\boldsymbol{u}}$	filtered velocity (m/s)
α_p	volume fraction of phase p (airflow) (-)
α_t	turbulent thermal diffusivity (m^2/s)
β^*, β	empirical constants (-)
μ_t	turbulent dynamic viscosity at sub-grid scales (kg/m.s)
ρ_p	mixture density of phase p (kg/m^3)
$\bar{\sigma}$	stress tensor due to molecular viscosity (Pa)
σ_k, σ_ω	turbulent Prandtl numbers for $k\ and\ \omega$ (-)
$\bar{\tau}$	subgrid-scale stress (Pa)
C_c	Cunningham correction factor (-)
C_D	drag coefficient (-)
d_d	diameter of droplet (m)
$\boldsymbol{F_i}$	body force (N/m^3)
h	enthalpy (J/kg)
k	thermal conductivity of the continuous phase (airflow) (W/m.K)

m_d	mass of droplet (kg)
λ	molecular mean free path (m)
μ	dynamic viscosity of mixture (kg/m.s)
ρ	density of mixture (air, water vapor, and droplet vapor) (kg/m^3)
ρ_d	density of droplet (kg/m^3)
$CD_{k\omega}$	cross-diffusion term (-)
Nu	Nusselt number (-)
Pr	Prandtl number (-)
Sh	Sherwood number (-)
V	computational cell volume (m^3)
Y	random number between 0 and 1 (-)
b	actual collision parameter (m)
d	distance to the closest wall (m)
f	function that accounts for the size ratio between the two droplets (-)
k	turbulent kinetic energy (m^2/s^2)
y	distance to the nearest wall (m)
σ	surface tension (N/m)
ω	specific dissipation rate (1/s)

9.8 References

Adamczyk, W.P., Klimanek, A., Białecki, R.A., Węcel, G., Kozołub, P., Czakiert, T., 2014. Comparison of the standard Euler-Euler and hybrid Euler-Lagrange approaches for modeling particle transport in a pilot-scale circulating fluidized bed. Particuology 15, 129–137. https://doi.org/10.1016/j.partic.2013.06.008

Aghaei, Y., Sajadi, B., Ahmadi, G., 2023. The effect of the mucus layer and the inhaled air conditions on the droplets fate in the human nasal cavity: A numerical study. J. Aerosol Sci. 171, 106163. https://doi.org/10.1016/j.jaerosci.2023.106163

Ahookhosh, K., Saidi, M., Mohammadpourfard, M., Aminfar, H., Hamishehkar, H., Farnoud, A., Schmid, O., 2021. Flow structure and particle deposition analyses for optimization of a pressurized metered dose inhaler (pMDI) in a model of tracheobronchial airway. Eur. J. Pharm. Sci. 164, 105911. https://doi.org/10.1016/j.ejps.2021.105911

Anderson, T.B., Jackson, R., 1967. Fluid mechanical description of fluidized beds: Equations of Motion. Ind. Eng. Chem. Fundam. 6, 527–539. https://doi.org/10.1021/i160024a007

ANSYS, 2024. ANSYS Fluent Theory Guide, ANSYS Inc., USA.

Ariyaratne, W.K.H., Manjula, E.V.P.J., Ratnayake, C., Melaaen, M.C., 2018. CFD approaches for modeling gas-solids multiphase flows - A review. Proc. 9th EUROSIM Congr. Model. Simulation, EUROSIM 2016, 57th SIMS Conf. Simul. Model. SIMS 2016 142, 680–686. https://doi.org/10.3384/ecp17142680

Balachandar, S., Eaton, J.K., 2010. Turbulent Dispersed Multiphase Flow. Annu. Rev. Fluid Mech. 42, 111–133. https://doi.org/https://doi.org/10.1146/annurev.fluid.010908.165243

Ball, C.G., Uddin, M., Pollard, A., 2008. High resolution turbulence modelling of airflow in an idealised human extra-thoracic airway. Comput. Fluids 37, 943–964. https://doi.org/10.1016/j.compfluid.2007.07.021

Biswas, R., Hanania, N.A., Sabharwal, A., 2017. Factors determining in vitro lung deposition of albuterol aerosol delivered by ventolin metered-dose inhaler. J. Aerosol Med. Pulm. Drug Deliv. 30, 256–266. https://doi.org/10.1089/jamp.2015.1278

Borojeni, A.A.T., Gu, W., Asgharian, B., Price, O., Kuprat, A.P., Singh, R.K., Colby, S., Corley, R.A., Darquenne, C., 2023. In silico quantification of intersubject variability on aerosol deposition in the oral airway. Pharmaceutics 15, 160. https://doi.org/10.3390/pharmaceutics15010160

Brambilla, G., Church, T., Lewis, D., Meakin, B., 2011. Plume temperature emitted from metered dose inhalers. Int. J. Pharm. 405, 9–15. https://doi.org/10.1016/j.ijpharm.2010.11.037

Burman, B.C., Cundall, P.A., Strack, O.D.L., 1980. A discrete numerical model for granular assemblies. Geotechnique 30, 331–336. https://doi.org/10.1680/geot.1980.30.3.331

Chen, X., Wang, J., 2014. A comparison of two-fluid model, dense discrete particle model and CFD-DEM method for modeling impinging gas-solid flows. Powder Technol. 254, 94–102. https://doi.org/10.1016/j.powtec.2013.12.056

Cheng, Y.S., Fu, C.S., Yazzie, D., Zhou, Y., 2001. Respiratory deposition patterns of salbutamol

pMDI with CFC and HFA-134a formulations in a human airway replica 14, 255–266. https://doi.org/10.1089/08942680152484180

Cheng, Y.S., Zhou, Y., Su, W.C., 2015. Deposition of particles in human mouth-throat replicas and a USP induction port. J. Aerosol Med. Pulm. Drug Deliv. 28, 147–155. https://doi.org/10.1089/jamp.2013.1105

Cristea, E.D., Conti, P., 2018. Hybrid eulerian multiphase-dense discrete phase model approach for numerical simulation of dense particle-laden turbulent flows within vertical multi-stage cyclone heat exchanger. Am. Soc. Mech. Eng. Fluids Eng. Div. FEDSM 2, 1–15. https://doi.org/10.1115/FEDSM2018-83058

Crowe, C.T., Schwarzkopf, J.D., Sommerfeld, M., Tsuji, Y., 2011. Dams and Reservoirs under Changing Challenges, 2nd ed. CRC Press, Boca Raton, FL. https://doi.org/10.1201/b11669

Cui, X., 2011. CFD Study of the Flow Field and Particle Dispersion and Deposition in the Upper Human Respiratory System. Heidelberg University, Heidelberg, Germany.

Cui, X.G., Gutheil, E., 2011. Large eddy simulation of the unsteady flow-field in an idealized human mouth-throat configuration. J. Biomech. 44, 2768–2774. https://doi.org/10.1016/j.jbiomech.2011.08.019

Dastoorian, F., Pakzad, L., Kozinski, J., Behzadfar, E., 2022. A CFD Investigation on the Aerosol Drug Delivery in the Mouth–Throat Airway Using a Pressurized Metered-Dose Inhaler Device. Processes 10, 1230. https://doi.org/10.3390/pr10071230

Delvadia, R.R., Longest, P.W., Byron, P.R., 2012. In Vitro Tests for Aerosol Deposition. I: Scaling a Physical Model of the Upper Airways to Predict Drug Deposition Variation in Normal Humans. J. Aerosol Med. Pulm. Drug Deliv. 25, 32–40. https://doi.org/10.1089/jamp.2011.0905

Delvadia, R.R., Wei, X., Longest, P.W., Venitz, J., Byron, P.R., 2016. In Vitro Tests for Aerosol Deposition. IV: Simulating Variations in Human Breath Profiles for Realistic DPI Testing. J. Aerosol Med. Pulm. Drug Deliv. 29, 196–206. https://doi.org/10.1089/jamp.2015.1215

Duke, D.J., Nguyen, D.T., Dos Reis, L.G., Silva, D.M., Neild, A., Edgington-Mitchell, D., Young, P.M., Honnery, D.R., 2021. Increasing the fine particle fraction of pressurised metered dose inhaler solutions with novel actuator shapes. Int. J. Pharm. 597, 120341.

https://doi.org/10.1016/j.ijpharm.2021.120341

Duke, D.J., Scott, H.N., Kusangaya, A.J., Kastengren, A.L., Matusik, K., Young, P., Lewis, D., Honnery, D., 2019. Drug distribution transients in solution and suspension-based pressurised metered dose inhaler sprays. Int. J. Pharm. 566, 463–475. https://doi.org/10.1016/j.ijpharm.2019.05.067

Elghobashi, S., 1994. On predicting particle-laden turbulent flows. Appl. Sci. Res. 52, 309–329. https://doi.org/10.1007/BF00936835

Feng, Y., Kleinstreuer, C., 2014. Micron-particle transport, interactions and deposition in triple lung-airway bifurcations using a novel modeling approach. J. Aerosol Sci. 71, 1–15. https://doi.org/10.1016/j.jaerosci.2014.01.003

Feng, Y., Zhao, J., Hayati, H., Sperry, T., Yi, H., 2021a. Tutorial : Understanding the transport , deposition , and translocation of particles in human respiratory systems using Computational Fluid-Particle Dynamics and Physiologically Based Toxicokinetic models. J. Aerosol Sci. 151, 105672. https://doi.org/10.1016/j.jaerosci.2020.105672

Feng, Y., Zhao, J., Hayati, H., Sperry, T., Yi, H., 2021b. Tutorial: Understanding the transport, deposition, and translocation of particles in human respiratory systems using Computational Fluid-Particle Dynamics and Physiologically Based Toxicokinetic models. J. Aerosol Sci. 151, 105672. https://doi.org/10.1016/j.jaerosci.2020.105672

Finlay, W.H., 2019. The Mechanics of Inhaled Pharmaceutical Aerosols: An Introduction. Elsevier Science.

Gessner, T., 2001. Dynamic mesh adaption for supersonic combustion waves modeled with detailed reaction mechanisms. Freiburg (Breisgau), Univ., Diss.

Golshahi, L., Noga, M.L., Vehring, R., Finlay, W.H., 2013. An in vitro study on the deposition of micrometer-sized particles in the extrathoracic airways of adults during tidal oral breathing. Ann. Biomed. Eng. 41, 979–989. https://doi.org/10.1007/s10439-013-0747-0

Huang, F., Zhu, Q., Zhou, X., Gou, D., Yu, J., Li, R., Tong, Z., Yang, R., 2021. Role of CFD based in silico modelling in establishing an in vitro-in vivo correlation of aerosol deposition in the respiratory tract. Adv. Drug Deliv. Rev. https://doi.org/10.1016/j.addr.2020.09.007

Islam, M.S., Paul, G., Ong, H.X., Young, P.M., Gu, Y.T., Saha, S.C., 2020. A review of respiratory anatomical development, air flow characterization and particle deposition. Int. J. Environ. Res. Public Health 17. https://doi.org/10.3390/ijerph17020380

Islam, M.S., Saha, S.C., Sauret, E., Ong, H., Young, P., Gu, Y., 2019. Euler–Lagrange approach to investigate respiratory anatomical shape effects on aerosol particle transport and deposition. Toxicol. Res. Appl. 3, 239784731989467. https://doi.org/10.1177/2397847319894675

Jahed, M., Kozinski, J., Pakzad, L., 2025. Experimental and numerical investigation of drug delivery in patient-specific male and female airways : Role of airway wall motion , breathing patterns , and mucus layer. J. Drug Deliv. Sci. Technol. 113, 107409. https://doi.org/10.1016/j.jddst.2025.107409

Jahed, M., Kozinski, J., Pakzad, L., 2024. Mucus, airway and plume temperature effects on pMDI-drug delivery in a mouth-throat airway: Experimental and numerical studies. J. Aerosol Sci. 181, 106436. https://doi.org/10.1016/j.jaerosci.2024.106436

Jayaraju, S.T., Brouns, M., Lacor, C., Belkassem, B., Verbanck, S., 2008. Large eddy and detached eddy simulations of fluid flow and particle deposition in a human mouth-throat. J. Aerosol Sci. 39, 862–875. https://doi.org/10.1016/j.jaerosci.2008.06.002

Koullapis, P., Kassinos, S.C., Muela, J., Perez-Segarra, C., Rigola, J., Lehmkuhl, O., Cui, Y., Sommerfeld, M., Elcner, J., Jicha, M., Saveljic, I., Filipovic, N., Lizal, F., Nicolaou, L., 2018. Regional aerosol deposition in the human airways: The SimInhale benchmark case and a critical assessment of in silico methods. Eur. J. Pharm. Sci. 113, 77–94. https://doi.org/10.1016/j.ejps.2017.09.003

Kropotova, S., Strizhak, P., 2021. Collisions of liquid droplets in a gaseous medium under conditions of intense phase transformations: Review. Energies 14. https://doi.org/10.3390/en14196150

Liu, H., Ma, S., Hu, T., Ma, D., 2023. Computational investigation of flow characteristics and particle deposition patterns in a realistic human airway model under different breathing conditions. Respir. Physiol. Neurobiol. 314, 104085. https://doi.org/10.1016/j.resp.2023.104085

Longest, P.W., Hindle, M., 2010. CFD simulations of enhanced condensational growth (ECG) applied to respiratory drug delivery with comparisons to in vitro data. J. Aerosol Sci. 41, 805–820. https://doi.org/10.1016/j.jaerosci.2010.04.006

Longest, P.W., Hindle, M., 2009. Evaluation of the respimat soft mist inhaler using a concurrent cfd and in vitro approach. J. Aerosol Med. Pulm. Drug Deliv. 22, 99–112. https://doi.org/10.1089/jamp.2008.0708

Longest, P.W., Hindle, M., Das Choudhuri, S., Xi, J., 2008. Comparison of ambient and spray aerosol deposition in a standard induction port and more realistic mouth-throat geometry. J. Aerosol Sci. 39, 572–591. https://doi.org/10.1016/j.jaerosci.2008.03.008

Longest, P.W., Tian, G., Delvadia, R., Hindle, M., 2012. Development of a stochastic individual path (SIP) model for predicting the deposition of pharmaceutical aerosols: Effects of turbulence, polydisperse aerosol size, and evaluation of multiple lung lobes. Aerosol Sci. Technol. 46, 1271–1285. https://doi.org/10.1080/02786826.2012.708799

McKiernan, A.P., 2019. Inhaler spray investigation using high-speed phase-contrast X-Ray and schlieren imaging. Pharm. Res. 36. https://doi.org/10.1007/s11095-019-2657-9

Mirzaei, M., Clausen, S., Wu, H., Zakrzewski, S., Nakhaei, M., Zhou, H., Martin Jønck, K., Arendt Jensen, P., Lin, W., 2023. CFD simulation and experimental validation of multiphase flow in industrial cyclone preheaters. Chem. Eng. J. 465, 1–15. https://doi.org/10.1016/j.cej.2023.142757

Mohammadkhani, M., Kozinski, J., Pakzad, L., 2026. A Novel End - to - End Simulation Framework for Internal Flow in pMDIs : Coupled Modeling of Cavitation , Flash Boiling , and Atomization.

Mohammadkhani, M., Kozinski, J., Pakzad, L., 2025a. Atomization characteristics of soft mist inhaler (SMI) devices: aerosolized particle delivery through the respiratory tract—an innovative numerical and experimental study. J. Aerosol Sci. 106593. https://doi.org/10.1016/j.jaerosci.2025.106593

Mohammadkhani, M., Kozinski, J., Pakzad, L., 2025b. Grid-induced aerosol optimization in pMDIs : A multiscale design , simulation , and experimental study. Int. J. Pharm. 684, 126087. https://doi.org/10.1016/j.ijpharm.2025.126087

Morsi, S.A., Alexander, A.J., 1972. An investigation of particle trajectories in two-phase flow systems. J. Fluid Mech. 55, 193–208. https://doi.org/10.1017/S0022112072001806

Narayanan, J.K., Lin, J., Feng, Y., Cui, X., 2022. Numerical study on the impact of mucus layer and inlet air-temperatures on the particle deposition in a highly idealized mouth-throat model using LES. Powder Technol. 395, 455–475. https://doi.org/10.1016/j.powtec.2021.09.073

Newman, S., 2015. RDD Online Respiratory Drug Delivery, Metered Dose Inhalers [WWW Document]. 2015-08-18. URL http://www.rddonline.com/education/online_training/MDIs/player.html

Nicoud, F., Ducros, F., 1999. Subgrid-scale stress modelling based on the square of the velocity. Flow Meas. Instrum. 62, 183–200. https://doi.org/https://doi.org/10.1023/A:1009995426001

O'Rourke, P.J., 1981. Collective drop effects on vaporizing liquid sprays. Los Alamos National Lab., NM (USA).

Rahman, M.M., Zhao, M., Islam, M.S., Dong, K., Saha, S.C., 2021. Aging effects on airflow distribution and micron-particle transport and deposition in a human lung using CFD-DPM approach. Adv. Powder Technol. 32, 3506–3516. https://doi.org/10.1016/j.apt.2021.08.003

Ranz, W.E., Marshall, W.R., 1952. Evaporation from drops : Part II. Chem. Eng. Prog. 48, 173–180.

Sadeghi, T., Fatehi, P., Pakzad, L., 2025. Aerosol drug delivery in pediatric airways: in vitro and CFD insights into tongue position and inhalation patterns using soft mist inhalers. Int. J. Pharm. 683, 126059. https://doi.org/10.1016/j.ijpharm.2025.126059

Sadeghi, T., Pakzad, L., Fatehi, P., 2023. Evaluation of soft mist inhaler aerosol velocity, size, and deposition inside the mouth - A computational fluid dynamics study. J. Biomech. Eng. 145. https://doi.org/10.1115/1.4056967

Sarkar, S., Peri, S.P., Chaudhuri, B., 2017. Investigation of multiphase multicomponent aerosol flow dictating pMDI-spacer interactions. Int. J. Pharm. 529, 264–274. https://doi.org/10.1016/j.ijpharm.2017.07.005

Sazhin, S.S., 2022. Droplets and Sprays: Simple Models of Complex Processes, 1st ed,

Mathematical Engineering. Springer International Publishing, Cham. https://doi.org/10.1007/978-3-030-99746-5

Sheth, P., Grimes, M.R., Stein, S.W., Myrdal, P.B., 2017. Impact of droplet evaporation rate on resulting in vitro performance parameters of pressurized metered dose inhalers. Int. J. Pharm. 528, 360–371. https://doi.org/10.1016/j.ijpharm.2017.06.014

Shi, M., Frank, F., Wang, L., Xu, F., Lu, T.J., Grigoropoulos, C.P., 2019. Role of Jakob number in Leidenfrost phenomena unveiled by theoretical modeling. https://doi.org/10.1063/1.5082266

Sommerfeld, M., 2001. Validation of a stochastic Lagrangian modelling approach for inter-particle collisions in homogeneous isotropic turbulence. Int. J. Multiph. Flow 27, 1829–1858. https://doi.org/10.1016/S0301-9322(01)00035-0

Sou, T., Bergström, C.A.S., 2021. Contemporary formulation development for inhaled pharmaceuticals. J. Pharm. Sci. 110, 66–86. https://doi.org/10.1016/j.xphs.2020.09.006

Stahlhofen, W., Rudolf, G., James, A.C., 1989. Intercomparison of experimental regional aerosol deposition data. J. Aerosol Med. Depos. Clear. Eff. Lung 2, 285–308. https://doi.org/10.1089/jam.1989.2.285

Stein, S.W., Sheth, P., Hodson, P.D., Myrdal, P.B., 2014. Advances in metered dose inhaler technology: Hardware development. AAPS PharmSciTech 15, 326–338. https://doi.org/10.1208/s12249-013-0062-y

Talaat, M., Si, X., Xi, J., 2022. Effect of MDI actuation timing on inhalation dosimetry in a human respiratory tract model. Pharmaceuticals 15, 61. https://doi.org/10.3390/ph15010061

Versteeg, H.K., Hargrave, G.K., Myatt, B.J., Lewis, D.A., Church, T., Brambilla, G., 2017. Using phase doppler anemometry and high speed imaging to analyze MDI spray plume dynamics. Respir. Drug Deliv. Eur.

Wilcox, D.C., 1993. Turbulence Modelling for CFD 3rd Edition, Turbulence Modeling for CFD.

Williams, J., Menendez Montes, J.M., Cunningham, S., Wolfram, U., Ozel, A., 2025. Deposition simulations of realistic dosages in patient-specific airways with two- and four-way coupling. Int. J. Pharm. 669, 1–31. https://doi.org/10.1016/j.ijpharm.2024.125019

Worth Longest, P., Hindle, M., 2009. Evaluation of the respimat soft mist inhaler using a concurrent cfd and in vitro approach. J. Aerosol Med. Pulm. Drug Deliv. 22, 99–112. https://doi.org/10.1089/jamp.2008.0708

Wu, C., Yan, W., Chen, R., Liu, Y., Li, G., 2022. Numerical study on targeted delivery of magnetic drug particles in realistic human lung. Powder Technol. 397, 116984. https://doi.org/10.1016/j.powtec.2021.11.028

Wu, W., Duan, L., Duan, Y., Li, L., Liu, D., Pallarès, D., 2023. Three-dimensional full-loop numerical simulation of coal and sludge co-combustion in a circulating fluidized bed. Fuel 337, 120464. https://doi.org/10.1016/j.fuel.2022.127235

Xi, J., Longest, P.W., 2008. Effects of oral airway geometry characteristics on the diffusional deposition of inhaled nanoparticles. J. Biomech. Eng. 130, 13–17. https://doi.org/10.1115/1.2838039

Xi, J., Longest, P.W., 2007. Transport and deposition of micro-aerosols in realistic and simplified models of the oral airway. Ann. Biomed. Eng. 35, 560–581. https://doi.org/10.1007/s10439-006-9245-y

Xi, J., Yuan, J.E., Yang, M., Si, X., Zhou, Y., Cheng, Y.S., 2016. Parametric study on mouth–throat geometrical factors on deposition of orally inhaled aerosols. J. Aerosol Sci. 99, 94–106. https://doi.org/10.1016/j.jaerosci.2016.01.014

Xu, C., Zheng, X., Shen, S., 2021. A numerical study of the effects of ambient temperature and humidity on the particle growth and deposition in the human airway. Environ. Res. 200, 111751. https://doi.org/10.1016/j.envres.2021.111751

Yu, D., Chen, Z., 2021. Theoretical analysis on droplet vaporization at elevated temperatures and pressures, International Journal of Heat and Mass Transfer. Elsevier Ltd. https://doi.org/10.1016/j.ijheatmasstransfer.2020.120542

Zhang, Z., Kim, C.S., Kleinstreuer, C., 2006. Water vapor transport and its effects on the deposition of hygroscopic droplets in a human upper airway model. Aerosol Sci. Technol. 40, 1–16. https://doi.org/10.1080/02786820500461154

Zhang, Z., Kleinstreuer, C., Kim, C.S., 2002. Micro-particle transport and deposition in a human oral airway model. J. Aerosol Sci. 33, 1635–1652. https://doi.org/10.1016/S0021-

8502(02)00122-2

Zhao, Y., Raco, J., Kourmatzis, A., Diasinos, S., Chan, H.K., Yang, R., Cheng, S., 2020. The effects of upper airway tissue motion on airflow dynamics. J. Biomech. 99, 109506. https://doi.org/10.1016/j.jbiomech.2019.109506

Zhou, Y., Sun, J., Cheng, Y.S., 2011. Comparison of deposition in the USP and physical mouth-throat models with solid and liquid particles. J. Aerosol Med. Pulm. Drug Deliv. 24, 277–284. https://doi.org/10.1089/jamp.2011.0882

Chapter 10- Concluding Remarks and Future Recommendations

10.1 Novelty and Original Contributions

This study introduces several novel contributions to the fields of inhalation aerosol modeling, multiphase CFD, and respiratory biomechanics. The main innovations of the work are summarized below:

- **Plume behavior across environmental conditions:**

A systematic characterization of pMDI plume dynamics under varying environmental setups, directly comparing confined (airway-attached) versus open-air releases.

- **Thermal interactions with inhaled air and mucus:**

New insights into the coupled thermal interactions between cold pMDI plumes, inhaled air temperature, and the airway mucus layer, with quantification of their effects on droplet evaporation, cooling, and size evolution.

- **Patient-specific anatomy and disease effects:**

The first quantitative evaluation of how patient-specific factors—such as gender, COPD pathology, and variations in airway dimensions—alter airflow patterns and drug deposition profiles in the upper respiratory tract.

- **Physiologically based, time-dependent wall deformation:**

Development and validation of a realistic, time-dependent wall-motion UDF capturing airway deformation based on physiological measurements, enabling CFD simulations within dynamically deforming upper-airway geometries.

- **Impact of real-life breathing irregularities:**

Assessment of how clinically observed breathing deviations (e.g., pauses, premature exhalations, coughing) influence drug delivery efficiency, offering actionable insights to support physicians in refining patient inhalation instructions.

- **Fully coupled pMDI plume–airflow modeling and turbulence-framework comparison:**

Establishment of the first fully coupled CFD framework integrating pMDI plume generation with patient-specific airway airflow, accompanied by a comprehensive comparison of three advanced turbulence–particle modeling approaches (LES–DPM, k–ω–DPM, and k–ω–DDPM) for pMDI applications.

10.2 Summary of Findings

This study presents a comprehensive computational fluid dynamics (CFD) investigation into aerosol transport and drug deposition from pressurized metered-dose inhalers (pMDIs). A series of studies was conducted to investigate the impact of device design, thermal and geometric factors, breathing irregularities, and multiphase modelling frameworks on drug delivery efficiency in the human respiratory tract.

The first part of this thesis introduces a novel modelling framework that examines the impact of nozzle geometry and actuator design on plume formation and particle deposition. For the first time, aerosol sprays from both conventional and twin nozzles were simulated and systematically compared under open-air and realistic mouth–throat (MT) inhalation conditions using a Large-Eddy Simulation–Discrete Phase Model (LES–DPM). The twin nozzles produced two converging sprays that merged rapidly upon exiting the orifices, forming a narrower, faster plume composed of finer droplets. Despite this higher initial velocity, the twin nozzle increased deposition within the MT region and reduced delivery efficiency to distal airways. These findings highlight the importance of balancing jet momentum and plume width rather than simply increasing injection velocity. It is also emphasized that the need to model spray development in realistic airway geometries, as open-air results do not accurately represent in vivo inhalation conditions.

The second study establishes a comprehensive, fully coupled thermal–aerosol modeling framework that simultaneously accounts for all major parameters influencing inhaled droplet behavior. LES–DPM simulations evaluated varying plume and ambient air temperatures, along with airway walls featuring tissue and mucus layers. Raising the plume temperature from –54 °C to 10 °C enhanced droplet evaporation by 21% and reduced mean particle diameter by 34%, yet paradoxically increased deposition by up to 18% due to altered local airflow. Ambient air

temperature had a minimal effect on overall deposition. The inclusion of a mucus layer introduced localized moisture gradients, reducing total deposition by approximately 11%, which highlights its regulatory role in near-wall dynamics. This demonstrates that incorporating even a thin mucus layer improves physiological accuracy in CFD simulations with negligible computational overhead.

The third study presents a detailed patient-specific modelling framework, which, for the first time in the Multiphase Flow Research (MFR) lab, employs CT-derived airway geometries to capture realistic anatomical features. Building on this foundation, the study further explores broader research challenges in incorporating gender-specific airway differences and dynamic wall motion into aerosol transport modeling. Airflow and particle deposition were evaluated in male and female airway models under both healthy and COPD-like flow conditions, with and without airway deformation. Narrower female airways exhibited higher velocities and turbulence, leading to stronger inertial impaction and a 48% increase in particle loss in the upper airway. Wider male airways allowed deeper penetration, with only 32% upper-airway losses. COPD-like flows, characterized by gradual acceleration, reduced turbulence and shifted deposition to deeper regions, thereby improving lung delivery by up to 16%. Airway wall motion modestly decreased deposition (~4%) due to transient volume changes, with limited impact on the brief 0.1 s pMDI spray. These results highlight the potential for personalized inhaler design tailored to gender-specific anatomy and disease state.

The fourth study offers a new perspective on inhaler aerosol research by investigating the impact of breathing irregularities, including inhalation pauses, unintentional exhalation, and coughing, on aerosol transport and deposition patterns. LES–DPM simulations, validated against experimental data, showed that unsteady inhalation disrupted vortex formation, increased turbulence kinetic energy (TKE), and shifted particle deposition proximally. Coughing generated the highest TKE, redirecting over 80% of the emitted dose to the upper airway, while premature exhalation caused up to 28% particle loss, particularly for submicron and fine particles (<2 μm). These findings underscore the crucial importance of proper inhalation technique in minimizing drug loss and ensuring effective lung delivery.

Finally, three computational frameworks—LES–DPM, k–ω–DPM, and k–ω–Dense Discrete Phase Model (DDPM)—were compared to capture dense aerosol behavior during high-speed

pMDI injection. The integration of the DDPM approach enables a detailed analysis of particle–particle and particle–air interactions, offering new insights into the behaviour of dense aerosols. All models reproduced experimental deposition trends, with LES–DPM and k–ω–DPM closely matching in-vitro data, while k–ω–DDPM underpredicted total deposition by 7%. DDPM revealed unique regional deposition patterns and size redistribution due to interphase and interparticle coupling, leading to plume deceleration and reduced oral impaction. LES–DPM effectively captured transient turbulent mixing, while DDPM provided a more physically realistic description of dense spray behavior, bridging the gap between dilute-phase and fully coupled multiphase models. Future integration of DDPM with LES is expected to further enhance predictive accuracy in transient aerosol flows.

Overall, this study makes substantial and influential contributions to the field of aerosol drug delivery by integrating multiphase flow modeling, medical imaging, and rigorous experimental validation using NGI and HPLC. Aerosol transport was investigated in realistic, patient-specific airway geometries using advanced LES and DPM/DDPM frameworks implemented in ANSYS Fluent and augmented with user-defined functions to capture plume dynamics, airway structure, and mucus-layer effects. The resulting findings—published in leading journals including *the Journal of Aerosol Science, the Journal of Drug Delivery Science and Technology, Biomechanics and Modeling in Mechanobiology*, and *Pharmaceutical Research*, with one additional manuscript currently under review in *Powder Technology*—have significantly advanced understanding of how anatomical and physiological variability governs pulmonary drug deposition. These contributions provide critical insights for optimizing inhaler design and improving targeted aerosol delivery. The breadth and impact of this work are further demonstrated through dissemination at national (CSChE 2023) and international (Respiratory Drug Delivery 2025) conferences, with selection of the RDD 2025 abstract for the prestigious *Posters on the Podium (POP)* session, recognizing both research excellence and presentation quality.

10.3 Limitations and Future Recommendations

Although this research provides extensive insight into aerosol transport and deposition in the upper airway, several aspects can be further improved:

(a) Device Modeling – Simulations started at the actuator outlet, excluding internal canister and nozzle flows. Future work should model the entire pMDI assembly, including the valve and

expansion chamber, to capture two-phase expansion, atomization, and droplet breakup, thereby linking internal device physics with external spray behavior.

(b) Distal Lung Deposition – The study focused on the mouth to the fourth bronchial generation (G4). Extending the computational domain deeper into the lungs would allow assessment of total drug delivery efficiency, including deposition mechanisms such as sedimentation and diffusion in distal bronchioles and alveoli. Integrating patient-specific CT- or MRI-based airway geometries with machine-learning-assisted CFD could reduce computational cost and enable faster, personalized predictions.

(c) Dense-phase Turbulence Coupling – The DDPM framework was limited to the k–ω turbulence model. Coupling DDPM with LES would capture dense-phase interactions alongside transient turbulence structures, leading to more realistic predictions of spray dispersion and regional deposition.

(d) Mucus and Wall Motion – The mucus layer was treated as stationary. Modeling viscoelastic mucus motion and airway wall deformation would provide a more accurate representation of particle–wall interactions and local drug retention.

(e) Experimental Validation – Further in-vitro validation under realistic breathing, temperature, and humidity conditions is essential. Advanced diagnostics, such as high-speed imaging or particle image velocimetry (PIV), in transparent airway models can provide high-quality datasets for validating CFD predictions.